**FUSION MATERIALS
SEMIANNUAL PROGRESS REPORT
FOR THE PERIOD ENDING**

December 31, 2011

**Prepared for
DOE Office of Fusion Energy Sciences
(AT 60 20 10 0)**

DATE PUBLISHED: April 2011

**Prepared by
OAK RIDGE NATIONAL LABORATORY
Oak Ridge, Tennessee 37831
Managed by
UT-Battelle, LLC
For the
U.S. DEPARTMENT OF ENERGY**

FOREWORD

This is the fifty-first in a series of semiannual technical progress reports on fusion materials science activity supported by the Fusion Energy Sciences Program of the U.S. Department of Energy. It covers the period ending December 31, 2011. This report focuses on research addressing the effects on materials properties and performance of exposure to the neutronic, thermal and chemical environments anticipated in the chambers of fusion experiments and energy systems. This research is a major element of the national effort to establish the materials knowledge base for an economically and environmentally attractive fusion energy source. Research activities on issues related to the interaction of materials with plasmas are reported separately.

The results reported are the products of a national effort involving a number of national laboratories and universities. A large fraction of this work, particularly in relation to fission reactor irradiations, is carried out collaboratively with partners in Japan, Russia, and the European Union. The purpose of this series of reports is to provide a working technical record for the use of program participants, and to provide a means of communicating the efforts of fusion materials scientists to the broader fusion community, both nationally and worldwide.

This report has been compiled under the guidance of F. W. (Bill) Wiffen and Betty Waddell, Oak Ridge National Laboratory. Their efforts, and the efforts of the many persons who made technical contributions, are gratefully acknowledged.

Peter J. Pappano
Research Division
Office of Fusion Energy Sciences

TABLE OF CONTENTS

TABLE OF CONTENTS

tip of the AP needle that focus both solute and matrix atoms into a smaller detector area. These topology changes are due to higher evaporation rates of the solutes and, in some cases, nearby matrix atoms that cause flattening or dimpling of the tip at the nano-oxides. The rapid evaporation rates are also accompanied by multiple hits and/or pre-evaporation events that can lead to undercounting of some solute species. These measurement artifacts are amplified in reconstructions that do not take them into account, for example, by placing atoms actually evaporated from a lower layer in a surface position. These phenomena are well known to APT practitioners, but their implications have not been widely recognized or well treated. However, atom probe data sets contain information that can provide insight on these phenomena, and perhaps eventually contribute to their resolution. A key piece of information is the spatially resolved sequence of atom emissions that are visualized in reconstruction software in color-coded detector hit maps. The hit maps show that the nano-oxides (and Cu rich precipitates in a ferrite matrix) evaporate much more rapidly than randomly located matrix atoms, and focus into the center of the solute rich region. Matrix atoms near the nano-oxides evaporate even more rapidly and focus more intensely than the solutes. Simple volume conservation considerations dictate that the higher evaporation rates lead to changes in the tip morphology resulting in the trajectory aberrations. Crude estimates of the degree of flattening-dimpling are possible, but more detailed understanding of the tip shape evolution will require additional observations and integration with field emission and atomic bond energy models. The hit maps also reveal that when the surface of a tip approaches a NF the thin layer of matrix atoms between the NF and the tip surface rapidly evaporates, forming a pre-dimple. Hit maps also show that un-ranged detector noise is concentrated at the nano-oxides, possibly partly due to DC pre-emission or unresolved multiple hit events. Solute specific multiple event frequencies are presented and other artifacts, like nano-oxide tops and bottoms, are described.

D. T. Hoelzer, E. T. Manneschmidt, and M. A. Sokolov (Oak Ridge National Laboratory)

Three heats of the advanced ODS 14YWT-SM12 ferritic alloy were produced with different extrusion temperatures and plates of each heat were fabricated with two different rolling conditions. The 14YWT-SM12 was a "clean" heat that was produced with improved mechanical alloying conditions to achieve low C (128 wppm) and N (117 wppm) levels and elevated O (1184 wppm) level. Plates of three SM12 heats were obtained by extruding at 850ºC, 1000ºC and 1150ºC temperatures followed by rolling at 1000ºC to 50% reduction in thickness in either the parallel (PR) or cross (CR) directions with reference to the extrusion direction. Specimens were fabricated from four plates of the SM12 heat with different thermal-mechanical treatments (TMT) and supplied for assembly of the JP30/31 capsules. The reference characterization of the microstructure and mechanical properties of the three SM12 heats was initiated. Results obtained from tensile tests at 25ºC showed slightly lower strengths, but significantly higher uniform (>9%) and total elongations in all the 14YWT-SM12 heats compared to results obtained from previous 14YWT heats. The general microstructural characteristics observed by SEM analysis showed that slightly larger grains with less uniformity in grain size had formed in the SM12 heats compared to

TABLE OF CONTENTS

previous 14YWT heats. The observed differences in the mechanical properties and grain structures of the SM12 heats compared to previous 14YWT heats were most likely due to lowering the O, C and N levels during ball milling.

This is the Abstract for an ICFRM-15 paper submitted for publication in the Proceedings.

3.   CERAMIC COMPOSITE STRUCTURAL MATERIAL DEVELOPMENT

To investigate the irradiation effects on interfacial shear properties such as an interfacial debond shear strength (IDSS) and an interfacial friction stress (IFS), the single fiber push-out tests were applied to Hi-Nicalon Type-S fiber reinforced chemical-vapor-infiltration (CVI) SiC matrix composites neutron irradiated up to 70 dpa at 300~800 ºC. Test results demonstrated no significant irradiation-enhanced degradation of interfacial shear properties expected at any doses (i.e., a slight decrease at lower doses <10 dpa and apparent improvement at higher doses >10 dpa). The irradiation-induced stress is a primary source to affect the F/M interfacial stresses. At higher doses ~70dpa, volume expansion by disordering of PyC possibly induced a residual clamping stress, eventually improving interfacial shear properties. A good correlation between the F/M interfacial strength and the macro strength for certain irradiation conditions was obtained. Interfacial functions sustained but fiber (Hi-Nicalon Type-S) deterioration was implied by irradiation at 70dpa. In the future we must clearly define the irradiation-induced change in thermal expansivity. The differential swelling between the fiber and matrix and irradiation creep are also critically important.

This is the Extended Abstract for an ICFRM-15 paper submitted for publication in the Proceedings.

In a previous report, a fairly substantial correction due to contact resistance at a silicon carbide composite-metal (either gold or porous nickel) electrode interface was required to

TABLE OF CONTENTS

arrive at reliable transverse electrical conductivity values for the composite. A semi-logarithmic plot of the inverse specific contact resistance vs. 1000/K was nearly linear over a temperature range ~100-700°C, with an effective thermal activation energy of ~0.3 eV, which suggested that the contact resistance was due to electron tunneling through a Schottky-type barrier at the composite SiC seal coat/metallic interface. For the FCI-application, additional contact resistance at SiC composite wall/liquid Pb-Li interfaces could potentially and beneficially reduce the transverse electrical conductivity.

In this report, we further examine the behavior of the contact resistance; in particular, by examining contact resistance for a single pure, monolithic but polycrystalline CVD-SiC disc sample with nickel electrodes applied by physical vapor deposition (PVD). After making contact resistance measurements with the as-applied Ni electrodes, a heat treatment at 900°C was performed to lower the contact resistance, presumably by the formation of nickel silicide (NiSi) at the SiC-electrode interface. Using a 2/4-probe dc electric set up, we were able to simultaneously measure the total resistance across the sample disc with and without contact resistance from ambient up to 700ºC, with the difference representing the temperature dependent behavior of the contact resistance alone. Surprisingly, the specific contact resistance values for each electrode type at all temperatures were almost identical (~1000 Ω-cm^2 at RT decreasing continuously to <2 Ω-cm^2 at 700°C). The temperature dependence indicated a thermally activated interfacial conductance with effective activation energy of ~0.24 eV, a value slightly greater than that for ultra high-purity CVD-SiC (0.21eV). Apparently, the electrical conductance of the CVD-SiC/metal (Ni or NiSi) interface depends mostly on the near surface SiC electrical conductivity properties rather than the type of metallic conductor.

The use of SiC composites in fusion environments likely requires joining of plates using reactive joining or brazing. One promising reactive joining method uses solid-state displacement reactions between Si and TiC to produce Ti_3SiC_2 + SiC. We continue to explore the processing envelope for this joint for the TITAN collaboration in order to produce optimal joints to undergo irradiation studies in HFIR. The TITAN collaboration has designed miniature torsion joints for preparation, testing, and irradiation in HFIR. PNNL synthesized 40 miniature torsion joints and several were tested for shear strength prior to irradiation testing in HFIR. The resulting tests indicated that 1) joint fixture alignment problems cause joint strengths to be lower than optimal, 2) that non-planar torsion test failures limit the effectiveness of the miniature specimen design, and 3) that several joints that were well aligned had high shear strengths and promising mechanical properties. In summary, we now show conclusively that high joint strengths cause non-planar shear fracture and complicate strength analysis for miniature torsion specimens.

TABLE OF CONTENTS

TABLE OF CONTENTS

This is the Abstract for an ICFRM-15 paper submitted for publication in the Proceedings.

Additional results are presented on the characterization of V-4Cr-4Ti tensile specimens and MHD coatings exposed to flowing Li. The alloy tensile specimens showed dynamic strain aging (DSA) at 500°C and the DSA amplitude varied with yield and ultimate tensile strength. Grain size and hardness measurements also were made on these specimens. For the MHD specimens, electron energy loss spectroscopy (EELS) and x-ray photoelectron spectroscopy (XPS) both found no evidence of Li in one coating after the exposure. A high temperature vacuum rig is being reconstructed to measure the electrical resistance of the coatings after exposure.

This is the Abstract for an ICFRM-15 paper submitted for publication in the Proceedings.

A series of Pb-Li capsule experiments were conducted to study the dissimilar material interaction between Fe and SiC using both materials as specimens and capsules. Because of uncertainties associated with the mass change data, metallographic cross-sections were completed to study the reactions observed at 500°-700°C after 1,000h in Pb-Li.

This is the Abstract for an ICFRM-15 paper submitted for publication in the Proceedings.

TABLE OF CONTENTS

Standard uniaxial tensile tests cannot provide generally transferable post-yield information on deformation and ductile failure for materials with low uniform strain limits. Deformation mediated failure is not only controlled by the intrinsic constitutive properties, but also extrinsic factors, especially the loading-specimen geometry. A self-consistent approach is used to derive true stress-stain constitutive [s(e)] laws, for candidate fusion reactor structural materials encompassing a range of unirradiated and irradiated conditions. In this report, unirradiated F82H with 0 to 80% of cold-work and neutron and spallation proton irradiated F82H were evaluated. The approach is based on simultaneous measurements and finite element method (FEM) simulations of engineering stress-strain s(e) curves, that are consistent only for a unique s(e) law. TEM observations of the selected deformed specimens were also performed to obtain microstructural insight. The most important and surprising result is that the s(e) of the irradiated alloys are consistently higher that for unirradiated condition over a wide range of strain. The s(e) after neutron irradiation are higher than in the 80% cold worked unirradiated condition at high strains. For deformation conditions that do not lead to plastic flow instabilities the higher strength levels are an asset even if accompanied by the low initial stain hardening rates following neutron irradiations. Further, there is evidence that high levels of He may suppress the initial loss strain hardening. If verified by additional experiment and modeling, these conclusions will have a tremendous impact on assessing the effects of irradiation service on the failure limits of fusion structures.

The results of this simulation study show that the size of TEM imaged He bubbles, represented by the inner diameter of the first dark Fresnel ring under defocused condition (D_{in}), deviated from the actual bubble size (D_o). D_{in} was found to be larger than D_o when imaged with a highly incoherent electron beam, but smaller than D_o if the beam is coherent. The deviation of D_{in} from D_o increases with increasing defocus. On the other hand, the electron beam accelerating voltage, bubble size, bubble position, and TEM sample thickness do not significantly affect the value of D_0/D_o. This study also suggests that He bubbles can be differentiated from argon (Ar) bubbles by differences in Fresnel contrast.

TABLE OF CONTENTS

The feasibility of fusion energy depends on developing advanced structural materials that can sustain extended component lifetimes in an ultra-severe environment, including up to 200 displacements per atom (dpa) and 2000 appm He. Helium and displacement defects individually and synergistically drive complex microstructural evolutions that degrade many performance-sustaining properties. Managing helium is perhaps the greatest challenge facing fusion structural materials. Here we show that an in situ helium injection fission reactor irradiation at 500°C to ≈ 25 dpa and 1450 appm helium produced populations of both bubbles and growing voids in a leading candidate tempered martensitic steel Eurofer97. The voids, which would be absent at low helium contents, are precursors to rapid swelling, suggesting that tempered martensitic steels may not tolerate extended service in the fusion environment. In contrast, only an ultrahigh density of tiny bubbles form in a companion nano-dispersion strengthened ferritic alloy, MA957. It is expected that the bubbles will inhibit swelling and other deleterious manifestations of irradiation effects at much higher dpa in materials with a high density of stable nano-dispersoids.

This is the Extended Abstract for a paper in preparation for journal submission.

Helium generation and accumulation is important under DT fusion irradiation conditions. Ballistic resolutioning of He from bubbles could limit bubble growth by ejecting gas atoms back into the metal matrix. Molecular dynamics simulation has been used to study this process in iron as a surrogate for structural materials. A newly-developed Fe-He interatomic potential was employed. The primary variables examined were: irradiation temperature (100 and 600K), iron knock-on atom energy (5 and 20 keV), bubble radius (~0.5 and 1.0 nm), and He-to-vacancy ratio in the bubble (0.25, 0.5 and 1.0). Helium ejection by high-energy iron recoils was clearly observed on a time scale consistent with a ballistic mechanism. The results are summarized.

TABLE OF CONTENTS

TABLE OF CONTENTS

point defects and point defect clusters. The three aspects of materials strength that we are studying are:

a) Computation of dislocation mobility functions (stress-velocity relations) as a function of temperature and dislocation character. This will be done via molecular dynamics (MD) simulations of single dislocation motion under applied shear stress. This is a fundamental input to dislocation dynamics (DD) simulations and also provides fundamental insights into the high-temperature plastic behavior of ferritic materials.

b) Simulations of dislocation-obstacle interactions using MD and DD. This subtask includes simulating the effect on dislocation glide of precipitates (e.g., α' Cr precipitates), ODS particles, and irradiation induced defect clusters (e.g. voids, dislocation loops, etc.).

c) Implementation of this information (dislocation mobilities and dislocation-defect interaction rules) into DD codes that will allow us to study plasticity of single crystals Fe alloys under relevant irradiation conditions.

1.1   Effects of Alloying Elements and Thermochemical Treatment on 9Cr Reduced Activation Ferritic-Martensitic (RAFM) Steels — L. Tan, Y. Yang and J.T. Busby (Oak Ridge National Laboratory)

<u>This is the Extended Abstract for an ICFRM-15 paper submitted for publication in the Proceedings.</u>

RAFM steels are one of the candidate structural materials for fusion reactors, in which tantalum (Ta) and tungsten (W) are alloyed to replace niobium (Nb) and molybdenum (Mo) in conventional FM steels, respectively. This paper, using three RAFM heats, presents the effects of Ta and the primary austenite stabilizer carbon (C) on microstructure and strength. Thermomechanical treatment (TMT) was applied to the experimental heats, leading to significant increases in strength, attributable to the TMT-refined sub-grains and precipitates. The Ta-alloying favored the formation of (V,Ta)(N,C) and (Ta,V)C, which exhibited greater strength. Fractographic analysis together with microstructural characterization revealed the beneficial effects of TMT and Ta-alloying. However, extra C content, favoring a larger amount of $M_{23}C_6$ precipitates, did not show strengthening effect.
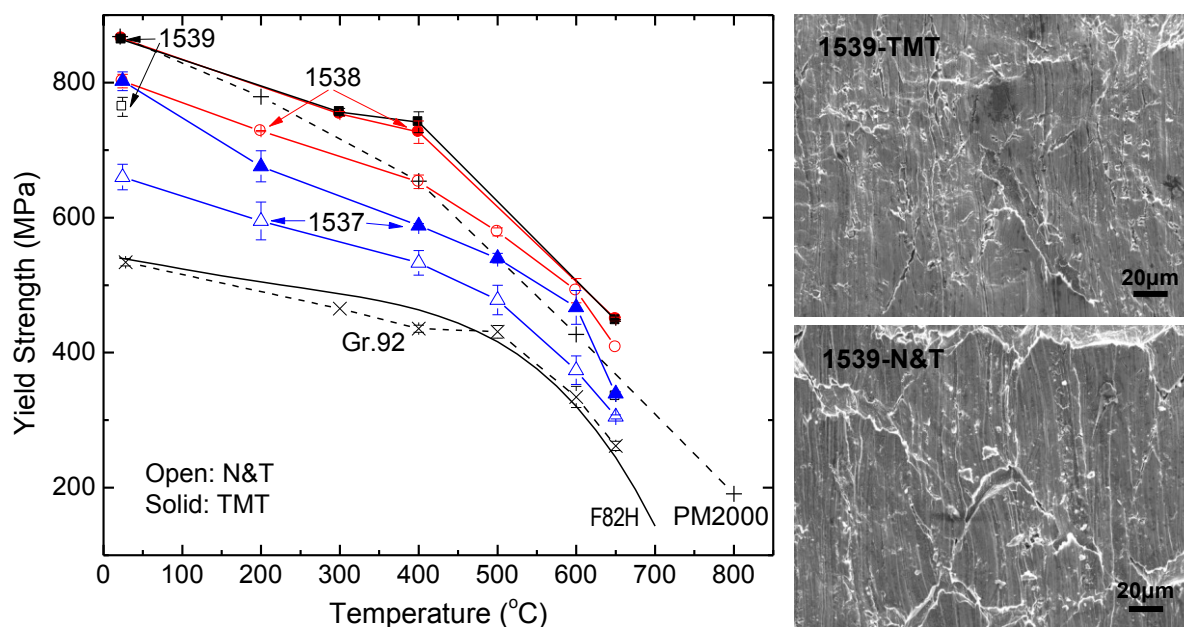
Figure 1. Yield strength of heats 1537, 1538, and 1539 in the conventional normalization and tempering (N&T) and TMT conditions, compared to the literature data of Grade 92, F82H, and ODS steel PM2000. Triangles, circles, and squares denote the samples of 1537, 1538, and 1539, respectively. The SEM images, using heat 1539 samples in the N&T and TMT conditions as examples, show the side surface morphologies close to the necking area of the tensile-fractured samples tested at room temperature with the loading axis along the vertical direction of the images.

1.2 Irradiation Creep Behavior of F82H IEA Heat and B-Doped F82H Irradiated at 573 and 673K up to 5dpa —— M. Ando, T. Nozawa, T. Hirose, H. Tanigawa, and E. Wakai (Japan Atomic Energy Agency), R. E. Stoller and Janie Myers (Oak Ridge National Laboratory)

OBJECTIVE

This report is a result of creep tube measurements for F82H IEA heat and Boron-doped F82H irradiated at 573 and 673 K in HFIR MFE-RB-15J capsule. The objectives of this work are to obtain irradiation creep data of F82H and to investigate the effect of helium on irradiation creep behavior.

SUMMARY

The 34 pressurized tubes irradiated in MFE-RB15J capsule have been measured by a laser profilometer in hot cell. The irradiation creep of F82H IEA and ^{10}BN-F82H exhibited similar behavior below 573 K up to 5dpa. The irradiation creep strain in F82H irradiated at 573K and 673 K was almost linearly dependent on the Hoop stress level for stresses below 300 MPa and 200 MPa, respectively. The creep strain of ^{10}BN-F82H was similar to that of F82H IEA at each Hoop stress level except 340 MPa at 573 K irradiation.

PROGRESS AND STATUS

Introduction

Reduced activation ferritic/martensitic steels (RAFM) are the most promising candidates for blanket structural materials for fusion reactors. Irradiation creep has been recognized as one of the most important properties for engineering data due to the blanket structural design. Several researchers have reported on irradiation creep and void swelling behavior of austenitic stainless steels and ferritic steels irradiated above 673 K in FFTF, HFIR, and other fission reactors [1-3]. In addition, some results of irradiation creep experiments on RAFM (F82H and JLF-1) above 663 K have been reported by the Japan/US collaboration program for fusion materials [4]. For fusion reactors, it is anticipated that irradiation creep of RAFM at lower temperatures could be also significant, and this would have a large impact on the life expectancy of a water-cooled solid breeder blanket system. However, irradiation creep behavior of RAFM at temperatures below 673 K has scarcely been reported [5]. In a fusion reactor, some transmutations (mainly helium) are produced by high-energy neutrons in the first wall. The effect of helium on irradiation creep behavior has not been reported in F82H.

The objectives of this work are to provide irradiation creep data of F82H IEA heat for blanket structural materials database. The effects of helium on irradiation creep behavior are also reported using BN-F82H.

Experimental

The materials studied were F82H IEA heat and Boron-doped F82H provided by Japan Atomic Energy Agency. The chemical compositions of these materials are given in Table 1. Boron-doped F82H steels were provided to investigate the effect of helium on irradiation creep. In this experiment, two types of Boron-doped F82H were prepared by a co-doping of Boron and Nitrogen in F82H steel [6, 7]. One is ^{10}BN-F82H which produced helium atoms by the reaction ^{10}B (n, a) ^{7}Li during irradiation. The other is ^{11}BN-F82H which did not produce helium. These BN co-doped

F82H steels show that mechanical properties were improved by a suppression of boron localization.

Table 1. Chemical composition of F82H and B-doped F82H (mass%).

	C	Cr	W	V	Ta	Mn	Si	P	S	N	B
F82H **EA** heat	0.090	7.71	1.95	0.16	0.020	0.16	0.11	0.002	0.0020	0.006	0.0002
^{10}BN–F82H	0.099	8.09	2.10	0.30	0.039	0.10	0.10	0.006	0.0008	0.020	0.0059
^{11}BN–F82H	0.088	8.08	2.09	0.31	0.043	0.10	0.11	0.006	0.0010	0.020	0.0053

The tube specimens had dimensions of 4.57 mm outside diameter and 25.4 mm length with a 0.25 mm wall thickness as shown in Fig. 1. The hoop stresses ranged from 0 to 380 MPa at the each irradiation temperature. The diameter of these tubes was measured by a non-contacting laser profilometer system (Beta Lasermike Model162) at Oak Ridge National Laboratory (ORNL) prior to irradiation.
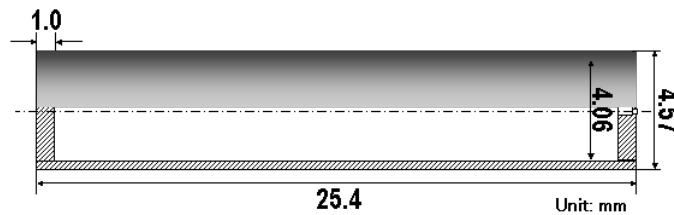
Fig. 1. Geometry of the pressurized tube specimen.

Irradiation was performed in High Flux Isotope Reactor (HFIR) to atomic displacement levels up to 5 dpa in the RB-15J capsule [8]. Nominal irradiation temperatures were 573 and 673 K in this experiment.

The tubes were measured with a laser profilometer system capable of a precision of ±250 nm. Each tube was measured three times after irradiation. The average diameter of the central three-fifths of each tube was used in the analysis of the data. A creep strain was calculated from tube diameter measured before and after irradiation.

Results and Discussion

Table 2 shows results of irradiation creep measurements for pressurized tube specimens irradiated at 573 and 673 K.

Table 2. Results of creep tube measurements for RB15J.

Specimen ID	Strain %	Hoop Stress MPa	Tempreture K	Dose dpa	Material
OXP0	0.56106	380	573	3.7	F82H IEA
OXP2	0.19426	340	573	4.2	F82H IEA
OXP3	0.10199	300	573	3.7	F82H IEA
OVP1	0.07804	250	573	4.2	F82H IEA
OZP4	0.04084	250	573	3.7	F82H IEA
OXP6	0.09114	200	573	4.2	F82H IEA
OXP7	0.08823	200	573	4.2	F82H IEA
OXP9	0.02406	150	573	3.7	F82H IEA
OZP0	−0.03977	150	573	4.2	F82H IEA
OZP1	0.00583	100	573	4.2	F82H IEA
OWP1	0.07638	100	573	4.2	F82H IEA
OXP5	0.02926	0	573	3.7	F82H IEA
OYP3	0.34470	250	673	5.7	F82H IEA
OZP2	0.24479	250	673	5.7	F82H IEA
OYP5	0.15722	200	673	5.7	F82H IEA
OXP8	0.12050	200	673	5.7	F82H IEA
OXP1	0.15132	170	673	5.7	F82H IEA
OYP9	0.05398	150	673	5.7	F82H IEA
OWP0	0.07321	100	673	5.7	F82H IEA
OYPB	−0.14052	100	673	5.7	F82H IEA
OXPA	−0.00791	0	673	5.7	F82H IEA
DXP0	0.28687	340	573	3.7	[10]BN−F82H
DXP1	0.09482	250	573	3.7	[10]BN−F82H
DXP2	0.06477	200	573	4.2	[10]BN−F82H
DXP3	0.06543	150	573	4.2	[10]BN−F82H
DZP2	0.02269	0	573	3.7	[10]BN−F82H
DYP6	0.28239	250	673	5.8	[10]BN−F82H
DYP7	0.11017	200	673	5.8	[10]BN−F82H
DYP8	0.10329	150	673	5.8	[10]BN−F82H
DYP9	0.04431	0	673	5.8	[10]BN−F82H
EYP8	0.20079	250	673	5.8	[11]BN−F82H
EYP9	0.10608	200	673	5.8	[11]BN−F82H
EZP0	0.07613	150	673	5.8	[11]BN−F82H
EXP0	−0.00260	0	673	5.8	[11]BN−F82H

In this experiment, a total of 34 tubes were measured in the hot cell. A creep strain is calculated from the change in the outer diameter of tube following irradiation. Using the measured diameters, a creep strain is calculated by the following expression:

$$\varepsilon = 1.15 \times \frac{\Delta D}{D_o}$$

where ΔD is the change in the tube's outer diameter before and after irradiation, D_o is the outer diameter before irradiation. The outer diameter strain is converted to the mid-wall strain by a factor of 1.15 [9].

Fig. 2 (a) shows the relationship between the creep strain (e) and the Hoop stress (s_{Hoop}) in F82H IEA and BN-F82H irradiated at 573 K. F82H IEA and BN-F82H exhibit similar irradiation creep behavior at 573 K up to 5dpa.

(a)

(b)
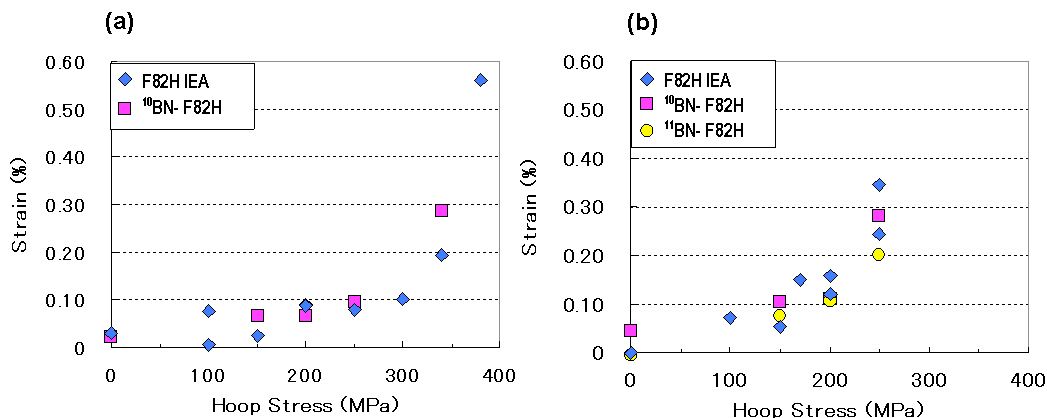
Fig. 2. Hoop stress dependence of irradiation creep at (a) 573 K and (b) 673 K.

The irradiation creep strain in F82H is nearly linearly dependent on the Hoop stress level for stress levels below 300 MPa. However, the creep strain becomes nonlinear at higher stress levels. Fig. 2 (b) shows the results of 673 K irradiation. In this case, the irradiation creep strain of F82H is linearly below 200 MPa. At higher stress levels, the creep strain increased in F82H IEA because thermal creep gradually had also occurred during irradiation.

In this experiment, stress-free tubes were included to monitor swelling. For 573 K irradiation, the data from each stress-free tube show that swelling is very small in this condition, below 0.02 %.

The effect of helium on irradiation creep of F82H was also examined using [10]BN and [11]BN-F82H. Helium production after irradiation was estimated to be about 300 appm and was controlled using a thermal neutron shielded capsule. The creep strain of [10]BN-F82H was similar to that of F82H IEA at each Hoop stress level except 340 MPa at 573 K irradiation. For 673 K irradiation, the creep strain of some [10]BN-F82H tubes was larger than that of F82H IEA tubes (including stress free tube). It is suggested that a swelling caused in each [10]BN-F82H because small helium babbles might be produced by a reaction of [10]B(n, a)[7]Li.

REFERENCES

[1] A. F. Rowcliffe and M. L. Grossbeck, *J. Nucl. Mater.* **122-123** (1984) 181.
[2] M. L. Grossbeck and J. A. Horak, *J. Nucl. Mater.* **155-157** (1988) 1001.
[3] F. A. Garner and R. J. Puigh, *J. Nucl. Mater.* **179-181** (1991) 577.
[4] A. Kohyama, Y. Kohno, K. Asakura, M. Yoshino, C. Namba, and C. R. Eiholzer, *J. Nucl. Mater.* **212-215** (1994) 751.
[5] M. Ando, M. Li, H. Tanigawa, et al., *J. Nucl. Mater.* **367-370** (2007) 122.
[6] E. Wakai, M. Sato, T. Sawai, K. Shiba, and S. Jitsukawa, *Mater. Trans.* **45** (2) (2004) 407.
[7] N. Okubo, E. Wakai, S. Matsukawa, K. Furuya, H. Tanigawa, and S. Jitsukawa, *Mater. Trans.* **46** (2) (2005) 194.
[8] T. Hirose, M. Ando, H. Tanigawa, N. Okubo, J. L. McDuffee, D. W. Heatherly, R. G. Sitterson, R.E. Stoller and T. Yamamoto, Fusion Materials Semiannual Progress Report for Period Ending June 30, 2009, DOE/ER-0313/46, U. S. Department of Energy, 72.
[9] E. R. Gilbert and L. D. Blackburn, *Trans. ASME, J. Eng. Mater. & Technol.* (1977) 168.

2.1   The Structure of Nanoscale Precipitates and Precipitate Interfaces in an Oxide Dispersion Strengthened Steel, — J. Ciston (National Center for Electron Microscopy, Lawrence Berkeley National Laboratory), Y. Wu and G. R. Odette (Materials Department, University of California, Santa Barbara), P. Hosemann (Department of Nuclear Engineering University of California, Berkeley)

OBJECTIVE

The objective of this work is to characterize the detailed structure of nano-scale oxides in and referece ODS alloy MA957 including the interfaces with the ferritic matrix.

SUMMARY
Fusion energy will require developing new, high performance irradiation tolerant structural materials, like oxide dispersion strengthened nanostructured ferritic (ODS) alloys [1]. Fe-14Cr based NFA contain an ultrahigh density of Y-Ti-O enriched nanofeatures (NF) that provide both outstanding high temperature properties and remarkable tolerance to irradiation damage, including the transmutation product He. Understanding the detailed characteristics of the NF is critical to optimizing ODS alloys, but this remains an unresolved issue and a subject of continuing controversy.

PROGRESS AND STATUS

Experimental Methods

We present the initial results of a study on a reference NFA, MA957, using the TEAM 0.5 aberration corrected instrument at the Lawrence Berkeley National Laboratory National Center for Electron Microscopy. The MA957 examined is in a friction stir welded and annealed (FSW-A) condition that has been previously self-consistently characterized by a number of different techniques. Previous TEM measurements showed that this alloy contains $\approx 2.3 \times 10^{23}$ $Y_2Ti_2O_7$ pyrochlore polyhedral oxides per m^3 with an average diameter of ≈ 2.4 nm and a near stoichiometric composition [2]. However, previous structure and composition measurements, which were made on extracted oxides, proved to be difficult to impossible when the oxides were embedded in the Fe-Cr matrix.

The FSW-A foil was FIB thinned further prior to examination using the TEAM 0.5. The characterization included STEM EELS profiles and HAADF imaging as well as HREM focal series imaging. The resulting rich and detailed database is under continuing analysis, but there are already several important preliminary results.

Preliminary Results

The $Y_2Ti_2O_7$ pyrochlore structure of he nanooxides found in previous studies was confirmed. and $[001]_{fe}//[1\text{-}10]_{ox}\text{-}(100)Fe//(100)_{ox}$ orientation relationship for the several oxide inclusions were confirmed. The HRTEM image and indexed FFT shown in Figure 1 are for a $\approx 1.8 \times 3.8$ nm feature. The FFT is consistent with a fluorite structure for the oxide phase with measured d-spacings of the (400) and (222) planes that are slightly larger than for the bulk oxide by ≈ 6.7 and 3.3%, respectively. This small oxide appears to be fully coherent with the ferrite matrix. The exit wave phase from a focal series restoration of a larger 6.2×10.1 nm particle is shown in Figure 2. In this larger particle, the $Y_2Ti_2O_7$ exhibits smaller d-spacing differences from the bulk

of 1.4 and 1.2%, respectively. The larger particle is coherent with the bcc matrix along the vertical edges, but is incoherent at the top and bottom horizontal edges. In addition, it can be clearly observed from the exit wave that the Fe-Cr matix is strained in tension along the top and bottom edge of the particle. The EELS Ti profile in Figure 3 as well as HAADF count (not shown) profiles suggest that the feature has beveled edges in the beam direction, and is not a true rectangular prism. While the oxide is enriched with Ti relatice to the matrix, there does not appear to be significant Ti segregation at the interface [3].
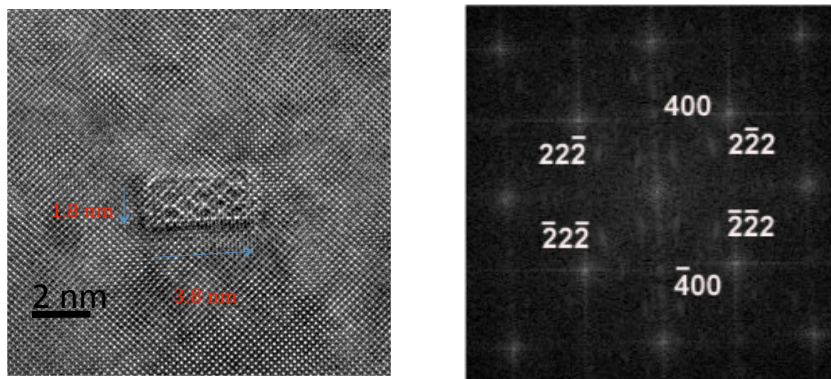
Fig 1. HRTEM image of a NF in FSW-A MA957 (left) and the corresponding FFT indexed to the $Y_2Ti_2O_7$ phase (right).
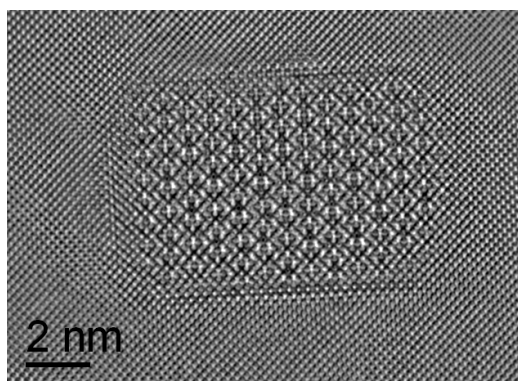
Fig 2. Phase of restored exit wave of FSW-A MA957 particle indicating direction-dependant interfacial coherence.
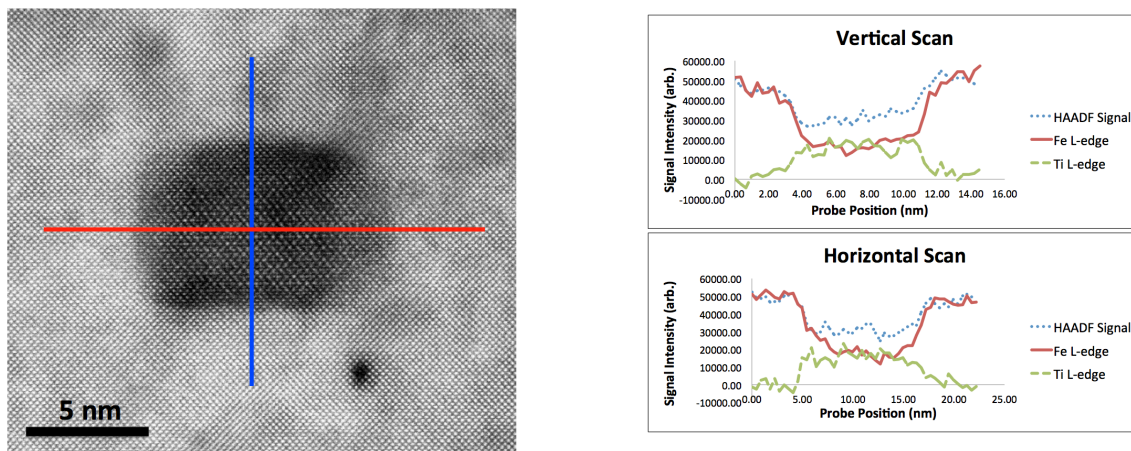
Fig 3. HAADF-STEM image of particle in Figure 2 with corresponding EELS line scans in horizontal and vertical directions for 0.5nm probe.

FUTURE WORK

The results summarized here are just a small part of the research plan for using the TEAM 0.5 microscope. We have alrady colleted extenive data using a variety of TEM methods on a variety of MA957 conditions that remains to be analyzed. Future studies will include ofhter ODS alloys and variants, dual ion irradiated alloys and meso-macroscale interfaces between single crystal $Y_2Ti_2O_7$ and electron beam physical vapor depsited Fe films.

ACKNOWLEDGMENTS

REFERENCES

[1] G. R. Odette, M. J. Alinger and B. D. Wirth, Annual Review of Material Research 38 (2008) 471.
[2] Y. Wu, E. Haney, N. Cunningham and G. R. Odette, DOE Fus. Reac. Mat. Semiann. Prog. Rep. June 30, 2011, DOE/ER-0313/50 (2011) 25; submitted to Acta Materialia.

2.2   Recent Progress on Understanding and Quantifying Atom Probe Tomography Artifacts for High Evaporation Rate nm-scale Phases in Fe Based Alloys — P. Wells, N. J. Cunningham and G. R. Odette (University of California Santa Barbara)

OBJECTIVE

Atom probe tomography (APT) is a key technique for characterizing the small Y-Ti-O nano-oxides in nanostructured ferritic alloys (NFAs). The objective of this study is to address composition discrepancies between TEM measurements and APT, focusing on APT artifacts.

SUMMARY

Preferential undercounting and trajectory aberrations in APT measurements were investigated. The higher than physical atom densities observed in NFs are due to trajectory aberrations that are associated with local changes in the surface topology of the tip of the AP needle that focus both solute and matrix atoms into a smaller detector area. These topology changes are due to higher evaporation rates of the solutes and, in some cases, nearby matrix atoms that cause flattening or dimpling of the tip at the nano-oxides.   The rapid evaporation rates are also accompanied by multiple hits and/or pre-evaporation events that can lead to undercounting of some solute species. These measurement artifacts are amplified in reconstructions that do not take them into account, for example, by placing atoms actually evaporated from a lower layer in a surface position. These phenomena are well known to APT practitioners, but their implications have not been widely recognized or well treated. However, atom probe data sets contain information that can provide insight on these phenomena, and perhaps eventually contribute to their resolution. A key piece of information is the spatially resolved sequence of atom emissions that are visualized in reconstruction software in color-coded detector hit maps. The hit maps show that the nano-oxides (and Cu rich precipitates in a ferrite matrix) evaporate much more rapidly than randomly located matrix atoms, and focus into the center of the solute rich region. Matrix atoms near the nano-oxides evaporate even more rapidly and focus more intensely than the solutes.   Simple volume conservation considerations dictate that the higher evaporation rates lead to changes in the tip morphology resulting in the trajectory aberrations. Crude estimates of the degree of flattening-dimpling are possible, but more detailed understanding of the tip shape evolution will require additional observations and integration with field emission and atomic bond energy models. The hit maps also reveal that when the surface of a tip approaches a NF the thin layer of matrix atoms between the NF and the tip surface rapidly evaporates, forming a pre-dimple. Hit maps also show that un-ranged detector noise is concentrated at the nano-oxides, possibly partly due to DC pre-emission or unresolved multiple hit events. Solute specific multiple event frequencies are presented and other artifacts, like nano-oxide tops and bottoms, are described.

PROGRESS AND STATUS

Introduction and Background

Nano-structured ferritic alloys (NFA) have high tensile and creep strength permitting operation up to 800°C, manifest remarkable resistance to radiation damage and can manage a high concentration of He [1]. These outstanding properties derive from an ultrahigh density of Y-Ti-O enriched nano-features (NF) that provide dispersion strengthening, help stabilize dislocation and

fine grain structures, reduce excess concentrations of displacement defects and trap He in fine bubbles [1]. The NF size, number density, and composition have been the focus of recent research on numerous alloys including MA957 [2,3,4]. A detailed understanding of the NF is needed since the number density and size distribution govern the geometric sink strength, while the NF-matrix interface is critical to defect and He trapping, dislocation pinning-detachment processes and the thermal and irradiation stability. Further, detailed knowledge about the effects of compositional and processing variables that control the NF character is critical to the design of alloys with an optimal balance of properties.

Characterization of the NFs is difficult due to their small sizes that are near the resolution limit of many experimental techniques. Therefore, characterization with a complementary set of state of the art tools is needed to mitigate the limitations of individual methods. Two core characterization tools used in this research include APT and TEM. Conventional bright-field TEM resolves all but the smallest NFs by contrast differences with the matrix, but other TEM techniques are required for determining their structure and composition. These include high angle annular dark field (HAADF) imaging, electron energy loss spectroscopy (EELS), energy dispersive x-ray spectroscopy (EDS) and high resolution TEM (HRTEM). The larger (>15 nm) Y-Ti-O rich features appear to be either Y_2TiO_5 or $Y_2Ti_2O_7$ [5,6,7,8]. Most TEM studies have shown that the smallest NFs ($\leq$ 5 nm) in MA957 are near stoichiometric $Y_2Ti_2O_7$ [6,7,8,9,10,11,12], although both non-stoichiometric rock salt and amorphous NF structures have been reported [13,14]. A recently initiated collaboration between UCSB, UCB and LBNL using the advanced aberration corrected TEAM 0.5 microscope at the LBNL National Electron Microscopy Center has shown the NFs in MA957 are primarily coherent $Y_2Ti_2O_7$ [15].

Atom probe tomography (ATP) was the first technique used to study the smallest NFs ($\leq$ 5 nm) [16,17] and APT continues to be a major tool used to characterize NFAs. APT and TEM NF number densities and size distributions are generally in good agreement especially considering the individual limitations of both techniques [18,19]. However, standard interpretations of APT data suggest the NFs are far from equilibrium, coherent, transition phase (sub-oxide) solute clusters with lower Y/Ti and O/(Ti + Y) ratios compared to $Y_2Ti_2O_7$ [16,17,18,19]. For example, the average specimen Y/Ti ratio of the NFs in MA957 measured at UCSB using a Cameca 3000X HR LEAP and IVAS reconstruction software ranged from 0.27 to 0.46. The corresponding average O/(Y + Ti) ratio ranged from 0.63 to 0.80. The IVAS APT reconstructions also show very high Fe and Cr contents of $\approx$ 50 to 75 % even in the center of small NFs. We believe the inconsistency between $Y_2Ti_2O_7$ versus these compositions is in large part due to artifacts in the APT method [20,21,22]. The artifacts include DC pre-emission and unresolved multiple hits of more weakly bonded species like Y and O [15,20], surface diffusion, especially interstitial elements like O, perhaps stimulated by the high electric fields, and the presence of nearby low index pole zones. Further, structures like precipitate-matrix interfaces, isolated surface atoms versus those on ledges and ledge kinks and uneven temperature distributions during the laser pulsing may also lead to large local variations in the binding energies and field emission evaporation rates.

However, perhaps the most important APT artifacts are due to differences in the evaporation fields and/or the electric fields of second phase particles and the evaporation fields for the matrix atoms. Differences in local evaporation rates directly affect the local topology of the APT needle tip. While this issue has long been recognized it has not been dealt with in an effective and quantitative way. However, a recent study by Oberdorfer and G. Schmitz that simulated local lower evaporation fields and higher electric fields associated with more weakly bonded phases

and dielectric phases like oxides, respectively, showed more rapid evaporation and flattening or dimpling of the region in the vicinity of the feature [23]. This results in topology induced ion trajectory aberrations due to the change in the local magnification factor. Both solute and matrix atoms are focused into the center of the precipitate region. Such trajectory aberrations are signaled by a higher than physical atom density near the center of the precipitates as well as artificially high concentrations of matrix atom (Fe and Cr). A recent unpublished simulation we have seen also shows that dimpling not only leads to a focusing effect, but it can actually result in crossovers in the ion trajectories that further complicate reliable reconstructions.

Coupled with assumptions used in the reconstruction algorithms and sometimes imprecise calibration of d-spacings, these artifacts also lead to distortion of the shapes of second phase particles (flattening and elongation) as well as features with chemically segregated tops and bottoms in some cases (when there are no physical tops and bottoms along the APT axial z-direction) and even large shifts in the location of the constituents in a binary alloy feature [24].

This work focuses on the mechanisms responsible for the APT-TEM composition discrepancy with TEM associated with preferential ion species undercounting and trajectory aberrations.

Experimental Procedures

APT is a destructive microscopy method that identifies the position and species of atoms within sharp needle samples with tip diameters of 100 nm or less. Feature numbers, sizes, compositions and spatial compositional variations were measured in NFA MA957 using a Cameca 3000X HR LEAP instrument with a variety of experimental conditions including sample temperatures between 30 and 70 K using both 200 or 250 kHz laser and voltage pulse modes and a 20-25% voltage pulse fraction or laser energies from 0.05 to 0. 5 nJ. Reconstructions and analysis of the 3-dimenstional data was performed using the Imago Interactive Visualization and Analysis Software (IVAS) package.

Precipitates were identified and their composition measured using the maximum separation distance method for the solute ions of interest, namely Y, Ti and O, including their complex forms like TiO and YO [25,26]. One-dimensional composition and density profiles through the NFs and larger precipitates were used to observe and compare the atom distributions perpendicular (X and Y directions) and parallel (Z direction) to the tip axis.

The evaporation sequence was also investigated using so-called detector hit maps and by analyzing the multiple hits on the detector during a single voltage or laser pulse. The mass to charge ratio of the field-emitted species is determined by the time of flight between the voltage, or laser, pulse that causes the ion to evaporate and when it hits the detector. The ions are field evaporated at a rate determined by the temperature as well as the standing bias and pulse voltages. The position the atoms hit the detector (X_d, Y_d) is used in conjunction with reconstruction software to determine the corresponding atom (X, Y) position on the tip based on its curvature defining a focal point assumed to be determined by the radius of an ideal hemisphere. The tip is then eroded by an increment of DZ for each hit that depends on the atomic volume of the evaporated species and the detector efficiency. Thus each detected ion is associated with an X, Y and Z position in the reconstruction. In the case of pure metals it is possible to reconstruct the atomic planes and plane d-spacing's; and using deviations from nominal d-spacings to adjust the reconstruction parameters so that they are consistent. In the case of a pure metal or the matrix of a phase-separated system, the evaporation rates and

sequence vary with the distance to the center of a faceted planar pole and by the field evaporation statistics and local arrangement of surface atoms.

However, the situation is much more complex for phase separated regions on an alloy since the evaporation field varies between the atomic/ionic species and its local environment that effectively determine its binding energy to the surface [27,28]. First we will digress to discuss the much studied and debated Fe-Cu system. One example of profound effects of the species and local environment is the evaporation of Cu atoms dissolved in a Fe matrix. Bulk Cu has a lower bulk evaporation field than Fe (30 vs 33 V/nm). However, the differences in evaporation fields are magnified when the Cu is dissolved in Fe, since the Fe-Fe and Cu-Cu bonds are much stronger than the Fe-Cu bonds. Thus Cu is preferentially evaporated at a higher rate than Fe. Indeed this effect is so strong that at higher temperatures most of the Cu pre-evaporates between laser or voltage pulses. For example in one study the ratio of the measured Cu to bulk Cu decreases from about 1 at 50°K to 0.2 at 120 °K [29]. We have observed similar effect in a simple Fe-Cu-Mn alloy containing both dissolved Cu and Cu precipitates. Note the 3kT/2 energy difference between 60 and 120°K is equivalent to only ≈ 0.0075 eV. Such small differences are comparable to or less than excess energies associated with atoms in a bcc versus fcc crystal structure, at interfaces, associated with defects and subject to coherency strains. Even ignoring pre-evaporation, higher local field emission of atoms from a second phase particle lead to the changes in local topology noted above, resulting in flattening or dimpling of the tip surface (which is any event not an ideal hemisphere) that produces trajectory aberrations. Further, as noted above the electric fields are higher at a non-conducting dielectric phase like an oxide, also leading to enhanced evaporation and local flattening or dimpling.   These concepts are schematically illustrated in Figure 1. While these phenomena have been recognized for some time, current reconstruction algorithms do not take pre-emission, surface diffusion, preferential evaporation or trajectory aberrations into account.
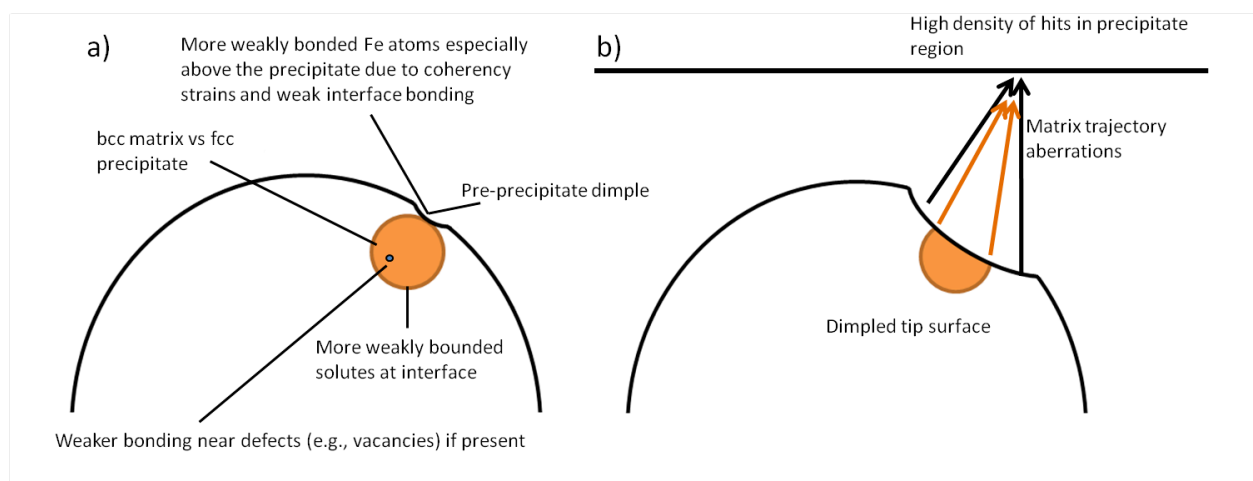
Figure 1.   a) Tip showing concepts of strain effects and weak interface bonds before a precipitate is encountered that cause a pre-precipitate dimple. b) Dimpling of tip caused by evaporation of higher field precipitate leading to Fe trajectory aberrations.

RESULTS

Hit Map Analysis

Considerable insight and ultimately perhaps some degree of quantification and resolution of these issues can be obtained by examining the spatially correlated sequence of emissions that are now currently available in the IVAS software. IVAS also provides information from the detector that is then used to create a visualization of the spatially dependent evaporation rates in the form of color-coded hit maps (HM) for the individual species. An example of a typical HM is shown in Figure 2. This HM is taken from an irradiated pressure vessel steel that contains a high density of Cu-Mn-Ni precipitates. This sample was run on our LEAP 3000X HR in voltage mode at 60K and 15% pulse fraction. Here the tip surface has been divided into X-Y bins roughly ≈ 1 nm in size. The color-coding shows the number of either matrix Fe atoms (Figure 2a and c) or solute atoms (Figure 2b and d). The atom hits are binned at each point for a range of about 20,000 atoms. Figures 2a and b show the emissions before the precipitate is encountered. These HM also clearly show that the matrix Fe atoms (Fig. 2a) above the actual precipitates preferentially evaporate, probably due to a combination of weaker local bonding and coherency stains. This creates a pre-dimple even before the precipitate emerges at the tip (Fig. 2b). Figures 2c and d show the corresponding HM in the precipitate itself, demonstrating that the matrix Fe atoms are focused into the precipitate region (bright red spot in Figure 2c) along with the solute atoms (the light blue spot in Figure 2d).
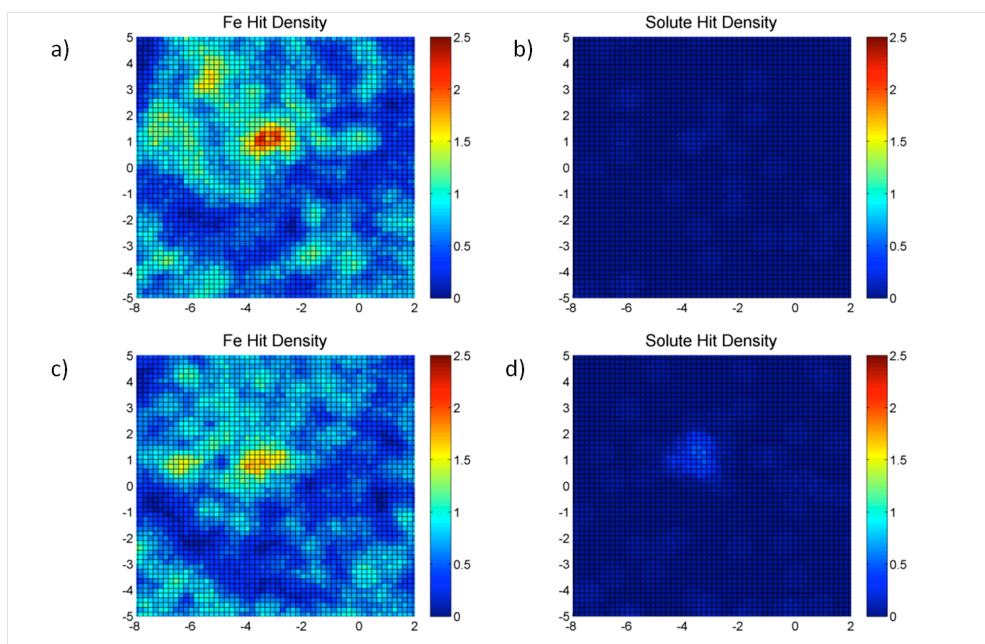
Figure 2. a-b) HM showing hits before the precipitate is uncovered for a) Fe, b) solutes; c-d) HM showing hits during precipitate evaporation for c) Fe and d) solute.

Figure 3a and b shows another HM of the spatial distribution of the Fe and Ni in a region with a Cu-Ni-Mn precipitate. Figure 3c shows the HM distribution of the HM noise that is defined as the un-ranged ions that form the background in the charge to mass spectrum shown in Figure 3d. The spatial correlation of the HM for noise with that for the precipitate presumably arises from a pre-evaporation event, or evaporation of atoms between voltage or laser pulses, making it impossible to determine the time of flight of the incoming atom. It is not possible to distinguish between the different elements that make up the noise, but the fact that it is highly localized in the precipitate region and given that pre-emission and multiples are biased for more weakly bonded atoms (see below) it seems likely that the localized noise partially rationalizes the differences in the APT vs TEM in the solute content as well.

The number of excess Fe atom hits above the precipitates suggests that the pre-dimple could be up to 4 or 5 atom layers. However, because the dimpling effect also leads to matrix trajectory aberrations, it is difficult to discriminate the relative contributions of pre-dimpling the Fe above the precipitate versus trajectory aberration contributions from the surrounding Fe matrix. That is the dimple may be shallow and larger in diameter or deeper and smaller in diameter. More quantitative treatment of these phenomena are summarized in the future work section.

Figure 4 and 5 show similar phenomena occur in the Fe-Cr matrix containing nano-oxide precipitates. Again preferential matrix atom evaporation takes place before the nano-oxide is encountered forming a pre-dimple (Figs. 4a and b). Trajectory aberrations of solutes and matrix atoms are observed as the precipitate evaporates (Figs. 4c and d). A spatially correlated increase in noise at the nano-oxide location is also observed (Fig. 5). Thus pre-emission and multiples may rationalize the low Y/Ti ratios.
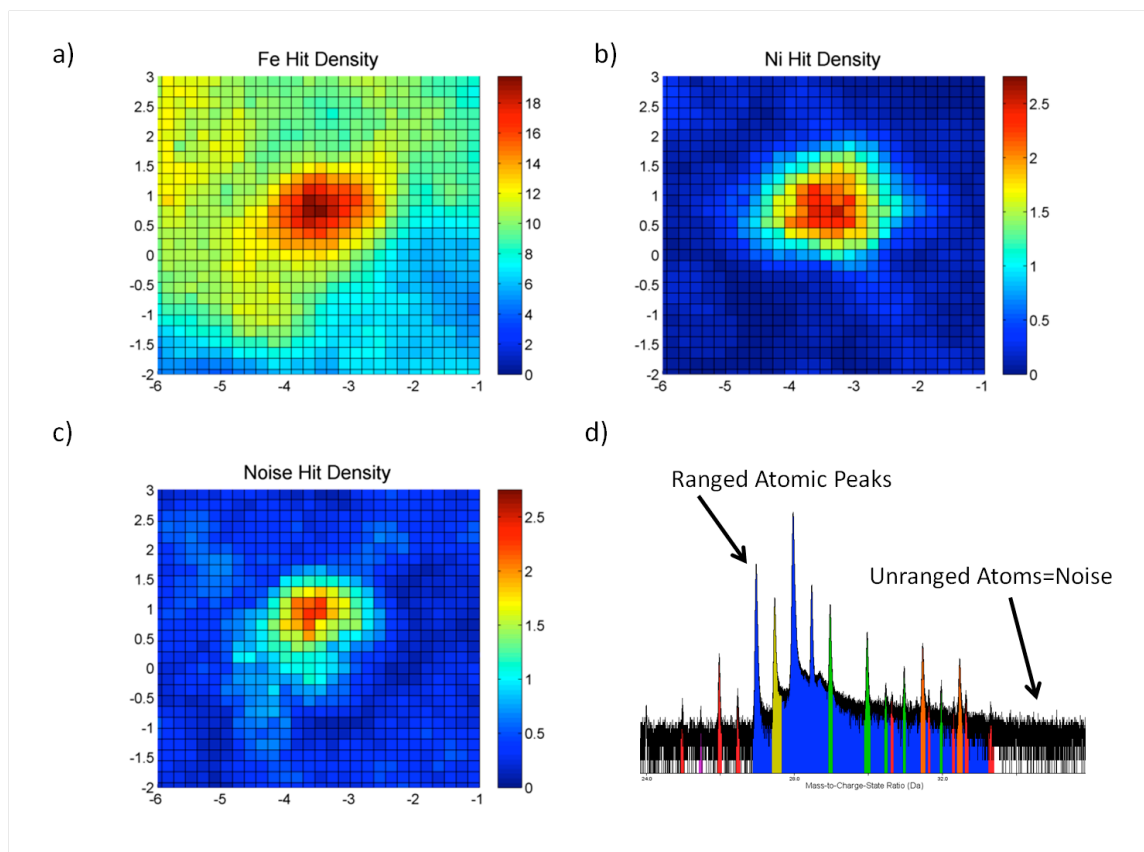
Figure 3. a-b) HM showing hits during precipitate evaporation for a) Fe, b) solutes and c) noise.   Note the different scales between figures a versus b & c, d) the mass spectrum is shown is to clarify the meaning of noise.

Atom Densities and Possible Feature Shape and Composition Distribution Artifacts

Figure 6 shows a much higher density in the nano-oxide compared to the matrix, indicating the presence of trajectory aberrations. The trajectory aberrations coupled with the reconstruction algorithm assumptions produce nano-oxides shapes with either high or low aspect ratios in the Z vs X-Y directions, depending on the size of the nano-oxide (or precipitate). The smallest nano-oxides (≈ 2-3 nm diameter) appear compressed in the Z direction whereas the larger nano-oxides appear elongated in the Z direction as shown in the examples in Figure 7. Once the precipitate is exposed on the tip surface it quickly evaporates and the reconstruction algorithm places the solutes artificially high in the Z direction. For larger precipitates that take longer to evaporate the trajectory aberrations may focus the precipitate ions more narrowly in the x-y direction perhaps elongating the nano-oxides.
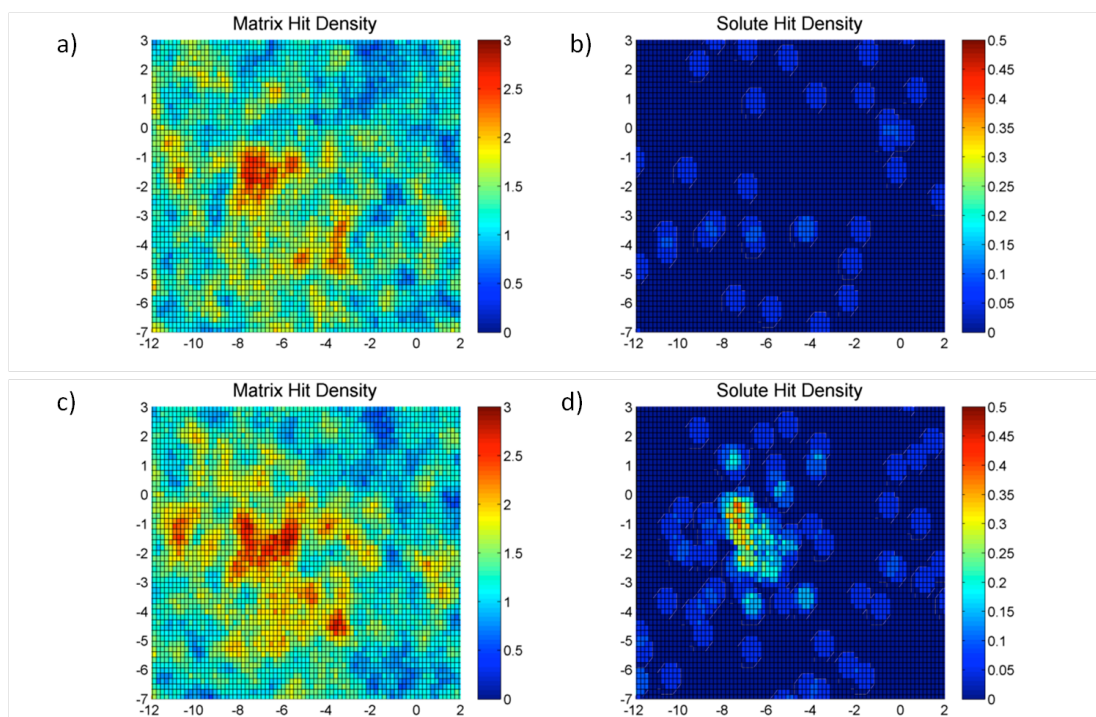
Figure 4. a-b) HM showing hits before the precipitate is uncovered for a) Fe+Cr, b) solutes; c-d) HM showing hits during precipitate evaporation for c) Fe+Cr and d) solutes. Note scale difference between matrix atom (a and c) and solute atoms (b and d).
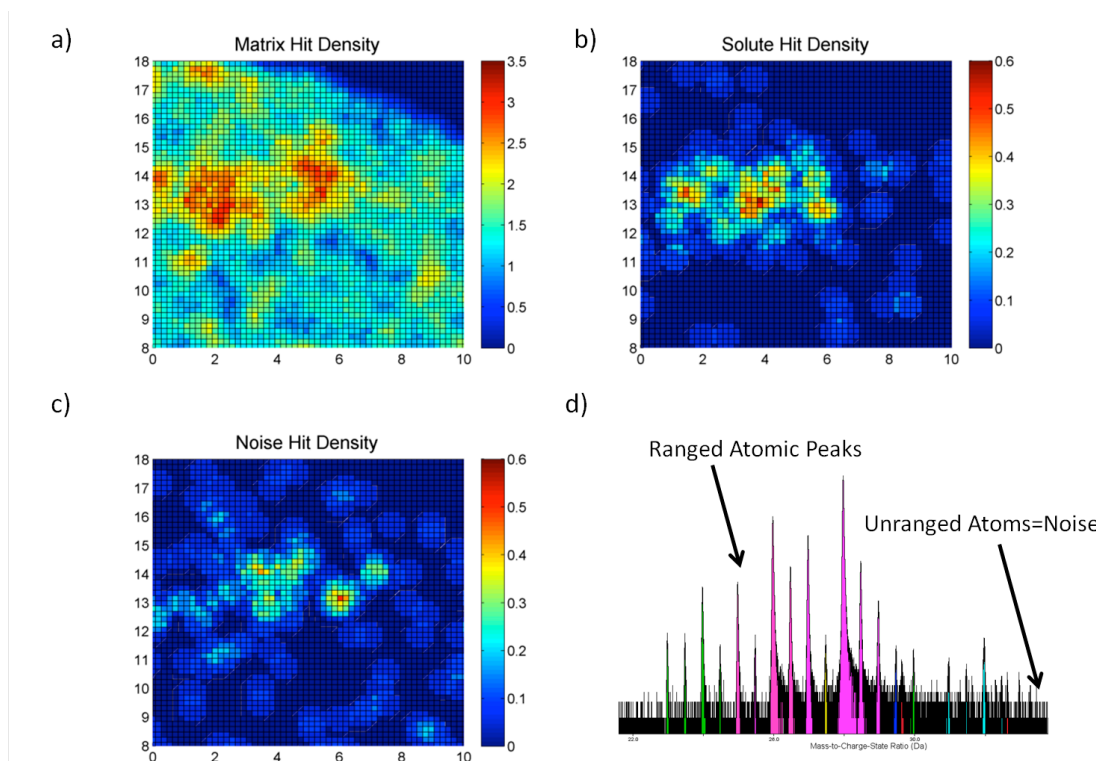
Figure 5. HM showing hits during precipitate evaporation for a) Fe+Cr, b) solutes and c) noise. The mass spectrum is shown to clarify the definition of noise. Note the scale difference between figures a, b & c.
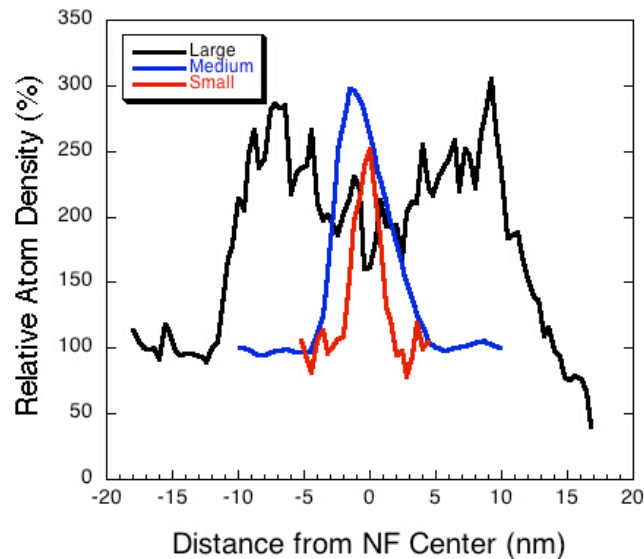
Figure 6. One-dimensional Z direction profile through a large, medium and small nano-oxide showing higher atom density compared to the matrix.

Another artifact is shown in the one-dimensional composition profiles of Figure 7 for a large, medim and small precipitate where a high concentration of TiO ions occurs near the bottom of the oxide and a small elemental Ti peak is observed at the top. Since the precipitates would not have "tops" and "bottoms" this is obviously an APT artifact.   The ion distribution is more symmetric in the X-Y direction as seen in Figure 7b for the large precipitate.

The low APT Y/Ti ratio could in principle be due to excess Ti segregation in the ferrite matrix adjacent to the nano-oxide. Assuming a $Y_2Ti_2O_7$ structure and using the Y count gives the equivalent spherical size shown in Table 1 for the nano-oxides in Figure 7. The excess Ti is also given. Assuming this excess is due to 100% Ti segregation to the NF-matrix interface the required layer thickness, also given in Table 1, is only the order of one or two atoms assuming a TiO (cubic) structure. If these interface Ti atoms evaporate at a higher field than the nano-oxide solutes, trajectory aberrations could place them inside the NF volume. After the NF is removed, remnants of the Ti segregation could evaporate more slowly producing the TiO tails seen in the reconstructions.
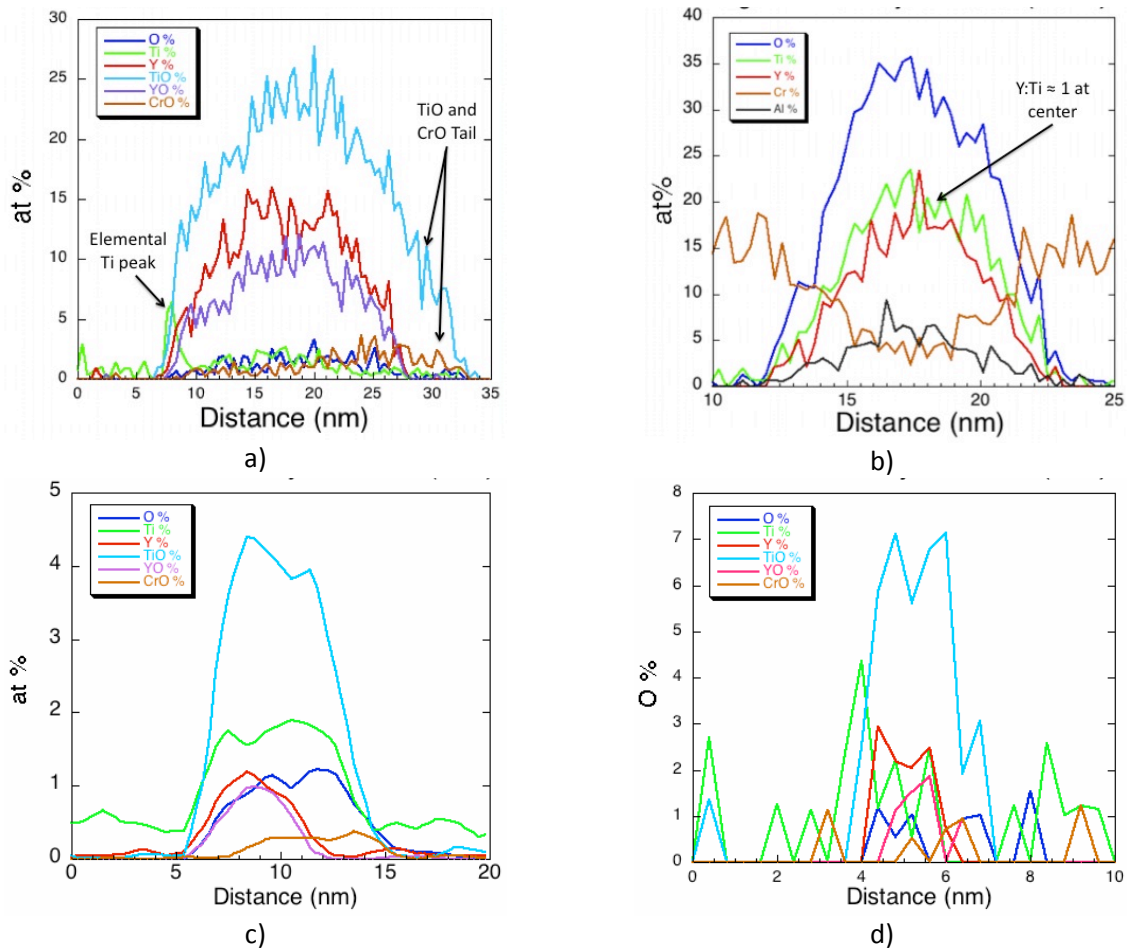
Figure 7. One-dimensional composition profiles of a) large NF along z direction; b) large NF perpendicular to z-direction; c) medium NF along z direction; and d) small NF along z direction.

Table 1. Calculated diameter based on assumed $Y_2Ti_2O_7$ structure and Y count with required Ti segregation volume thickness to account for the excess Ti.

NF	$Y_2Ti_2O_7$ Diameter (nm)	Segregated Ti thickness (nm)
Large N_Y = 5,429, N_{Ti} = 8,289	12.16	0.29
Medium N_Y = 174 N_{Ti} = 659	3.8	0.18
Small N_Y = 35 N_{Ti} = 125	2.4	0.23

Another possible explanation for the low Y/Ti ratio is preferential undercounting due to pre-emissions and multiple detector events. Multiple ions removed during a single voltage or laser pulse are still resolved by the delay line detector as long as they are not of the same species. If they are the same species <u>and</u> hit the detector too closely together in time, then they are not counted since their exact position cannot be determined.   Since the nano-oxide solutes evaporate rapidly from the same area on the tip then they may be preferentially undercounted, especially if they evaporate more often in pairs. Table 2 shows the percent of atoms counted during a multiple event for a typical MA957 tip. Oxygen has the highest multiple ion evaporation rate of 74%. YO ions follow at 64% and Y and TiO at 47% and 49%, respectively. In contrast, only 2% of the Fe ions involve multiples events. The issue of multiples need further analysis, but it is noted that the Y emissions are almost entirely from the nano-oxides.

Table 2. Percent of atoms evaporated during a multiple event.

Fe	Cr	CrO	Ti	TiO	Y	YO	O
2.0	5.5	74.0	6.6	48.5	46.8	64.2	74.4

CONCLUSIONS

We believe that the composition differences in Y-Ti-O nano-oxides observed by APT and TEM are at least partly due to a combination of trajectory aberrations and solute under counts due to pre-emission and unresolved multiples. Our hypothesis is that the excess Fe content in nano-oxides is primarily caused by trajectory aberrations caused by local flattening or dimpling of the tip due to preferential evaporation due to a higher local electric field near the dielectric phase and perhaps more weakly bound solutes.   Analysis of HM shows that matrix directly above the precipitate is also preferentially evaporated, probably due to weaker interfacial bonds and coherency strain effects, creating a pre-dimple even before the precipitate is reached. Differences in Y/Ti ratio can be explained with two hypotheses.   The first is that Y atoms could be preferentially undercounted due to pre-evaporation and/or because of unresolved multiple events. We assume that pre-emission of an element produces a uniform background noise in the mass spectrum. HM show a large increase in noise focused in the precipitate region during precipitate evaporation. Y and YO evaporate as multiples over 50% of the time. However, much more work needs to be done to confirm that preferential undercounting is indeed happening. A second hypothesis regarding the Y/Ti ratio is that there could be a Ti shell around the nano-oxides that is not detected by TEM methods since it might be only a few atom layers thick. The combination of APT measurement artifacts and reconstruction assumptions can also lead to distortion of the nano-oxide shapes and composition distribution artifacts.

FUTURE RESEARCH

Future work will be directed at observing the topology of the tip using high resolution TEM and FIM methods. We will also carry out additional analysis of the solute specific and spatially correlated emission sequences and integrate this information with simulations of field emission. For example, we are collaborating with Cameca in their simulations of low evaporation field precipitates.   These simulations include precipitates with core shell structures with different evaporation fields that are aimed at, for example, understanding chemically segregated tops and bottoms. These simulations will also show the evolution of the local surface topology and the

corresponding trajectory aberrations. This information will be combined with the empirical quantitative emission sequence assessments to develop a more robust approach to APT reconstructions. Further, we will carry out systematic measurements of the evaporation time-temperature kinetics and link this information to atomistic simulations of atomic bonding energies.

REFERENCES

[1] G. R. Odette, M. J. Alinger, and B. D. Wirth, Annual Review of Materials Research, Vol. **38**, 2008, 472.

[2] Y. Wu, E. Haney, N. Cunningham and G. R. Odette, submitted to Acta Mater 2010; under review.

[3] A. Etienne, N. J. Cunningham, Y. Wu, et al., *Mat. Sci. & Tech*. 2011; 27-4:724.

[4] N. J. Cunningham, G. R. Odette, E. Stergar, E. A. Marquis, A. Etienne, C. Hatzoglou, B. Radiguet, and P. Pareige, "Inter-Laboratory Atom Probe Tomography Characterization Study of the Nanofeatures and the Bulk and Matrix Compositions of US MA957," DOE Fusion Reactor Materials Program Semiannual Report, Vol. **50**, 2011, 41-46. DOE/ER-0313/50.

[5] R. Kasada, N. Toda, K. Yutani, H. S. Cho, H. Kishimoto, and A. Kimura, *J. Nucl. Mater.,* **367-370** (2007) 222-228.

[6] H. Sakasegawa, L. Chaffron, F. Legendre, L. Boulanger, T. Cozzika, M. Brocq, and Y. de Carlan, *J. Nucl. Mater.,* **284** (2009) 115-118.

[7] S. Yamashita, N. Akasaka, and S. Ohnuki, *J. Nucl. Mater.* **329-333** (2004) 377-381.

[8] M. Klimienkau, R. Lindau, and A. Moslang, *Micron* **36** (2005) 1-8.

[9] M. Klimienkau, R. Lindau, and A. Moslang, *J. Nucl. Mater,* **329-333** (2004) 347-351.

[10] M. C. Brandes, L. Kovarik, M. K. Miller and M. J. Mills, *J. Mater. Sci.* (2012) 47:3913.

[11] J. Ribis and Y. de Carlan, *Acta Materialia* (2012) 60:238.

[12] A. Hirata, T. Fujita, Y. R. Wen, J. H. Schneibel, C. T. Liu and M. W. Chen, *Nature Mater.* (2011) 10:922.

[13] M. C. Brandes, L. Kovarik, M. K. Miller and M. J. Mills, *J. Mater. Sci. (*2012) 47:3913.

[14] A. Hirata, T. Fujita, Y. R. Wen, et al., *Nature Mater.* (2011) 10:922.

[15] J. Ciston, Y. Wu, G. R. Odette and P. Hosemann, "The Structure of Nanoscale Precipitates and Precipitate Interfaces in an Oxide Dispersion Strengthened Steel," Fusion Materials Semiannual Progress Report for the Period Ending December 31, 2011, DOE-ER-0313/51;2012: in press.

[16] M. K. Miller, D.T. Hoelzer, E. A. Kenik, K. F. Russell, *J. Nucl. Mater.* **329-333** (2004) 338-341.

[17] M. K. Miller, D. T. Hoelzer, E. A. Kenik, and K. F. Russell, *Intermetallics* **13** (2005) 387-392.

[18] N. J. Cunningham, G. R. Odette, and E. Stergar, "Further Atom Probe Tomography Studies of Nanostructured Ferritic Alloy MA957 in Three Conditions," DOE Fusion Reactor Materials Program Semiannual Report, Vol. **49**, 2010, 11-16. DOE/ER-0313/49.

[19] N. J. Cunningham, A. Etienne, Y. Wu, E. M. Haney, and G. R. Odette, "On the Oxide Nanofeatures and Precipitates in the Nano-Structured Ferritic Alloy MA957: A Multiple Technique Study of Heat to Heat Variations and the Effects of Friction Stir Welding and Long Term Thermal Aging," DOE Fusion Reactor Materials Program Semiannual Report, Vol. **48**, 2010, 60-67. DEO/ER-0313/48.

[20] E. A. Marquis and J. Hyde, *Mater. Sci. Eng.* (2010) 69:37.

[21] E. A. Marquis, *Appl. Phys. Lett*. (2008) 93:181904.

[22] C. A. Williams, E. A. Marquis, A. Cerezo and G. D. W. Smith, *J. Nucl. Mater*. (2010) 400:37.

[23] C. Oberdorfer and G. Schmitz, *Microsc. Microanal*. (2011) 17:15.

[24] E. A. Marquis and F. Vurpillot, *Microsc. Microanal*. **14** (2008) 561.

[25] D. Vaumousse, A. Cerezo, P. J. Warren, *Ultramicroscop,* **95** (2003) 215.

[26] J. M. Hyde, C. A. English, G. E. Lucas, M. A. Kirk Jr., R. G. Elliman (Eds.), Proc. of the MRS 2000 Fall Meeting, Symp. R: Microstructural Processes in Irradiated Materials 650, Materials Research Society (2000/2001) R6.6.1.

[27] F. Vurpillot, A. Bostel, and D. Blavette, *App. Phys. Lett.* (2000) 76:3127.

[28] B. Gault, M. P. Moody, F. de Geuser, D. Haley, L. T. Stephenson, and S. P. Ringer, *App. Phys. Lett.* (2009) 95:034103.

[29] Y. Yamaguchi, J. Takahashi, and K. Kawakami, *Ultramicroscopy* **109** (2009) 541-544.

2.3 Specimen Preparation and characterization of 14YWT (SM12 heat) for the JP-30/31 HFIR Experiments — D. T. Hoelzer, E. T. Manneschmidt and M. A. Sokolov (Oak Ridge National Laboratory)

OBJECTIVE

To fabricate specimens from the advanced oxide dispersion strengthened (ODS) 14YWT (SM12 heat) ferritic alloy for the JP-30 and JP-31 HFIR target irradiation experiments and conduct the reference characterization of the microstructure and mechanical properties of three SM12 heats that were produced with different extrusion temperatures and rolling conditions to compare with PIE results that will be obtained in the future.

SUMMARY

Three heats of the advanced ODS 14YWT-SM12 ferritic alloy were produced with different extrusion temperatures and plates of each heat were fabricated with two different rolling conditions. The 14YWT-SM12 was a "clean" heat that was produced with improved mechanical alloying conditions to achieve low C (128 wppm) and N (117 wppm) levels and elevated O (1184 wppm) level. Plates of three SM12 heats were obtained by extruding at 850ºC, 1000ºC and 1150ºC temperatures followed by rolling at 1000ºC to 50% reduction in thickness in either the parallel (PR) or cross (CR) directions with reference to the extrusion direction. Specimens were fabricated from four plates of the SM12 heat with different thermal-mechanical treatments (TMT) and supplied for assembly of the JP30/31 capsules. The reference characterization of the microstructure and mechanical properties of the three SM12 heats was initiated. Results obtained from tensile tests at 25ºC showed slightly lower strengths, but significantly higher uniform (>9%) and total elongations in all the 14YWT-SM12 heats compared to results obtained from previous 14YWT heats. The general microstructural characteristics observed by SEM analysis showed that slightly larger grains with less uniformity in grain size had formed in the SM12 heats compared to previous 14YWT heats. The observed differences in the mechanical properties and grain structures of the SM12 heats compared to previous 14YWT heats were most likely due to lowering the O, C and N levels during ball milling.

PROGRESS AND STATUS

Introduction

The new target irradiation experiment (JP-30/31) was developed within the framework of the U.S.DOE-JAEA collaboration on fusion materials to investigate the effects of neutron irradiation at different temperatures on the microstructure stability and mechanical properties of reduced-activation ferritic/martensitic (RAFM) steels and the advanced dispersion strengthened ferritic alloys and FM steels [1]. The JP-30/31 experiment was modified from the JP-28 and JP-29 experiments by designing the capsules to increase the neutron irradiation temperature for one of the sub-capsules from 500ºC (JP-28/29) to 650ºC (JP-30/31) while maintaining similar irradiation temperatures of 300ºC and 400ºC for the other two sub-capsules [2]. The estimated neutron fluence of the JP-30/31 experiment is ~20 dpa. One of the primary reasons for raising the irradiation temperature to 650ºC was to investigate the effects of irradiation on the microstructure stability and mechanical properties of advanced dispersion strengthened materials, such as oxide dispersion strengthened (ODS) alloys that are being developed specifically for nuclear energy components that required higher operating temperatures.

The U.S. Fusion Materials program selected the advanced ODS 14YWT ferritic alloy for the JP-30/31 experiment since a fairly large background on processing, microstructure analysis and mechanical properties characterization have been obtained from studies of 14YWT heats produced in the past. For the JP-30/31 experiment, the 14YWT (SM12 heat) was used for preparation of specimens. The 14YWT-SM12 was produced in the Core Materials Technologies project of the Fuel Cycle Research and Development (FCRD) NE program. The primary goal of the project was to optimize the processing conditions for scale-up production of the ~55 kg heat of 14YWT. A key processing factor investigated in this project was to improve the ball milling conditions to minimize the C and N contents while maintaining a high O content, which is required for forming the high concentration of nano-scale oxide particles that is characteristic of 14YWT heats. The purpose of this report is to cover the processing conditions used for producing three 14YWT-SM12 heats, the type and number of specimens that were prepared for the JP30/31 HFIR experiment and the preliminary results obtained from the reference characterization of the microstructures and mechanical properties of the 14YWT-SM12 heats.

Processing of the 14YWT-SM12 Heats

The 14YWT-SM12 heat was produced by mechanical alloying (MA) using gas atomized powder produced by Special Metals with nominal composition of Fe-14Cr-3W-0.4Ti (Fe pre-alloyed) and nano-size (17-31 nm) Y_2O_3 powder produced by Nanophase, Inc. The blended powder consisting of 99.7% Fe pre-alloyed and 0.3% Y_2O_3 powder (wt. %) was ball milled using the Zoz CM08 high energy attritor mill for 40 h in an Ar atmosphere. Three ball milling runs consisting of 1.0 kg of blended powder each were performed, which generated 3.0 kg of ball milled powder. The new ball milling conditions developed in the FCRD program resulted in significantly lower O, C and N levels in the SM12 heat compared to previous 14YWT heats such as the SM11 heat as shown in Table 1. In the table, the amount of O that was picked up during ball milling was determined by subtracting both the O level in the atomized powder (~150 wppm) and the O level from the Y_2O_3 powder (683 wppm) from that of the ball milled powder. The results indicated that the O, C and N levels picked up during ball milling were significantly lower in the SM12 powder compared to the SM11 powder.

For consolidation of the 3.0 kg of ball milled powder by extrusion, the powder was first separated into 4 equal batches of 750 g. Three of the batches of ball milled powder were sealed in 2.9 inch diameter mild steel cans and degassed at 400ºC in vacuum before being hermetically sealed. The sealed cans were first annealed at 850ºC for 1 h. The cans were then annealed for 1 at three different temperatures corresponding to the extrusion temperatures. One can was extruded at 1150ºC (SM12a heat), one was extruded at 1000ºC (SM12c heat) and the last one was extruded at 850ºC (SM12d heat). The cans were extruded through a rectangular shaped die to form bars. Extruding the cans at different temperatures was intended

Table 1. Comparison of the O, C and N levels of the SM11 and SM12 heats of 14YWT.

Element	14YWT-SM11			14YWT-SM12		
(wppm)	Atomized	Milled	Pickup	Atomized	Milled	Pickup
O	150	2590	1802	150	1184	396
C	100	346	246	100	128	28
N	50	1911	1861	50	117	67

to alter both the grain size and oxide particle dispersion between the 14YWT-SM12 heats and to study which condition may provide the best combination of mechanical properties before and after irradiation.

After extrusion, the bars of the three 14YWT-SM12 heats were annealed at 1000ºC for 1 h in vacuum and then were cut into 3 sections of equal lengths for rolling. The rolling procedure used for each heat was performed by rolling one bar parallel (PR) and another bar normal, or cross (CR), to the extrusion direction to form plates as shown in Figure 1. The rolling of the bars into plates was conducted at 1000ºC with a reduction in thickness of ~50%. The cross rolling (CR) was performed to investigate whether the anisotropy in the mechanical properties that is typical of mechanically alloyed ODS alloys could be minimized.

Figure 1. Digital image of SM12a showing the three cut sections of the extruded bar in the as extruded condition (center), hot rolled parallel to the extrusion axis (right) and hot rolled normal (cross) to the extrusion axis (left).

Preparation of Specimens for the JP-30/31 HFIR Experiment

Specimens for the JP30/31 HFIR experiment were fabricated from the three PR plates of each heat (SM12a, SM12c and SM12d) and from the CR plate of the SM12d heat. There were six types of specimens that were prepared. The specimens consisted of miniature tensile (SSJ3; 5 x 1.4 x 0.75 mm gage), 5 notch fracture toughness bend bar (M5PCCVN; 54 x 3.3 x 1.65 mm), disk compact tension fracture toughness (DCT; ~ø12.5 x 0.2 mm), tuning fork type specimens for atom probe analysis (APFIM; 16 x 1.14 x 0.5 mm), TEM disks (ø3 x 0.25 mm) and miniature multi-purpose coupons (MMPC; 16 x 1.15 x 1 mm). The list showing the type and number of specimens that were prepared from the four plates is shown in Table 2.

Table 2. The specimens fabricated from the 14YWT-SM12 heats for the JP-30/31 experiment.

Capsule	14YWT Heat	Extrusion Temperature	Specimen Type	Quantity
300ºC	SM12a-PR	1150ºC	APFIM	2
			TEM	4
	SM12c-PR	1000ºC	APFIM	2
			TEM	4
	SM12d-PR	850ºC	APFIM	2
			TEM	4
			SS-J3	4
			DCT	6
400ºC	SM12a-PR	1150ºC	APFIM	2
			TEM	4
	SM12c-PR	1000ºC	TEM	4
	SM12d-PR	850ºC	APFIM	2
			TEM	4
650ºC	SM12a-PR	1150ºC	APFIM	2
			TEM	4
			SS-J3	6
	SM12c-PR	1000ºC	APFIM	2
			TEM	4
			SS-J3	6
	SM12d-PR	850ºC	APFIM	2
			TEM	4
			SS-J3	6
			DCT	9
	SM12d-CR	850ºC	M5PCVVN	4
			SS-J3	4
			MMPC	5

The assignment of the specimens for the sub-capsules that will be neutron irradiated at 300ºC, 400ºC and 650ºC is also shown in Table 2. The test matrix emphasized that PIE will consist of microstructural analysis at each irradiation temperature and mechanical properties examination only at the low (300ºC) and high (650ºC) irradiation temperatures. Both tensile and fracture toughness properties will be measured at the two irradiation temperatures.

Reference Characterization Study of the 14YWT-SM12 Heats

The detailed characterization of the microstructure and mechanical properties of the 14YWT-SM12 heats was performed to allow comparison with irradiated specimens from the JP30/31

experiment and also to investigate the role that the different processing and fabrication conditions had on the grain structure and nano-scale oxide particle dispersion that formed in the heats and to determine how differences in the microstructures affected the mechanical properties.   The reference characterization study will focus on microstructure analysis using SEM, TEM and possibly Atom Probe and on mechanical properties characterization using hardness, tensile and fracture toughness tests.

Samples obtained from the plates of SM12a (1150ºC), SM12c (1000ºC), and SM12d (850ºC) in the PR condition and SM12d (850ºC) in the CR condition were mounted and polished for Vickers Hardness measurements and microstructural analysis by SEM. The Vickers Hardness Number (VHN) obtained from the four samples is shown in Figure 2. The results showed the expected trend of an increase in hardness with decrease in extrusion temperature, but the range between the lowest and highest hardness value was relatively small (~42 VHN, or ~10%). The largest difference in hardness occurred between the 850ºC heats (SM12d PR and CR) and the 1000ºC heat (SM12c PR). The microstructure of the samples was characterized with the SEM using back scattered electrons (BSE) to improve imaging ultra-small grains common to 14YWT heats. The BSE images observed in Figure 3 were obtained at low magnification to show the uniformity of grain sizes that were present in the heats.   As shown in this figure, all of the SM12 heats showed grain sizes that were not very uniform compared to previous 14YWT heats. At the higher magnification shown in Figure 4, the BSE images revealed that the
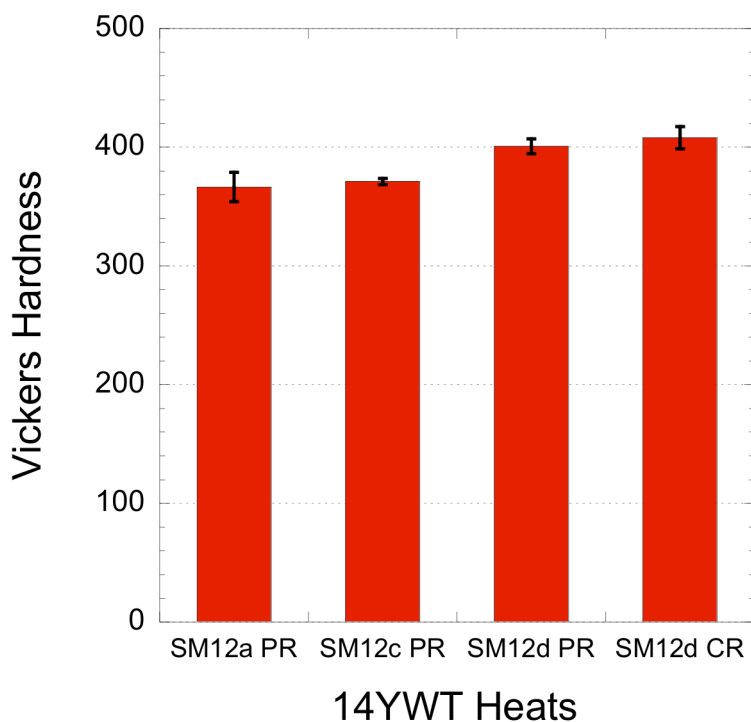
Figure 2. Comparison of Vickers Hardness for the 14YWT-SM12 heats.

(a)   (b)

(c)   (d)
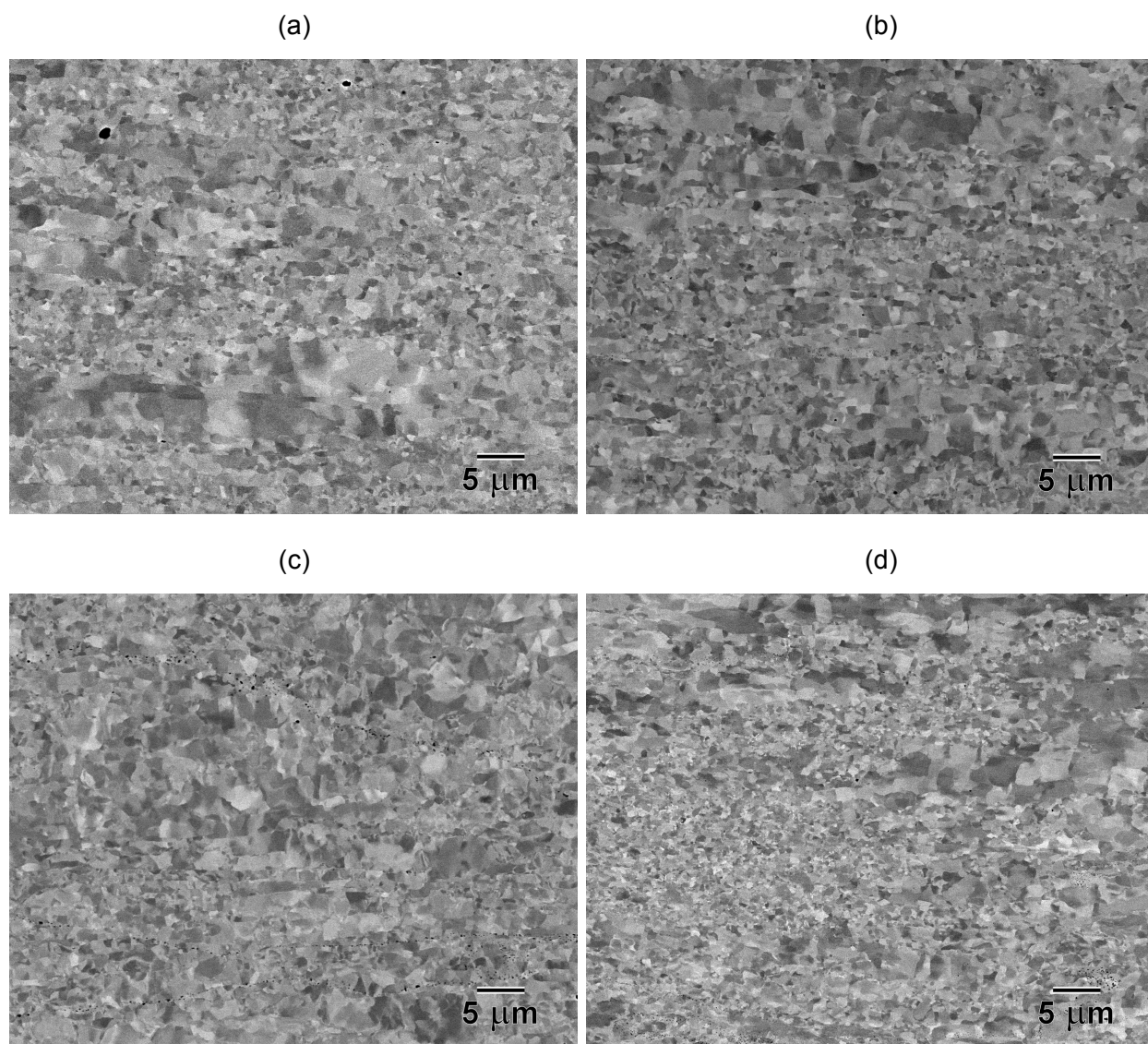
Figure 3. SEM BSE images at a relatively low magnification showing the variation in grain size observed in the microstructures of the (a) SM12a PR, (b) SM12c PR, (c) SM12d PR and (d) SM12d CR heats.

grain were also slightly larger in size compared to previous 14YWT heats. In addition, small dark imaging particles were observed (Figures 4c and 4d) usually distributed in clusters along interfaces that were most likely prior surfaces of the ball milled powder. Interestingly, the comparison of both sets of BSE images shown in Figures 3 and 4 indicated that the different extrusion temperatures and rolling conditions had very little effect on the microstructures since they were very similar in the SM12 heats.

Tensile tests were performed on SS-J3 specimens of the SM12 heats at room temperature (25ºC) using a strain rate of 1×10^{-3} s^{-1}. The stress strain curves shown in Figure 5 revealed slightly lower strengths, but significantly higher uniform and total elongations in all the

(a)   (b)

(c)   (d)
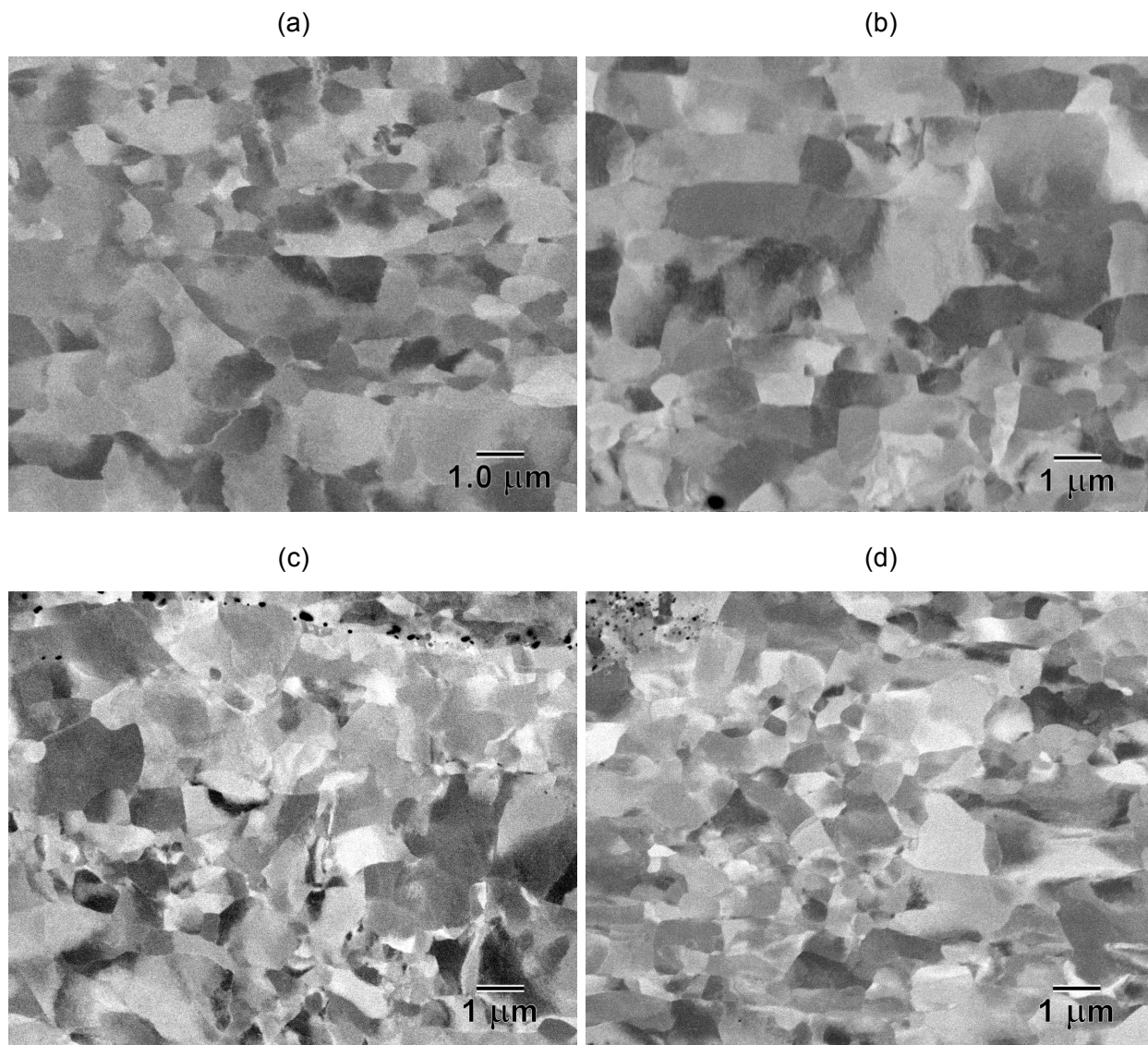
Figure 4. SEM BSE images at high magnification showing the grain size observed in the microstructures of the (a) SM12a PR, (b) SM12c PR, (c) SM12d PR and (d) SM12d CR heats.

14YWT-SM12 heats compared to results obtained from previous 14YWT heats. All of the SM12 heats possessed uniform elongations that were greater than 9%, which is significantly better than the 1 to 2% uniform elongation typically observed in previous 14YWT heats. The yield and ultimate tensile stresses and uniform and total elongations measured from the stress-strain curves of the SM12 heats are shown in the plot in Figure 6. Interestingly, the measured values showed essentially no differences between the heats, indicating that differences in the extrusion temperature and rolling conditions had very little effect on the tensile deformation behavior. The

yield stress and ultimate tensile strengths of the SM12 heats were all near ~1.0 GPa and ~1.2 GPa, respectively. In a similar manner, the uniform and total elongations were nearly constant for each SM12 heat and were ~9-10% and ~21-24%, respectively.

The combination of relatively high strength with much improved ductility properties was most likely due to the lower C and N levels that were achieved in producing the SM12 heat. Furthermore, the lower strength and higher ductility of the SM12 heats compared to previous 14YWT heats may also be due to the larger grain sizes that were observed. However, further microstructural characterization using TEM analysis to investigate the nano-scale oxide particle dispersions in the SM12 heats is necessary to obtain a better understanding of the relationship between processing, mechanical properties and microstructure of the 14YWT-SM12 heats.
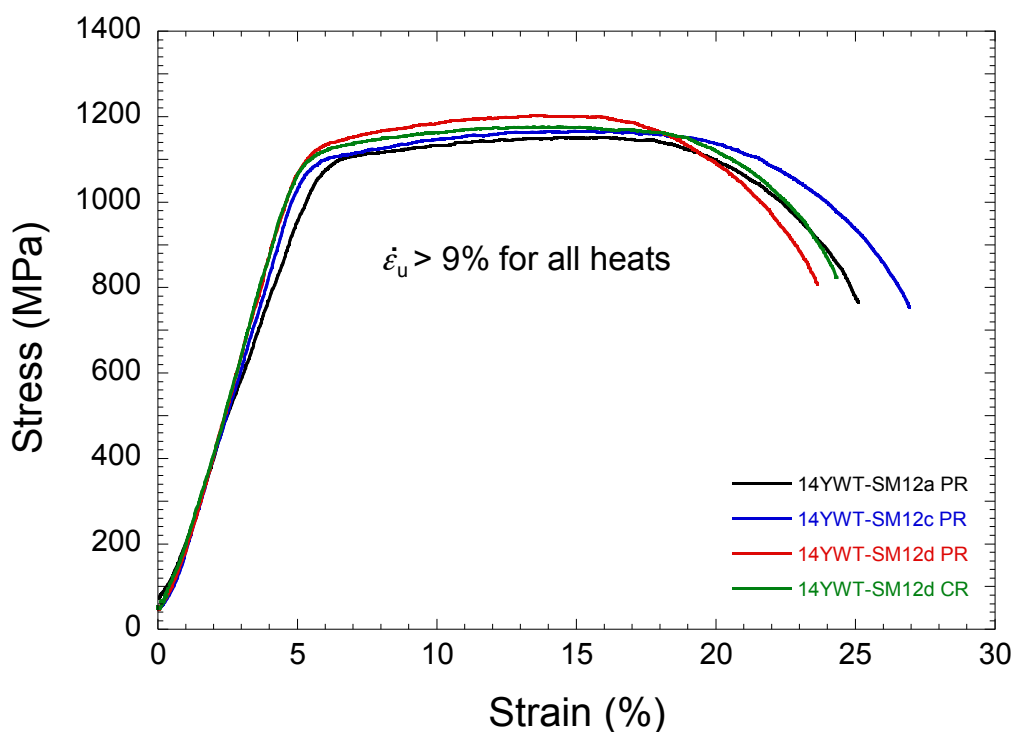
Figure 5. Stress-strain curves of the SM12a PR, SM12c PR, SM12d PR and SM12d CR heats obtained from tensile tests at 25°C using a strain rate of 1×10^{-3} s^{-1}.
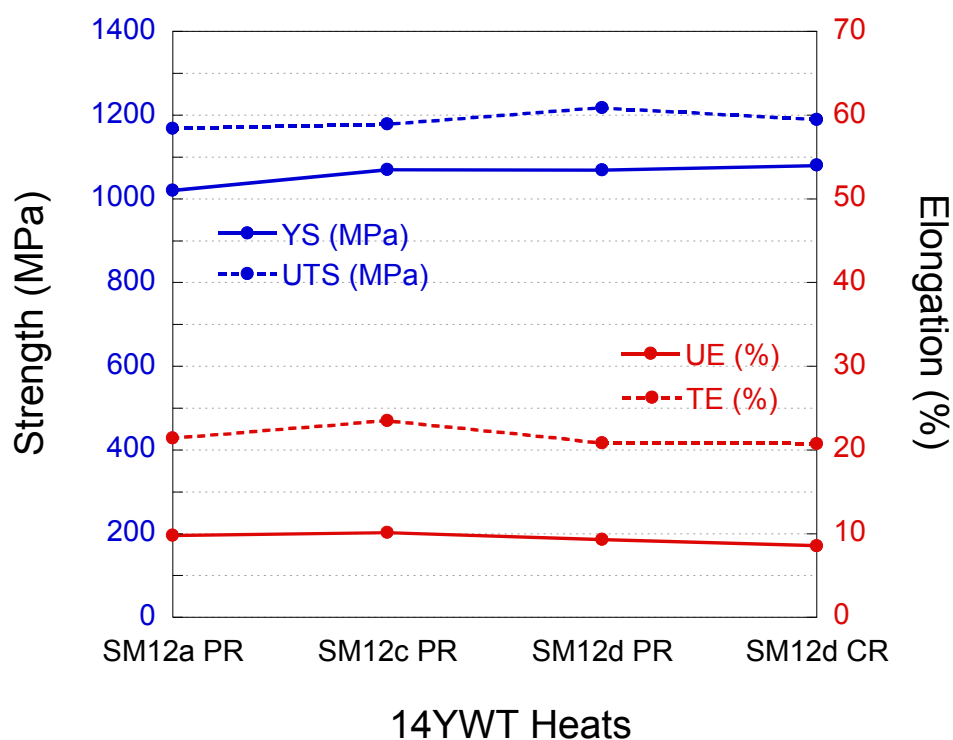
Figure 6. Comparison of the tensile properties of the SM12a PR, SM12c PR, SM12d PR and SM12d CR heats obtained from tensile tests at 25ºC using a strain rate of 1 x 10^{-3} s^{-1}.

SUMMARY

Three heats of the advanced ODS 14YWT-SM12 ferritic alloy were produced by extrusion at 850ºC, 1000ºC and 1150ºC. Improved mechanical processing conditions led to low C and N levels and elevated O level for 14YWT-SM12. Plates of the three SM12 heats were fabricated by rolling at 1000ºC to 50% reduction in thickness in the parallel (PR) and cross (CR) rolling directions with reference to the extrusion direction. Specimens were fabricated from four plates of the SM12 heats and supplied for assembly of the JP30/31 capsules for the JP-30/31 HFIR irradiation experiments. The reference characterization of the microstructure and mechanical properties of the three SM12 heats was initiated. Results obtained from tensile tests at 25ºC showed slightly lower strengths, but significantly higher uniform (>9%) and total elongations in all the 14YWT-SM12 heats compared to results obtained from previous 14YWT heats. The general microstructural characteristics observed by SEM analysis showed that slightly larger grains with less uniformity in grain size had formed in the SM12 heats compared to previous 14YWT heats. The observed differences in the mechanical properties and grain structures of the SM12 heats compared to previous 14YWT heats were most likely due to lowering the O, C and N levels during ball milling.

FUTURE WORK

Detailed characterization of the microstructure and mechanical properties of the 14YWT-SM12 heats will continue. TEM specimens will be jet-polished soon and examined. Plates of the SM12a PR, SM12c PR and SM12d PR will be submitted to the machine shop for fabricating a number of SS-J3 tensile and DCT fracture toughness specimens for further mechanical properties testing. The tensile tests will emphasize elevated temperatures while the fracture toughness tests will focus on determining the fracture toughness transition temperature and possibly the fracture toughness at elevated temperatures. The goal is to have a sufficiently large number of SS-J3 and DCT specimens prepared so that several specimens can heat treated at similar temperatures for the same period of time that specimens in the JP-30/31 experiment will be experience. Comparison of the microstructure and mechanical properties that will be obtained from the annealed and irradiated specimens of the SM12 heats will provide valuable information about the effect of time at temperature so that a more accurate assessment of the effect that neutron irradiation may have on changes in the microstructures and mechanical properties can be determined.

ACKNOWLEDGEMENT

REFERENCE

1. T. Nozawa, T. Hirose, H. Tanigawa, M. Ando, J. L. McDuffee, D. W. Heatherly, R. G. Sitterson, M. A. Sokolov, L. Tan, D. T. Hoelzer, R. E. Stoller, L. L. Snead, and T. Yamamoto, in the current Fusion Materials Semiannual Progress Report for Period Ending December 31, 2011, U.S. Department of Energy.

2. D. K. Felde, D. W. Heatherly, S. H. Kim, R. G. Sitterson, R. E. Stoller, C. Wang, M. Ando and H. Tanigawa, Fusion Materials Semiannual Progress Report for Period Ending June 30, 2005, DOE/ER-0313/38, U.S. Department of Energy, 153.

2.4 Joining of 14YWT and F82H by Friction Stir Welding - D. T. Hoelzer, M. A. Sokolov and Z. Feng (Oak Ridge National Laboratory)

This is the Abstract for an ICFRM-15 paper submitted for publication in the Proceedings.

The feasibility of using friction stir welding (FSW) to join specimens of the advanced oxide dispersion strengthened (ODS) 14YWT nanostructured ferritic alloy (NFA) and a plate of F82H tempered martensitic steel (TMS) was investigated. The sample used in the FSW experiment consisted of spot welding four specimens of 14YWT that were prepared from prior tested dual notch fracture toughness bend bars, into a corresponding slot that was machined in a F82H plate. Successful FSW was performed using a polycrystalline boron nitride tool (PCBN). Bonding (i.e., welds) between both 14YWT/14YWT plate and 14YWT/ F82H plate was successful. Joints, characterized by light microscopy and SEM analysis, were observed to be relatively narrow in width. The ultra-fine grain size associated with 14YWT increased by a factor of up to 3 while that of F82H was refined by a considerable amount in the thermomechanically affected zones (TMAZ) due to FSW. In addition, porosity was observed in the TMAZ of 14YWT on both the advancing side of the FSW joint and at the interface between F82H and 14YWT. Vickers hardness (VH) measurements from the FSW zones showed an ~20% decrease in hardness of 14YWT (from ~500 VH to ~380VH) and an ~100% increase in hardness of F82H (from ~220 VH to ~440VH). Further refinements in the FSW process will be required to minimize defects including porosity.

3.1   Strength and Microstructures of the Fiber/Matrix Interface of Neutron-Irradiated SiC/SiC Composites — T. Nozawa and H. Tanigawa (Japan Atomic Energy Agency), P. Dou, H. Bei, Y. Katoh, L. L. Snead, and R. E. Stoller (Oak Ridge National Laboratory)

OBJECTIVE

This work was carried out under the collaboration on fusion materials between the U.S. DOE and the Japan Atomic Energy Agency (JAEA). This study primarily aims to identify the dose-dependent strength of the fiber/matrix (F/M) interface of SiC/SiC composites coupled with summarizing the irradiation-induced microstructural changes of SiC fiber and matrix, and pyrolytic carbon (PyC) as an F/M interphase. High-dose irradiation up to 70 dpa was specifically focused on. Identifying the micro- and macro-strength interaction is another objective of this study.

SUMMARY

To investigate the irradiation effects on interfacial shear properties such as an interfacial debond shear strength (IDSS) and an interfacial friction stress (IFS), the single fiber push-out tests were applied to Hi-Nicalon Type-S fiber reinforced chemical-vapor-infiltration (CVI) SiC matrix composites neutron irradiated up to 70 dpa at 300~800 ºC. Test results demonstrated no significant irradiation-enhanced degradation of interfacial shear properties expected at any doses (i.e., a slight decrease at lower doses <10 dpa and apparent improvement at higher doses >10 dpa). The irradiation-induced stress is a primary source to affect the F/M interfacial stresses. At higher doses ~70dpa, volume expansion by disordering of PyC possibly induced a residual clamping stress, eventually improving interfacial shear properties. A good correlation between the F/M interfacial strength and the macro strength for certain irradiation conditions was obtained. Interfacial functions sustained but fiber (Hi-Nicalon Type-S) deterioration was implied by irradiation at 70dpa. In the future we must clearly define the irradiation-induced change in thermal expansivity. The differential swelling between the fiber and matrix and irradiation creep are also critically important.

PROGRESS AND STATUS

Introduction

A silicon carbide composite (SiC/SiC composite) is a candidate for the advanced blanket system of a fusion DEMO reactor due to the excellent thermo-mechanical and physical/chemical properties. Since composite's functions are readily affected by the fiber/matrix (F/M) interfacial properties, the irradiation stability of the interface needs to be proven for the practical design of the DEMO components.

The authors have investigated the effects of neutron irradiation on the interfacial shear properties and test results by lower dose irradiation (<7.7 dpa) were well-summarized in [1]. Through the entire work, the F/M interfacial strength was evaluated by the single fiber push-out test technique with the modified shear-lag model, which gives the IDSS and the IDS with consideration of thermal stress, irradiation-induced stress, toughness-induced stress and Poisson's expansion. From the key findings of this work, both the IDSS and the IFS first decreased and slightly recovered with increasing irradiation up to 10 dpa. The probable explanation of such changes is a radiation-induced dimensional change of PyC, which shows a turn-around behavior of irradiation-induced swelling. Also it was found that the decrease of the interfacial friction stress at 7.7 dpa at 800 ºC

was significant. It is speculated that a decreasing surface roughness by the irradiation-enhanced change of the cracking path at the F/M interface from the inside PyC interphase to the fiber surface affects the result, although this is still uncertain because of the scarce of data of the irradiation-induced morphology change of the PyC interface. In contrast, at higher doses up to 40 dpa, there was no significant degradation of the bend strength, implying no potential degradation of the F/M interfacial strength. This is somehow surprising since it has been believed that carbon materials are generally instable by higher dose irradiation and needs to be confirmed by the individual interface tests. Of particular important is to identify a correlation between the nano-strength and the irradiation-induced microstructures.

EXPERIMENTAL PROCEDURE

Material

A satin-weave (S/W) CVI-SiC/SiC composite was tested. The reinforcement was highly-crystalline and near-stoichiometric Hi-Nicalon Type-S SiC fibers. The multilayered PyC/SiC interface (20 nm PyC x 5 with 100 nm SiC inserts) was formed (Fig. 1).   The fiber volume fraction was approximately 35 %. The details of S/W composites are described in [2, 3], respectively.

Neutron Irradiation

Rectangular flexural specimens with a size of 50.2 x 6.35 x 2.63 mm were irradiated by the HFIR flux trap fixed rabbit tube facility at Oak Ridge National Laboratory. The irradiation doses and temperatures were ~70 dpa and 325~800 ºC, respectively.

Post Irradiation Experiments

The original rectangular flexural specimen was cut into the miniature bars with as size of 25 x 3 x 1.2 mm. The bulk strength was then obtained by the 4-point bend test with loading/support spans of 10/20 mm. After the bend tests, the interfacial shear strengths were evaluated by the single fiber push-out test using a nano-indenter. By applying the modified double shear-lag (Hsueh) model, both the IDSS and the IFS are finally obtained. Note that the thermal and irradiation creep were not presently considered in the model due to the lack of data. The detailed analytical procedure was described in [1]. The microstructures of neutron irradiated composites were observed by the scanning electron microscopy (SEM) and the transmission electron microscopy (TEM).

RESULTS

Irradiation Effects on Interfacial Shear Properties

Figure 1 shows the effects of neutron irradiation on the interfacial shear properties. Both the IDSS and the IFS first decreased and increased with increasing neutron dose. Of particular emphasis is no serious degradation even in carbon instability region.   Instead, high-dose irradiation further improved interfacial shear properties. The temperature dependence is unclear but seemingly high-temperature irradiation tends to impact more on the interfacial shear properties.
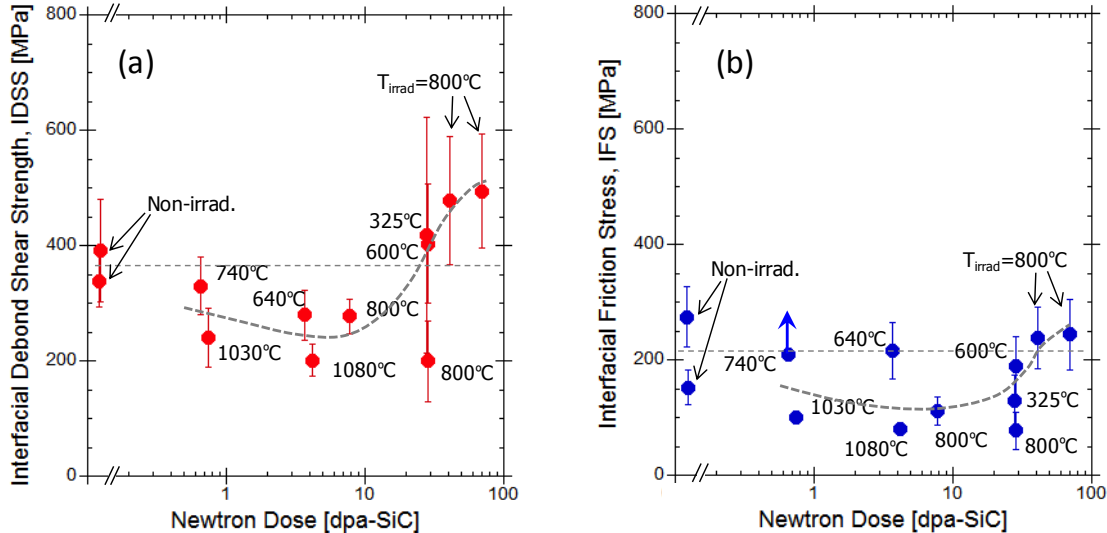
Fig. 1. Neutron irradiation effects on (a) the interfacial debond shear strength (IDSS) and (b) the interfacial friction stress (IFS) of Hi-Nicalon Type-S/multilayer/CVI-SiC composites.

The interfacial shear properties generally depend on (1) the residual strain and (2) the fiber surface roughness. Accordingly to the model calculation [1], comparably minor effect of the coefficient of thermal expansion (CTE) change of PyC itself is expected. There is in contrast a significant impact of the CTE changes of the fiber or the matrix even if there is a slight gap of CTEs between the fiber and the matrix. Radiation-induced CTE modification of the Hi-Nicalon Type-S SiC fiber and the CVI-SiC matrix is uncertain and needs to be identified in further experiments.

Irradiation-induced residual strain also influences the radial clamping stress at the F/M interface. Because of the significant swelling of PyC, i.e., "turn-around" behavior, and this undoubtedly affects the irradiation behavior of the interfacial shear properties. But this is unclear at higher doses because of instability of PyC itself. In contrast, a mild change of axial stresses between the fiber and the matrix is expected assuming the same swelling quantity of them. However, differential swelling between the fiber and the matrix may induce further stresses. If the fiber swells more than the matrix, the residual clamping stress tends to increase more, potentially improving the interfacial shear properties. This issue also needs to be clarified in future.

Figure 2 shows the typical microstructures of the F/M interface of Hi-Nicalon Type-S/multilayer/CVI-SiC composites by irradiation at 70 dpa at 800 °C. It is clearly shown that parts of PyC were disordered by irradiation. From this fact, the most probable explanation for the significant improvement of the interfacial shear properties by irradiation up to ~70 dpa is that disordered PyC due to instability by the high-dose irradiation gives a significant residual compressive stress at the F/M interface by its volumetric expansion. Because of instability of PyC itself, there was a fact that a crack can easily propagated within PyC. In contrast, it is very hard to identify the admissible degradation of the Hi-Nicalon Type-S SiC fiber and the SiC matrix. This needs to be further evaluated carefully.
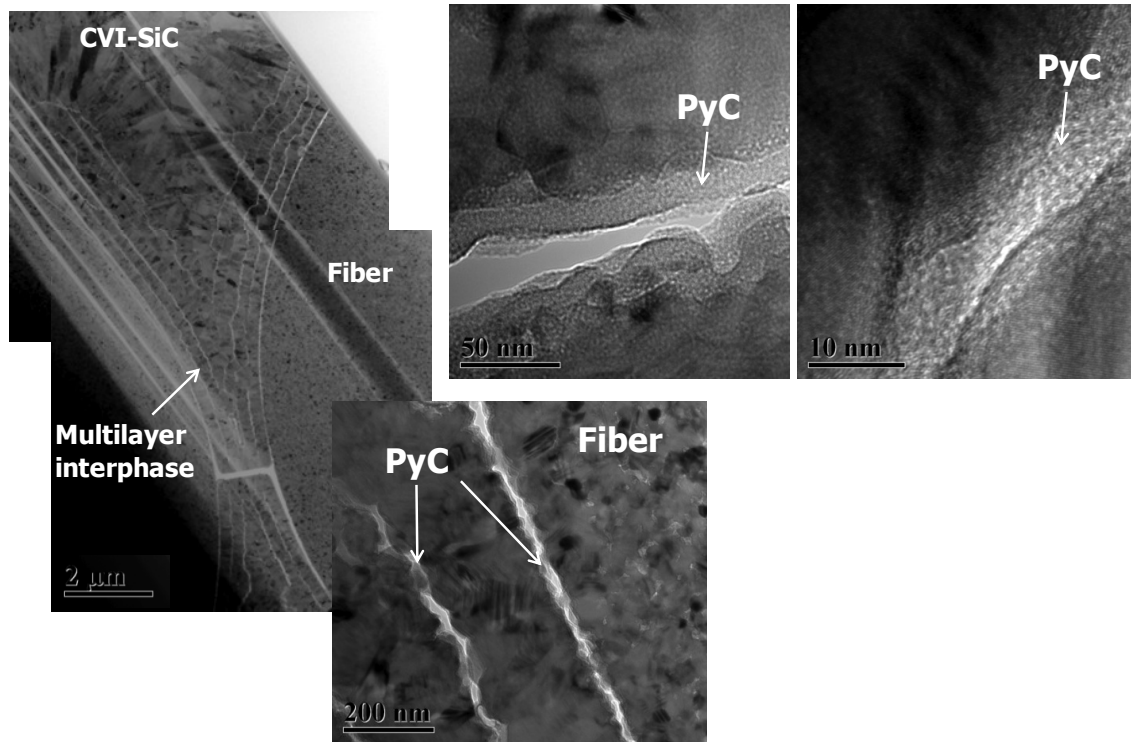
Fig. 2.   Typical microstructures of the F/M interface of Hi-Nicalon Type-S/multilayer/CVI-SiC composites.
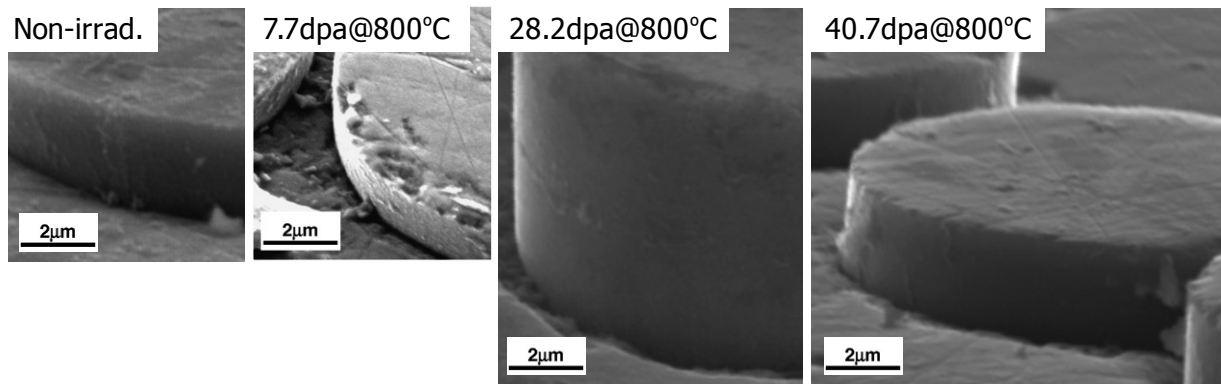
Fig. 3.   Typical surface appearances of pushed-out Hi-Nicalon Type-S fibers.

Figure 3 shows the typical surface appearances of pushed-out fibers.   There seems no clear change in the surface roughness.   It was therefore concluded that contribution of the roughness-induced clamping stress was very minor.

Correlation between Bulk Strength and Interfacial Shear Properties

Figure 4(a) shows neutron dose dependencies of the proportional limit tensile/flexural stress (PLS) and the IDSS, both of which are normalized by the non-irradiated test result. The PLS slightly decreased by irradiation but did not depend on the fluence so much, while, as aforementioned, the IDSS first decreased a little bit and remarkably improved with increasing neutron fluence. Katoh et al [4] claimed that the PLS depends on the true matrix cracking stress and the misfit stress (i.e., irradiation-induced stress). By separately discussing these two parameters, the test results supported no significant change of the true matrix cracking stress by irradiation reported. The post irradiation strength therefore depends primarily on the misfit stress. Since the IDSS is also dependent on the residual stress, the post irradiation PLS therefore depends on IDSS too. This is true at least by irradiation up to 10 dpa. But, from this point of discussion, the PLS at higher doses was not recovered more than expected from the result of the IDSS; the IDSS shows remarkable improvement by irradiation up to >40 dpa (Fig. 4(b)).
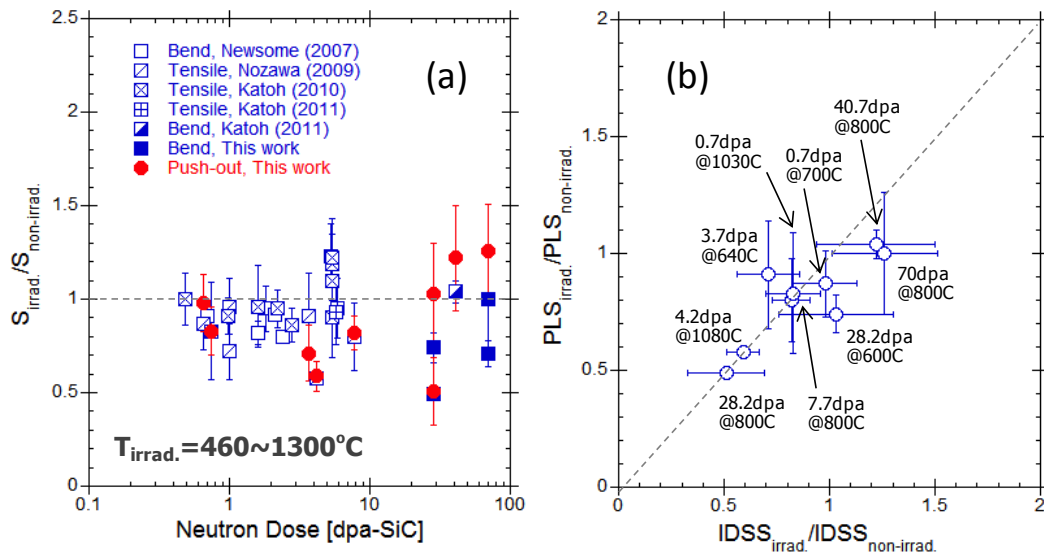
Fig. 4 – (a) Neutron dose dependencies of the proportional limit tensile/flexural stress (PLS) and the interfacial debond shear strength (IDSS) and (b) correlation between the PLS and the IDSS.
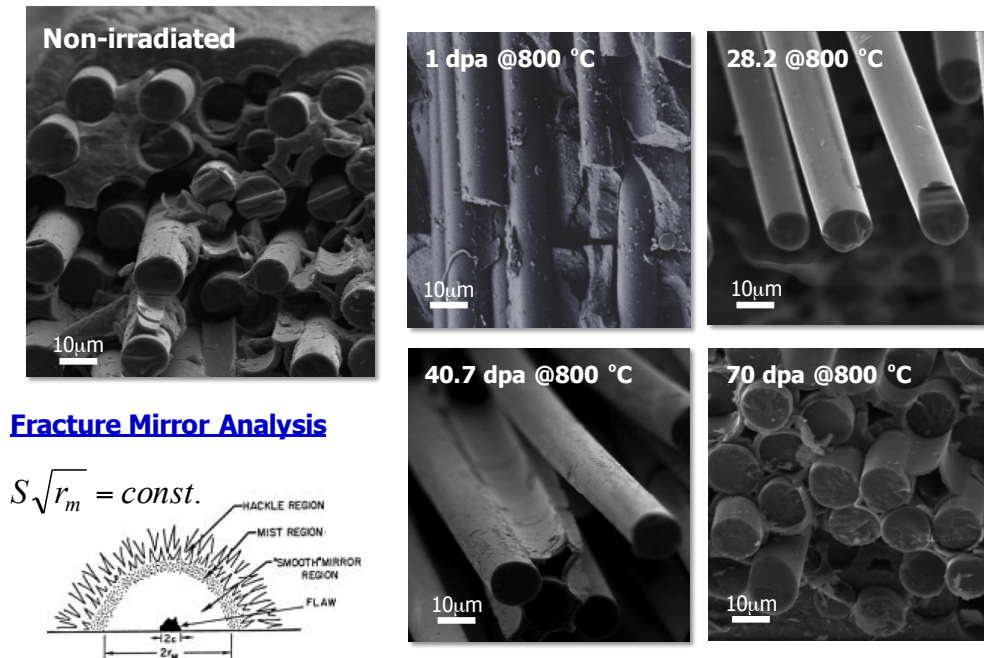
Fig. 5.   Typical flexural fracture surface images of Hi-Nicalon Type-S/multilayer/CVI-SiC composites before and after irradiation.

Figure 5 shows typical fracture surface images of Hi-Nicalon Type-S composites before and after irradiation. In each test condition, composites show moderate fiber pullouts, although the fiber pullout length is short due to the strong interfacial friction stress. For the non-irradiated case and some lower dose irradiation cases, the cross section of the fractured fiber is like a broken surface of amorphous based fibers, while, as clearly shown for the 70 dpa irradiation case, the fracture mirror was appeared by higher-dose irradiation. Theoretically, the individual fiber strength depends on the mirror radius as explained in embedded drawing in Fig. 5. In general, the fiber strength decreased with increasing the mirror radius. With the fact that the fracture mirror first appeared by higher dose irradiation (~70 dpa), the possible fiber degradation would be a key reason for the reduction of the bulk composite strength. Detailed microstructural observation will be planned to confirm this.

REFERENCES

[1] T. Nozawa, Y. Katoh, and L. L. Snead, *J. Nucl. Mater*. **384** (2009) 195.
[2] Y. Katoh, T. Nozawa, L. L. Snead, K. Ozawa, and H. Tanigawa, *J. Nucl. Mater.* **417** (2011) 400.
[3] G. Newsome, L. L. Snead, T. Hinoki, Y. Katoh, and D. Peters, J*. Nucl. Mater.* **371** (2007) 76.
[4] Y. Katoh, K. Ozawa, T. Hinoki, Y. Choi, L. L. Snead, and A. Hasegawa, *J. Nucl. Mater*. **417** (2011) 416.

3.2 Effects of Contact Resistance on Electrical Conductivity Measurements of SiC-Based Materials — G. E. Youngblood,* E. C. Thomsen and C. H. Henager, Jr. (Pacific Northwest National Laboratory)

This is the Extended Abstract for an ICFRM-15 paper submitted for publication in the Proceedings.

A combination 2/4-probe method was used to measure electrical resistances across a pure, monolithic CVD-SiC disc sample with contact resistance at the SiC/metallic electrode interfaces. By comparison of the almost simultaneous 2/4-probe measurements, the specific contact resistance and its temperature dependence were determined for two types of electrodes (sputtered gold and porous nickel) from RT to ~700°C. The specific contact resistance values (R_c) behaved similarly for each type of metallic electrode: R_c >~1000 Ω-cm^2 at RT, decreasing continuously to ~1-10 Ω-cm^2 at 700°C (see Fig. 1). The temperature dependence of the inverse R_c indicated thermally activated electrical conduction across the SiC/metallic interface with an apparent activation energy of ~0.3 eV (see Fig. 2). For a flow channel insert in a fusion reactor blanket made with SiC/SiC composite, contact resistance could beneficially reduce the transverse electrical conductivity by ~1/2.
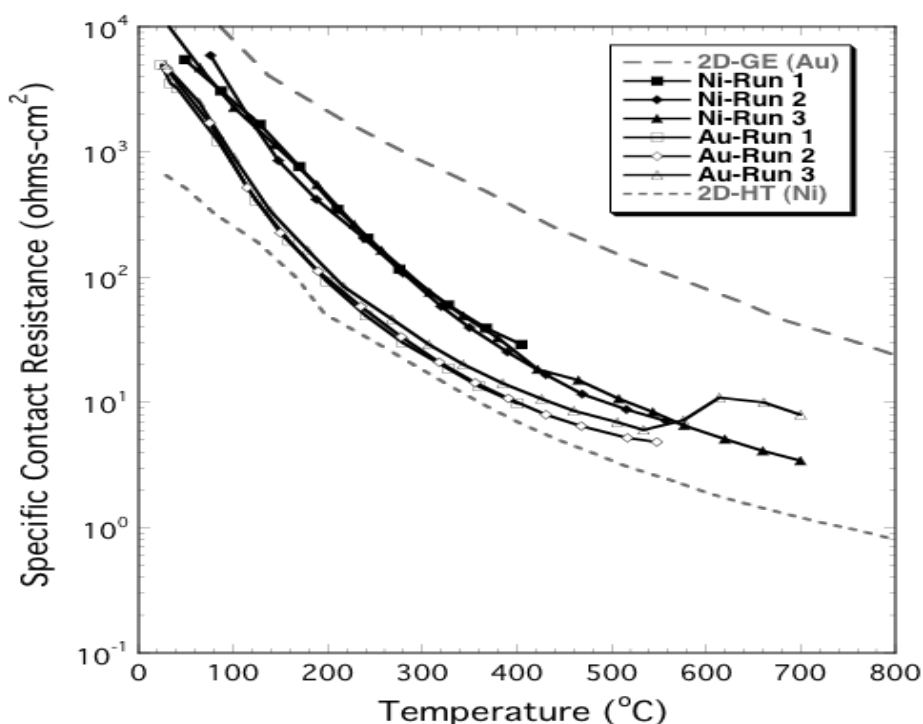
Figure 1. Specific R_c for CVD-SiC with sputtered Au or porous Ni electrodes, each during three successive heating cycles to 400, 550 and 700°C. The grey dashed lines indicate the envelope of R_c-values observed for similar sets of measurements for 2D-SiC/SiC composites with thin CVD-SiC seal coats [1].

The R_c-values determined for each set of temperature cycles to 400, 550 and 700°C were reproducible, except for the unexplained deviation from a smooth curve for the Au-Run 3 data. In general, the magnitudes and temperature dependence of the R_c-data lie between the envelope of R_c-values observed earlier for 2D-SiC$_f$/CVI-SiC composite disc samples with thin seal coats of CVD-SiC on which similar metal electrodes were applied [1]. The R_c-values for the porous Ni electrodes appear to exceed the values for the Au electrodes, but this may be because the actual contact area for the porous Ni electrodes is less than the geometric area of the disc sample.
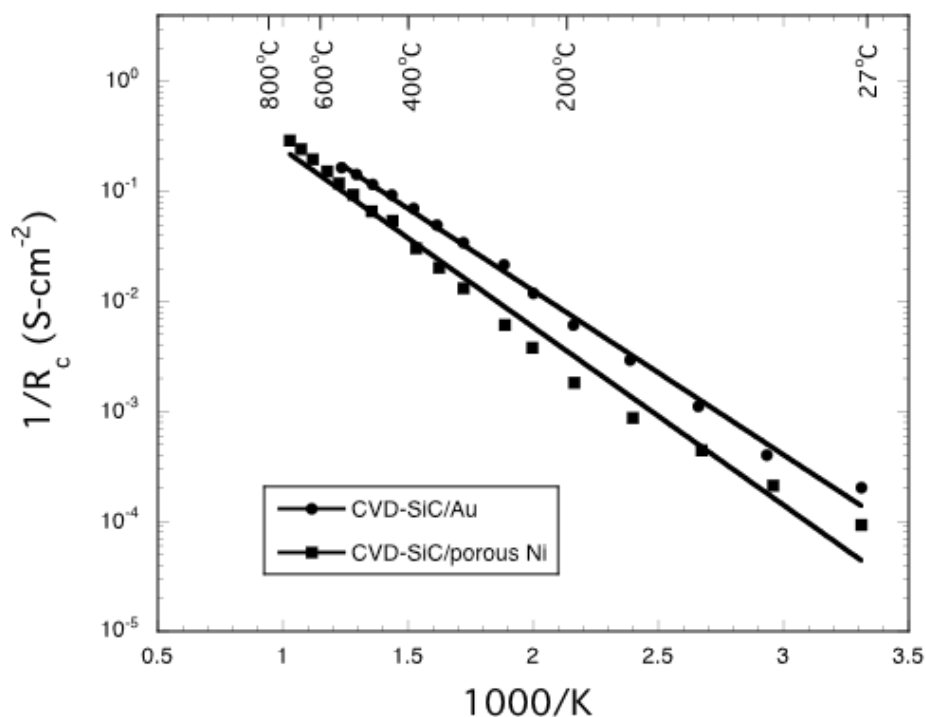
Figure 2. Inverse specific R_c for a CVD-SiC disc sample with either Au or porous Ni electrodes. Slopes of semi-log straight lines fit through the data indicate a thermal activation energy of ~0.3 eV.

The thermal activation energy of ~0.3 eV for the ~100-700°C temperature range suggests electron tunneling through a Schottky-type barrier at the semi-conductor SiC-metal electrode interface [2].

REFERENCES

[1] G. E. Youngblood, E. C. Thomsen and R. J. Shinavski, *Fus. Sci. and Tech.* **60** (2011) 364.
[2] J. Crofton, L. M. Porter and J. R. Williams, *Phys. Stat. Sol.* **(b) 202** (1997) 581.

3.3 Contact Resistance at a CVD-SiC/Ni Interface — G. E. Youngblood and E. Thomsen (Pacific Northwest National Laboratory)

OBJECTIVE

The primary objectives of this task are: (1) to assess the properties and behavior of SiC_f/SiC composites made from SiC fibers (with various SiC-type matrices, fiber coatings and architectures) before and after irradiation, and (2) to develop analytic models that describe these properties as a function of temperature and dose as well as composite architecture. In support of the U.S. dual-coolant lead-lithium (DCLL) fusion reactor blanket concept, recent efforts have focused on examining the electrical conductivity properties of SiC_f/SiC composites considered for application in FCI-structures.

SUMMARY

In a previous report, a fairly substantial correction due to contact resistance at a silicon carbide composite-metal (either gold or porous nickel) electrode interface was required to arrive at reliable transverse electrical conductivity values for the composite. A semi-logarithmic plot of the inverse specific contact resistance vs. 1000/K was nearly linear over a temperature range ~100-700°C, with an effective thermal activation energy of ~0.3 eV, which suggested that the contact resistance was due to electron tunneling through a Schottky-type barrier at the composite SiC seal coat/metallic interface. For the FCI-application, additional contact resistance at SiC composite wall/liquid Pb-Li interfaces could potentially and beneficially reduce the transverse electrical conductivity.

In this report, we further examine the behavior of the contact resistance; in particular, by examining contact resistance for a single pure, monolithic but polycrystalline CVD-SiC disc sample with nickel electrodes applied by physical vapor deposition (PVD). After making contact resistance measurements with the as-applied Ni electrodes, a heat treatment at 900°C was performed to lower the contact resistance, presumably by the formation of nickel silicide (NiSi) at the SiC-electrode interface. Using a 2/4-probe dc electric set up, we were able to simultaneously measure the total resistance across the sample disc with and without contact resistance from ambient up to 700ºC, with the difference representing the temperature dependent behavior of the contact resistance alone. Surprisingly, the specific contact resistance values for each electrode type at all temperatures were almost identical (~1000 Ω-cm^2 at RT decreasing continuously to <2 Ω-cm^2 at 700°C). The temperature dependence indicated a thermally activated interfacial conductance with effective activation energy of ~0.24 eV, a value slightly greater than that for ultra high-purity CVD-SiC (0.21eV). Apparently, the electrical conductance of the CVD-SiC/metal (Ni or NiSi) interface depends mostly on the near surface SiC electrical conductivity properties rather than the type of metallic conductor.

PROGRESS AND STATUS

Introduction

In the U.S. dual-coolant fusion reactor blanket (DCLL) concept, flow channel inserts (FCIs) made with silicon carbide (SiC) materials to thermally and electrically decouple flowing Pb-Li coolant from a steel first wall are being examined [1-4]. In an FCI made with fiber reinforced SiC/SiC composite (or SiC$_f$/SiC), the molten Pb-Li metal would interface directly to dense, pure SiC applied by chemical vapor deposition (CVD) as a seal coat to composite wall surfaces. A contact-type electrical resistance in series with the resistance of the insert wall itself may develop at the liquid metal/CVD-SiC interfaces. Such additional resistance would be beneficial, as it would reduce any transverse electrical current induced by the MHD-effect in the DCLL flow channels. Therefore, it is important to examine the properties of this expected contact resistance as it might relate to the design and operation of an FCI.

Morley et al. first examined this possibility by measuring the contact resistance (R_c) across a CVD-SiC/Pb-17%Li (molten eutectic composition) interface from 300-550°C, somewhat simulating the materials interaction conditions expected in an operating FCI [5]. Initially on heat up, they found that R_c-values were significant, decreased continuously with increasing temperature, but were rather irreproducible during the cooling leg or for different trials with nominally the same materials. In general, after heat up over a period of a few hours, R_c changed with additional exposure time, which indicated that chemical reactions were taking place in their experimental set up. Indeed, visual inspection of the interface after daylong exposures revealed a scale formation had formed on their SiC disc sample. Likely, chemical reactions at the CVD-SiC/Pb-Li interfaces were responsible for the somewhat erratic R_c-behavior that they observed. However, such chemical reactions were not expected based on observations by Pint, et al., who reported little dissolution of similar CVD-SiC samples immersed in static Pb-Li capsule tests for 2000-hr. exposures at 800°C in vacuum [6]. If SiC actually is chemically stable in liquid Pb-Li for T<800°C, then R_c for a SiC/Pb-Li interface should be reproducible with temperature cycling; and it must have a physical, not chemical explanation. With this apparent contradiction, we decided to examine the behavior of a SiC/metal interface further.

At this point, it is noted that the electronics industry has expended great effort over the last two decades to reduce contact resistance for metal electrodes attached to single-crystal SiC, a wide band-gap semiconductor (~2.3 eV for beta-SiC) of current interest for high power and high temperature electronic device applications [7]. In particular, nickel or nickel-chrome electrodes on semiconductor SiC appear to be preferred for these applications as they form a stable "ohmic" contact with very low resistance under suitable conditions [8]. One of the conditions needed to attain low R_c-values is a highly doped (~10^{19}/cm^3) SiC surface layer, i.e., for example with nitrogen for n-doping [9]. Another condition, besides extremely careful SiC surface preparation, is to give nickel electrodes (applied by sputtering or e-beam methods) a high temperature anneal to induce nickel-silicide formation [10]. With proper processing, ohmic contacts with specific R_c-values as low as 10^{-2} to even 10^{-6} Ω-cm^2 have been achieved [8].

However, during our measurements of the electrical conductivity (EC) of SiC$_f$/SiC composite disc samples with polycrystalline CVD-SiC seal coats we found that R_c was rather large for sputtered gold electrodes, as well as for porous nickel electrodes [11-14]. Furthermore, we found that the R_c-values as a function of temperature were similar for monolithic CVD-SiC and seal coat CVD-SiC, both in contact with metal electrodes [15]. Moreover, these R_c-values

appeared to mimic somewhat the R_c-values reported by Morley for their CVD-SiC/metallic liquid lead-lithium interface [5, 14].   However, in our case R_c-values were not erratic, but were reproducible for three heating and cooling cycles up to 700°C.   They also seemed to be rather independent of the type of metal electrode.   This electrical behavior suggested to us that R_c at a polycrystalline CVD-SiC/metallic interface depends primarily on the near surface electrical properties of the SiC and not the type of solid metal interfaced to the SiC.   Perhaps this could be the case when polycrystalline SiC is interfaced with molten Pb-Li, as in the FCI-application.   It is the purpose of this work to examine this possibility further.

Experimental Procedure

The furnace and a progressive development of our EC measurement system as well as previous experimental results for 2D-SiC/CVI-SiC composite and for dense, monolithic CVD-SiC materials have been described in Fusion Material Semiannual Progress Reports [4, 11-14].   We found that two-probe (2-pt.) resistance measurements across SiC or SiC$_f$/SiC composite disc samples contained a significant contribution from R_c at the SiC/metallic electrode interface and must be corrected to obtain reliable EC-values [12].   However, four-probe (4-pt.) measurements eliminated R_c contributions during standard potentiometric measurements on polycrystalline CVD-SiC disc samples [13].   Thus, comparison of 2/4-probe potentiometric resistance measurements yield values of R_c itself, i.e., $R_c = R(2-pt.) – R(4-pt.)$ [14].   Initially, we switched from 2-pt. to 4-pt. measurements by manually reconnecting external leads [13].   Therefore, we replaced this cumbersome measurement method by adding an electromechanical relay (National Instruments™ NI USB-9481) to our system that automatically makes almost simultaneous 2/4-pt. resistance measurements possible [16].

A 5-mm thick plate of high-purity, monolithic polycrystalline CVD-SiC, obtained from Rohm and Haas (Woburn, MA), was cut into a single sample disc (1-cm. dia. x 5-mm. thick).   Then two centrally located holes (1-mm. dia. x 1-mm. deep) were bored into opposite faces in which to seat potential probes for 4-pt. measurements.   The disc faces were diamond polished down to 0.5-µm grit, degreased, and carefully cleaned in a mild HF solution.   In previous work, we applied nickel electrodes by applying a NiO paste to the sample disc faces and reducing the NiO to porous Ni, a convenient first-try method.   In this new work, solid nickel film electrodes were applied to the disc faces by PVD at ~40°C.   The CVD-SiC disc was placed in a vacuum chamber ~5" directly above a 3.0" nickel target.   A small amount of argon was bled in and ionized by an applied voltage (~315V).   It required ~20 minutes to deposit a 0.25-µm thick nickel coating to each surface.   A removable wax plug prevented any nickel deposition in the central potential probe holes.   The disc sample was then mounted in an enclosed alumina tube in which a low-flow, reducing atmosphere (3% H_2 in argon) was maintained (Figure 1).
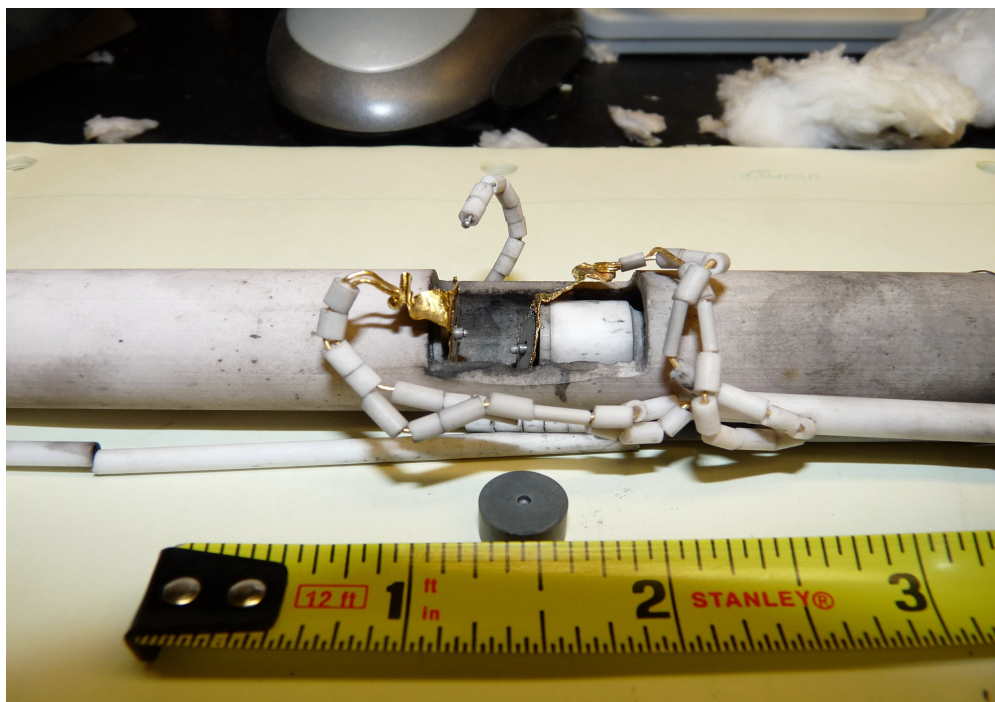
Figure 1. Alumina tube and sample mounting fixture with the CVD-SiC disc sample shown removed below.

For both 2/4-pt. measurements, gold current foils were pressed onto disc faces by external spring-loaded alumina pushrods that securely held the sample in place. An additional gold wire was soldered to the gold foil on each face to act as the 2-pt potential leads. For the 4-probe potential measurements, platinum wires with beaded ends were threaded inside alumina thermocouple tubes that were independently spring-loaded and pressed into the centrally located holes in the disc faces. With this setup, cyclic I-V voltammograms (DC current vs. applied voltage swept between ±0.1 volts) were performed at each temperature step. All resistance or EC determinations reported here and in [16] were made on the same CVD-SiC disc sample using our automated 2/4-probe system.

Electrical resistance values were calculated from the slopes of the cyclic voltammograms. EC-values were calculated from the appropriate sample geometry assuming linear current patterns. Over the tested ±0.1 voltage range and for all temperatures the I-V data were linear and passed through the origin, which indicates "Ohmic-type" conduction (see Figure 2).
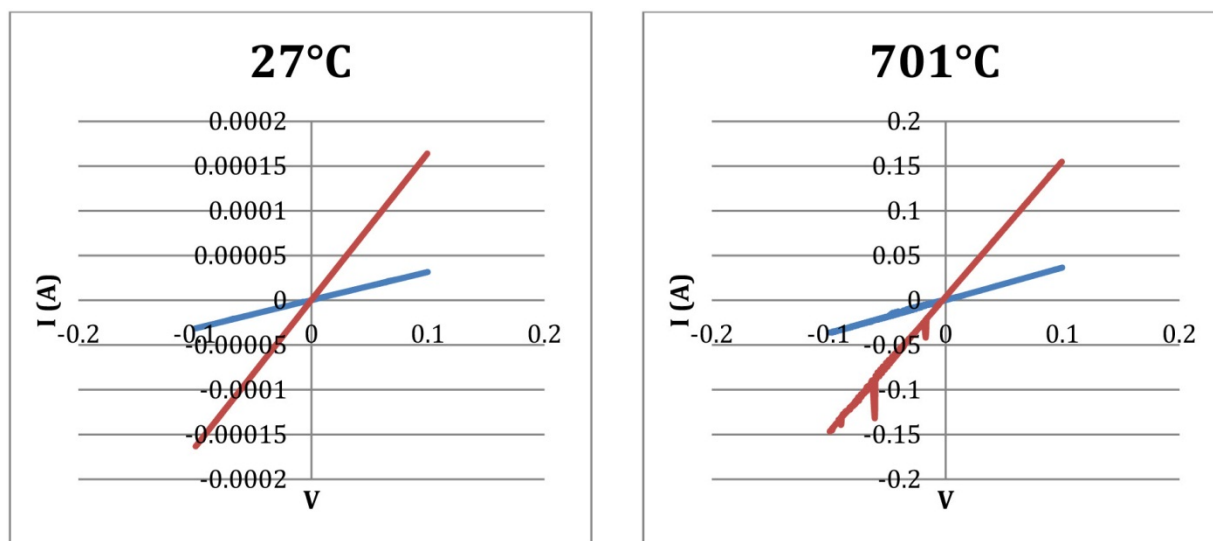
Figure 2. Typical examples showing linear behavior of I(V) potentiometric data for a low (27°C) and a high (701ºC) temperature. For each temperature, the applied voltage was swept in 0.001V steps through a range of ±0.1 volts. The slopes of the blue (red) lines represent the 2-pt. (4-pt.) resistance values at each temperature.

Resistance measurements were made in 40°C steps during three different temperature cycles, each cycle attaining a successively higher maximum temperature: RT to 400°C then back to RT, then RT to 550°C and back to RT, and finally RT to 700°C and back to RT. At each step the temperature was measured and measured again ten minutes later. If the two temperature measurements were within 2°C it was assumed that temperature equilibrium had been attained and I-V cycle proceeded. After completing the 2/4-pt. measurements at each temperature step, the temperature was changed to the next step at a rate of ~5°C per minute. Each temperature cycle required 20±5 hours.

For this same CVD-SiC sample, 2/4-pt. measurements were made for four different metallic electrodes: in order, evaporated Au, porous Ni, PVD-Ni, and heat-treated PVD-Ni. The heat treatment was performed in situ on the sample with the PVD-Ni electrode after completion of the 700°C cycle run. We heated and cooled the sample to 900°C (hold time 20 min.) in the reducing argon-3% hydrogen gas environment. This treatment should have been sufficient to completely convert the PVD-Ni to NiSi. In this reaction, Ni diffuses into and reacts with the SiC to give NiSi (or Ni_2Si), and leaves some small deposits of carbon at an interfacial region that no longer is abrupt [10].

Results for the first two types of electrodes were presented at ICFRM15 and will be published in JNM [16]. The results for the latter two types of electrodes are presented here.

Results

In Figure 3, the almost simultaneously measured 2/4-probe transverse resistance values (upper and lower curves, respectively) as a function of temperature for the polycrystalline CVD-SiC disc sample with the as-applied PVD-nickel electrodes are presented. For clarity, only the data for Run 3, the RT to 700°C cycle, is given. The data-curves for the just previously measured 400ºC

and 550°C cycles were exactly coincident with the 700°C cycle over their comparable temperature ranges. These 2/4-pt. transverse resistance values decrease continuously from ~3000/700 ohms at RT to ~2/0.7 ohms at 700°C, respectively. The difference between the two curves represents the contact resistance for the SiC/PVD nickel interface as a function of temperature.
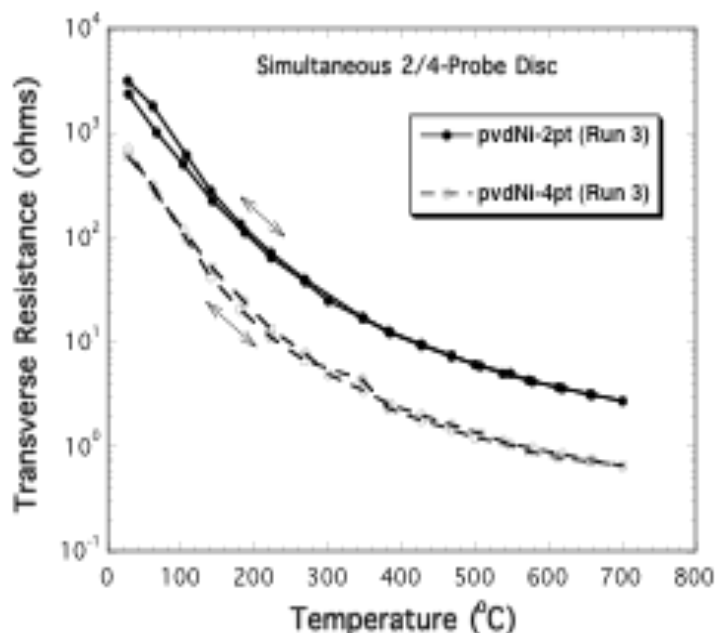
Figure 3. Transverse resistance measurements as a function of temperature for monolithic CVD-SiC disc sample with PVD-Nickel electrodes. The sample temperature was cycled in 40°C steps from RT -> 700°C -> RT. The upper (lower) curves indicate 2-pt. (4-pt.) probe data.

In Figure 4, the EC-values determined from the 4-pt. resistance measurements for our disc sample of CVD-SiC with the PVD-nickel electrodes (before and after the 900°C heat treatment) as a function of inverse temperature are presented. The curves are coincident, as expected for 4-pt. potentiometric measurements that are independent of contact resistance. The EC-values increase from ~0.05 S/m at RT up to ~50 S/m at 700°C, in line with values expected for ultra high-purity CVD-SiC [17]. In this semi-logarithmic plot, the EC-values decrease almost linearly with increasing inverse temperature. For the 300-700°C range, the apparent activation energy is ~0.21 eV, but is slightly larger for T<300°C.

Accurate 4-probe EC-values normally are obtained for bar samples where uniform one-dimensional current patterns are expected for homogenous materials. In our case, the two centrally placed holes in the disc faces for the potential probes, which are only ~2.6 mm. apart, certainly disrupt the assumption of uniform 1D-current distribution. Nevertheless, the reasonable agreement of the magnitudes and temperature dependence of our EC-values with reference values for CVD-SiC suggest consistency of our results.

In Figure 5, specific R_c-values as a function of temperature (the difference between the 2/4 pt. resistance values shown in Figure 3 after adjusting to specific values by multiplying R_c by the geometric disc face areas less the areas of the potential probe holes) for our CVD-SiC sample interfaced with either as-applied PVD-nickel or heat-treated PVD-nickel are given. The R_c-

values decreased continuously with increasing temperature from ~1000 Ω-cm^2 at RT down to <2 Ω-cm^2 at 700°C for each type of metallic interface.

In Figure 6, inverse specific R_c-values are shown plotted against reciprocal temperature in a semi-log form. The almost coincident data exhibit perfect linear dependence with an effective thermal activation energy of 0.24 eV over the ~200-700°C temperature range.
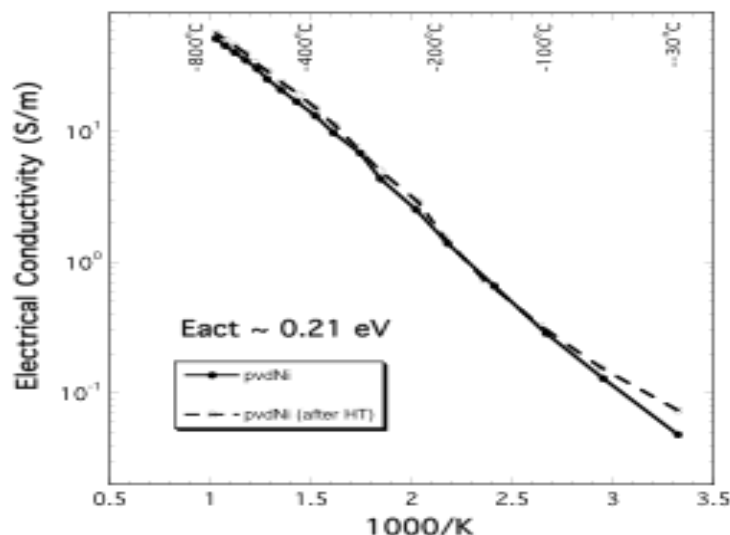
Figure 4. Electrical conductivity as a function of inverse temperature for a monolithic CVD-SiC disc sample with PVD-Nickel electrodes, as applied or heat-treated when using 4-probe measurements. The apparent activation energy determined from the best-fit straight line through the 300-700°C data is ~0.21 eV.
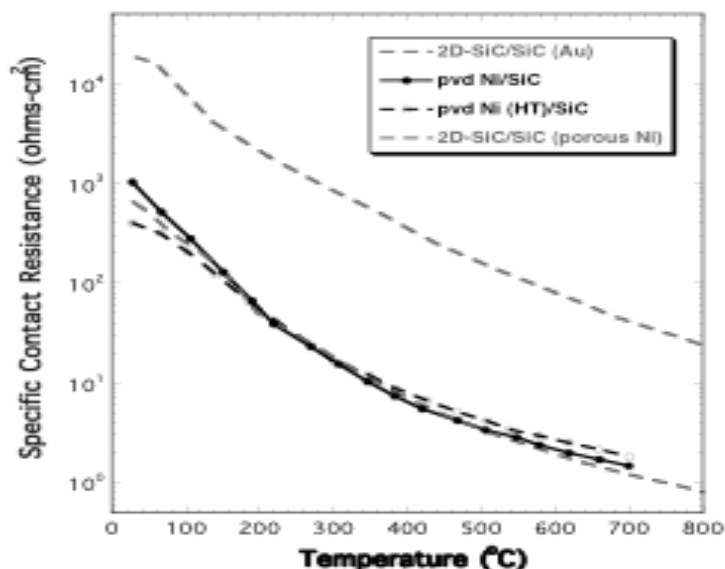
Figure 5. Specific contact resistance as a function of temperature for a monolithic CVD-SiC disc sample with as-applied or heat-treated PVD-Nickel electrodes. The grey dashed lines mark the range of R_c-values determined for various different SiC/SiC composites, but all with thin CVD-SiC seal coats upon which similar metallic electrodes were applied [15].
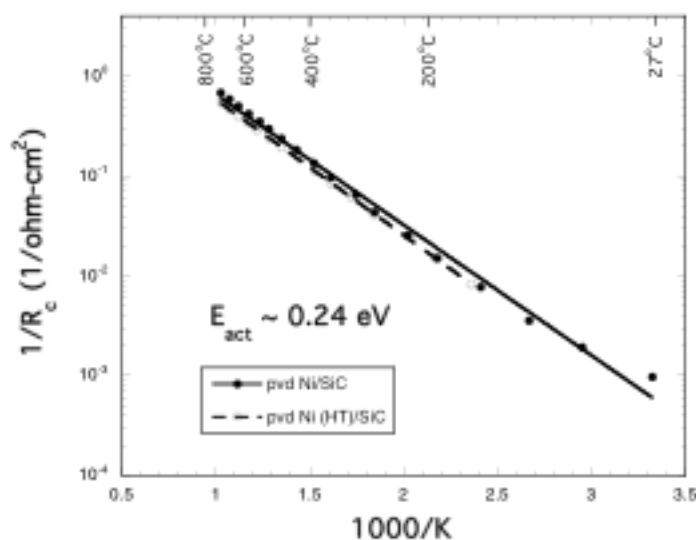
Figure 6. Inverse specific contact resistance of a CVD-SiC/Ni interface as a function of inverse temperature. The nickel electrodes were applied by PVD and also were heat-treated. The effective activation energy for both cases is 0.24 eV.

ANALYSIS AND DISCUSSION

As noted, relatively flaw free single crystal SiC is a useful high temperature, wide band-gap semiconductor. As such, its electrical conductivity is sensitively controlled by impurity doping; for example, nitrogen for n-type, boron or aluminum for p-type. Polycrystalline CVD-SiC generally is high-purity (Rohm and Haas quoted <5 ppm impurity content for our material). The CVD-SiC seal coats on SiC_f/SiC composite also should be high-purity. However, the grain-boundaries and stacking faults in polycrystalline CVD-SiC provide numerous surface energy states that prevent its use in semiconductor devices. Nevertheless, high-purity CVD-SiC exhibits some attributes of single crystal SiC semiconductor material; namely, the EC is thermally activated and it exhibits extrinsic-type conduction over a wide temperature range. For nominally high-purity CVD-SiC materials from various sources, we have measured EC-activation energies from 0.11 up to 0.25 eV in the temperature range 300-800°C [11]. For these various CVD-SiC materials, EC-values ranged from ~0.1 to 20 S/m at RT up to a range of 40 to 200 S/m at 800°C. Curves for samples with higher (lower) EC-values as a function of temperature always had lower (higher) activation energies and lower (higher) purity content, respectively. The point is, it is very difficult to get reproducible EC-values for CVD-SiC even when using 4-probe measurements on bars because the values depend so sensitively on even minor differences in impurity content and type. Getting reproducible EC-values for disc samples is even more difficult because of their unfavorable geometry factor. For this reason, in this work we chose to use only a single disc sample throughout; repolishing and reapplying different electrode types to the same CVD-SiC sample to at least have the same bulk EC and same geometry factor. As expected, we were successful in getting reproducible 4-pt. EC-values for three types of metallic electrodes: porous Ni [16], PVD-Ni, and heat-treated PVD-Ni (Figure 4). However, we had to give up microstructural examinations of any particular metal interface to preserve the disc sample.

In Figure 5, the calculated specific R_c-values for the CVD-SiC interfaced with PVD-Ni or heat-treated PVD-Ni were large, and they were almost coincident. The coincidence was a surprise. We assumed that a Schottky-type barrier (normally formed at a semiconductor/metal interface) was responsible for the relatively large values of specific R_c (~2 Ω-cm^2 at 700°C, for instance) that we have routinely observed. In fact, over the ~RT to 700ºC temperature range R_c was responsible for ~75% of the total resistance across our CVD-SiC/PVD-Ni disc sample (see Figure 3). Our intention was to reduce R_c by converting the pure PVD-Ni to NiSi with the 900ºC heat treatment and achieve an "ohmic" interface with specific R_c-values of <0.01 Ω-cm^2, as accomplished in the electronics industry. It just didn't work out that way!

At least, the specific R_c-values were reproducible over the three successive temperature cycles to 400, 550 and 700°C. This observation indicated that no chemical interactions occurred at the interface during the measurements. Even the chemical reaction converting PVD-Ni to NiSi during the heat-treatment didn't change R_c.

Our specific R_c-values matched previously obtained values for porous Ni electrodes on SiC$_f$/SiC composite with CVD-SiC seal coat (lower grey dashed line in Figure 5). Also, these new R_c-values are only slightly less than the R_c-values we reported for CVD-SiC interfaced with either porous nickel or sputtered gold electrodes (see Figure 1 in [16]). These relatively large values of R_c stayed the same and were stable, regardless of the type metal electrode or application method used. Apparently, our method of preparing the polycrystalline CVD-SiC surface, or the conductive properties of the CVD-SiC surface itself, was mostly responsible for the large values of R_c encountered.

It should be mentioned that we have made low R_c-interfaces with SiC$_f$/SiC composite by grinding off the surface layer of CVD-SiC seal coat down into the carbon-coated fiber layers [18]. In this case, the numerous direct contacts of the highly conductive carbon network to the metal electrode provided very low R_c. Similarly, Katoh et al. have quoted specific R_c-values <0.01 Ω-cm^2 for Ni electrodes applied to SiC$_f$/SiC (with seal coat removed) after heat treatment at >550°C [17]. Thus, 2-pt. resistance measurements are entirely appropriate for determining the transverse EC of SiC$_f$/SiC with carbon coated SiC fabric layers once the seal coat is removed. Minor corrections for the resistive contribution of the thin CVD-SiC seal coat are easily made [13].

In Figure 6, we examine the conductive property of the CVD-SiC/PVD-Ni interface (as applied or heat-treated) by plotting the inverse specific R_c vs. 1000/K. We assume that this inverse value is proportional to an interfacial conductance. Interestingly, the data lie on a nearly straight line from 200-700°C. For both metallic interfaces, the line slopes yield an effective activation energy of 0.24 eV, a value very close to the EC activation energy (0.21 eV) determined for our CVD-SiC sample (Figure 4). The closeness of these two conduction activation energy values suggests that the interfacial conductance truly is controlled by conduction in the near surface CVD-SiC, and not in the metallic electrode or at a Schottky-type semiconductor/metal barrier as we propose in reference [16]. This observation may be very important for the operation of an FCI made with SiC$_f$/SiC composite and containing the metallic liquid Pb-17Li alloy if the fairly large R_c-contribution is stable over long exposures.

A future test will examine this last point further. A new CVD-SiC/PVD-Ni disc sample will be held at first 550°C, then 700°C for a number of days to test the chemical stability of the interface using our 2/4-probe method. If that checks out, the sample will be removed from the sample

holder and resurfaced. Then a SiO_2 layer will be applied by a brief oxidation treatment of the sample in air prior to reapplying PVD-Ni electrodes and performing R_c measurements again.

CONCLUSIONS

(1) PVD-Ni metallic electrodes form an "ohmic" type interface with polycrystalline CVD-SiC with fairly high specific R_c-values. The R_c-values appear to be reproducible up to 700°C.
(2) The R_c-values do not appear to be due to a Schottky-type semiconductor/metal interfacial barrier, but do appear to be directly dependent on the near surface EC-properties of the SiC, and independent of the type of metallic nickel.

REFERENCES

[1]   N. B. Morley, Y. Katoh, S. Malang, B. A. Pint, A. R. Raffray, S. Sharafat, S. Smolentsev, and G. E. Youngblood, *Fusion Eng. Des.* **83** (2008) 920.
[2]   S. Smolentsev and S. Malang, *Fusion Sci. Tech.* **56** (2009) 201.
[3]   S. Malang, M. Tillack, C. P. C. Wong, N. Morley, and S. Smolentsev, *Fusion Sci. Tech.* **60** (2011) 249.
[4]   G. E. Youngblood, R. J. Kurtz, and R. H. Jones, Fusion Materials Semiannual Progress Report for Period Ending December 31, 2004, DOE/ER-0313/37, U.S. Department of Energy, 3.
[5]   N. B. Morley, A. Medina, and M. A. Abdou, *Fusion Sci. Tech.* **56** (2009) 195.
[6]   B. A. Pint, J. L. Moser, and P. F. Tortorelli, *J. Nucl. Mater.* **367-370** (2007) 1150.
[7]   P. G. Neudeck, in *Encyclopedia of Materials: Science and Technology*, Eds., K.H.J. Bushchow, et al. (Elsevier Science, Oxford, 2001) 8508-8519.
[8]   J. Crofton, L. M. Porter, and J. R. Williams, *Phys. Status Solidi* **(b) 202** (1997) 581.
[9]   C. Rado, S. Kalogeropoulou, and N. Eustathopoulos, *Mater. Sci. Forum* **207-209** (1996) 425.
[10] O. V. Aleksandrov and V. V. Kozlovski, *Semiconductors* **43** (2009) 885.
[11] G. E. Youngblood, E. Thomsen, and G. Coffey, Fusion Materials Semiannual Progress Report for Period Ending December 31, 2005, DOE/ER-0313/39, U.S. Department of Energy, 46.
[12] G. E. Youngblood, E. Thomsen, and G. Coffey, Fusion Materials Semiannual Progress Report for Period Ending December 31, 2006, DOE/ER-0313/41, U.S. Department of Energy, 17.
[13] G. E. Youngblood and E. Thomsen, Fusion Materials Semiannual Progress Report for Period Ending December 31, 2008, DOE/ER-0313/45, U.S. Department of Energy, 35.
[14] G. E. Youngblood, E. Thomsen, and R. J. Shinavski, Fusion Materials Semiannual Progress Report for Period Ending December 31, 2009, DOE/ER-0313/47, U.S. Department of Energy, 34.
[15] G. E. Youngblood, E. C. Thomsen, and R. J. Shinavski, Fusion Sci. Tech. 60 (2011) 364.
[16] G. E. Youngblood, E. C. Thomsen, and J. Henager C.H, Effects of Contact Resistance on Electrical Conductivity Measurements of SiC-Based Materials. 2012. ICFRM15 Poster and extended abstract this volume.
[17] Y. Katoh, S. Kondo, and L. L. Snead, *J. Nucl. Mater.* **386-388** (2009) 639.
[18] G. E. Youngblood, E. Thomsen, and R. J. Shinavski, Fusion Materials Semiannual Progress Report for Period Ending June 30, 2010, DOE/ER-0313/48, U.S. Department of Energy, 12.

3.4 Low Activation Joining of SiC/SiC Composites for Fusion Applications: Miniature Torsion Specimen Shear Testing — C. H. Henager, Jr. and R. J. Kurtz (Pacific Northwest National Laboratory), A. Ventrella and M. Ferraris (Politecnico di Torino)

OBJECTIVE

This work discusses the latest developments in TiC + Si displacement reaction joining at PNNL based on mechanical property test results from miniature torsion joints tested at Politecnico di Torino.

SUMMARY

The use of SiC composites in fusion environments likely requires joining of plates using reactive joining or brazing. One promising reactive joining method uses solid-state displacement reactions between Si and TiC to produce Ti_3SiC_2 + SiC. We continue to explore the processing envelope for this joint for the TITAN collaboration in order to produce optimal joints to undergo irradiation studies in HFIR. The TITAN collaboration has designed miniature torsion joints for preparation, testing, and irradiation in HFIR. PNNL synthesized 40 miniature torsion joints and several were tested for shear strength prior to irradiation testing in HFIR. The resulting tests indicated that 1) joint fixture alignment problems cause joint strengths to be lower than optimal, 2) that non-planar torsion test failures limit the effectiveness of the miniature specimen design, and 3) that several joints that were well aligned had high shear strengths and promising mechanical properties. In summary, we now show conclusively that high joint strengths cause non-planar shear fracture and complicate strength analysis for miniature torsion specimens.

PROGRESS AND STATUS

Introduction

SiC is an excellent material for fusion reactor environments, including first wall plasma facing materials and breeder materials. SiC is low-activation, temperature-resistant, and radiation damage tolerant compared to most materials. In the form of woven or braided composites with high-strength SiC fibers it has the requisite mechanical, thermal, and electrical properties to be a useful and versatile material system for fusion applications, especially since microstructural tailoring during processing allows control over the physical properties of interest [1-6]. However, it is difficult to mechanically join large sections of such materials using conventional fasteners so the analog of welding is being pursued for these ceramic materials [2, 4-15]. Such methods include metallic brazes [8, 16], glass ceramics [7, 17], preceramic polymers [15], and displacement reactions [2, 6]. This paper reports on the current status of SiC and SiC-composite joining for fusion applications based on displacement reactions between Si and TiC. Recent results from Torino have indicated that the miniature torsion specimens fail out-of-plane for strong enough joints [18] and fail to provide the necessary unirradiated joint strengths required for in-reactor testing purposes. The purpose of this recent joining study is to help understand the effects of joint strength on torsion test results.

Experimental Procedure

Joints are made using a tape calendaring process using organic binders and plasticizers together with a mixture of TiC and Si powders, with 99.99% purity, average diameters less than

45 µm, and a TiC:Si ratio of 3:2. The flexible tapes were 200 µm thick and were cut to a disk shape and applied between two CVD SiC miniature torsion specimens as shown in Figure 1. The green joints are placed within a graphite fixture shown in Figure 2 that allows for alignment of the torsion joints and for applied compressive force during heating in an inert gas furnace enclosure. Joints were formed by heating the torsion coupons in argon to 1698K at 10K/min and holding for 2 hours at varied amounts of applied pressure. A series of joints were produced using 40 MPa, 30 MPa, 20 MPa, 10 MPa, and 5 MPa pressures under identical heating and other processing parameters. The resulting joints were dense and approximately 15 µm thick. They were prepared for optical and scanning electron microscopy using standard ceramographic cutting, grinding, and polishing methods.

(a)   (b)
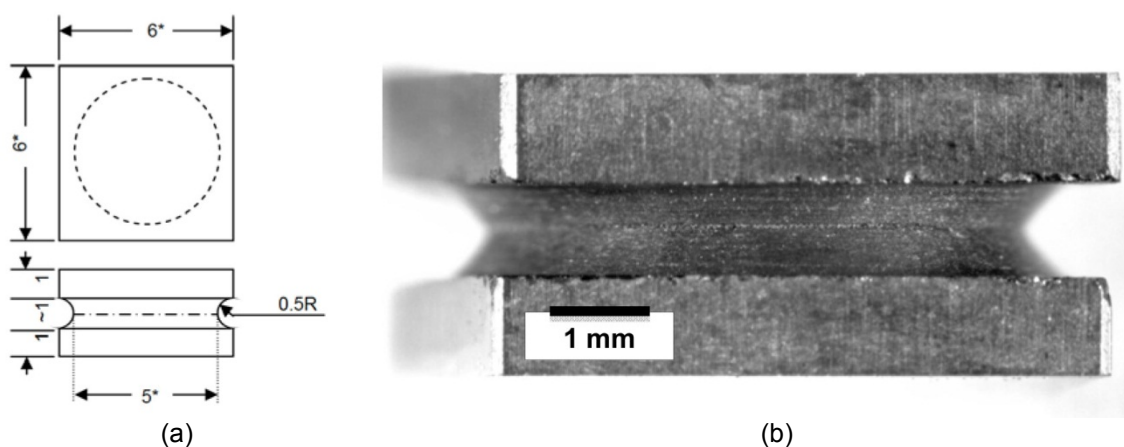
Figure 1. (a) Drawing of miniature torsion joining specimen for HFIR irradiation. Dimensions are shown in mm in (a). Shown in (b) is a photomicrograph of a PNNL fabricated torsion specimen. The joint line is visible along the specimen horizontal centerline.

(a)   (b)
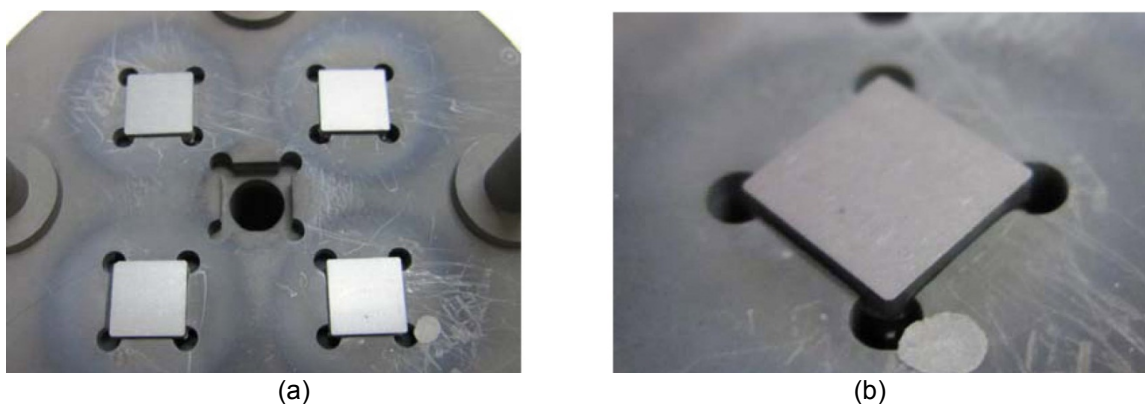
Figure 2. (a) Photomicrograph of graphite joining fixtures with 4 torsion joints ready for processing. The central hole in this photo allows an alumina-sheathed thermocouple to be placed close to the joints during processing. Shown in (b) is a close-up photomicrograph of a single joint held in place prior to processing. The torsion joints are 6-mm square and slightly less than 3-mm in height.

The joints were sent to Prof. M. Ferraris of Politecnico di Torino, Torino, Italy for testing as part of the TITAN collaboration. The joints are tested in torsion by Dr. Ventrella using a test fixture as shown in Figure 3. The hourglass specimens are held in place using the square top and bottom specimen shapes with the joint joining the two half specimens as shown in Figure 1 along the circular center region. The test places the joint in pure shear and presumably tests the shear strength more accurately than other tests, such as notched shear tests with problematic bending moments and stress concentrations.

RESULTS

Figure 1 shows the torsion specimen drawing and a fabricated joint at PNNL prior to any testing. Figure 2 shows the joints placed into the graphite alignment fixture prior to processing in argon at 1698K for 2 hours.
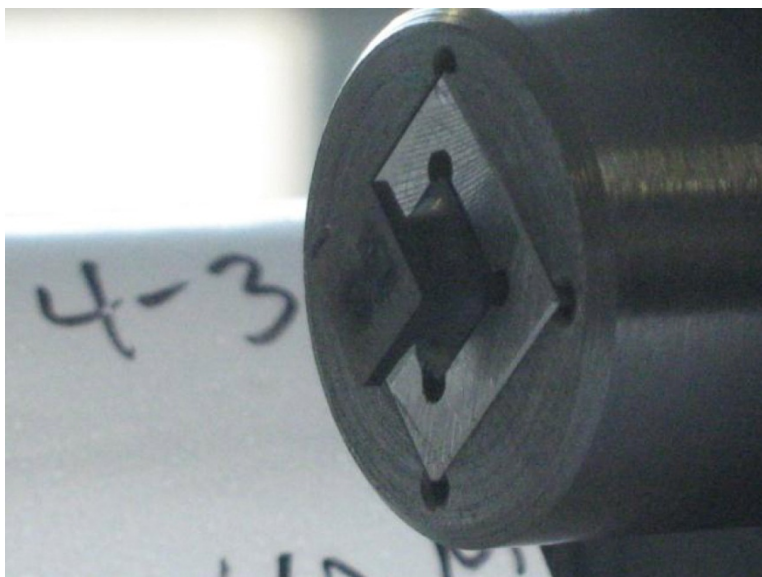
Figure 3.   PNNL joint specimen 4-3 in the torsion test holder at Politecnico di Torino prior to testing. This particular specimen was one of the first batch that was taller, thus, it was almost 4-mm in height compared to 3-mm height shown in Figure 1. The test methods were the same, however.

Figure 4 shows the test results for the joint pressure study for the 30 MPa and smaller joining stresses. All of the 40 MPa joints tested earlier had failed out-of-plane, as did the 30 and 20 MPa joints. The shear strengths reported here are based on the force required to fail the torsion sample but these calculations are not really valid since the failure occurred out-of-plane. However, joints made weak enough be reducing the joining stresses to 10 or 5 MPa could be made to fail in the plane of the test joint. These data show conclusively that the miniature torsion shear test cannot be used as designed for these high-strength joints.

The previous data from Torino showing good results for epoxy joints only reinforces this conclusion.   Joints stronger than about 70 or 80 MPa cannot be reliably tested with this

specimen design. Figure 5 shows that epoxy-joined SiC fails repeatedly and accurately at about 67 ± 16.6 MPa as determined by this test technique.

Figure 6 illustrates the appearance of an out-of-plane shear test for one of the PNNL joining specimens. It should be readily apparent that the specimen fracture involves more of the SiC torsion specimen than of the Ti_3SiC_2/SiC composite joint. This strength data, therefore, is not representative of the strength of the joint. Without a proper baseline joint strength then in-reactor test results will be less meaningful since it will then be difficult to sort out radiation damage to the joints.
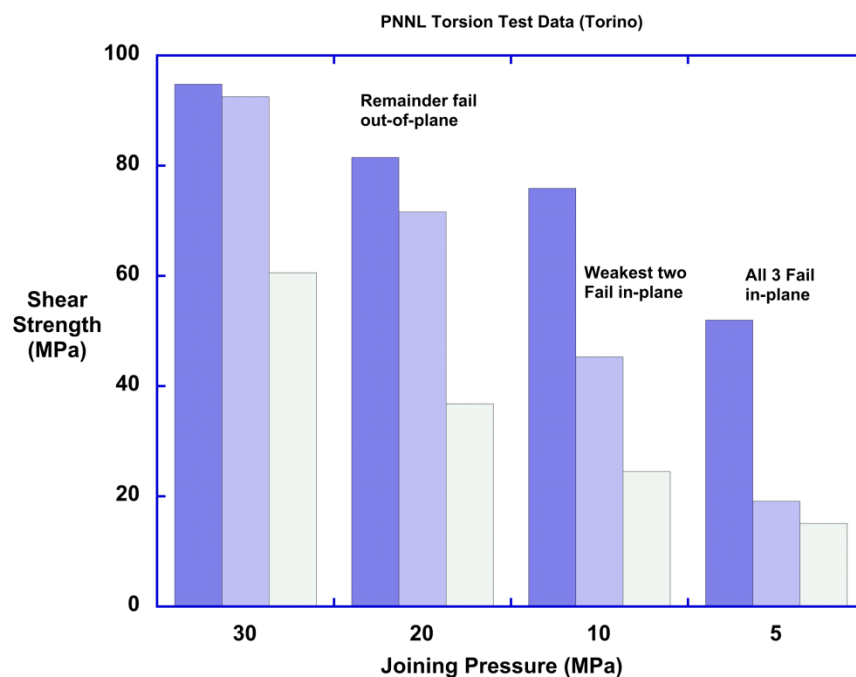
Figure 4. Bar graph of individual joint shear strengths measured in torsion for PNNL SiC specimens joined using TiC+Si displacement reaction joints at the indicated joining pressure. Joints purposefully made weak by bonding at 10 MPa and 5 MPa routinely failed in-plane and gave representative strengths. Joints made stronger by joining at 20 MPa greater joining pressures all failed out-of-plane and gave erroneous shear strengths.   The various shaded bars indicate individual tests at each condition.
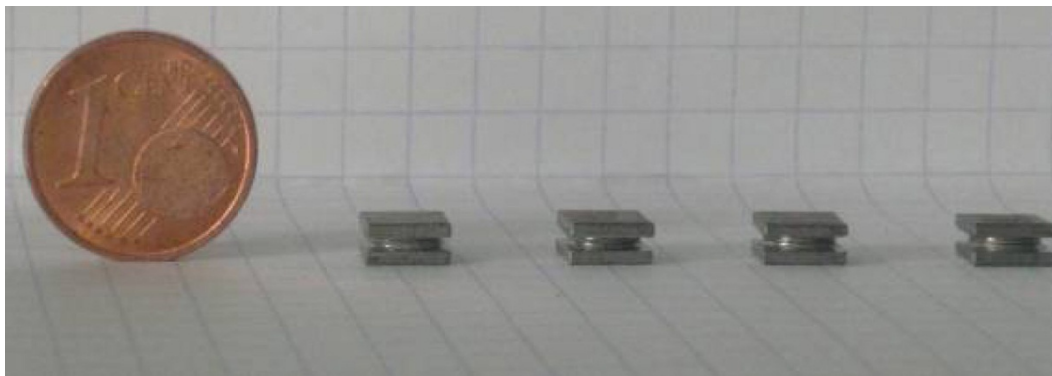
(a)
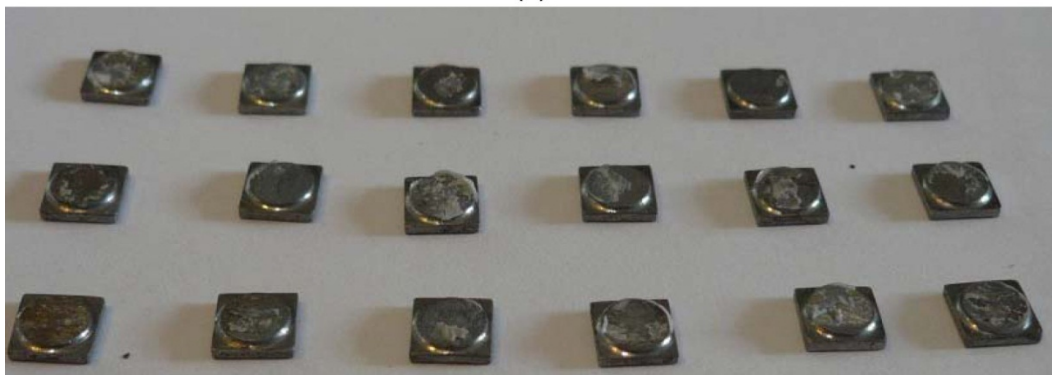
(b)

Figure 5. Data from Torino with epoxy-joined SiC specimens showing in-plane fractures for all tested samples. The average shear strength of these joints was 67 ± 16.6 MPa.
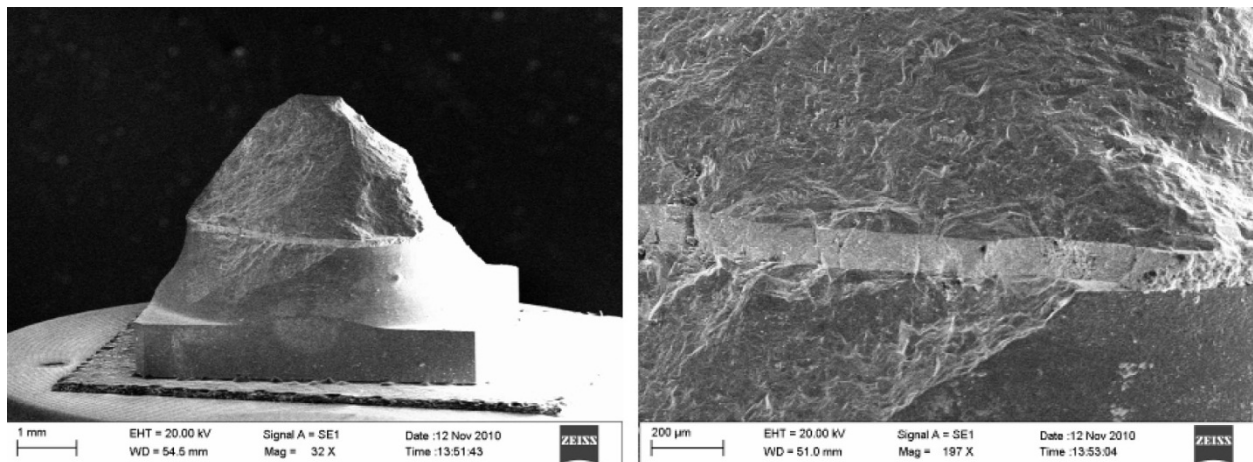
Figure 6. Photomicrograph of failed joint showing out-of-plane fracture typical of the high-strength joint failures that populate Figure 4 data.

REFERENCES

[1]   Y. Katoh, L. L. Snead, C. H. Henager Jr, A. Hasegawa, A. Kohyama, B. Riccardi, and H. Hegeman, *J. Nucl. Mater.* **367-370 A** (2007) 659.

[2]   C. H. J. Henager, Y. Shin, Y. Blum, L. A. Giannuzzi, B. W. Kempshall, and S. M. Schwarz, *J. Nucl. Mater.* **367-370** (2007) 1139.

[3]   P. Yvon and F. Carre, *J. Nucl. Mater.* **385** (2009) 217.

[4]   T. Nozawa, T. Hinoki, A. Hasegawa, A. Kohyama, Y. Katoh, L. L. Snead, C. H. Henager Jr, and J. B. J. Hegeman, *J. Nucl. Mater.* **386-388** (2009).

[5]   H.-C. Jung, Y.-H. Park, J.-S. Park, T. Hinoki, and A. Kohyama, *J. Nucl. Mater.* **386-388** (2009) 847.

[6]   C. H. Henager, Jr. and R. J. Kurtz, *J. Nucl. Mater.* in press (2011).

[7]   M. Ferraris, P. Appendino, V. Casalegno, F. Smeacetto, and M. Salvo, *Adv. Sci. Tech.* **33** (2003) 141.

[8]   B. Riccardi, C. A. Nannetti, T. Petrisor, and M. Sacchetti, *J. Nucl. Mater.* **307-311** (2002) 1237.

[9]   R. H. Jones, L. Giancarli, A. Hasegawa, Y. Katoh, A. Kohyama, B. Riccardi, L. L. Snead, and W. J. Weber, *J. Nucl. Mater.* **307-311** (2002) 1057.

[10] R. L. Bruce, S. K. Guharay, F. Mako, W. Sherwood, and E. Lara-Curzio, IEEE/NPSS Symposium on Fusion Engineering (2002) 1078.

[11] M. Zucchetti, M. Ferraris, and M. Salvo, *Fusion Eng. Des.* **58-59** (2001) 939.

[12] A. R. Raffray, R. Jones, G. Aiello, M. Billone, L. Giancarli, H. Golfier, A. Hasegawa, Y. Katoh, A. Kohyama, S. Nishio, B. Riccardi, and M. S. Tillack, *Fusion Eng. Des.* **55** (2001) 55.

[13] C. A. Lewinsohn, R. H. Jones, T. Nozawa, M. Kotani, Y. Katoh, A. Kohyama, and M. Singh, *Ceram. Eng. Sci. Proc.* **22** (2001) 621.

[14] C. A. Lewinsohn, M. Singh, T. Shibayama, T. Hinoki, M. Ando, Y. Katoh, and A. Kohyama, *J. Nucl. Mater.* **283-287** (2000) 1258.

[15] P. Colombo, B. Riccardi, A. Donato, and G. Scarinci, *J. Nucl. Mater.* **278** (2000) 127.

[16] B. Riccardi, C. A. Nannetti, T. Petrisor, J. Woltersdorf, E. Pippel, S. Libera, and L. Pilloni, *J. Nucl. Mater.* **329-333** (2004) 562.

[17] Y. Katoh, M. Kotani, A. Kohyama, M. Montorsi, M. Salvo, and M. Ferraris, *J. Nucl. Mater.* **283-287** (2000) 1262.

[18] C. Henager, Jr., R. Kurtz, and M. Ferraris, in *Fusion Reactor Materials Program Semiannual Progress Report for Period Ending December 31, 2010*, Eds., F. Wiffen, R. Godfrey, and B. Waddell (Oak Ridge National Laboratory, Oak Ridge, TN, 2011) 25-30.

4.1 Development of Micro-Engineered Textured Tungsten Coatings for High Heat Flux Applications — S. Sharafat[1], A. Aoyama[1], B. Williams[2], and N. Ghoniem[1], ([1]University of California, Los Angles, [2]Ultramet Inc.)

This is the Abstract for an ICFRM-15 paper submitted for publication in the Proceedings.

Thermo-mechanical performance of plasma facing components (PFCs) can be enhanced by micro-engineering the surface. For example, castellation of a surface can reduce thermal stress due to high heat loads and thus provide higher thermo-mechanical resilience.   Recently, fabrication of a variety of micro-sized refractory dendrites with reproducible geometric characteristics, such as density, height, and aspect ratio has been demonstrated. Compared to a flat surface exposed to high heat loads, the ability of dendrites to deform independently minimizes near-surface thermal stress, resulting in improved thermo-mechanical performance. Thus, the use of dendrites offers a unique micro-engineering approach to enhance the performance of PFC structures. A brief overview of W, Re, and Mo dendritic structures is given along with micrographs which show dendrite coated surfaces. The thermal responses of representative dendrite structures were analyzed as a function of aspect ratios and dendrite geometry. The heat management capability of needle-like dendrites exposed to a surface energy of up to 1 MJ/m2 was analyzed and compared to a flat surface. It is found that dendrite structures can significantly reduce thermal stress in the substrate when compared to flat surfaces. Implications of dendritic surface features on sputter erosion rates are also discussed briefly.

4.2 Multiphysics Model of Thermochemical and Helium-Induced Damage of Tungsten Under Plasma Heat Transients —Tamer Crosby (University of California, Los Angeles), Nasr M. Ghoniem (University of California, Los Angeles)

This is the Abstract for an ICFRM-15 paper submitted for publication in the Proceedings.

The combination of transient heating and bombardment by helium and hydrogen atoms has experimentally proved to lead to severe surface and sub-surface damage. Here we present a computational model to determine the relationship between the thermomechanical loading conditions and the onset of damage and failure of tungsten surfaces. The model is based on thermoelasticity fracture damage developed using the phase field method. The distribution of helium bubbles inside the grains and on grain boundaries is simulated with a space-dependent rate theory. The model is also coupled with a transient heat conduction analysis for temperature distributions inside the material. The results have shown the effects of helium bubbles on reducing tungsten surface energy. Further, a temperature gradient in the material that was equal to 10 K/μm, resulted in cracks propagating to deep distances from the tungsten surface.

4.3   Ab Initio Study of Grain Boundary Properties of Tungsten Alloys —
W. Setyawan and R. J. Kurtz (Pacific Northwest National Laboratory)

OBJECTIVE

The objective of this research is to support the search for tungsten alloys with increased grain boundary cohesion using ab initio methods.

SUMMARY

Density functional theory was employed to investigate the grain boundary (GB) property of W-TM alloys (TM: fifth and sixth row transition metals). GB strengthening was found for Hf, Ta, Nb, Ru, Re, Os and Ir for $\Sigma 27\{525\}$ and to a lesser degree for $\Sigma 11\{323\}$. Lower valence solutes strengthen the GB at certain substitutional sites, while higher valence elements enforce it at other positions. For $\Sigma 3\{112\}$, the alloys exhibit reduced cleavage energies. Hence, allowing with TMs increases the GB cohesion more effectively for large-angle GBs whose cleavage energy is, in general, inherently lower than the low-angle ones. Electron density analysis elucidates the mechanism of charge addition or depletion of the GB bonding region upon TM substitution at various positions leading to stronger or weaker intergranular cohesion, respectively.

PROGRESS AND STATUS

Introduction

The development of novel W-based materials that are suitable for future fusion reactors is likely to involve synergistic advancements in intrinsic W alloys [1, 2], grain boundary engineering [3, 4] and W-based composites [5, 6]. In all of these areas, understanding and controlling the characteristics of materials at intergrain regions are important. Alloying with Re has been shown to reduce the ductile-brittle transition temperature (DBTT) to 600°C and to increase the recrystallization temperature to 1400°C [1]. Recent ab initio study showed that Re significantly enhances the intergranular strength [7]. This study was intended to add to the body of knowledge of the effects of transition metals (TMs) on the grain boundary (GB) cohesion. We included three model structures namely $\Sigma 27<110>\{525\}$, $\Sigma 11<110>\{323\}$ and $\Sigma 3<110>\{112\}$ and investigated the transition metals from the fifth and sixth row of the periodic table.

Formalism

Starting from general-twin slab configurations, molecular dynamics (MD) simulations were performed to search for the ground state structure of the GBs. We used the interatomic potential developed by Ackland and Thetford [8]. Systematic interfacial shifts and atoms relaxations were done to achieve the most stable configurations. The structures obtained from the MD were further optimized via ab initio method. VASP software was used to perform the quantum mechanical calculations based on the density functional theory (DFT). Accurate projector-augmented-wave pseudopotentials with Perdew-Burke-Ernzerhof exchange-correlation functionals were employed [9–11]. Plane-wave energy cutoffs and k-point sampling of the Brillouin zone were carefully checked for convergence. Structures were fully relaxed with a tolerance of 1 meV. For non-slab configurations, a force tolerance of 10 meV/A was used. At the end of volume-nonconserving relaxations, an additional static calculation was performed to avoid numerical errors due to basis incompleteness.

The necessary slab thickness for the DFT calculations was determined from the convergence tests of the {525}, {323} and {112} surface energies. A total of 62, 38 and 23 layers which include one GB interface and two free surfaces were required for the $\Sigma27$, $\Sigma11$ and $\Sigma3$, respectively. Supercells containing 124 ($\Sigma27$), 76 ($\Sigma11$) and 138 ($\Sigma3$) atoms were used to obtain planar concentrations of 1.37, 2.15 and 1.37 solute/nm^2, respectively. Using the atomic volume of bcc (0.016 nm^3), these concentrations correspond to a three-dimensional value of 2.6, 5.0 and 2.6 at. %.

RESULTS

Figure 1 shows the structure of the GBs as viewed from the <110> direction. The structures consist of two alternating layers along this direction which are represented by different colors. To study the cohesion, cleavage energies were calculated from the GB energy and the energies of the cleavaged halves. The cleavage plane was taken at a position indicated by the dashed line in Figure 1. Several GB sites were investigated as the substitutional positions. Representative transition metals from the fifth and sixth rows of the periodic table were studied. The results are presented on the right panel of Figure 1 and arranged with an increasing atomic number.

The results for the $\Sigma27$ have been presented in Ref. [7]. Five GB sites were studied for this GB. Three sites with distinct properties are included in this report to allow comparison with other GBs. In general, for each substitutional site, the cleavage energy forms a smooth curve as a function of the solute. The maximum of each curve represents the best GB strengthener for the corresponding site. Interestingly, a similar set of curves was observed for the fifth- and sixth-row solutes. This indicates that the effect of the TMs on the GB cohesion is closely related to the electronic valence and how the occupancy of the d-orbitals varies across different atomic environments. For all the three GBs, the sixth-row TMs exhibit higher cleavage energies than the corresponding fifth-row elements.

For $\Sigma27$ and $\Sigma11$, Ru, Re, Os and Ir considerably increase the cleavage energy when they are at position A, while Hf and Ta do so at position D. Zr and Nb also show a strengthening property at site A for $\Sigma27$. As we go from $\Sigma27 \rightarrow \Sigma11 \rightarrow \Sigma3$, the alloys become less effective. In fact, the data on $\Sigma3$ shows that very limited increase of cohesion was obtained with Ru, Re and Os at position F. Comparison of GB energy among different substitutional sites revealed that the more stable the site, the higher the cleavage energy. Therefore, energetically, the strengthening property of a solute is preferred even though there are spurious sites. This relation holds true for each solute. For $\Sigma27$, we have calculated segregation energies defined as the GB energies minus the energies of the solute if it were in the grain's interior [7]. These energies represent the stability of the substitution with respect to a bulk position. In general, higher valence TMs show more tendency to be at the GB.

Comparison with different concentrations showed that, at low concentration regime, the strengthening property is proportional to the planar concentration of the solute. In this regime, we have investigated the property of ternary alloys by placing Re, Or, or Ru at site A and Hf, Ta, or Nb at site D of the $\Sigma27$. The results showed a strengthening property of roughly the sum of contributions from each solute. This suggests that by employing both lower valence and higher valence solute, further improvements could be achieved. A significant increase of cleavage energy is indicated in several TMs for the $\Sigma27$. Meanwhile, for $\Sigma3$, the data show that most likely TMs have adverse effects on the GB cohesion. However, the cleavage energy of pure $\Sigma3$

is significantly higher than that of $\Sigma27$. In fact, even the worse case of decohesion in $\Sigma3$ (Pd) still exhibits a higher cleavage energy than the best case of cohesion in $\Sigma27$ (Os not Hf since Hf solubility is less than the simulated concentration).

The strengthening property of TMs in this study can be understood from the electron distribution plot. Figure 2 shows examples of such plot for $\Sigma27$ with Os or Hf at position A (left panel) or D (right panel). The charge density of the pure material is depicted in the center panel. GB bonds are indicated with the arrows. For position A, substitution of W with a lower valence element such as Hf results in a weaker bond since there are fewer electrons available for bonding. On the other hand, higher valence solutes such as Re and Os will strengthen the GB bonds. However, this trend does not continue towards Pt since most of the d-electrons are already paired and unavailable for bonding. For site D, the situation is reversed. Atom at this site is not responsible for GB bonds as much as atom at position A. Introduction of Hf at position D increases the charge density of the GB bonds. This indicates that electrons are partially transferred from Hf at site D to atoms at site A resulting in stronger bonds. Meanwhile, Os at position D tends to deplete the electrons from the bonding site A, lowering the GB cohesion.
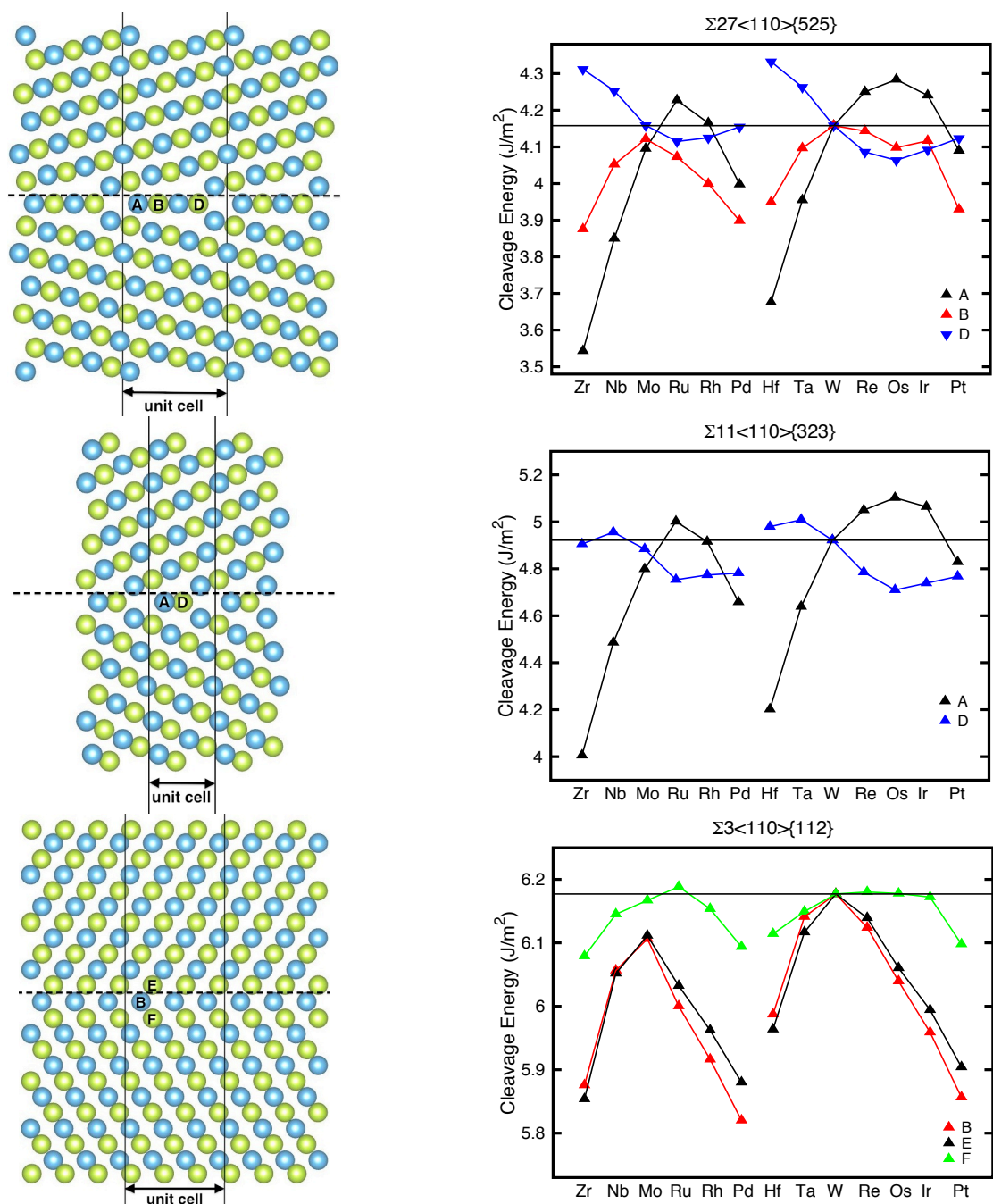
Figure 1. Grain boundary structures of W-TM alloys viewed from the <110> direction (left panel) and cleavage energies (right panel). The dashed line indicates the cleavage plane. The corresponding solute concentrations are 2.6 (Σ27), 5.0 (Σ11) and 2.6 (Σ3) at. %.
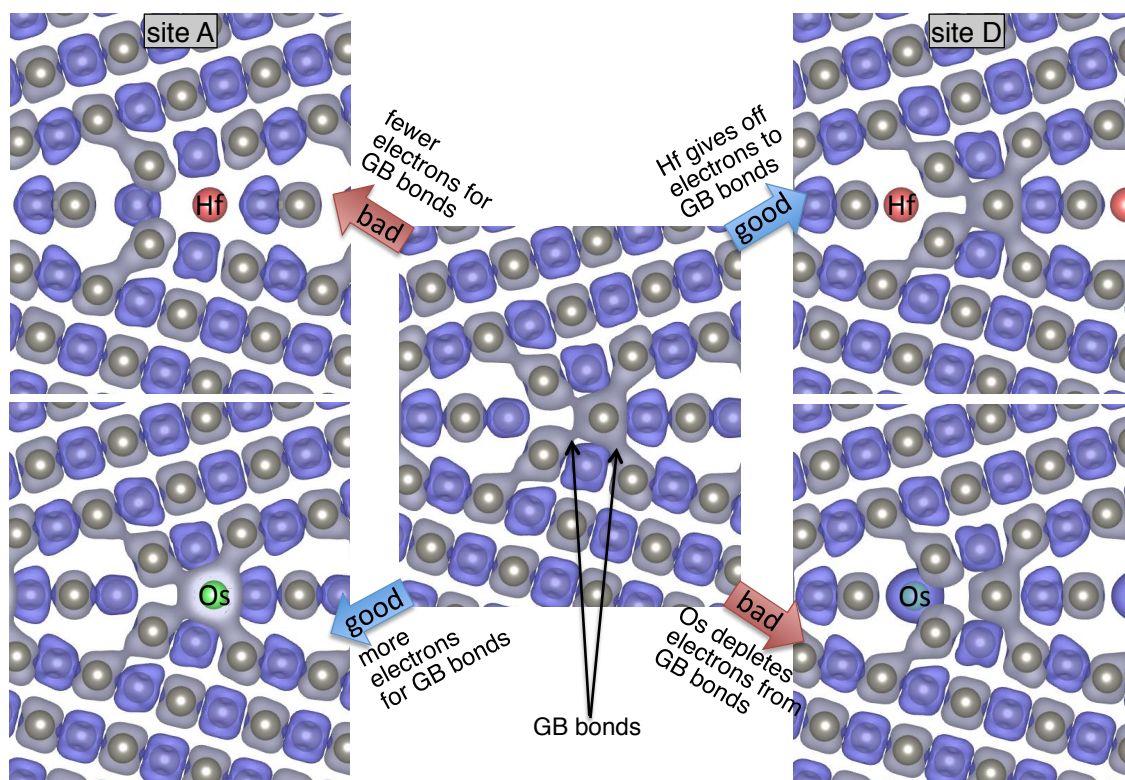
Figure 2. Electron density of the Σ27{525} grain boundary with Hf or Os at substitutional site A or D. GB strengthening is revealed by the charge increase in the GB bond regions.

REFERENCES

[1]   Y. Mutoh, et al., *J. Mat. Sci.* **30** (1995) 770.
[2]   S. Wurster, et al., *J. Nuc. Mat.* **413** (2011) 166.
[3]   L. J. Kecskes, et al., *Mat. Sci. Eng. A* **467** (2007) 33.
[4]   M. Faleschini, et al., *J. Nuc. Mat.* **367** (2007) 800.
[5]   E. Lassner and W. -D. Schubert, "Tungsten," Springer (1995).
[6]   Y. Ishiyama, et al., *Mat. Sci. Eng. A* **473** (2008) 7.
[7]   W. Setyawan and R. J. Kurtz, *Scrip. Mat.* (2012) doi: 10.1016/j.scriptamat.2012.01.002.
[8]   G. J. Ackland and R. Thetford, *Phil. Mag. A* **56** (1987) 15.
[9]   P. E. Blöchl, *Phys. Rev. B* **50** (1994) 17953.
[10] G. Kresse and D. Joubert, *Phys. Rev. B* **59** (1999) 1758.
[11] J. P. Perdew, K. Burke and M. Ernzerhof, *Phys. Rev. Lett.* **77** (1996) 3865.

5.1 Neutron Radiation Induced Structural Changes Affecting Optical Performance of Dielectric Mirrors — K. J. Leonard and L. L. Snead *(Oak Ridge National Laboratory)*

OBJECTIVE

The purpose of the irradiated dielectric mirror examinations is to establish the radiation and thermal limits of these materials and to identify the causes of degradation in optical performance. This research can further be applied towards understanding the radiation behavior of multi-layered devices such as electronic components for sensor and diagnostic applications.

SUMMARY

Dielectric mirrors consisting of alternating layers of HfO_2/SiO_2 and Al_2O_3/SiO_2 on sapphire substrates were irradiated at 175°C to damage levels up to 0.1 dpa. No significant changes were measured in the optical properties after irradiation, but absolute reflectivity values in the HfO_2/SiO_2 mirrors degraded during post-irradiation thermal anneals up to 400°C. Microstructural examination is being completed to examine the cause. A second round of irradiations to 1 and 4 dpa are being initiated to determine the upper irradiation and thermal limits.

PROGRESS

Multilayered thin-film dielectric mirrors can significantly improve transmission of reflected electromagnetic energy, greater than 99% as compared to metallic mirrors such as aluminum (80-90%) or silver and gold (<40%) in the UV range. Therefore their use as focusing mirrors for inertial confinement systems as well as incorporation into plasma diagnostic systems for magnetic confinement systems has been considered. However, little is known about their longevity and sensitivity to displacement radiation, or the mechanisms for optical degradation that take place in the material.

In earlier work [1], we reported on the optical performance of dielectric mirrors following neutron irradiation at 175°C to damage levels of 0.001, 0.01 and 0.1 dpa along with subsequent annealing treatments of the irradiated samples at 300 and 400°C for 1.5 hours. The mirrors, designed for optimum reflectivity at a wavelength of 248 nm consisting of HfO_2/SiO_2 and Al_2O_3/SiO_2 bi-layer coatings on sapphire substrates, survived irradiation without delamination or cracking and showed only minor shifting in peak reflectivity with irradiation. Subsequent annealing of the irradiated samples resulted in a loss of reflectivity in the HfO_2/SiO_2, while the Al_2O_3/SiO_2 mirror type remained unaffected. No change in reflectivity was observed in the unirradiated materials annealed up to 400°C. Those results indicated an impressive (more than an order of magnitude higher) irradiation resistance as compared to the literature data and suggested a wider applicability of dielectric mirror in fusion systems.

The radiation and thermal-induced changes in the microstructure of the dielectric mirrors examined by X-ray diffraction and transmission electron microscopy (TEM) is being completed. While increased Si concentration in the Al_2O_3 film layers has been measured with increasing irradiation dose and in post irradiation thermal anneals, the individual film layers remain amorphous and show no indication of compound formation,

suggesting stability of the Al_2O_3/SiO_2 mirror to higher irradiation dose and thermal levels. The HfO_2 layers in the HfO_2/SiO_2 mirrors show changes in crystallinity with irradiation dose, starting from monoclinic structured crystallites in an amorphous film layer for the unirradiated mirrors to fully crystalline films in the 0.1 dpa material consisting of monoclinic and either tetragonal or cubic crystallites. In both mirror types, the SiO_2 layers remain amorphous. Though changes in crystallinity are observed in the HfO_2/SiO_2 mirror with increasing dose, no loss in reflectivity is observed to 0.1 dpa. The microstructural cause for the degradation of the mirrors during post-irradiation annealing is currently being examined.

In addition to the concluding microstructural examinations of the mirrors irradiated to 0.1 dpa, work has initiated on irradiations to 1 and 4 dpa at HFIR. The completion date of the irradiations is expected to be late July 2012, with post-irradiation examination to begin following a one month cooling and capsule disassembly. Optical examinations will include changes in relative spectral reflectance versus wavelength and absolute reflectance at 248 nm for the HfO_2/SiO_2 and Al_2O_3/SiO_2 mirrors in the as-irradiated and post-irradiated annealed conditions. Transmission electron microscopy and X-ray diffraction will again be used to evaluate the microstructural effects contributing to the optical property changes and mirror stability.

The optimum performance of diagnostic materials under severe radiation environments is critical to safe functioning of fusion reactors. Understanding the mechanisms for degradation that impose limitations to the operating range of a given material or component is key to both improving reliability and designing more radiation tolerant systems. The dielectric mirror research work will aid in determining the upper radiation and thermal limits for use in laser control of inertial confinement fusion systems as well as diagnostic systems for both fusion reactor types. Furthermore, examining the radiation induced structural changes in the films will be beneficial for the development of other thin-film based electronic components and sensors used fusion applications.

1. L. L. Snead, K. J. Leonard, G. E. Jellison Jr., M. Sawan and T. Lehecka, "Irradiation effects on dielectric mirrors for fusion power reactor application," *Fusion Sci. and Technol*. **56**, 2 (2009) 1069-1077.

6.1   Characterization of Specimens Exposed in a Li Loop —   K. A. Unocic, M. J. Lance, and B. A. Pint (*Oak Ridge National Laboratory*)

This is the Abstract for an ICFRM-15 paper submitted for publication in the Proceedings.

A monometallic V-4Cr-4Ti thermal convection loop was run for 2,350 h with a peak temperature of 700°C and Li flow rate of 2-3 cm/s. Specimens of V-4Cr-4Ti exposed in the hot and cold leg were tensile tested in vacuum at 500°C showing an increase in the 0.2% yield and ultimate tensile strengths and a decrease in the serration amplitude with decreasing exposure temperature in the loop. However, only minor changes in ductility were measured. With the higher temperature exposures, there was a decrease in Vickers hardness measured but little change in the grain size. Characterization of the microstructure after exposure at 627°C in the loop showed an increase in the density of Ti- and N-rich grain boundary and matrix precipitates near the specimen surface after exposure corresponding to an increase in the hardness in the near-surface region. Two-layer V/Y_2O_3 coatings on V-4Cr-4Ti substrates also were exposed in the loop and initial room temperature characterization has been conducted.

6.2 ADDITIONAL CHARACTERIZATION OF V-4CR-4TI AND MHD COATINGS EXPOSED TO FLOWING Li – B. A. Pint and K. A. Unocic (Oak Ridge National Laboratory)

OBJECTIVE

A flowing Li thermal convection loop was operated with V-4Cr-4Ti specimens and multi-layer electrically-insulating coatings needed to reduce the magneto hydrodynamic (MHD) force in the first wall of a lithium cooled blanket. Both types of specimens are now being characterized to examine the effect of exposure in flowing Li.

SUMMARY

Additional results are presented on the characterization of V-4Cr-4Ti tensile specimens and MHD coatings exposed to flowing Li. The alloy tensile specimens showed dynamic strain aging (DSA) at 500°C and the DSA amplitude varied with yield and ultimate tensile strength. Grain size and hardness measurements also were made on these specimens. For the MHD specimens, electron energy loss spectroscopy (EELS) and x-ray photoelectron spectroscopy (XPS) both found no evidence of Li in one coating after the exposure. A high temperature vacuum rig is being reconstructed to measure the electrical resistance of the coatings after exposure.

PROGRESS AND STATUS

Introduction

Previous reports[1-3] presented 500°C tensile behavior of V-4Cr-4Ti after various exposures including flowing Li in a thermal convection loop with a peak temperature of 700°C for 2,355h.[4] The results were unusual and more characterization was warranted which is now being undertaken along with more analysis of the data. Also, the dual layer (Y_2O_3/V) MHD coatings deposited by physical vapor deposition that were exposed in the loop were not fully characterized because a method was not apparent to evaluate the electrical resistivity without damaging the coatings. A micro-milling technique is being used to cut specimens out of the coated specimens for characterization and electrical measurements. Focused ion beam (FIB) milling is being used to prepare specimens for transmission electron microscopy (TEM). These results were obtained since the most recent publication.[3]

Experimental Procedure

Details of the thermal convection loop exposure have been presented previously.[4] The specimens consisted of miniature tensile specimens (type SS-3: 25 x 4 x 0.9mm), tab specimens and specimens with a dual layer MHD coating linked in a chain held together with V-4Cr-4Ti wire. The tensile specimens were annealed for 1h at 1050°C prior to exposure in Li. The exposure temperature for each specimen is estimated by using a linear extrapolation of the temperatures measured at the top and bottom of the each leg.[4] Tensile testing was conducted at 500°C in a vacuum with a base pressure of 10^{-6} Pa (10^{-8} Torr) and a strain rate of 10^{-3} s^{-1}. After tensile testing the specimens are now being characterized using various techniques including light microscopy to measure the grain size and hardness measurements across the specimen cross-section. In order to look for the presence of Li in the coatings after loop exposure, TEM specimens are being prepared by FIB and EELS and XPS were employed.

Results and Discussion

Figure 1 shows the amplitude of the DSA serrations measured during tensile testing at 500°C as a function of the measured yield stress at 500°C. The results from the loop-exposed specimens are compared to
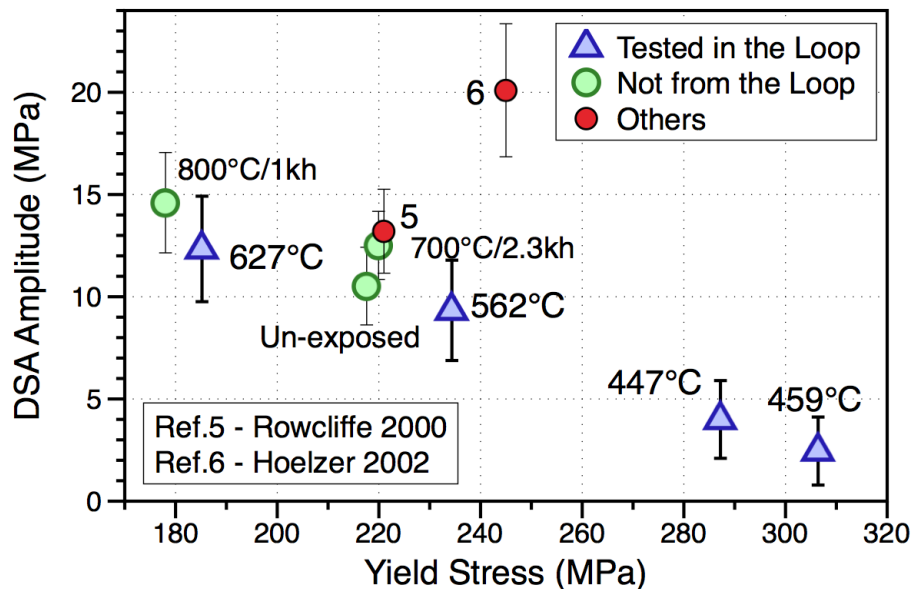
Figure 1. Amplitude of the dynamic strain aging observed at 500°C as a function of 500°C yield stress for V-4Cr-4Ti specimens exposed in the Li loop, other exposures and other reports from the literature. The bars note the standard deviation of the measurements.

specimens from the same batch of V-4Cr-4Ti with the same processing history: (1) as-processed/un-exposed, (2) after a 2,350h anneal at 700°C in a quartz ampoule and (3) after a 1,000h exposure to isothermal Li at 800°C. In addition, the results from two previous studies also are shown for reference.[5,6] The general trend is that the amplitude decreased with increasing yield stress. A similar relationship was observed with the ultimate tensile strength. One explanation [7] for these results is that at the lower temperatures, O is depleted from the matrix decreasing the amplitude but little uptake occurs. At higher temperatures, O is more strongly depleted but high N uptake increases the amplitude. The thermal anneal had very little effect on the yield stress or amplitude.

Figure 2 shows average grain size and hardness measurements from some of the same specimens as shown in Figure 1. The grain size was not significantly affected by these exposures. In contrast, the hardness changed significantly. The highest temperature exposures strongly decreased the hardness. For the Li exposures, this is consistent with the removal of O from the matrix. However, it was surprising that the 700°C anneal reduced the hardness to a similar degree where no chemical change would be expected.

For the MHD coatings, Figures 3 and 4 show TEM images from a FIB thinned section through the V/Y_2O_3 coated V-4Cr-4Ti specimen exposed at 427°C at the bottom of the hot leg.[3,4] Because the thickness of the coating, only the Y_2O_3 near the V-4Cr-4Ti interface could be thinned and imaged. Figure 3 shows a macro image of the thinned specimen and Figure 4 shows higher magnification images where the EELS analyses were performed in the metal near the Y_2O_3 interface and in the Y_2O_3 coating. The alloy-Y_2O_3 interface looks intact, Figure 4a. The Y_2O_3 coating has a columnar grain structure with porosity at the column boundaries typical of the physical vapor deposition process, Figure 4b.[8] Figure 5 shows EELS spectra from both areas in Figure 4 and there is no indication of Li. The specimen was then examined by XPS and again no Li was detected, Figure 6. It must be noted that Li is very mobile even at room temperature and may have been removed or diffused away during specimen preparation. However, in
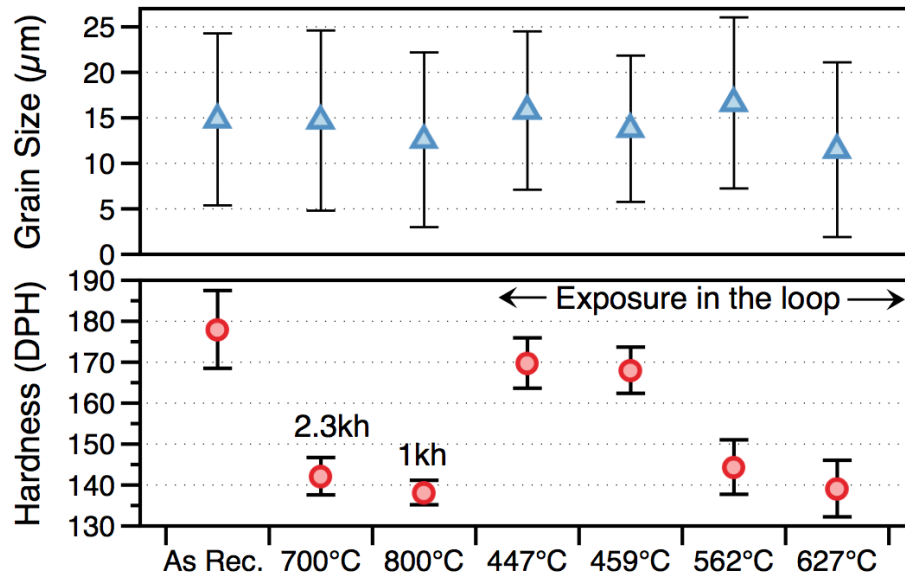
Figure 2. Average hardness and grain size measurements from V-4Cr-4Ti specimens exposed in the Li loop and other exposures. The bars mark standard deviations for both measurements.

prior work, Li tends to form compounds with Y_2O_3 when present in sufficient quantity.[9,10]

The performance metric for the MHD coating is maintaining sufficient electrical resistance at 500°-800°C after exposure to flowing Li. Therefore, a high temperature vacuum rig is being assembled for measuring electrical resistance of the coatings. In addition to this specimen, the other MHD coatings (3 from the hot and cold legs were exposed in the loop and one was annealed at 700°C for 2,350h) will be measured and characterized.
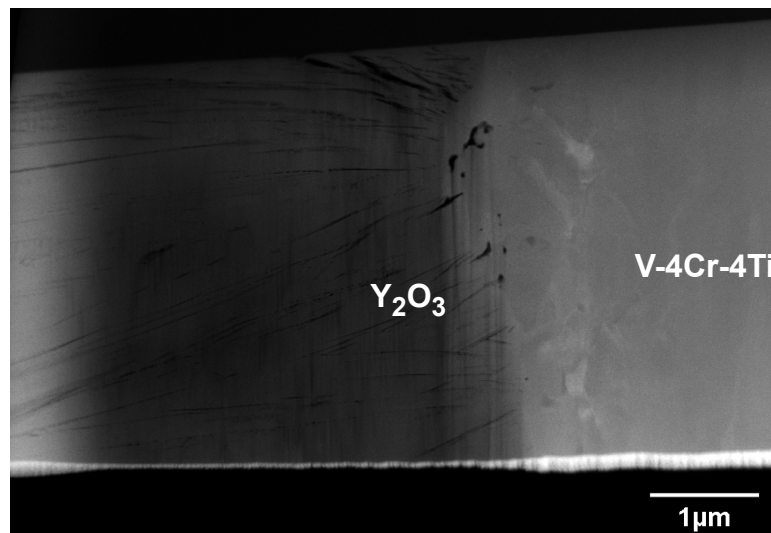
Figure 3. TEM bright field image of the FIB section through the Y_2O_3 coating and V-4Cr-4Ti substrate that was characterized.
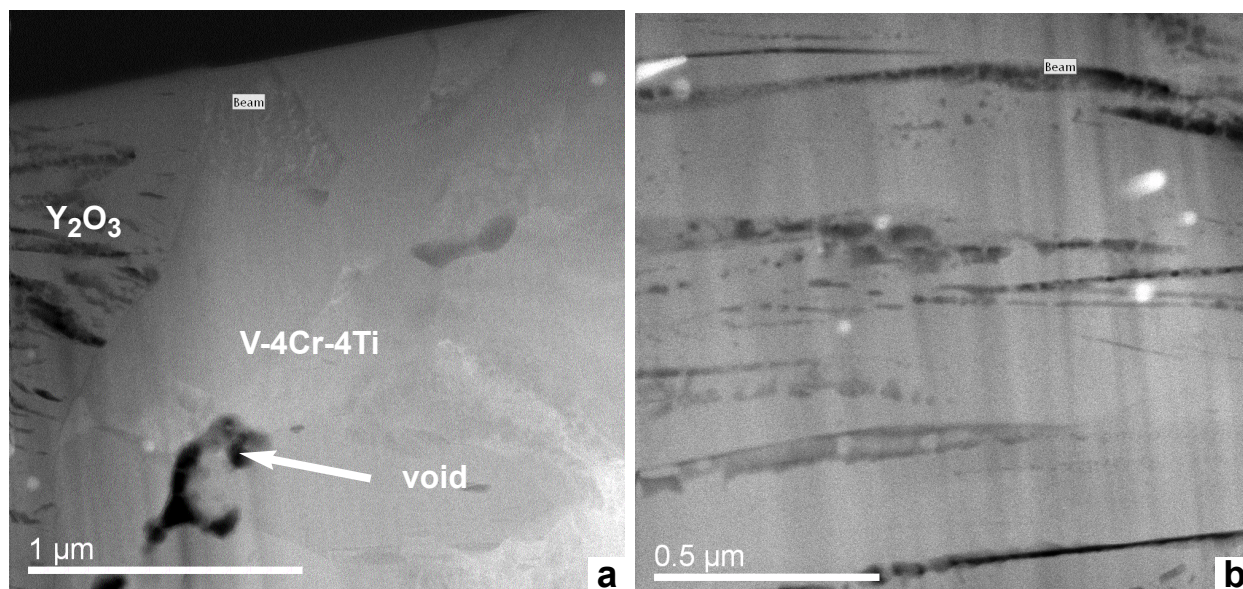
Figure 4. High angle annular dark field TEM images of the V/Y_2O_3 coating on V-4Cr-4Ti after exposure in flowing Li at 427°C.
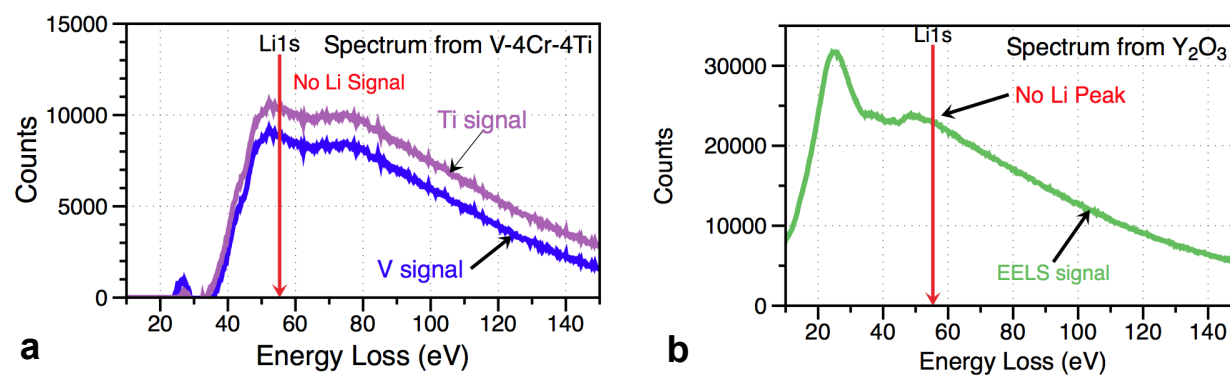
Figure 5. EELS spectra for (a) V-4Cr-4Ti and (b) Y_2O_3 coating showing no Li detected.
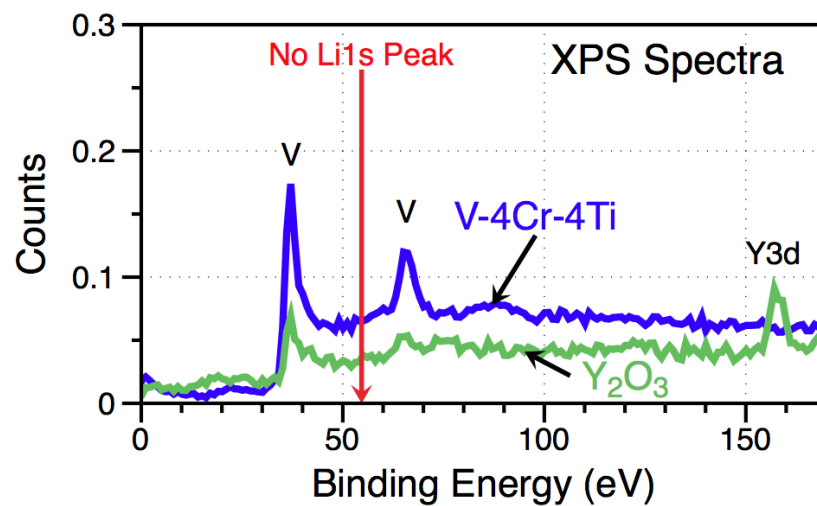
Figure 6. XPS spectra from the alloy and Y_2O_3 MHD coating indicating no Li detection.

70

References

[1]   B. A. Pint, DOE/ER-0313/45 (2008) 11.
[2]   B. A. Pint, DOE/ER-0313/46 (2009) 1.
[3]   K. A. Unocic, M. Lance and B. A. Pint, submitted to J. Nucl. Mater.
[4]   B. A. Pint, et al., J. Nucl. Mater. 386-388 (2009) 712.
[5]   A. F. Rowcliffe, S. J. Zinkle and D. T. Hoelzer, J. Nucl. Mater. 283-287 (2000) 508.
[6]   D. T. Hoelzer and A. F. Rowcliffe, J. Nucl. Mater. 307-311 (2002) 596.
[7]   T. Muroga, private communication (2012).
[8]   A. F. Jankowski, C. K. Saw, J. L. Ferreira, J. S. Harper, J. P. Hayes and B. A. Pint, J. Mater. Sci. 42 (2007) 5722.
[9]   T. Terai, et al., J. Nucl. Mater. 233-237 (1996) 1421.
[10]   B. A. Pint, K. L. More, H. M. Meyer and J. R. DiStefano, Fusion Sci. Technol. 47 (2005) 851.

6.3 Pb-Li Compatibility Issues for DEMO — B. A. Pint and K. A. Unocic (Oak Ridge National Laboratory)

This is the Abstract for an ICFRM-15 paper submitted for publication in the Proceedings.

The current dual coolant fusion blanket concept is limited to a ~475°C wall temperature due to dissolution/redeposition of the FeCr steel in Pb-Li. Higher wall temperatures could be achieved if compatibility issues can be controlled. Isothermal capsule experiments have demonstrated that thin (<50μm) Al-rich coatings on Gr.92 steel can reduce mass loss in Pb-Li for up to 5,000h at 700°C and that similar coating performance was obtained for coated oxide dispersion strengthened FeCr steels at 700°C. Dissimilar material experiments at 700°C suggested a possible reaction between Fe and SiC in Pb-Li that needs to be further studied as it could limit the blanket temperatures.

6.4 COMPATIBILITY OF MATERIALS EXPOSED TO ISOTHERMAL Pb-Li – B. A. Pint and K. A. Unocic (Oak Ridge National Laboratory, USA)

OBJECTIVE

One proposed U.S. test blanket module (TBM) for ITER uses ferritic-martensitic alloys with both eutectic Pb-Li and He coolants at ~475°C. In order for this blanket concept to operate at higher temperatures (~700°C) for a DEMO-type reactor, several Pb-Li compatibility issues need to be addressed. Some of the issues currently being investigated are the behavior of dispersion strengthened Fe-Cr alloys compared to conventional wrought material, the performance of Al-rich coatings to inhibit corrosion and dissimilar material interaction between SiC and ferritic steel.

SUMMARY

A series of Pb-Li capsule experiments were conducted to study the dissimilar material interaction between Fe and SiC using both materials as specimens and capsules. Because of uncertainties associated with the mass change data, metallographic cross-sections were completed to study the reactions observed at 500°-700°C after 1,000 h in Pb-Li.

PROGRESS AND STATUS

Introduction

A current focus of the U.S. fusion materials program is to address issues associated with the dual coolant Pb-Li (DCLL) blanket concept[1] for a test blanket module (TBM) for ITER and enhanced concepts for a DEMO-type fusion reactor. A DCLL blanket has both He and eutectic Pb-17 at.%Li coolants and uses reduced activation ferritic-martensitic (FM) steel as the structural material with a SiC/SiC composite flow channel insert (FCI). Thus, recent U.S. compatibility research has examined issues with Pb-Li.[2-8] Compared to Li,[9] a wider range of materials can be compatible with Pb-Li because of the low activity of Li.[10] In particular, SiC readily dissolves in Li, but not Pb-17Li.[2,4,11] However, like Pb, Pb-Li dissolves Fe, Cr and especially Ni from many conventional alloys above 500°C.[12,13] This is not a concern for a DCLL TBM operating at <500°C. However, a DCLL blanket for a commercial reactor would be more attractive with a higher maximum operating temperature, perhaps >600°C if ODS ferritic steels[14] were used. Even at 550°C, a recent study of Eurofer 97 (Fe-Cr-W) showed a very high dissolution rate in flowing Pb-Li.[13] Therefore, preliminary Pb-Li compatibility capsule experiments are being conducted at 500°-700°C in order to investigate several concepts before flowing Pb-Li compatibility tests are conducted. One concern is the potential dissimilar material effects between Fe and SiC because Fe forms more thermodynamically stable carbides than Si.[15] A series of capsule experiments have been completed [7,8] and characterization of all of the specimens is in progress. A large mass loss for Fe in a steel capsule could not be repeated in a second experiment and the large mass loss is not consistent with a smaller loss observed in a Mo capsule.

Experimental Procedure

Static capsule tests were performed using Fe (mild steel) or SiC inner capsules and type 304 stainless steel (SS) outer capsules to protect the inner capsule from oxidation. Since the SiC capsule cannot be sealed, it is placed inside a Mo capsule and held shut by a Mo wire welded into the Mo capsule lid that is welded shut.   For the Fe capsules, the specimens were ~1.5 mm thick and 4-5 cm^2 in surface area with a 600 grit surface finish and were held with 1 mm diameter Mo wire. (Mo can be considered to be essentially inert under these conditions.) For the SiC capsules, a chemical vapor deposition (CVD) SiC spacer is used to hold a specimen that is ~1.5 mm thick and 2-3 cm^2 in surface area. Unalloyed Fe

specimens were used (rather than FM steel) to simplify the experiment and the CVD SiC specimen was high-purity material from Rohm & Haas. For the Fe capsules, the capsules were loaded with 125g of Pb-Li in an Ar-filled glove box. For the smaller CVD SiC capsules, only 20g of Pb-Li was used. The Pb-Li for the Fe capsules was commercially manufactured. The Pb-Li for the SiC capsules was melted and cast at ORNL and had Li values of 15.6-16.5at%. The, Fe, Mo and SS capsules were welded shut in a glove box to prevent the uptake of impurities during the isothermal exposure. After exposure, residual Pb-Li on the specimen surface was removed by soaking in a 1:1:1 mixture of acetic acid, hydrogen peroxide and ethanol for up to 72h. Mass change was measured with a Mettler-Toledo balance with an accuracy of 0.01mg/cm^2. The specimens were metallographically mounted in epoxy to study the surface reaction product, which is in progress.

Results and Discussion

Figure 1 shows the mass change for the unalloyed Fe and SiC specimens in steel and SiC capsules at 500°-700°C.[7,8] The first Fe specimen exposed at 700°C in a steel capsule had a mass loss of -16.4mg/cm^2. Since this was 3-4X higher than losses measured for 9Cr steel, this experiment was repeated, and a small mass gain was measured for the second specimen, Figure 1. An Fe specimen in a Mo capsule at 700°C had a mass loss of -4.5mg/cm^2 which is consistent with mass losses for 9Cr steels. The SiC specimens in SiC capsules were damaged during loading and unloading, thus chipping dominated the mass changes. The scatter in the results suggests that characterization rather than just mass change is needed.

Figure 2 shows polished cross-sections of the specimens in Figure 1 (except 2i is the Fe specimen with the large mass loss.) While C transport cannot be ruled out by these results, it appears that O may be a more important factor. For the SiC specimen in the steel capsule, the SiC specimen may getter all of the O in the Pb-Li resulting in a thick oxide (Figure 2k) and a mass gain. With a SiC capsule, O may react with the capsule wall as well as the specimen, resulting in a thinner oxide layer (Figure 2l). A similar
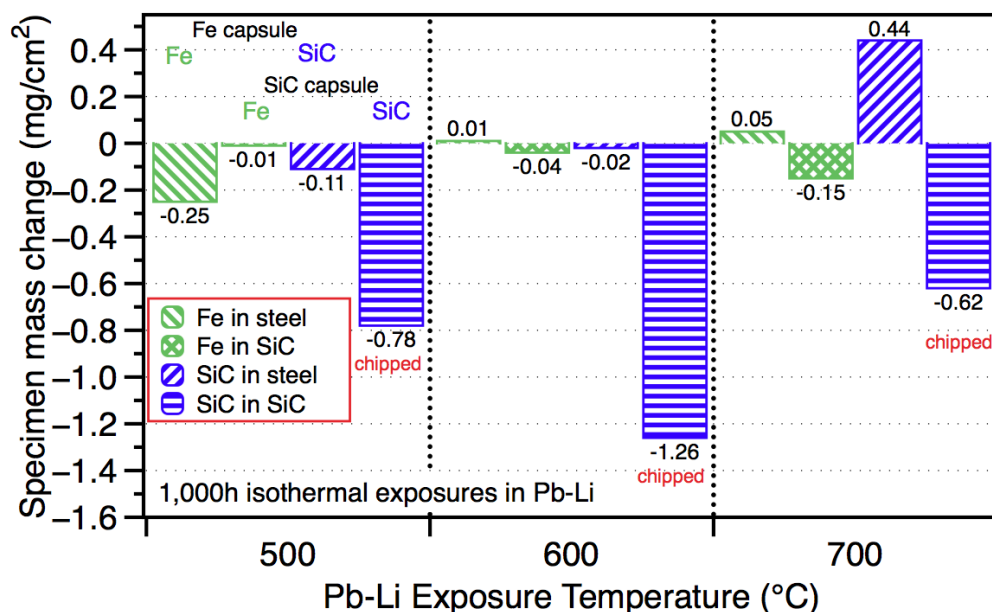
Figure 1. Specimen mass change from a series of capsule experiments with carbon steel or CVD SiC capsules and Fe and CVD SiC specimens exposed to Pb-Li for 1,000h at each temperature.
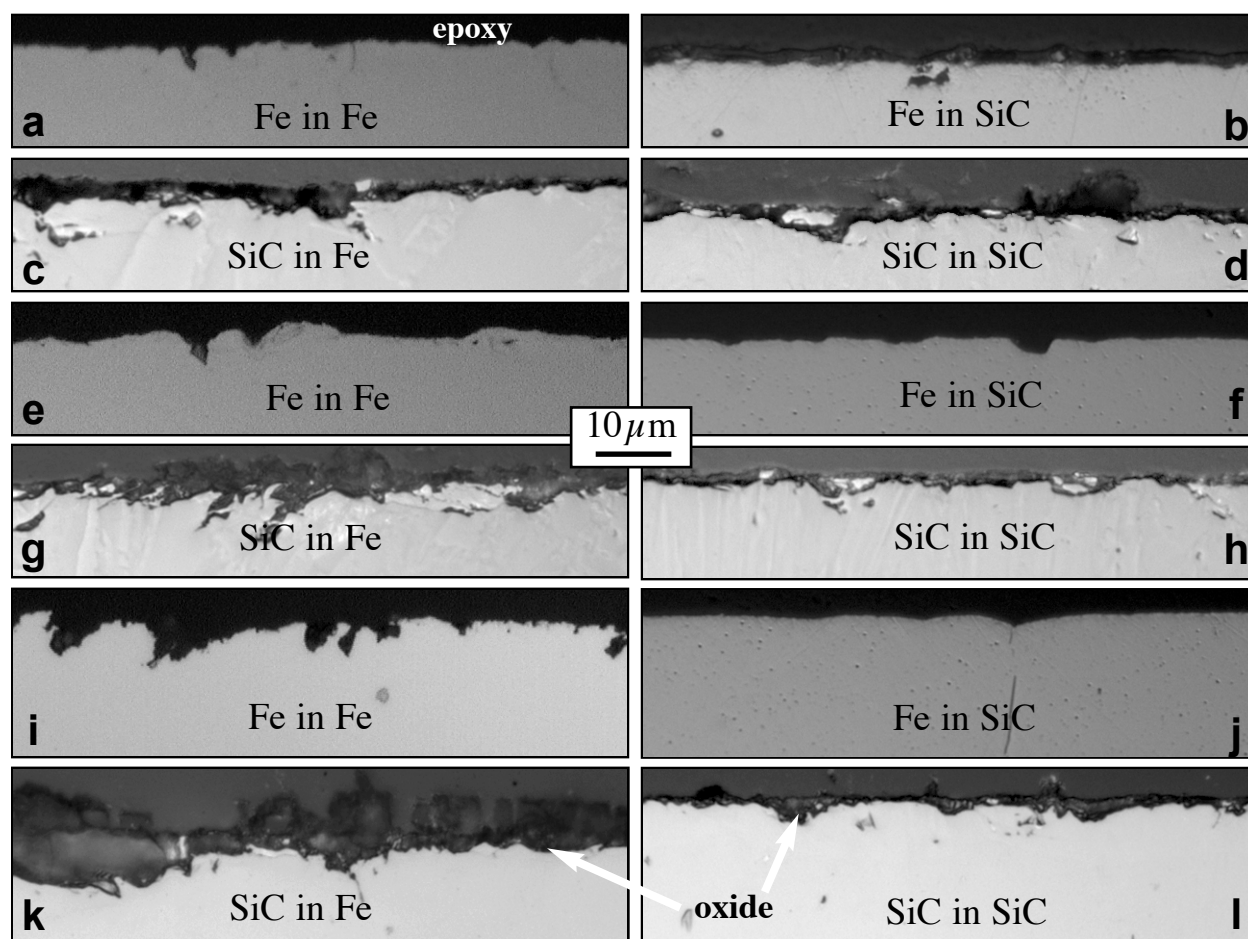
Figure 2. Polished cross-sections of Fe (a,b,e,f,i,j) and SiC (c,d,g,h,k,l) specimens after 1000h exposures in Pb-Li at (a-d) 500°C, (e-h) 600°C and (i-l) 700°C exposed in steel (a,c,e,g,i,k) or SiC capsules (b,d,f,h,j,l). Oxides were noted on the SiC specimens but not on the Fe specimens.

difference was observed at 600*C (Figures 2g and 2h). At 500°C, it was difficult to observe a difference. For the Fe specimens, a progressive roughening of the specimens surface was observed with increasing temperature in the steel capsules (Figures 2a, 2e and 2i). In these experiments, the Pb-Li could become saturated with Fe as both the specimen and walls dissolved. This could reduce the mass loss of the specimen. For the Fe specimen in a SiC capsule, all of the Fe dissolution would be expected from the specimen. However, relatively little dissolution was observed, even at 700°C, Figure 1.

One difference between the two types of capsule experiments is the specimen surface area to Pb-Li volume ratio. In the SiC capsule the ratio is 1.5 (2.7 cm^2 vs. 1.8 cm^3) while in the Fe capsule it is 0.5 for just the specimen (5 cm^2 vs. 11 cm^3). However, if the capsule wall also is considered (as the Fe capsule also may dissolve) the ratio is 2.5 because of the large surface area of the capsule in contact with ~11cm^3 of Pb-Li. While this difference needs to be considered in the results, it does not appear sufficient to explain the range of results observed. Further characterization is needed of these specimens including more characterization of the oxide on the SiC and hardness measurements of the Fe specimens as a possible indicator of C pickup.

In addition to exposing Fe specimens in Fe and Mo capsules, two additional capsule tests were performed. A coated and pre-oxidized 316 specimen was exposed at 700°C to study coating behavior on an austenitic steel at this temperature. A small mass gain of 0.2mg/cm^2 was observed. Also a pre-oxidized PM2000 (ODS FeCrAl) specimen [3] was again exposed at 600°C for 1000h to determine if the α-Al$_2$O$_3$ thermally grown oxide would transform to LiAlO$_2$. Curiously, the oxide appeared to be removed at this temperature after cleaning, similar to the previous result. The oxide was retained after Pb-Li exposures at 500°, 700° and 800°C.

References

[1]   M. Abdou, D. Sze, C. Wong, M. Sawan, A. Ying, N. B. Morley and S. Malang, Fus. Sci. Tech., 47 (2005) 475.
[2]   B. A. Pint, Fus. Sci. Tech. 52 (2007) 829.
[3]   B. A. Pint and K. L. More, J. Nucl. Mater. 376 (2008) 108.
[4]   B. A. Pint, Mater. Sci. Forum 595-598 (2008) 549.
[5]   B. A. Pint, J. Nucl. Mater. 417 (2011) 1195.
[6]   B. A. Pint, L. R. Walker and K. A. Unocic, Mater. High Temp. (2012) in press.
[7]   B. A. Pint and K. A. Unocic, submitted to J. Nucl. Mater.
[8]   B. A. Pint and K. A. Unocic, DOE/ER-0313/50 (2011) 115.
[9]   J. E. Battles, Intern. Mater. Rev. 34 (1989) 1.
[10]   P. Hubberstey, J. Nucl. Mater. 247 (1997) 208.
[11]   T. Yoneoka, S. Tanaka and T. Terai, Mater. Trans. 42 (2001) 1019.
[12]   O. K. Chopra, D. L. Smith, P. F. Tortorelli, J. H. DeVan and D. K. Sze, Fusion Technol., 8 (1985) 1956.
[13]   J. Konys, W. Krauss, J. Novotny, H. Steiner, Z. Voss and O. Wedemeyer, J. Nucl. Mater. 386-88 (2009) 678.
[14]   S. Ukai and M. Fujiwara, J. Nucl. Mater. 307 (2002) 749.
[15]   M. W. Chase, Jr. et al., Editors, JANAF Thermochemical Tables Third Edition, American Institute of Physics, New York, NY, (1986).

7.1 Continuum Modeling of Plastic Flow Localization in Irradiated fcc Metals — G. Po and N. M. Ghoniem (University of California, Los Angeles)

This is the Abstract for an ICFRM-15 paper submitted for publication in the Proceedings.

Under mechanical loading, neutron or ion irradiated metals may develop a mechanical instability characterized by the localization of plastic flow in narrow channels that are free of irradiation-induced defects. It is still unclear whether the resulting highly heterogeneous deformation plays a significant role in crack nucleation, fracture propagation and premature failure of structural components used in nuclear applications. Modeling of the phenomenon is an intrinsically multiscale problem since its onset and propagation depend of the interaction between the macroscopic elasto-plastic deformation process and the evolution of the underlying dislocation and defect microstructure. In this work, we develop a two-dimensional continuum model of plastic flow localization based on the continuum theory of dislocations. This framework allows a mechanism-based description of deformation in which plastic distortion is directly calculated from the evolution of dislocation density tensor fields on each slip system. The dislocation densities mutually interact through the self-consistent stress field derived from the deformation gradient and through back and flow stress corrections. The interaction between dislocation fields and irradiation-induced defects (mainly stacking fault tetrahedra (SFTs) in fcc metals) is two-fold. First, the flow stress depends locally on the SFT density. Second, based on existing Molecular Dynamics (MD) simulation results, dislocation fluxes are included as sink terms in the evolution equation of the SFT density. The model is implemented numerically using the Finite Element Method (FEM) and simulation results, showing plastic flow localization under simple loading conditions, are presented.

7.2 Constitutive, Damage and Plasticity Laws for Candidate Fusion Alloys —
T. Yamamoto and G. R. Odette, Y. Wu (University of California Santa Barbara)

OBJECTIVE

Objectives of this study is to derive true stress-stain constitutive [s(e)] and damage laws, as well as coupled plasticity rules for candidate fusion reactor structural materials, that provide with key elements of a failure evaluation model of fusion reactor structures. For that purpose we need to establish a self-consistent approach to derive [s(e)] beyond the strain range that standard uniaxial tensile tests can probe, especially in irradiated alloys that immediately neck in standard tensile tests.

SUMMARY

Standard uniaxial tensile tests cannot provide generally transferable post-yield information on deformation and ductile failure for materials with low uniform strain limits. Deformation mediated failure is not only controlled by the intrinsic constitutive properties, but also extrinsic factors, especially the loading-specimen geometry. A self-consistent approach is used to derive true stress-stain constitutive [s(e)] laws, for candidate fusion reactor structural materials encompassing a range of unirradiated and irradiated conditions. In this report, unirradiated F82H with 0 to 80% of cold-work and neutron and spallation proton irradiated F82H were evaluated. The approach is based on simultaneous measurements and finite element method (FEM) simulations of engineering stress-strain s(e) curves, that are consistent only for a unique s(e) law. TEM observations of the selected deformed specimens were also performed to obtain microstructural insight. The most important and surprising result is that the s(e) of the irradiated alloys are consistently higher that for unirradiated condition over a wide range of strain. The s(e) after neutron irradiation are higher than in the 80% cold worked unirradiated condition at high strains. For deformation conditions that do not lead to plastic flow instabilities the higher strength levels are an asset even if accompanied by the low initial stain hardening rates following neutron irradiations. Further, there is evidence that high levels of He may suppress the initial loss strain hardening. If verified by additional experiment and modeling, these conclusions will have a tremendous impact on assessing the effects of irradiation service on the failure limits of fusion structures.

PROGRESS AND STATUS

Introduction

Deformation controlled failure of a structure is mediated by the interaction of a number of intrinsic properties, including constitutive properties and plasticity laws, as well as extrinsic factors, such as geometry and loading conditions. Standard techniques, such as the uniaxial tensile test, cannot provide all of the information relevant to predicting deformation and failure, especially for irradiated materials where low ductility limits the strain range that can be probed. Accordingly, we report progress in developing advanced methods to predict local deformation limits for fusion structures in terms of structural stress-strain [s(e)] or load-displacement (P- D) behavior, accounting for both intrinsic and extrinsic factors. The first step requires developing a self-consistent set of constitutive and plasticity laws for materials of interest, both unirradiated and irradiated.

Approach

The approach is to measure P-D or engineering stress-strain [s(e)] curves and characterize and quantify large geometry changes (LGC) and deformation-flow (micro to macro) patterns of strain distributions (SD) for a wide variety of test geometries to access high stains and bound key structural conditions. Examples are shown in Fig.1. The experimental information is combined with finite element modeling (FEM) of the corresponding specimen(s) during testing to simulate LGC behavior, P-D/s(e) and SD. The true-stress/strain constitutive equation s(e) used in the finite element analysis can be varied, and the computed values of P-D/s(e), LGC and SD compared to the measured values. Differences are used to adjust the $\sigma(\varepsilon)$, and the process proceeds iteratively to obtain a maximum self-consistency.
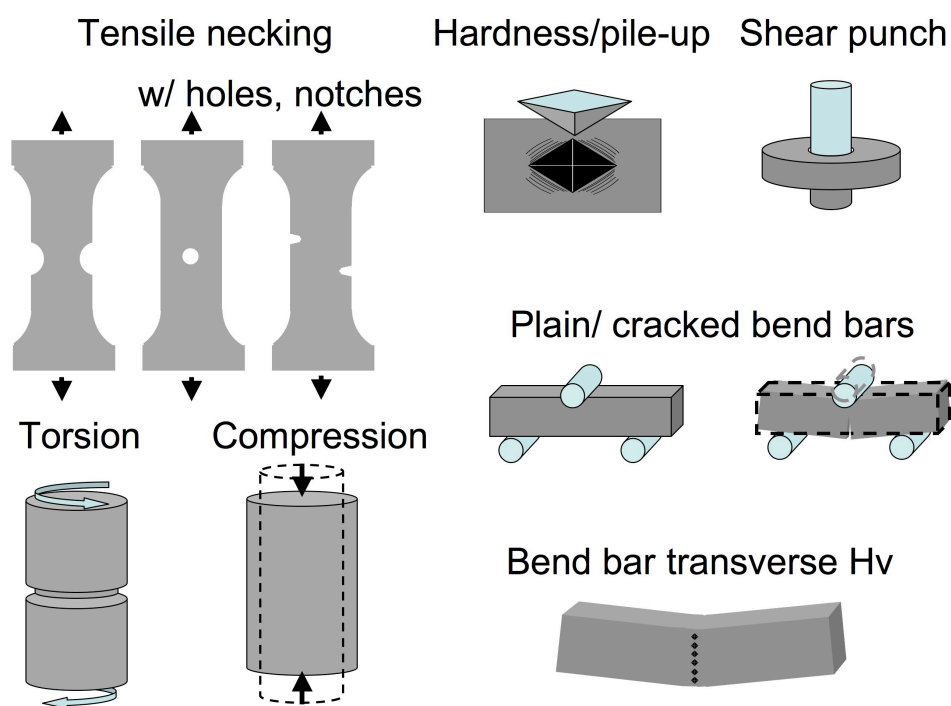
Figure 1.   Examples of test techniques that can probe high strain behavior of structural materials coupled with finite element simulations to derive a self-consistent constitutive [s(e)] behavior of the materials.

Experimental Details

The alloy used in the research is a tempered martensitic steel, F82H.   The Chemical composition of F82H alloy shown in Table 1. The as-tempered (AT) condition was rolled into two thickness reductions to produce 20% and 80% of cold work (CW), respectively. Miniature flat sheet SS-J2 type tensile specimens shown in Fig. 2 with thickness of 0.5 mm were prepared for those three conditions.   The specimens were tested on a MTS load frame at room temperature. Tensile specimens of the same geometry except with a thicker 0.75 mm thickness had been irradiated in HFIR to 7 and 18 dpa at 300 ^{o}C and tested at room temperature.   The

results have been reported by Hirose et al. [1]. Tong and Dai reported tensile test results of the same material irradiated in STIP-III (spallation target irradiation program) [2]. The specimen with 5 x 1 x 0.4 (mm) gauge sections were irradiated at $305^{o}C$ to13 dpa and 995 appm He.

Table 1. Chemical composition of F82H IEA heat.

Cr	W	V	Mn	Ta	Ni	Cu	Ti	Mo	Fe
7.82	1.98	0.19	0.1	0.04	0.02	0.01	0.004	0.0026	Bal.
Nb	Co	Al	Si	S	C	N	B	P	
0.0002	0.0024	0.001	0.07	0.001	0.09	0.007	0.0002	0.003	

Transmission electron microscope (TEM) characterization was performed on the AT and 80% CW conditions both in the undeformed tabs and the highly deformed region near the fracture surface using the focus ion beam (FIB) micro-machining method. Dislocation density was measured using the so-called two-circles method [3].

Finite Element Method Analyses

The finite element (FE) simulations of tensile tests were performed using the ABAQUS 6.9 software package for a three-dimensional mesh, consisting of ≈ 1400 brick elements that, as shown in Fig. 2, models 1/8 of gauge section partially including the end tab. The s(e)data was directly converted to s(e) up to the necking instability strain (or uniform elongation), e_u. The strain hardening ds/de data at $e < e_u$ was fitted to modified Voce-Mecking model based on the competing dislocation dynamics storage with increasing strain and annihilation controlled by the dislocation density, r. As Spatig et. al. has showed [4], the model can be given in terms of the strain hardening, s_{sh} as shown in Eq. (1), based on the dislocation hardening theory, s_{sh} = Mamb√r, where M is Taylor factor, a is the strength factor, m is shear modulus and b is Burgers vector.

$$d\sigma/d\varepsilon = P_1/\sigma_{sh} - P_2\sigma_{sh} = P_1/(\sigma_t - \sigma_o) - P_2(\sigma_t - \sigma_o) \tag{1}$$

The fitted P_1, P_2, and s_o were used to extrapolate s(e) up to a steady state saturation at ds/de = 0. The initial s(e) is then iteratively adjusted until the FE engineering s(e) prediction matches the experimental curve.

Figure 2. Geometry of SS-J type tensile specimens. SS-J2 with 0.5 mm thickness and SS-J3 with 0.75 mm thickness were used in this research.	Figure 3. An example of 3D model used in a finite element method simulation of tensile tests
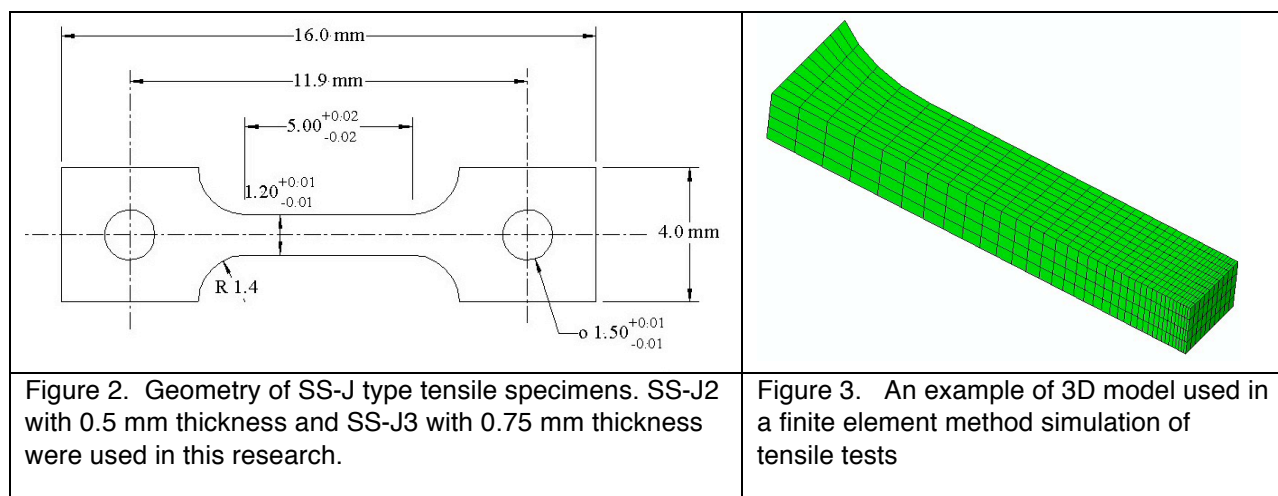
Results and Discussion

Figures 4a-f show the results of iterative FE simulations of F82H IEA tensile stress strain curves for (a) AT, (b) 20% CW, (c) 80% CW, (d) 7 dpa and (e) 18 dpa neutron irradiated and (f) STIP irradiated (13 dpa and 995 appm He) conditions. The green dotted line shows final s(e) model, and the blue solid and red dashed lines show FE simulated and experimental engineering s(e) curves, respectively. In all cases the converged FE simulation is in good agreement with experimental s(e) curve over a wide range of e. As are summarized in Fig. 5, the derived s(e) models vary significantly for the different alloy conditions. The as tempered (AT) alloy s(e) does not saturate up to very high strains and strain hardens rate $d\sigma/de > \approx 300$ MPa reaching $\sigma_{sh,at} \approx 300$ MPa at $e_p \approx 0.8$. The 20% CW condition $\sigma_{sh,20}$ does not saturate up to $e_p \approx 1$, but ds/de continuously decreases at high strains. The 80% CW condition $\sigma_{sh,80}$ saturates almost immediately, at a constant s(e) that is ≈ 400 MPa higher than σ_y in AT condition. The true CW
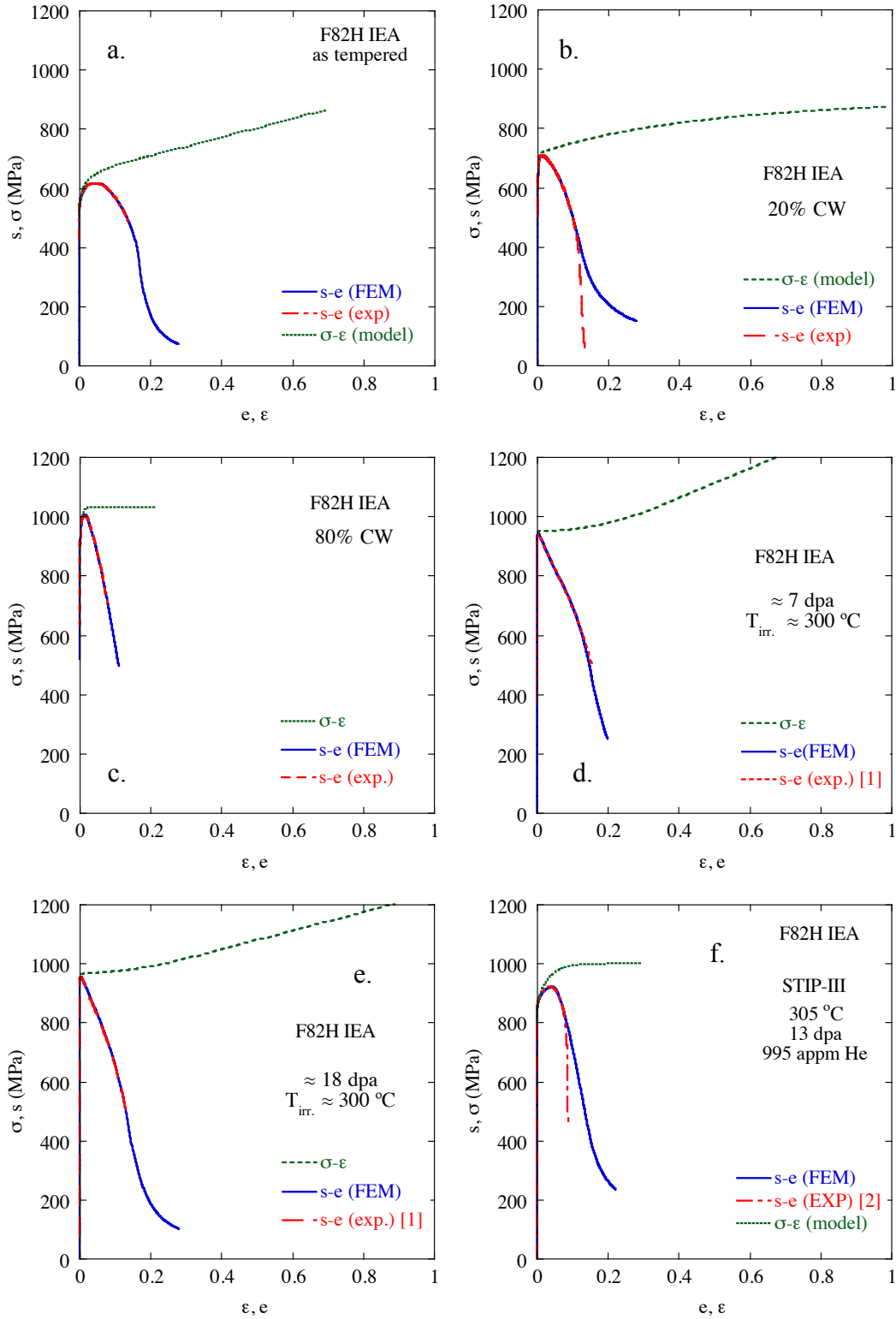
Figure 4. Final s(e) model for FE simulation of tensile s(e) curve in comparison with the experimental s(e) of F82H IEa for (a) AT, (b) 20% CW, (c) 80% CW, (d) 7 dpa and (e) 18 dpa neutron irradiated, and (f) spallation proton irradiated (13 dpa and 995 appm He) conditions.
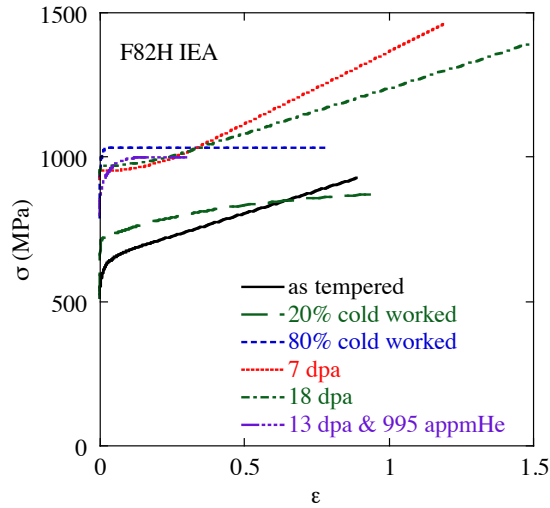
Figure 5. Comparison of model s(e) curves of F82H IEA alloy for various conditions.

Table 2. Dislocation density measured in TEM observation of tested tensile specimens in undeformed end tab and most deformed near fracture surface locations.

	Base	Deformed
As tempered	$6 \times 10^{14} m^{-2}$	$1 \times 10^{15} m^{-2}$
80%CW	$2 \times 10^{15} m^{-2}$	$2 \times 10^{15} m^{-2}$

rolling primary strains are 0.22 and 1.60 of the 20 and 80% CW conditions, respectively. Note the $s_{at}(0.22)$ for the AT condition is approximately equal to the s_y in the CW alloy with the same primary strain. The AT s(0.62) is also similar to the $s_{20}(0.4)$ suggesting that the tensile and CW strains are additive. Assuming a constant ≈ 300 MPa the AT reaches the saturated s_{80} ≈ 1032 MPa at an extrapolated e ≈ 1.34, which is ≈ 0.3 lower than the true primary strain of 80% CW. However, the corresponding ds/de Is much lower in the 20% CW condition, suggesting that much higher e would be needed to reach flow stress saturation in this case, possibly explaining the difference in saturation strain. Table 2 shows the dislocation densities in the AT and 80% CW conditions with no further tensile deformation and at the fracture e ≈ 0.7 in the AT case. Assuming a constant rate of dislocation storage of ≈ $0.6 \times 10^{15}/m^2$ and additional strain of ≈ 1.7 would be needed in the AT condition to yield the saturated density of $2 \times 10^{15}/m^2$ or a total e ≈ 2.4 versus ≈ 1.6 for the 80% CW condition. Thus the saturation dislocation density and s appear to be 1 -2 x $10^{15}/m^2$ and 1030 respectively in the unirradiated F82H.

Both neutron irradiated conditions have low strain hardening up to e ≈ 0.3, resulting in immediate necking. However, at higher e the ds/de is between ≈ 300 and 600 MPa that is equal to or greater than in the AT condition. The analysis suggests that a high rate of ds/de persists at 1200 MPa at between e of 0.7 and 0.9. Thus there appears to be something fundamentally different for neutron irradiation and strain evolved microstructures compared to those created by deformation strains alone. However, in contrast to the neutron case, strain hardening begins immediately in the spallation proton irradiation condition, with high He as well as displacement damage, and rapidly approaches a saturation level similar to that in the AT and 80 CW alloys. If the mechanisms associated with such behavior could be understood it might be possible to design alloys that avoid loss of uniform strain capacity. More generally for deformation conditions that do not lead to plastic instabilities, the higher strength of irradiated alloys is an asset rather than a liability, as seen in Fig. 5.

CONCLUSIONS

The tools used in the work to derived true s(e) laws in as-tempered, cold-worked and irradiated F82H IEA over the wide range of strain are now used routinely in analysis of deformation and fracture phenomena including conditions pertinent to fusion structures. The various trends s(e) behavior are complex and suggest a strong role of microstructure that is alternatively produced by displacement damage (mostly loops), cold work (network dislocation and subgrain structures) and high He irradiations (loops and bubbles). Notably, in many cases associated with stable plastic deformation, the higher strength of irradiated alloys over a wide range of strains should be considered to be an asset rather than a liability.

FUTURE WORK

In addition to a wide range of applications, future research will be directed at understanding the combined interactive effects of processing; irradiation and strain evolved microstructures, with an eye to optimizing alloy and structural performance. Future research will also be focused on a major limitation of these studies to date, by characterizing and modeling deformation induced damage development that leads to fracture of leading candidate fusion alloys.

ACKNOWLEDGEMENTS

REFERENCES

1. T. Hirose et al., *J. Nucl. Mater.* **417** (2011) 108. (ICFRM-14)
2. Z. Tong and Y. Dai, J. Nucl. Mater. **398** (2010) 43.
3. B. Hirsch, A. Howie, R. B. Nicholson, D. W. Pashley and M. J. Whelan, Electron Microscopy of Thin Crystals (1965) 423.
4. P. Satig, G. R. Odette, G. E. Lucas, M. Victoria, *J. Nucl. Mater.* **307-311** (2002) 536.

7.3   Multiscale Simulation of Transmission Electron Microscopy Imaging of Helium Bubbles in Iron — B. Yao, D. J. Edwards, and R. J. Kurtz (Pacific Northwest National Laboratory), G. R. Odette and T. Yamamoto (University of California Santa Barbara)

OBJECTIVE

The objective of this task is to establish the size correlation between transmission electron microscopy (TEM) imaged helium (He) bubbles and the actual bubbles in an iron (Fe) matrix.

SUMMARY

The results of this simulation study show that the size of TEM imaged He bubbles, represented by the inner diameter of the first dark Fresnel ring under defocused condition (D_{in}), deviated from the actual bubble size (D_o). D_{in} was found to be larger than D_o when imaged with a highly incoherent electron beam, but smaller than D_o if the beam is coherent. The deviation of D_{in} from D_o increases with increasing defocus. On the other hand, the electron beam accelerating voltage, bubble size, bubble position, and TEM sample thickness do not significantly affect the value of D_0/D_o. This study also suggests that He bubbles can be differentiated from argon (Ar) bubbles by differences in Fresnel contrast.

PROGRESS AND STATUS

Introduction

Formation of nanoscale He bubbles in reduced activation ferritic/martensitic steels may lead to degradation of mechanical properties of materials [1-3]. One strategy to control the fate of He and its effect on mechanical properties of materials is through limiting the size of He bubbles with designed material composition and structure [4]. Based on established theories [4-7], a critical radius exists for the transition of He bubbles to voids. Below a critical size He bubbles are stable, while above the critical size, He bubbles transition to unstably growing voids. TEM has been commonly used for the characterization of He bubbles. Due to their small size (typically less than 5 nanometers in diameter), a defocus of 0.5 µm to 1µm is required to reveal the Fresnel rings of the bubbles. The size of Fresnel ring can be utilized to represent the bubble size. In order to accurately quantify the bubble size, one question arises: what is the relationship between the size of Fresnel rings formed during under-focused imaging and that of the actual He bubbles?

Over 40 years ago, pioneering work was conducted by Rühle and Wilkens [8-10] and Foreman et al. [11] to establish this relationship. Their approach is based on multi-beam Bloch wave calculations using column approximations. Their results indicate that the inner diameter of the first dark Fresnel ring (D_{in}) in an under-focused condition is slightly larger than the actual cavity diameter (D_0) [8]. Their calculations were based on several important assumptions: 1) the foil was relatively thick (e.g., $t_{min} \approx 6\xi_g$, where ξ_g is the extinction length); 2) the cavity was not too close to either of the foil surfaces; and 3) the microscope resolution was not better than ~ 7Å [8]. Obviously, with the improvements in microscopes and the ability to image smaller features, some of these assumptions may not be valid today.

This paper presents our study of multislice simulation of TEM imaging of He bubbles in Fe. It is known that the multislice simulation is more suitable to deal with complicated situations than

Bloch wave calculations [12]. The multislice simulation through Fast Fourier Transformation (FFT) is able to include millions of electron beams, and no special assumptions are required. Consequently, it may provide simulation results closer to the actual situation. The main objective of this study is to re-examine the size correlation between imaged Fresnel rings and the actual bubbles. Effects of a variety of imaging and specimen conditions were examined.

Methods

The program developed by Kirkland [12] was chosen for the multislice simulation of TEM images in this study. Large super-lattices containing a He bubble inside were generated according to the required interface of simulation software. Specimen variables explored in this study include sample thickness, bubble size, and bubble position along the thickness direction. Variations in imaging conditions include electron-beam incoherency, accelerating voltage (keV), and defocus. In order to accurately quantify the size of Fresnel rings from simulated images with the same standard, a post-processing program was developed to generate an average-intensity profile along the bubble radius direction. A representative simulated bubble image and its intensity profile are shown in Fig. 1(a) and Fig. 1(b), respectively. The X-axis in Fig. 1(b) indicates the distance from the bubble center with a step of one pixel, and Y-axis corresponds to an average intensity of all pixels on an annular ring. This formal analytical procedure is introduced because human vision is not sensitive to slight variations in image intensity. Through this approach, the uncertainty of determining Fresnel ring size in simulated TEM images is greatly reduced.

(a)   (b)
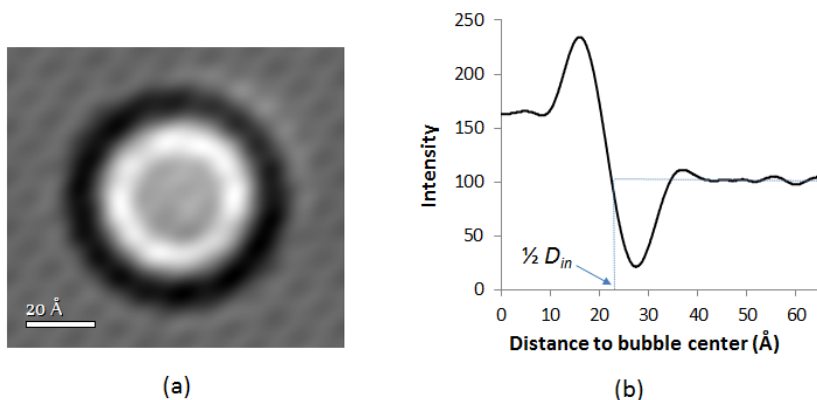
Fig. 1. (a) A representative simulated TEM image of a 5nm-He bubble with V = 200 keV, Δf = -500 nm, C_s= 1mm, and a deviation of illumination semi-angle of 0.5 mrad; (b) the corresponding average-intensity profile of the image.

Results and Discussion

Electron-beam incoherency was found to have a significant influence on the deviation of imaged bubble size from the actual one, as demonstrated by Fig. 2. The term D_{in} in the figure indicates the inner diameter of the first dark Fresnel ring in the under-focused condition, and D_0 is the actual bubble size in diameter (5 nm for the present simulations). D_{in}/D_0 represents the deviation of imaged Fresnel ring from the actual bubble size. The uncertainty of the data comes from the measurement of the size of Fresnel rings, as illustrated in Fig. 1. The coherency considered here is limited to spatial coherency. A small deviation in defocus and illumination angle was introduced to include the effects of partial coherence [12]. A small spread of defocus

(e.g., 50 Å) was found to have no detectable influence on the value of D_{in}/D_0 (results not shown). However, the effect of a deviation of illumination semi-angle ($\Delta\alpha$) is much stronger, as clearly revealed by Fig. 2. Other related parameters for the simulations include an accelerating voltage of 200 keV, a C_s of 1 mm, a super-lattice containing a 5 nm He bubble located in the center of TEM foil, a total foil thickness of 52 nm, and a defocus of 500 nm.

Fig. 2 is helpful to understand differences between results obtained in this simulation study and the previous calculations by Rühle and Wilkens [8]. Both studies confirm that the actual bubble size is close to the inner diameter of the first dark Fresnel ring. However, the Bloch wave calculations [8] predicted a value of D_{in}/D_0 greater than 1, while our simulations using coherent electron beams gave values of D_{in} less than D_0 (as will be shown later). This difference is most likely related to the incoherency of electron beams. The assumption [8] that the microscope resolution is not better than ~ 7 Å may be valid for microscopes equipped with tungsten or LaB_6 filaments, but it certainly is not applicable to FEG-TEMs.
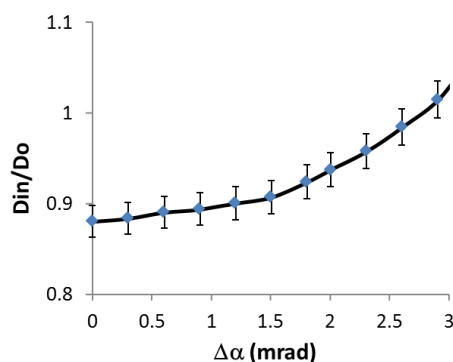
Fig. 2. Effect of D_{in}/D_0 as a function of the deviation of illumination semi-angle ($\Delta\alpha$).

Fig. 3 presents the effects of defocus and accelerating voltage of electron beam on D_{in}/D_0. The simulated samples have a thickness of 52 nm, and the bubble is located in the center of the membrane. A small beam-incoherency ($\Delta\alpha$ = 0.3 mard) was selected for the simulations. It is clearly shown in the figure that the ratio of D_{in}/D_0 generally decreases with increasing defocus. The electron beam accelerating voltage was found to have a very small influence on the change of imaged bubble size. The imaged He bubbles at a defocus of 1μm are about 85% of the actual bubble size.
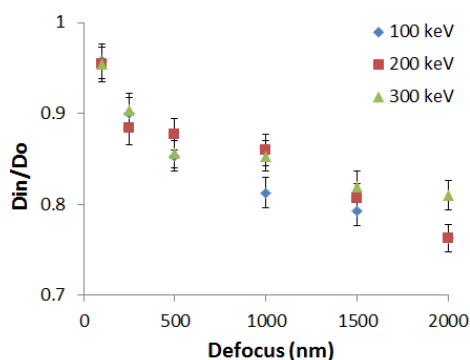
Fig. 3. A trend of D_{in}/D_0 at different electron-beam accelerating voltages as a function of defocus.

Effects of other factors, including bubble size, bubble position in the depth of membrane, and TEM sample thickness were also examined. Bubble size and position in the TEM sample thickness were found to have a negligible effect on D_{in}/D_0. The sample thickness may have a small effect. For samples thinner than 35 nm, D_{in}/D_0 slightly increases with increasing thickness, while above that, D_{in}/D_0 generally remains constant. As effects from these factors are not significant, corresponding simulation results are not presented in this report.

The ion-milling induced artifacts of Ar bubbles may cause an overestimation of He bubble density, especially in small-size range (e.g., ≤ 1 nm), or limit the TEM resolution for the examination of small He bubbles. As the atomic potential of Ar is much higher than that of He [12], it might be possible to distinguish these two types of bubbles by their image contrast. For this purpose, TEM images of a He bubble, an Ar bubble and a void with the same size (3 nm) and imaging conditions (200 eV, 1mm of C_s, 26 nm in thickness, 0.3 mrad of $\Delta\alpha$, and a defocus of 500 nm) were simulated. The results are shown in Fig. 4. Under the selected imaging conditions, the void and the He bubble give the same contrast, which suggests that the He/Vacancy ratio and standoff distance between He atoms and the Fe matrix is not a concern in TEM imaging simulations. On the other hand, the Ar bubble has a much weaker contrast under the same imaging condition. The results can be understood as Ar atoms (with an atomic number of 18) scatter the electron beam more effectively than He atoms (with an atomic number of 2). The simulation results suggest that it is possible to differentiate He bubbles from Ar bubbles during TEM examination. However, the simulation results also revealed that a larger electron-beam incoherency and defocus may greatly change the relative contrast of He and Ar bubbles. More quantitative studies are required for a more comprehensive understanding.
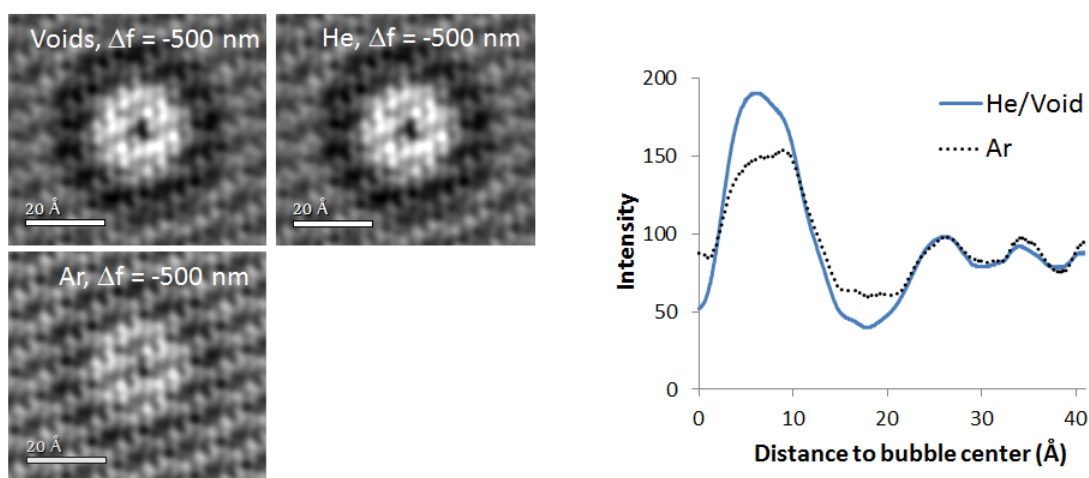
Fig. 4. (a) Simulated TEM images and (b) average-intensity profiles of a void, He bubble, and Ar bubble in Fe matrix. The defocus is 500 nm and illumination spread semi-angle is 0.3 mrad.

CONCLUSIONS

In summary, we found through multislice simulation and TEM characterization that:

1) The beam incoherency was found to have a great influence on the ratio of inner diameter of the first dark Fresnel ring to the actual bubble size, D_{in}/D_0.
2) It was also shown that D_{in}/D_0 decreases with increasing defocus. This general trend is not significantly influenced by the acceleration voltage and bubble size. With a defocus of 1 µm, D_{in} is about 85% of the actual bubble size.
3) Bubble size and position in the TEM sample thickness was found to have a negligible effect on D_{in}/D_0. The sample thickness effect was also shown to be very small.
4) Preliminary results suggest that the He bubbles and Ar bubbles can be distinguished by differences in contrast when imaged under the same conditions.

REFERENCES

[1]   M. Rieth, B. Dafferner, and H.-D Röhrig, *J. Nucl. Mater.* **258** (1998) 1147.
[2]   H. Ullmaier*, Nucl. Fusion* **24** (1984) 1039.
[3]   H. Trinkaus and H. Ullmaier, *J. Nucl. Mater.* **212** (1994) 303.
[4]   G. R. Odette, M. J. Alinger, and B. D. Wirth, *Annu. Rev. Mater. Res.* **38** (2008) 471.
[5]   L. K. Mansur and W. A. Coghlan, *J. Nucl. Mater.* **119** (1983) 1.
[6]   R. E. Stoller and G. R. Odette, *J. Nucl. Mater.* **131** (1985) 118.
[7]   C. A. Parker and K. C. Russell, *J. Nucl. Mater.* **119** (1983) 82.
[8]   M. Rühle and M. Wilkens, *Crystal Lattice Defects* **129** (1975) 6.
[9]   M. Rühle, *Phys. Status Solidi* **19** (1967) 263.
[10] M. Wilkens, in Electron Microscopy in Materials Science, II (Eds. U. Valdrè and E. Ruedl), 1975, p. 647, CEC, Brussels.
[11] A. J. E. Foreman, H. S. von Harrach and D. K. Saldin, *Philos. Mag. A* **45** (1982) 625.
[12] E. J. Kirkland, Advanced Computing in Electron Microscopy (Springer Science, New York, 2010), 2nd Edition.

7.4 Helium Effects in Advanced Structural Alloys: Progress on Solving a Grand Challenge to Fusion Energy — G. R. Odette, T. Yamamoto, Y. Wu, E. Stergar and N. J. Cunningham (University of California Santa Barbara), R. J. Kurtz and D. J. Edwards (Pacific Northwest National Laboratory)

OBJECTIVE

Our objective is to experimentally characterize the transport, fate and consequences of high levels of helium in leading candidate fusion alloys.

SUMMARY

The feasibility of fusion energy depends on developing advanced structural materials that can sustain extended component lifetimes in an ultra-severe environment, including up to 200 displacements per atom (dpa) and 2000 appm He. Helium and displacement defects individually and synergistically drive complex microstructural evolutions that degrade many performance-sustaining properties. Managing helium is perhaps the greatest challenge facing fusion structural materials. Here we show that an in situ helium injection fission reactor irradiation at 500°C to ≈ 25 dpa and 1450 appm helium produced populations of both bubbles and growing voids in a leading candidate tempered martensitic steel Eurofer97. The voids, which would be absent at low helium contents, are precursors to rapid swelling, suggesting that tempered martensitic steels may not tolerate extended service in the fusion environment. In contrast, only an ultrahigh density of tiny bubbles form in a companion nano-dispersion strengthened ferritic alloy, MA957. It is expected that the bubbles will inhibit swelling and other deleterious manifestations of irradiation effects at much higher dpa in materials with a high density of stable nano-dispersoids.

INTRODUCTION AND BACKGROUND

Fusion reactors will operate at high temperatures, under intense high-energy neutron fields and large time varying stresses, while exposed to chemically aggressive coolants [1]. High energy neutrons create excess vacancy and self-interstitial atom (SIA) defects by ejecting atoms from lattice sites, generating up to 200 displacements-per-atom (dpa), as well as up to 2000 appm He produced by neutron induced (n,a)) reactions [1-4]. Helium and dpa both individually and synergistically degrade a host of performance sustaining properties. For example, in leading candidate normalized and tempered 9Cr martensitic steels (TMS), grain boundary weakening by helium synergistically interacts with irradiation hardening to produce enormous elevations of the ductile to brittle transition temperature [5-7]. High helium contents may also degrade creep rupture properties at high temperatures and promote void swelling at intermediate temperatures [2-4,8]. Thus managing large quantities of helium is a grand challenge to achieving fusion energy.

Insoluble helium precipitates to form bubbles at elevated temperatures. Bubbles differ from growing voids in that they are smaller, gas pressure-stabilized cavities, containing m helium atoms, which grow only with the addition helium (m -> m+1). Bubble growth occurs up to a critical concentration, m = m*, where they convert to growing voids [2-4]. Larger voids grow by continuously collecting excess vacancies due to the preferential annihilation of the SIA (anti-) defects at biased dislocation sinks. TMS are swelling

resistant in a fission reactor environment where little helium is produced, but accumulating evidence suggests that at high He/dpa ratios growing voids nucleate from helium bubbles at m > m* [2-5]. However, if the bubble number density is very high, then m << m* in any individual bubble. Bubbles are also ideal point defect sinks and deeply trap additional helium that is generated at higher dpa. In this case m* increases and the swelling rate, if voids do manage to form, decreases with increasing bubble number density (N_b) [2-4].

Managing helium by creating a large number of small bubbles is a major objective of the development of an extremely promising alloy class that we call nanostructured ferritic alloys (NFA). NFA contain an ultrahigh density of 2-5 nm diameter Y-Ti-O oxides that are remarkably stable under thermal and irradiation exposure [2,3,9,10]. In addition to promoting high tensile, creep and fatigue strengths [2,3], the nano-dispersed oxides may enhance SIA-vacancy recombination and, most importantly, sequester helium by promoting the formation of a high number density of small, harmless bubbles with m << m*, thus mitigating void swelling [2-4,11]. Such a high matrix bubble sink strength also reduces the amount of helium reaching grain boundaries, thus reducing toughness loss at low-to-intermediate temperatures and potential degradation of creep rupture properties at high temperature [2-4]. Indeed, we have argued that a properly managed high density of nm-scale bubbles could turn helium from a liability to an asset [3].

Fission reactor irradiations normally produce << 1 appm He/dpa. Here we use a novel in situ helium injection (ISHI) technique in mixed spectrum fission reactor irradiations to study the effects of high helium contents on the bubble and void microstructures in TMS and NFA at fusion relevant dpa rates.

MATERIALS AND METHODS

The alloys characterized in this study include TMS and Eurofer97 [12,13], and a 14Cr ferritic stainless NFA, MA957, which has been the focus of many of our previous studies [2,3,10,11,14,15]. The composition of the 6.25 mm Eurofer97 plate used in this study is: 8.93Cr, 1.08W, 0.49Mn, 0.20V, 0.12C, 0.04Si, 0.021N, < 0.01(P, Cu, Co, Ti, Nb, B), bal. Fe (wt%) [12,13]. The plate was austenitized at 980°C for 27 minutes and air-cooled prior to tempering at 760°C for 90 minutes. As shown the transmission electron microscopy (TEM) micrograph in Fig. 1a, the martensite laths in Eurofer97 contain a high density of dislocations and dislocation cell substructures. Eurofer97 also contains alloy carbides distributed over a large size range.

The INCO MA957 used in this study was in the form of a hot extruded 25 mm diameter round bar [16,17]. The nominal MA957 composition is: 14.0Cr, 0.3Mo, 1.0Ti, 0.25Y_2O_3, bal. Fe (wt%) [14]. The specific processing and consolidation parameters for MA957 are proprietary, but the original patent gives the possible conditions including using powders of between -40 and -80 mesh size for each alloying element plus Y_2O_3; attritor milling for 24 h at 288 rpm using a 20:1 ball to powder mass ratio; and a 6:1 extrusion ratio at 1065°C [16]. MA957 contains a very high number density of ≈ 5.1±2x10^{23}/m^3 NFs with an average diameter of ≈ 2.8±0.4 nm [19]. The bright field TEM micrograph in Fig. 1b shows particularly clear images of the polyhedral oxides down to very small ≈ 1-2 nm sizes in a friction stir welded and annealed condition (FSW-A); note FSW and annealing does not significantly change the number density or the average size and size distribution of the oxides relative to the baseline, as-extruded condition [15,18]. The oxides in the size range < 5 nm are mainly cubic $Y_2Ti_2O_7$ pyrochlore complex oxides

[15]. Figure 1c shows a high resolution TEM micrograph of a $Y_2Ti_2O_7$ particle. MA957 also contains fine ≈ 0.5x5 μm ferrite grains, a high dislocation density and a variety of coarser scale precipitates.
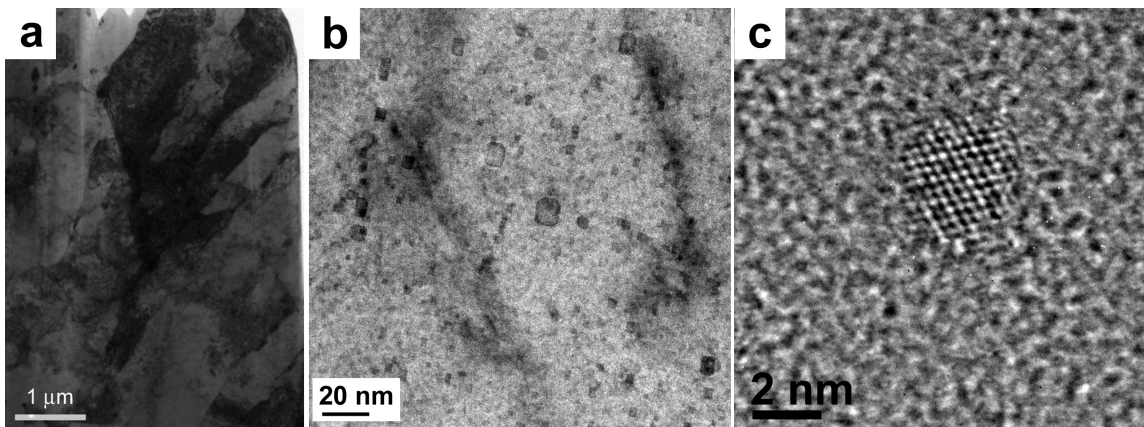
Figure 1.   a) Micrograph showing the high dislocation density and lath structure in Eurofer97; b) bright field in foil micrograph showing NF oxides in friction stirred welded and annealed MA957; and, c) a high resolution TEM image of an extracted NF oxide in MA957.

Helium is generated in fast fission and fusion environments by high energy neutron induced endoergic (n,a) reactions with threshold energies in the range of several MeV [4]. Since the energies of most of the fission neutrons are below the (n,a) threshold energy, reactor irradiations normally result in low concentrations of helium and low He/dpa [4].   In contrast the 14 MeV neutrons produced by the DT fusion reaction produce copious amounts of helium.   Thus the development of fusion structural materials will likely require a dedicated high-energy neutron source, like the International Fusion Materials Irradiation Facility (IFMIF), to carry out irradiations at a fusion relevant He/dpa ratio and dpa rate [21]. However, facilities such as IFMIF will not be available for some time.   Thus, as illustrated in Fig. 2, in the interim, we have designed and implemented a novel in situ helium implantation (ISHI) technique to produce high and controlled levels of He and He/dpa in mixed spectrum fission reactor irradiations [4,8,22,23].   The ISHI technique takes advantage of the fact that thermal neutrons in mixed spectrum fission reactors can produce helium by exoergic (n_{th},a) reactions in a limited number of isotopes, such as [10]B. The cross sections for these thermal neutron reactions are large relative to those for fast neutrons.   Thus the basic helium implantation concept is to use an implanter layer containing Ni, Li, B, or a fissionable isotope to inject high-energy a-particles from the (n_{th},a) reactions into an adjacent material of interest that is simultaneously undergoing fast neutron-induced dpa damage. In the case of Ni, the helium is generated by two-step reactions: [58]Ni(n_{th},g)[59]Ni(n_{th},a). In this study, we have used a thin NiAl layer to uniformly deposit 4.8 MeV a-particles up to a depth of 5-8 μm in the Fe based alloys, depending on the implanter layer thickness. The He/dpa ratio in the ISHI method can be controlled by varying the injector layer thickness, the concentration of the isotope that undergoes the (n_{th},a) reaction, and the thermal to fast neutron flux ratio [4,8,21,22]. Note [59]Ni must be bred from [58]Ni; thus for the Oak Ridge National Laboratory High Flux Isotope Reactor (HFIR) thermal to fast flux ratio, the helium generated in pure Ni increases from < 1 appm He/dpa, at very low

fluence, to a very broad maximum of ≈ 520 appm He/dpa aound 40 dpa. In this study, ≈ 1 to 4 μm NiAl implanter layers were electron beam deposited on TEM foils and extensively characterized prior to irradiation [24]. The HFIR ISHI experiments to date include a large matrix of Fe-based alloys covering a wide range of dpa, He/dpa (<1 to >50 appm He/dpa) and irradiation temperatures (300 to 500°C) [24].   The helium contents were estimated based on TEM measurements of the implanter layer thickness and composition.

Here we describe new data on the contrasting cavity distributions observed in the TMS, Eurofer97, and the NFA, MA957, following irradiation at 500°C to a neutron fluence of 25 dpa nominally producing ≈ 1400 to 1500 appm He. This helium content is more than two-thirds of the projected maximum end-of-life concentration expected to accumulate in an aggressive demonstration fusion reactor. Note that the nominal He/dpa ratio in HFIR is ≈ 56 to 60 appm/dpa, which is higher than the ≈ 10 appm/dpa in fusion spectra. The higher He/dpa in this study may decrease the incubation dpa (dpa*) for void formation, and may increase the helium bubble density to some extent relative to fusion conditions. However, the subsequent swelling is controlled primarily by the accumulation of dpa, and not the additional helium or the higher He/dpa ratio.

TEM specimens were prepared by focused ion beam micromachining (FIBing) at a low final current of 5.5 pA and voltage of 2 keV. The cavities were characterized using through-focus sequence imaging. They appear as white regions surrounded by a dark ring in the under-focused condition (typically -500 to -1000 nm) and as dark regions surrounded by white rings in the over-focused condition. Cavities were identified by careful comparative image analysis of the under and over-focused micrographs. Cavities were not observed in un-implanted regions, consistent with the well-known high swelling resistance of Eurofer97 and F82H in the absence of sufficient helium. The absolute diameters of the bubbles cannot be determined precisely, especially at small sizes, without detailed corrections. The cavity diameters reported here are the nominal values for the white spot diameter in the under-focused condition. Foil thicknesses were determined by convergent beam electron diffraction.

RESULTS AND ANALYSIS

We previously reported in situ helium implantation results for irradiations up to ≈ 9 dpa and 380 appm He [8,11].   Here, we first briefly summarize the key results of characterizing the TMS and NFA used in this study. We next describe the results of the in situ helium injection experiment, contrasting the behavior of the TMS and NFA. The bubble size distribution and an equation of state are used to estimate the helium content of the bubbles in MA957. Finally we use simple rate theory concepts to examine and extrapolate the significance of these new results.

$$^{58}Ni + n_{th} \longrightarrow \, ^{59}Ni + \gamma$$
$$^{59}Ni + n_{th} \longrightarrow \, ^{56}Fe + \, ^{4}He \; (4.76 MeV)$$

n_{th}

n_{th}

α

Ni

α

specimen

substrate

Ni (B, Li.) layer
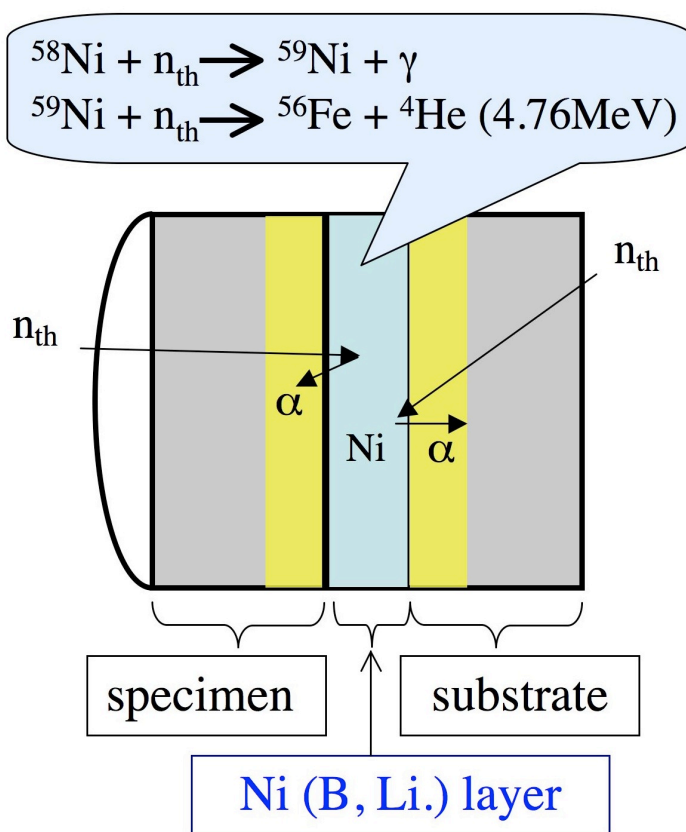
Figure 2. Schematic illustration of the ISHI method.

Figure 3a and b shows a typical example of through focus sequence micrographs for Eurofer97 and Figure 3c and d show the corresponding micrographs for MA957. Figure 4 shows the corresponding cavity size distributions. Clearly, the differences in the cavity size distributions in the two alloys are profound. Eurofer97 contains a bi-modal cavity size distribution, consisting of small bubbles and larger growing voids, with an apparent pinch-off size at d ≈ 2 nm. As previously observed, the voids are polyhedral, with low index facets that minimize the total surface energy. Assuming that the pinch-off marks the critical size, d*= 2r*, the bubbles and voids represent ≈ 52 and 48% of the total of ≈ 7.5×10^{22}/m³ cavities in Eurofer97, respectively. The corresponding average diameters, <d>, are ≈ 1.2 nm (bubbles) and ≈ 5 nm (voids). Helium inventory balances, as described for MA957 below, clearly show that the total helium content in the in situ helium implantation irradiated Eurofer97 is far too low for the larger, <d> = 5 nm cavities to be pressurized bubbles. Comprehensive examinations (not shown) suggest that the bubbles are primarily located on dislocations, or at least at the previous locations of dislocations, as well as on lath boundaries and carbide interfaces. The total swelling in Eurofer97 of about 0.5% is almost all due to the voids.

In contrast, there is a much higher density of helium bubbles, ≈ 7.8×10^{23}/m³, in the NFA MA957 with <d> ≈ 1.3 nm, and no voids. The bubbles are uniformly distributed

throughout the matrix In this case, presumably in association with small oxides. Other bubbles are more clearly visible on the interfaces of larger precipitates.
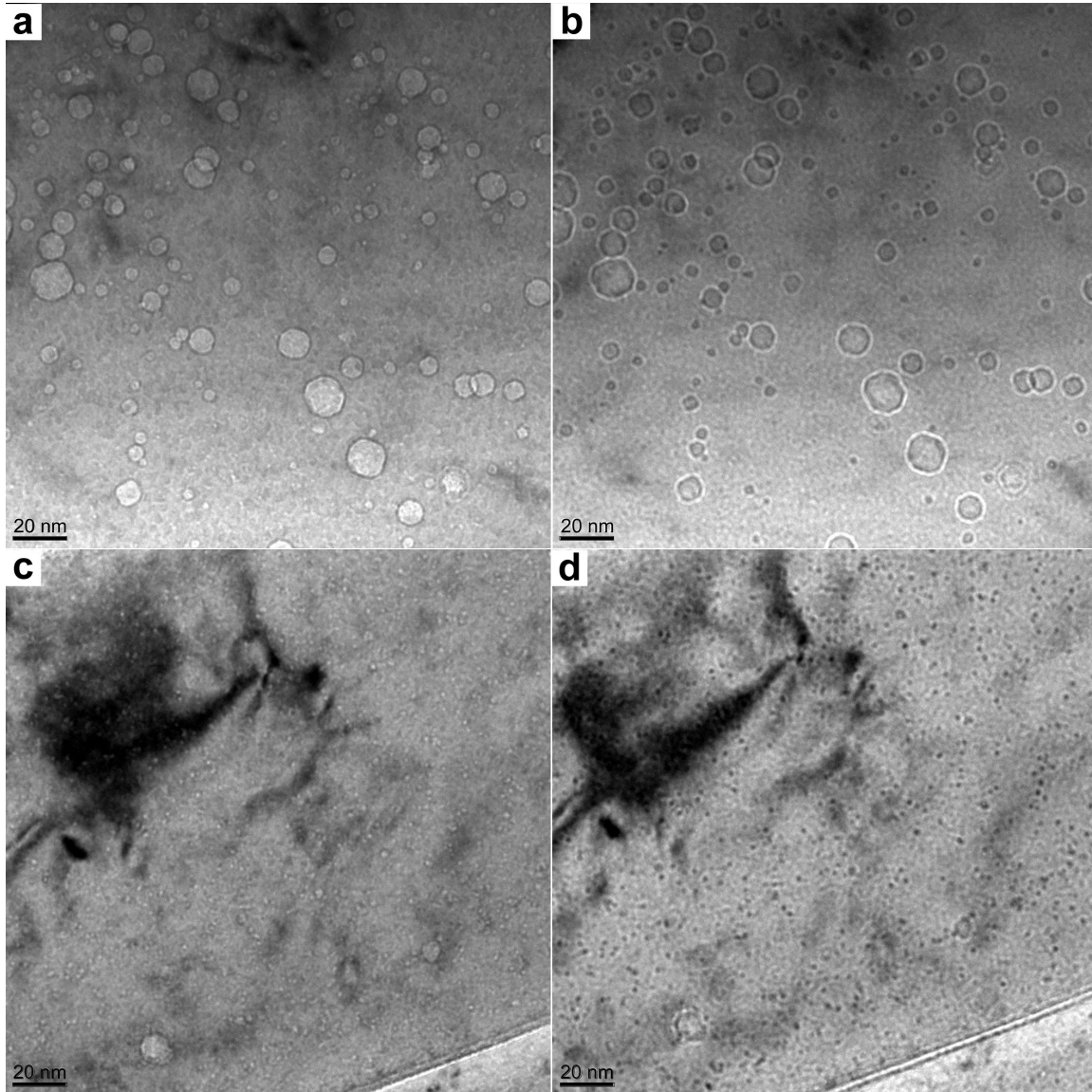
Figure 3. a and b) Under- and over-focused images of cavities in Eurofer97; c and d) under- and over-focused images of cavities in MA597.

It is useful to estimate the helium content of the bubbles in MA957. Assuming the simple capillary approximation for the helium gas pressure [25], p, is

$$p \approx 2g/r_b \approx [3zmkT]/[4\pi r_b^3].$$ [1]

Here g is the surface energy and z(p) is the helium compressibility factor. The concentration of helium atoms in the bubbles can be estimated as

$$He_{tb} \approx [8\pi g/3N_a kT]_{S_i}[N_{bi}r_i^2/z(r_i)]. \qquad\qquad [2]$$

The r_i and N_{bi} are the nominal radius of the i'th bubble size and number density, respectively; N_a is the number of atoms/m^3. Taking g = 2.5 J/m^2 and determining z(p) from a hard sphere high pressure equation of state [25], the estimated $He_{tb} \approx 1170$ appm, in reasonable qualitative agreement with the nominal total estimated helium content. However, this estimate is subject to various uncertainties. Briefly, the bubbles may be somewhat smaller than the nominal size determined in the under-focused condition [26,27], and the continuum equation of state may overestimate the He/V ratio and the He_{tb} in small bubbles [28]. However, as shown in Figure 5, the predicted helium density (He/nm^3) is in fair agreement with measurements obtained from electron energy loss spectroscopy (EELS) at small bubble sizes [29]. Further, lower values of g and contributions from invisible bubbles would lead to higher estimates of He_{tb}. Note, thermodynamic and kinetic considerations suggest that it is unlikely that a significant amount of helium remains in solution at 500°C.
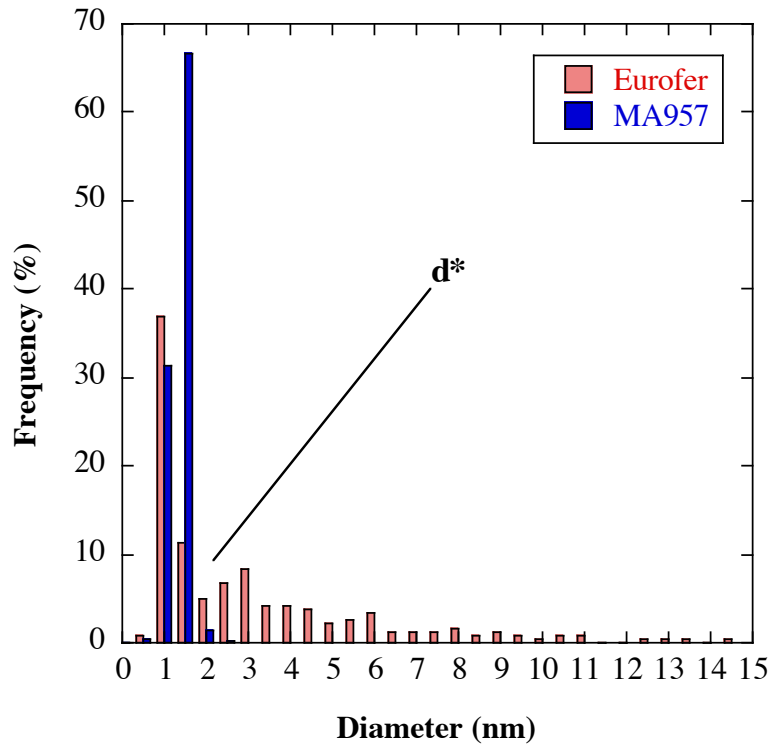
Figure 4. Comparison of the size distributions in Eurofer97 and MA957 irradiated to similar dpa and helium concentrations.

A simplified form of rate theory was used to assess the swelling resistance of the NFA based on scaling arguments, rather than a detailed numerical assessment [4]. In this framework, the effective vacancy super-saturation, L > 1, is the ratio of the net vacancy flux (vacancies minus SIA) at unbiased (neutral) sinks to the corresponding thermal vacancy flux in the absence of irradiation, where the latter is controlled by the self-diffusion coefficient, D_{sd}: L = $(D_v X_v - D_i X_i)/D_{sd}$. The critical helium content m* scales with $1/[\ln(L)]^2$. Hence for small L-1, m* scales as $1/[L-1]^2$. In the simplest case prior to the conversion of bubbles to voids, and neglecting other sinks, L-1 can be expressed in terms of the sink strengths for bubbles and dislocations, Z_b and Z_d, respectively, and a bias factor of dislocations for SIA (B). For B << 1, L-1 scales with $Z_d/[Z_b+Z_d]^2$. The sink strength for 7.5×10^{22}, 1.2 nm bubbles in Eurofer97 is $Z_b \approx 5.6\times10^{14}/m^2$ and $Z_b \approx 6.4\times10^{15}/m^2$ for the 7.8×10^{23}, 1.3 nm bubbles in MA957. A reasonable nominal value for the dislocation sink density is $Z_{rd} \approx 5\times10^{14}/m^2$ in both cases. Based on these values, m*[MA957]/m*[Eurofer97] ≈ 900. Since the helium is divided into ≈ 10 times more bubbles in MA957 compared to Eurofer97, the corresponding ratio of the incubation dpa, dpa*[MA957]/dpa*[Eurofer97], needed to form a significant population of voids would be even larger.
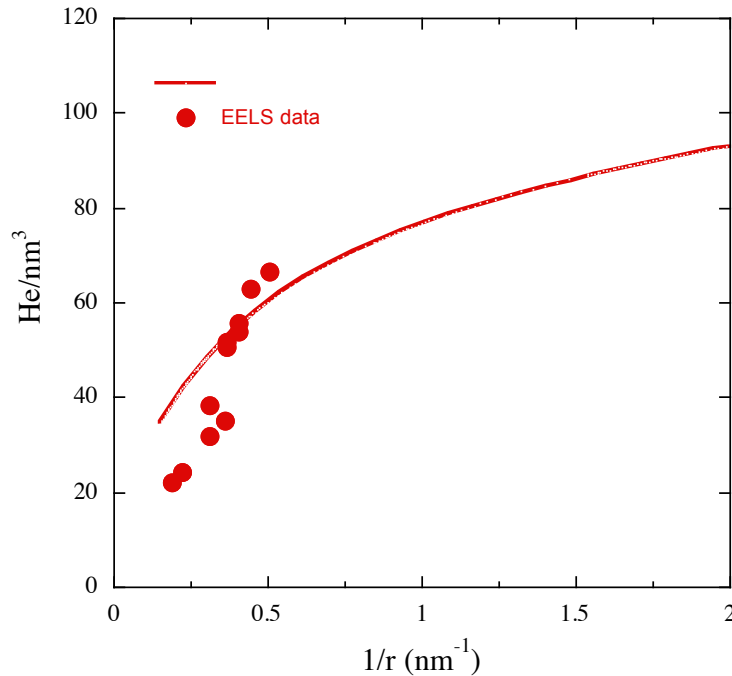
Figure 5. The EOS helium density compared to EELS measurements reported in the literature [29].

While the numerical values derived from these simple rate theory based scaling assessments should not be taken too seriously, they illustrate that persistent swelling resistance associated with a large population of small bubbles in NFA is to be expected. The critical bubble model and simple rate theory concepts can also be used to

approximately extrapolate these results to higher helium and dpa. Assuming no new bubbles are formed in MA957, then 2000 appm helium would increase the average bubble diameter from the nominal average of ≈ 1.3 to ≈ 1.5 nm, which is still well below the estimated r* and m* for the high bubble sink density in MA957. Note that in principle, the defect fluxes driving other irradiation effects are also reduced with increasing total sink strength; and the fraction of helium reaching grain boundaries would be likewise diminished at high bubble densities.

The prognosis for TMS swelling resistance at higher helium and dpa levels is much less promising. Higher helium would convert more bubbles to voids. A void (converted from bubbles) to dislocation sink strength ratio that is close to being balanced (≈ 0.5 to 2) would lead to an approximately maximum swelling rate [2,4]. A previous ISHI irradiation at 500°C of TMS F82H showed that voids begin to form at ≈ 200-400 appm He (9), and the results reported here further show they are the dominant sink at ≈ 1500 appm He. Once formed, the voids continue to grow with increasing dpa. Notably, helium plays a much smaller role in the post-incubation swelling regime. Garner has argued that the steady state swelling rate in bcc steels is about 0.2%/dpa [30]. Assuming this swelling rate, and that for fusion relevant conditions a large population of voids form by 1000 appm He and 100 dpa, then at 200 dpa the total swelling in TMS would reach a clearly intolerable level of more than 20%. Practical swelling limits would probably be much lower.

Thus this work leads two very important *proof of principle* conclusions: a) the helium rich fusion environment will limit extended service of TMS alloys at intermediate temperatures; and, b) NFA can manage helium and manifest persistent damage resistance, greatly extending the potential lifetimes of fusion structures.

SUMMARY AND CONCLUSIONS

The helium content in the present HFIR in situ helium implantation experiment is more than two-thirds of the end-of-life levels projected for fusion first wall and blanket structures. Key conclusions from this study include:

- The in situ helium implantation method provides a powerful new tool for characterizing the effects of He-dpa synergisms on microstructural evolutions in virtually any material.

- High helium contents promote the formation of a large population of voids in TMS that would be largely absent at lower helium and He/dpa levels.

- Essentially the same amount of helium is sequestered in a very high density of nm-scale bubbles in NFA, with no voids present.

- Simple rate theory scaling extrapolations suggest that NFA will remain irradiation damage tolerant up to much higher dpa and helium levels.

- In contrast, extrapolations for TMS suggest that the observed voids are precursors to significant void swelling at higher dpa, leading to the conclusion that TMS will not be suitable for service to 200 dpa in fusion first wall structures.

The results reported here will be extended to a much wider range of temperatures, dpa, He/dpa ratios and alloys based on the large existing and future matrix of ISHI irradiation conditions. Detailed models also being developed to assess the transport, fate and

consequences of helium are broadly consistent with the crude estimates of the behavior of NFA and TMS outlined above [31].

Finally, it is important to note that NFA are in a very early stage of development and qualification for fusion, advanced fission and other hostile service applications. However, we believe that their immense promise warrant a major science based research effort.

ACKNOWLEDGMENTS

REFERENCES

[1]   S. J. Zinkle and J. T. Busby, *Mater Today* (2009)**12**:12.

[2]   G. R. Odette, M. J. Alinger, and B. D. Wirth, *Annu. Rev. Mater. Res.* (2008) **38**:471.

[3]   G. R. Odette and D. T. Hoelzer, *JOM* (2010) 62:84.

[4]   Y. Dai, G. R. Odette, and T. Yamamoto, Comprehensive Nuclear Materials, Chapter 6, "The Effects of Helium in Irradiated Structural Alloys," 2012; in press.

[5]   T. Yamamoto, G. R. Odette, M. Salston, P. Miao, and Y. Dai, Trans. Am. Nucl. Soc. *(2008) 98:1111.*

[6]   T. Yamamoto, G. R. Odette, H. Kishimoto, J-W. Rensman and P. Miao, *J. Nucl. Mater.* (*2006*) **356**:27.

[7]   G. R. Odette, T. Yamamoto, H. J. Rathbun, M. Y. He, M. L. Hribernik, and J. W. Rensman, *J. Nucl. Mater. (2003)* **323**:313.

[8]   T. Yamamoto, G. R. Odette, P. Miao, et al., *J. Nucl. Mat*. (2009) **386:**338.

[9]   M. K. Miller, D. T. Hoelzer, E. A. Kenik, and K. F. Russell, *J. Nucl. Mater.* (2004) **329**:338.

[10]   N. J. Cunningham, et al., "Long-Term Thermal Aging Effects on the Microstructure of Ferritic Alloy MA957," in preparation.

[11]   G. R. Odette, P. Miao, D. J. Edwards, et al., *J. Nucl. Mater.* (2011) **417**:1001.

[12]   R. J. Kurtz, A. Alamo, E. Lucon, et al., *J. Nucl. Mater.* (2009) **386**:411.

[13]   H. E. Hofmans, NRG Report 20023/00.38153/P, 2000, Petten, The Netherlands.

[14]   M. J. Alinger, G. R. Odette and D. T. Hoelzer, *Acta Mater.* (2009) **57**:392.

[15]   Y. Wu, E. Haney, N. Cunningham and G. R. Odette, "Transmission Electron Microscopy Characterization of the Nanofeatures in Nanostructured Ferritic Alloy MA957," submitted to *Acta Mater.* (2011) under review.

[16]   J. J. Fisher, U.S. Patent No. 4,075,010, 1978.

[17]   H. L. Hamilton, D. S. Gelles, R. J. Lobsinger, G. D. Johnson, W. F. Brown, M. M. Paxton, R. J. Puigh, C. R. Eiholzer, C. Martinez, and M. A. Blotter, Technical Report, PNL-13168, 1991.

[18]   A. Etienne, N. J. Cunningham, Y. Wu, et al., *Mat. Sci. Tech.* (2011) **27-4**:724.

[19]   N. J. Cunningham, G. R. Odette, E. Stergar et al., DOE Fusion Materials Semiannual Progress Report, June 30, 2011; DOE/ER-0313/50: in press.

[20]   D. T. Hoelzer, J. P. Shingledecker, R. L. Klueh et al., Fusion Materials Semiannual Report 6/30/2010 2011; DOE/ER-313/48:50.

[21]   P. Garin and M. Sugimoto, *Fusion Eng. Des.* (2008) **83**:971.

[22]   G. R. Odette, *J. Nucl. Mater.* (1986) **141**:101.

[23]   L. K. Mansur and W. A. Coghlan, **"**Effects of Radiation on Materials": 14th International Symposium 1989 ASTM STP 1046; 2:315.

[24]   T. Yamamoto, G. R. Odette, and L. R. Greenwood, Fusion Materials Semiannual Report 6/30/2005 2005; DOE/ER-313/38:95.

[25]   R. E. Stoller and G. R. Odette, *J. Nucl. Mater.* (1985) **131**:118.

[26]   M. Ruhle and M. Wilkens, *Cryst. Latt. Defects* (1975) **6**:129.

[27]   X. Zhang, E. G. Fu, A. Misra, and M. J. Demkowicz**,** *JOM* (2010) **62-12**:75

[28]   D. Stewart, Y. Osetskiy, and R. E. Stoller, *J. Nucl. Mater.* (2011) **417**:1110.

[29]   S. Fréchard, M. Kociak, M. Walls, J. P. Chevalier, J. Henry, and D. Gorse, *J. Nucl. Mater.* (2009) **393**:102.

[30]   F. A. Garner, M. B. Toloczko, and B. H. Sencer, *J. Nucl. Mater.* (2000) **276**:123.

[31]   T. Yamamoto, G. R. Odette, R. J. Kurtz, and B. D. Wirth, Fusion Materials Semiannual Report 12/31/2010 2011; DOE/ER-313/49:73.

8.1   Nucleation of He Bubbles at Grain Boundaries of α-Fe — L. Yang, F. Gao, H. L. Heinisch and R. J. Kurtz (Pacific Northwest National Laboratory)[*]

This is the Extended Abstract for a paper in preparation for journal submission.

The formation of He bubbles in bulk or at grain boundaries (GBs) has major consequences for the structural integrity of first-wall materials. To gain insight into He effects, the accumulation of He atoms and nucleation of He bubbles in a Σ3<110>{112} GB of α-Fe is being studied using molecular dynamics with our newly developed Fe-He potential [1]. It is found that the accumulation of He atoms, the formation of He bubbles, and the evolution of the GB structure all depend on the He concentration and temperature. When a He concentration of 1% is introduced within the GB region at temperatures higher than 600 K, small He clusters are formed, and a few Fe self-interstitial atoms (SIAs) are emitted from the He clusters. The SIAs easily migrate to the nearby atomic planes and form <111> crowdions. At a He concentration of 5%, a few large He clusters are found, in platelet form, and dislocations are also formed at the peripheries of these large He clusters. At 10% He concentration the atomic structure of the GB is significantly changed due to the formation of large He clusters, and the large number of SIAs that are emitted can rearrange to form an extra atomic plane within the GB, resulting in the self-healing of the deformation induced by He accumulation and the GB climbing along the $[\bar{1}12]$ direction.

For this initial study, a Σ3<110>{112} GB has been employed to investigate the nucleation and growth of He clusters. He atoms are inserted randomly within 8 atomic layers near the GB at the He concentrations of 1%, 5% and 10%, which are the ratios of the number of He atoms to Fe atoms within the considered atomic layers. After He insertion, the cell was quenched to 0 K for 10 ps to achieve the minimum energy configuration, followed by a temperature rescaling to the required temperature. During the MD simulations at 300 K, almost all He atoms aggregate to the GB plane, and a few small He clusters are formed (He_n n=2-6). The emission of SIAs is not observed for these small clusters, but the displacements of the surrounding Fe atoms increase with the increasing size of the clusters.

The final distribution of He interstitials at 5% at 800 K is shown in Figure 1, from which it is clearly seen that some large He clusters are formed, and they exhibit platelet-like structures. Also a number of SIAs are emitted from the clusters, and they collect at the periphery of the large He clusters. It is of interest to note that the number of the collected SIAs is sufficiently large so as to lead to the formation of dislocation loops (see the insets in Figure 1). The population of these dislocation loops increases with increasing simulation time, and they are distributed at the periphery of the He clusters.

When the He concentration increases to 10%, many He clusters are formed after the simulation cell is quenched to 0 K, and some SIAs near the He clusters are spontaneously created due to the high He concentration. Similar to the simulations at lower concentrations, He atoms rapidly diffuse to the GB plane during the MD simulations at all the temperatures considered and form many larger He clusters with platelet-like structures. As a result, a large number of SIAs are

created. It is of interest to see that these SIAs do not cause a large deformation of the GB, and the atomic arrangements of the GB are similar to those of the original structure without He atoms. To understand this, the evolution of the GB structure as a function of the simulation time is explored. Figure 2 shows several snapshots of the GB structure simulated at 300 K, but includes only Fe atoms for clarification. The atomic plot at 3 ps shows that the GB structure is largely deformed and highly disordered. Longer time MD simulations clearly indicate that these disordered Fe atoms within the GB start to reconstruct at 10 ps, forming an extra atomic layer which is above the original GB plane. It is also observed that some single He atoms and small He clusters migrate quickly within the GB plane and are absorbed by the large He clusters at 300 K. At 1 ns, it can be clearly seen that a perfect GB plane forms, and the crystal heals itself by SIA accumulation and atomic reconstruction. It is of great interest to note that the GB plane climbs up one atomic plane along the $[\bar{1}\,12]$ direction, as shown at 1 ns in Figure 2.
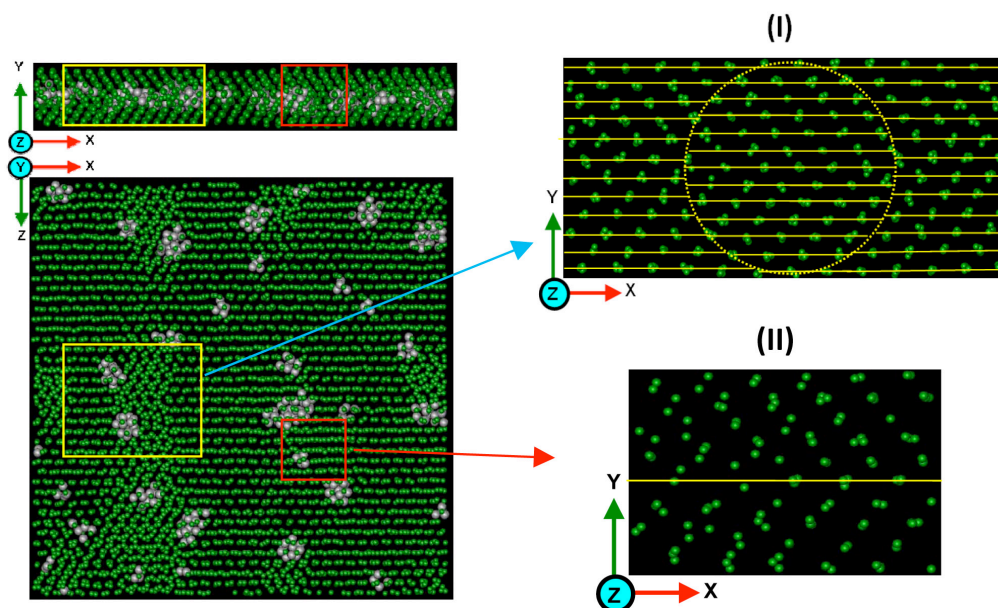
Figure 1. Final atomic configurations of Σ3 GB with a 5 % He concentration at 300 K in α-Fe. The He atoms are omitted from the inset figures I and II.
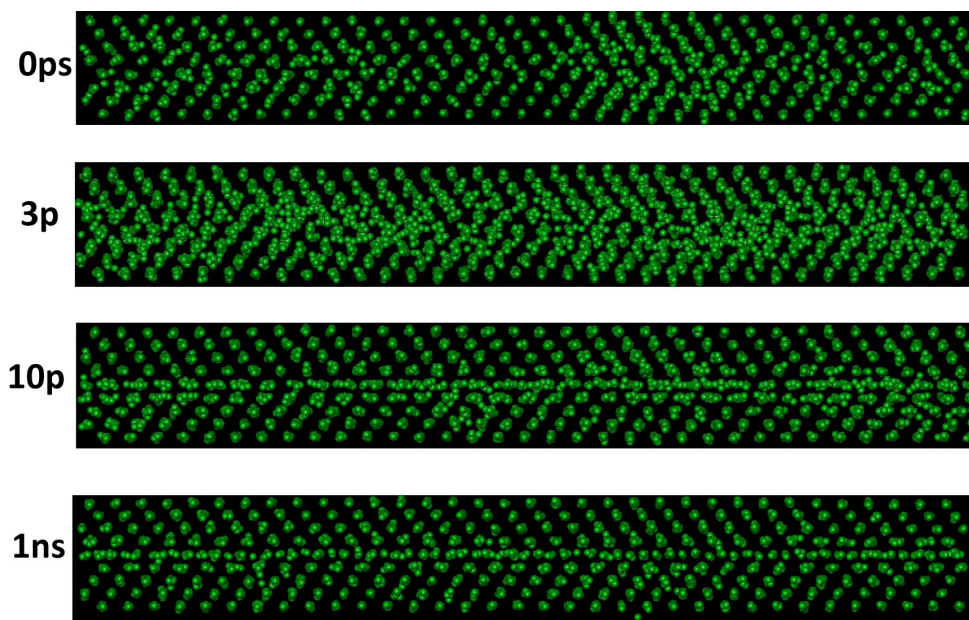
Figure 2. Four snapshots showing the structural evolution of the S3 GB with a 10% He concentration in a-Fe at 300 K, where the simulation time is indicated in each plot.

REFERENCE

[1] F. Gao, H. Q. Deng, H. L. Heinisch, R. J. Kurtz, *J. Nucl. Mater.* **418** (2011) 115.

8.2 Simulation of Ballistic Resolutioning of Helium from Bubbles in Iron by Molecular Dynamics — R. E. Stoller (Oak Ridge National Laboratory)

OBJECTIVE

The objective of this research is to develop an understanding of the mechanisms and processes that control the evolution of helium-stabilized cavities in fusion structural materials.

SUMMARY

Helium generation and accumulation is important under DT fusion irradiation conditions. Ballistic resolutioning of He from bubbles could limit bubble growth by ejecting gas atoms back into the metal matrix. Molecular dynamics simulation has been used to study this process in iron as a surrogate for structural materials. A newly developed Fe-He interatomic potential was employed. The primary variables examined were: irradiation temperature (100 and 600K), iron knock-on atom energy (5 and 20 keV), bubble radius (~0.5 and 1.0 nm), and He-to-vacancy ratio in the bubble (0.25, 0.5 and 1.0). Helium ejection by high-energy iron recoils was clearly observed on a time scale consistent with a ballistic mechanism. The results are summarized.

 PROGRESS AND STATUS

Introduction

The evolution of gas-stabilized bubbles in irradiated materials is inherently a dynamic process, involving a balance of growth and shrinkage mechanisms. Simplistically, the bubble volume will grow in units of atomic volume by absorbing vacancies and shrink by either emitting vacancies or absorbing interstitials. Absorption or emission of gas atoms will also change the bubble volume, although the incremental change is generally less than an atomic volume. The absolution volume change is dependent on the ratio of gas atoms to vacancies (i.e. pressure) in the bubble. In addition to the thermal and kinetic processes such as diffusion that lead to He absorption and emission from bubbles, the potential for high-energy recoils to remove gas atoms from bubbles has also been discussed and, to a limited extent, investigated [1-3]. This ballistic resolutioning mechanism is illustrated in Fig. 1. The conditions investigated in the present study are summarized in Table 1, and extend range of results of obtained previously and in Ref. 2. A more complete report on the results is being prepared for publication in the Journal of Nuclear Materials based on a presentation at the 15th International Conference on Fusion Reactor Materials.
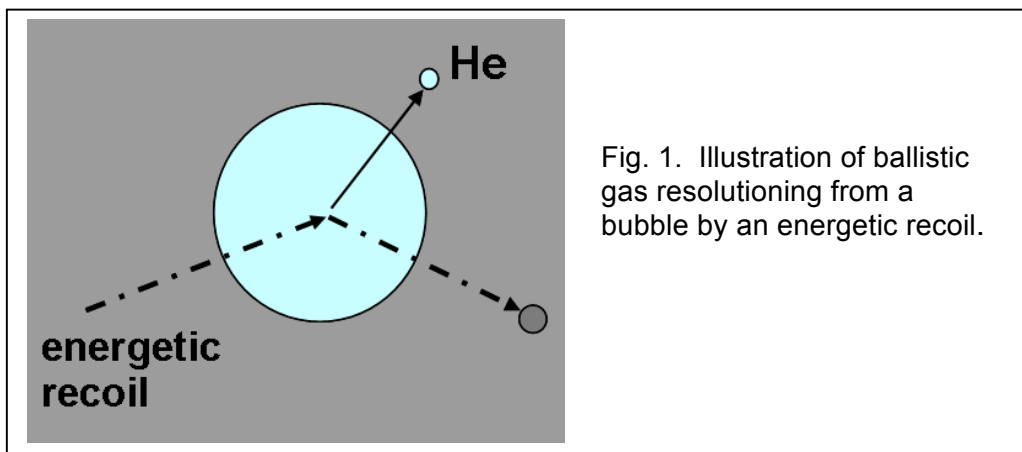
Fig. 1. Illustration of ballistic gas resolutioning from a bubble by an energetic recoil.

Table 1. Simulation conditions investigated				
Temperature (K)	Cascade energy (keV)	Bubble size		He to vacancy ratio
		Number of vacancies	Radius (nm)	
100	5	40	0.48	0.25, 1
	5	339	1.0	0.25, 0.5, 1
	20	40	0.48	0.25, 1
	20	339	1.0	0.25, 0.5, 1
600	5	40	0.48	0.25, 1
	5	339	1.0	0.25, 0.5, 1
	20	40	0.48	0.25, 1
	20	339	1.0	0.25, 0.5, 1

Approach

The basic computational approach employed in this investigation follows that published previously [2]. A newly developed Fe-He interatomic potential has been employed [4-6], with the iron matrix described by the potential of Ackland and co-workers from 1997 [7]. Constant pressure, periodic boundary conditions were employed in a cubic simulation cell of 70 or 80 lattice parameters, corresponding to 686k or 1024k atoms. Before initiating a ballistic event, a bubble of the desired size was created by removing the necessary number of iron atoms in an approximately spherical volume, and the number of helium atoms required to obtain the desired He-to-vacancy ratio shown in Table 1 were placed within the volume. Then, the atom block was thermally equilibrated at the specified temperature for approximately 25 ps. Consistent with the strong He-He and He-vacancy binding observed in previous work with these potentials, no thermal resolutioning was observed. The equilibrated atom configuration was saved and used as the starting point for the subsequent simulations. The ballistic cascade simulations were initiated by giving one of the Fe atoms located near the bubble a defined amount of kinetic energy and an initial direction oriented toward the bubble. Based on previous experience with the statistical nature of cascade simulations, between ten and twenty simulations were carried out for each of the conditions listed in Table 1, with variability ensured by the different PKA locations and in some cases by further equilibration of the starting configuration.

Each MD cascade simulation was continued until variables such as the number of defects, and the average kinetic and potential energy had stabilized for a few ps. The time required to reach this new pseudo-equilibrium depended on the PKA energy and irradiation temperature, varying between about 15 to 25 ps. The final atom configuration was then characterized by locating the He atoms and measuring the distance between any ejected He atoms and the

initial bubble surface, and by counting the number and distribution of the point defects (vacancies and interstitials) created by the cascade.

Results

The results are summarized in Figures 2 and 3. The red, blue, and green curves in Fig. 2 show the total number of He atoms displaced from the bubble surface by at least 1 lattice parameter, more than 10 lattice parameters, and between 5 and 10 lattice parameters, respectively. The rapid evolution of helium resolutioning is quite clear with the maximum number of He atoms ejected being reached by <40 fs. This time is quite short on the time scale of displacement cascade evolution in which the peak number of displaced atoms is not reached until >0.5 ps. This is shown by the black curve in Fig. 2, which plots the number of Frenkel defects created. This number is still increasing rapidly well after the number of He ejected has saturated. This is in contrast to the results observed by Parfitt and Grimes [3] for He bubbles in UO_2, where a delayed emission process was observed that arose from thermal mixing near the bubble surface.

Fig. 2.   Time dependence of He ejection from a 1 nm bubble and point defect formation in a 5 keV cascade at 100K. He/vacancy ratio is 1.0.
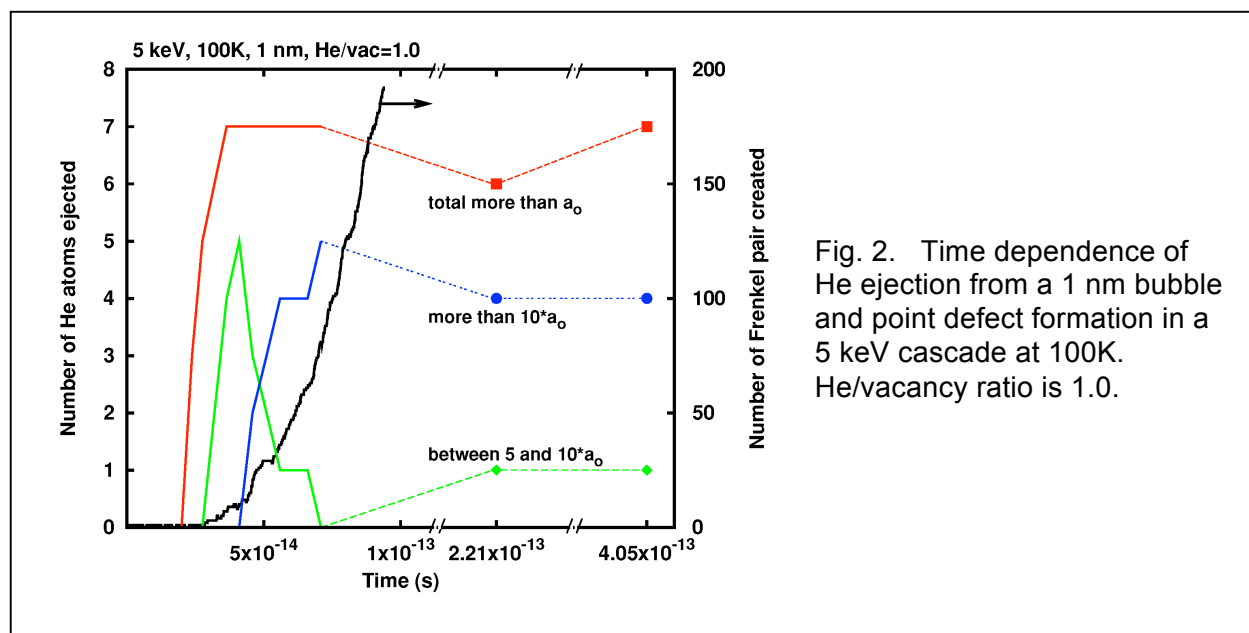
The dependence of He resolutioning on the irradiation conditions are shown in Fig.3 for a 1 nm bubble size (339 vacancies). The data points indicate the mean value and the error bars are the standard error of the mean. The trends are quite clear. At both 100 and 600K there is less resolutioning from 20 keV cascades than from 5 keV cascades. This seems somewhat counter-intuitive, but us a result of the reduced elastic scattering cross section as the particle energy increases. At either cascade energy, resolutioning is reduced at the higher temperature. This is consistent with the greater thermal motion of the He atoms making it more difficult for collisions which transfer large amounts of energy in elastic collisions. Lastly, it is clear that bubble pressure, represented by the He/vacancy ratio, has a strong influence of the number of He atoms ejected.

FURTHER WORK

Ongoing analysis of these results will provide guidance for developing ballistic resolutioning parameters that can be employed in reaction rate theory models of He-vacancy cluster dynamics. The use of atomistic-based resolutioning parameters will improve the fidelity of the higher length and time scale models used to predict microstructural evolution and the swelling and hardening produced by cavities in irradiated materials.
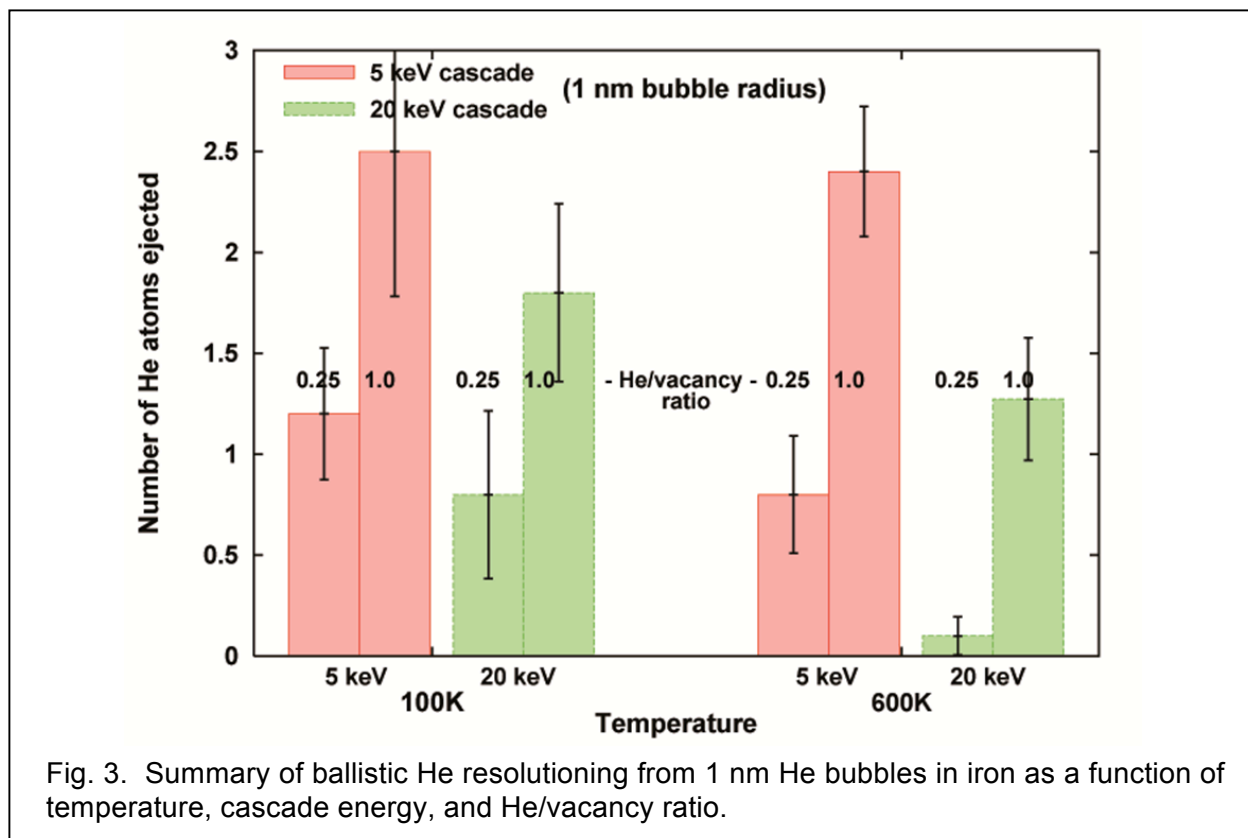
Fig. 3. Summary of ballistic He resolutioning from 1 nm He bubbles in iron as a function of temperature, cascade energy, and He/vacancy ratio.

REFERENCES

1. D. R. Olander, "Fundamental Aspects of Nuclear Reactor Fuel Elements," U.S. Technical Information Center, Energy Research and Development Administration, 1976.
2. R. E. Stoller and D. M. Stewart, *J. Nucl. Mater.* **417** (2011) 1106-1109.
3. D. C. Parfitt and R. W. Grimes, *J. Nucl. Mater*. **381** (2008) 216–222.
4. R. E. Stoller, S. I. Golubov, P. J. Kamenski, T. Seletskaia, and Yuri N. Osetsky, *Phil. Mag.* **90** (2010) 923-934.
5. D. M. Stewart, Yuri N. Osetsky, R. E. Stoller, S. I. Golubov, T. Seletskaia, P. J. Kamenski, "Atomistic Studies of Helium Defects Properties in BCC Iron: Comparison of He–Fe Potentials," *Phil. Mag. 90* (2010) 923.
6. D. M. Stewart**,** Yuri N. Osetskiy, and R. E. Stoller**, "**Atomistic Studies of Formation and Diffusion of Helium Clusters and Bubbles in BCC Iron*, J. Nucl. Mater.* **147** (2011) 1110-1114**.**
7**.** G. J. Ackland, D. J. Bacon, A. F. Calder, and T. Harry, *Phil. Mag. A* **75** (1997) 713-732.

8.3 Effect of Anisotropy, SIA Orientation and One-Dimensional Migration Mechanisms on Dislocation Bias in Irradiation Metals — D. Seif and N. M. Ghoniem (University of California, Los Angeles)

This is the Abstract for an ICFRM-15 paper submitted for publication in the Proceedings.

Swelling in metals exposed to neutron irradiation has long been known to be enhanced by the preferential absorption of interstitials rather than vacancies, to dislocations. A common measure of this preference is called the dislocation bias factor and is computed from the ratio of capture efficiencies of dislocations to interstitials and vacancies. Bias factors calculated through analytical and numerical means have been known to be approximately an order of magnitude larger than those expected by empirical swelling data. While this discrepancy has been justified by some in the past, it has remained an issue of debate among many. A major issue that has not been explored, however, is the effect of the numerous assumptions and approximations in previous studies. In this study, we explore the effect of three major assumptions of past studies. First, anisotropy in the displacement fields of both point defects and dislocations is accounted for in our calculations. This relieves the assumption that self-interstitial atoms (SIA) are centers of dilatation in isotropic media. Secondly, since SIAs have energetically preferred <110> orientations in dislocation stress fields, we use a spatially dependent elastic dipole tensor that accounts for preferred orientations. Lastly, since SIAs are known to undergo fast 1-D migration in the Burgers direction in the vicinity of dislocations, we specify a fraction of SIAs to migrate one-dimensionally using a modified SIA diffusion tensor. These attributes are implemented into a combined finite-element method (FEM) rate-theory (RT) approach to calculate dislocation bias factors in bcc iron and fcc copper. Our results show a significant increase in the bias when anisotropy and preferred SIA orientations are considered and decrease when SIAs undergo 1-D motion.

8.4   Dislocation vs. Production Bias Revisited with Accounted of Radiation-Induced Emission Bias: Void Swelling Under Electron and Light Ion Irradiation — V. I. Dubinko (NSC Kharkov Institute of Physics and Technology, Kharkov 61108, Ukraine), S. Y. Hu, Y. L. Li, C. H. Henager and R. J. Kurtz (Pacific Northwest National Laboratory)

This is the Extended Abstract of a manuscript submitted for publication in Philosophical Magazine & Philosophical Magazine Letters [1].

The preferential attraction to sinks of self-interstitial atoms (SIAs) over that of vacancies is the fundamental cause of the void swelling, and ultimately the evolution of microstructure in irradiated material. This preferential attraction is described mathematically in terms of bias factors that can be evaluated by solving diffusion equations for point defects (PDs) with drift terms included. The dislocation bias deduced from theory can be on the order of 0.5-1 (increasing with increasing sink strength) in a marked contrast with phenomenological values of 0.01-0.005 assumed in the early rate theory models in attempt to explain experimentally observed swelling rates [2]. Later this became one of the reasons that prompted the development of models based on production bias (PBM) as the main driver for swelling, which assumed that the dislocation bias was much lower than that predicted by theory. However, the PBM in its present form fails to account for important and common observations: the indefinite void growth often observed under cascade irradiation and the swelling saturation observed under high dose irradiation and in void lattices.

It is known that not all the energy of the primary knock-on atom (PKA) is spent for the production of stable defects. A considerable part of the PKA energy is spent for production of unstable Frenkel pairs (UFPs) [3, 4] and mobile lattice vibrations, such as focusons [5-8] and quodons [9-13], which can interact with extended defects and produce Schottky defects in their vicinity. A Schottky defect is a single vacancy or self-interstitial atom, or a small defect cluster, which can be emitted from extended defects (EDs) such as voids, dislocations and grain boundaries [14-20], and which does not require a counterpart of opposite sign in contrast to the bulk production of Frenkel pairs, in which the total numbers of vacancies and self-interstitial atoms *must be equal*. Another important difference between Frenkel and Schottky defects is the energy required for their formation. It is much lower for Schottky defects, especially for vacancies. It is well known that the Frenkel pair formation energy, $E_{FP}^{f,th}$, in metals under thermal equilibrium (when the crystal has enough time to adjust itself to the minimum free energy structure) is given by the sum of the SIA and vacancy formation energies, the former being is several times higher than the latter (e.g. in Cu, $E_{FP}^{f,th}$=3 eV, $E_{v}^{f,th}$=1.3 eV, $E_{FP}^{f,th}= E_{i}^{f,th}+E_{v}^{f,th}$=4.3 eV [21]). At the same time, the *ballistic* displacement energy required for stable Frenkel pair formation, $E_d \approx$25 eV, is much higher than the thermal value, and so it can exceed the energy of vacancy production by an order of magnitude, which should result in the biased formation of vacancies as compared to SIAs near the ED surfaces under irradiation. This biased PD formation may be called *the radiation-induced emission* of vacancies from EDs, since the number of vacancies formed at the ED surface exactly equals the number of vacancies escaped from the ED. As a result, the number of atoms in the ED immediately decreases or increases depending on the ED type. For example, the number of vacancies in a void or a vacancy loop will be *decreased* while the number of atoms in a SIA loop will be *increased* in response to this ballistic vacancy emission.

In this paper we modify the Frenkel pair 3-D diffusion model (FP3DM) with account of the radiation-induced vacancy emission from EDs and production bias. The swelling rate taking into account the absorption, emission and production biases can be expressed as [1]:

$$\frac{dS}{dt} = D_i \bar{c}_i \frac{k_{Vv}^2 k_{dv}^2}{k_v^2} B_{net} , \ B_{net} \equiv B_{ab} - B_{em} + B_p , \tag{1}$$

$$B_{ab} \equiv \frac{Z_v^V Z_i^d - Z_i^V Z_v^d}{Z_v^d} + \frac{Z_v^V k_{Gi}^2 - Z_i^V k_{Gv}^2}{Z_v^d \rho_d} , \tag{2}$$

$$B_{em} \equiv \frac{k_v^2}{k_d^2} Z_v^V \frac{\left(D_v \bar{c}_v^{eq} - D_v c_v^{eq,V} \right)}{D_i \bar{c}_i} , \tag{3}$$

$$B_p \equiv \frac{\varepsilon_i k_{eff} K}{k_{dv}^2 D_i \bar{c}_i} \left(1 - \frac{k_v^2 \bar{R}_v}{8 l_g} \right) , \tag{4}$$

where B_{net} is the net bias. B_{ab}, B_{em} and B_p are absorption, emission and production biases, respectively. B_p contains two new parameters, namely, k_{eff} and ε_i .

To demonstrate the modified model, we first evaluate the swelling rate observed in austenitic steel [2] and pure Fe-Ni-Cr alloy [22]. Figure 1 shows the comparison of the swelling rates measured and predicted by FP3DM and modified FP3DM. It can be seen that the swelling rate predicted by the modified FP3DM agrees with experimental data both qualitatively and qualitatively.
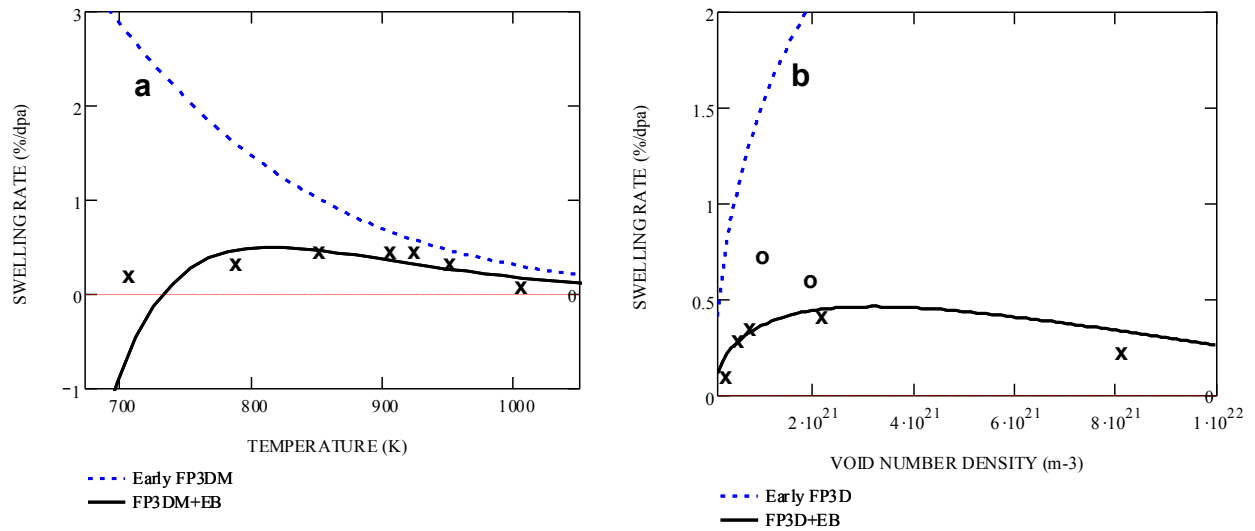
Figure 1. Dependence of the swelling rate predicted by FP3D and the modified (FP3D+EB) on temperature and the void number density vs. experimental data. Experimental data for austenitic steel [2] are shown in (a) and for a pure Fe-Ni-Cr alloy [22] in (b), where x and o represent residual gas and 10 appm pre-injected helium.

One can see in Figure 1 (a) that the modified theory predicts swelling rate to become negative below some threshold temperature, which could not be expected from early FP3D. The physical reason for this prediction is based on the decrease of the mean PD fluxes $\sim D_i \bar{c}_i$ with decreasing temperature due to more intense bulk recombination of PDs (or denser sink structure). As a result, the emission bias, B_{em}, which is inversely proportional to $D_i \bar{c}_i$, increases and prevails over the absorption bias, which should result in the void shrinkage. In order to test this prediction, one needs to produce voids at higher temperatures, and then continue irradiation at a lower temperature. Such experimental tests have been performed in several experimental setups [17-20, 23], one of which is described below. In experiments [17], nickel foils of 100 micron thickness have been irradiated with 1.2 MeV Cr ions at 873 K up to the total ion fluence of 10^{21} m^{-2}, which corresponded approximately to the irradiation dose of 25 displacements per atom (dpa) at the dose rate, $K = 7 \times 10^{-3} s^{-1}$. Examination of control samples in transmission electron microscope (TEM) has revealed formation of a high number density (~10^{21} m^3) of voids of 40-50 nm in diameter. The remaining foils have been irradiated subsequently up to the ion fluence of 10^{21} m^{-2} at two different temperatures, 798 K and 723 K, respectively. The resulting microstructure is shown in Figure 2, from which it is evident that the irradiation at lower temperatures has made the voids to <u>decrease in size</u>. The quantitative analysis of the void swelling confirms this conclusion: the void swelling has decreased by a factor of ~ 5 (Figure 3).
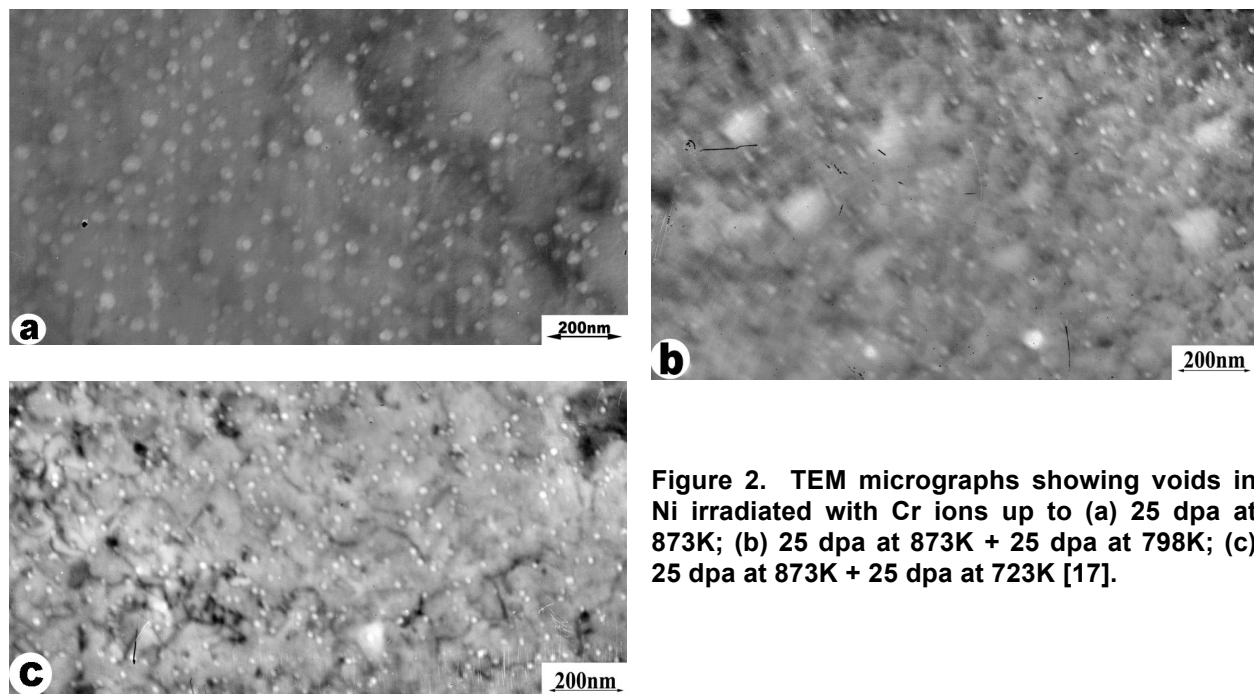
Figure 2. TEM micrographs showing voids in Ni irradiated with Cr ions up to (a) 25 dpa at 873K; (b) 25 dpa at 873K + 25 dpa at 798K; (c) 25 dpa at 873K + 25 dpa at 723K [17].
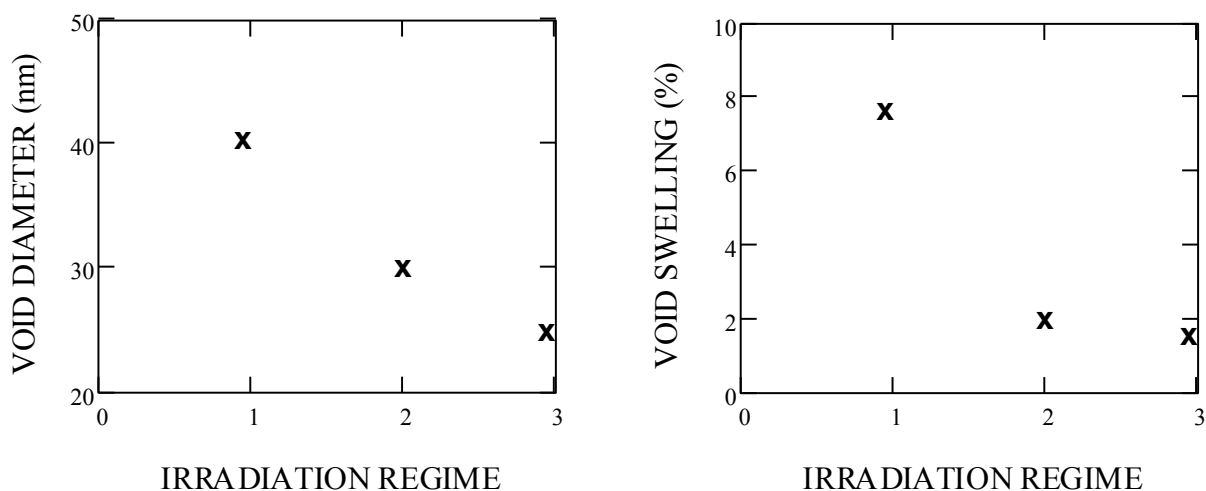
Figure 3. Mean void diameter and swelling in Ni irradiated with Cr ions up to 25 dpa at 873K (regime 1); 25 dpa at 873K + 25 dpa at 798K (regime 2) and 25 dpa at 873K + 25 dpa at 723K (regime 3). The size of symbols "x" corresponds to the mean error in void measurements [17].

Comparison of the PBM, FP3DM+EB and FP3DM+EB+PB models with experimental data [17] is shown in Figure 4. In the PBM their maximum values are estimated as follows [24, 25]: k_{eff} =0.1, ε_i = 0.2.
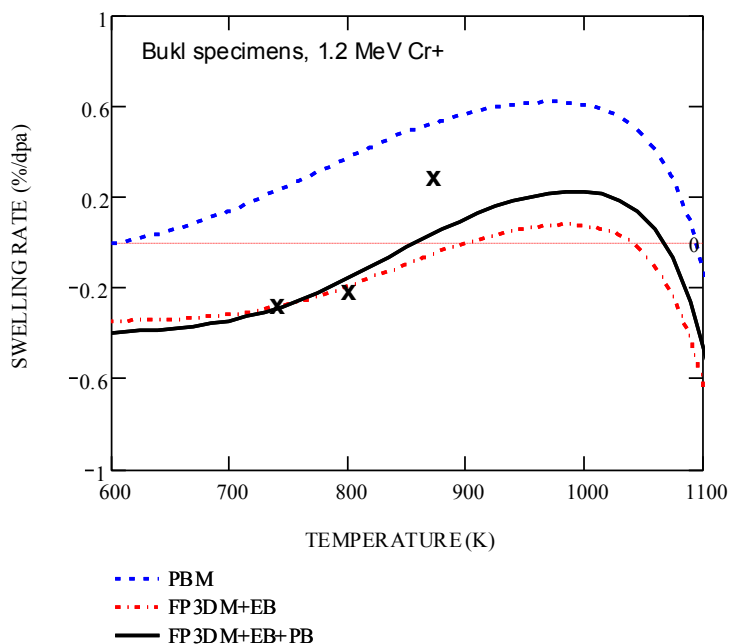
Figure 4. Temperature dependence of swelling rate in nickel bulk samples irradiated with 1.2 MeV Cr ions vs. experimental data [9]:

$$K = 7 \times 10^{-3} \text{ dpa/s},$$
$$\bar{R}_v = 20 \text{ nm},$$
$$N_v = 10^{21} \text{m}^{-3},$$
$$\rho_d = 2 \times 10^{14} \text{m}^{-2}.$$
$$l_Q^0 = 5 \times 10^3 b,$$
$$\Delta E_d = 0.5 \text{ eV},$$
$$k_{eff} = 0.1, \ \varepsilon_i = 0.2.$$

Other material parameters presented in Table 1.

One can see that the PBM cannot describe the observed low temperature reduction in swelling even qualitatively.   On the other hand, the FP3DM modified with emission bias along (FP3DM+EB) can explain the swelling reduction but predicts a somewhat lower swelling rate at elevated temperatures and a lower threshold temperature than observed. The best agreement with experiment shows the model FP3DM+EB+PB that takes into account all three constituents of swelling, based on the <u>absorption</u>, <u>emission</u> and <u>production</u> biases.

In [1] we present new experimental results on sub-threshold electron irradiation, where the emission bias appears to be the only driver for microstructure evolution.

OUTLOOK

In order to forecast the behavior of nuclear materials in real radiation environment, the generation rate and propagation range of <u>quodons</u> should be modeled in different crystal structures as functions of defect concentrations and types. These factors seem to be of a primary <u>technological importance</u> since they offer a new insight on design of radiation-resistant materials.

Table 1. Material parameters used in calculations.

Parameter	Value
Atomic spacing, b, m	3.23×10^{-10}
Atomic volume of the host lattice, ω, m^{-3}	2.36×10^{-29}
Matrix shear modulus, μ, GPa	95 (Ni), 55 (Cu)
Interstitial dilatation volume, Ω_i	1.2ω, 0.6ω
Vacancy dilatation volume, Ω_v	-0.6ω
Bulk recombination rate constant, β_r, m^{-2}	10^{21}
Displacement energy, E_d, eV	30
Cascade efficiency for the stable PF production, k_{eff}	0.1
Fraction of point defects in the in-cascade clusters, $\varepsilon_{i,v}$	0.2
Maximum focuson energy, E_F, eV	30
Migration energy of vacancies, E_{vm}, eV	1.1 (Ni), 0.98 (Cu)
Pre-exponent factor, D_v^0	10^{-5}
Thermal vacancy formation energy at a free surface, E_{vf}^{th}, eV	1.8 (Ni), 1.3 (Cu)
Thermal vacancy formation energy at a dislocation, E_{vf}^{th}, eV	$E_v^{d,th} = E_v^{S,th} + \gamma_{SF} b^2$.
Stocking fault energy, γ_{SF}, J/m^2	0.1
Ballistic vacancy formation energy at a free surface	$E_v^0 = E_{vf}^{th} + E_{vm}$
Ballistic vacancy formation energy at the surface of a cavity with radius R_C and gas pressure P_g	$E_v^0 + \left(P_g - 2\gamma / R_C\right)\omega$
Surface energy, γ, J/m^2	2
Ballistic–thermal vacancy formation energy difference at dislocations, E_v^d, eV	0.5
Focuson propagation range, l_F, b	10
Quodon propagation range, l_Q, b	5×10^3

REFERENCES

[1]   V. I. Dubinko, S. Y. Hu, Y. L. Li, C. H. Henager and R. J. Kurtz, submitted *to Philos. Mag.*
[2]   M. J. Makin, G. P. Walters and A. J. E. Foreman, *J. Nucl. Mater*. **95** (1980) 155.
[3]   Y. R. Zabrodsky and V. M. Koshkin, *DAN SSSR (in Russian)* **227** (1974) 1323.
[4]   V. L. Indenbom, *Pisma v ZhTF (in Russian)* **5** (1979) 489.
[5]   R. H. Silsbee, *J. Appl. Phys.* **28** (1957) 1246.
[6]   R. S. Nelson and M. W. Tompson, *Proc. Roy. Soc.* **259** (1960) 458.
[7]   G. Leibfried, *J. Appl. Phys.* **31** (1960) 117.
[8]   M. W. Tompson, Defects and Radiation Damage in Metals (Cambridge, 1969).
[9]   S. Flach and A. V. Gorbach, *Phys. Rep.* **467** (2008) 1.
[10] M. E. Manley, *Acta Materialia,* **58** (2010) 2926.
[11] M. E. Manley, D. L. Abernathy, N. I. Agladze and A. J. Sievers, Scientific Reports 1 (2011) doi: 10.1038/srep00004.
[12] F. M. Russell and J. C. Eilbeck, *Europhys. Lett.* **78** (2007) 10004.
[13] G. Abrasonis, W. Moller and X. X. Ma, *Phys. Rev. Lett.* **96** (2006) 065901.
[14] V. I. Dubinko and N. P. Lazarev, *Nucl. Instrum. Meth. B* **228** (2005) 187.
[15] V. I. Dubinko, Radiat. *Eff. Def. Solids* **160** (2005) 85.
[16] V. I. Dubinko and V. F. Klepikov, *J. Nucl. Mater.* **362** (2007) 146.
[17] V. I. Dubinko, A. G. Guglya, E. Melnichenko and R. Vasilenko, *J. Nucl. Mater.* **385** (2009) 228.
[18] V. I. Dubinko, A. G. Guglya and S.E. Donnelly, *Instr. Methods Phys. Res. B* **269** (2011) 1634.
[19] V. I. Dubinko and F. M. Russell, *J. Nucl. Mater.* **419** (2011) 378.
[20] V. I. Dubinko, in *Nuclear Materials*, ed. M. P. Hemsworth (Nova Science Publishers, Inc., 2011) 81.
[21] A. Suzuki and Y. Mishin, *Interface Science* **11** (2003) 131.
[22] G. P. Walters, *J. Nucl. Mater.* **136** (1985) 263.
[23] V. I. Dubinko, Investigation of the Void and Gas Bubble Formation and Dissolution Under Ion and Sub-Threshold Electron Irradiation, Technical Report T02-STCU 4962 (2011).
[24] A. V. Barashev and S. I. Golubov, in Proc. 2008 MRS Fall Meeting, Symposium R, 1125-R05-04, 2009.
[25] T. Okita and W. G. Wolfer, *J. Nucl. Mater.* **327** (2004) 130.

8.5 The Effects of Grain Boundaries on Radiation Damage Production by Displacement Cascades in α-Fe — H. L. Heinisch, R. J. Kurtz and F. Gao (Pacific Northwest National Laboratory)

This is the Extended Abstract for an ICFRM-15 paper submitted for publication in the Proceedings.

It is well known that grain boundaries in metals can be sinks for migrating defects such as mobile interstitial atoms, but less is known about the effects of grain boundaries on defect production and defect-grain boundary interactions due to displacement cascades in the vicinity of grain boundaries.   Molecular dynamics simulations were performed for displacement cascades in the vicinity of both a symmetric Σ3<110>{112} and a symmetric Σ11<110>{323} grain boundary (GB) in α-Fe to investigate cascade-GB interactions and defect creation near GBs. Both self-interstitial atoms and vacancies are created within the Σ11 GB as well as within the Σ3 GB, although fewer defects are trapped in the Σ3 GB than in the Σ11. See Figures 1-3 and typical cascades in Figure 4. The relative numbers of surviving vacancies and interstitials per cascade residing within the GB vary as a function of the distance of the primary knock-on atom from the GB, with more interstitials than vacancies arriving at the GB from distant cascades.   For both Σ3 and Σ11 GBs the total number of surviving defects per cascade increases somewhat with decreasing distance of the cascade from the GB, indicating that having some fraction of the defects trapped in the GB promotes the initial survival of more cascade defects overall relative to cascades in the perfect crystal. Molecular statics simulations of defect formation energies within the GBs (Figure 5) confirm that both vacancies and self-interstitials have lower defect formation energies in both the Σ3 and Σ11 GBs relative to their formation energies in the perfect crystal.
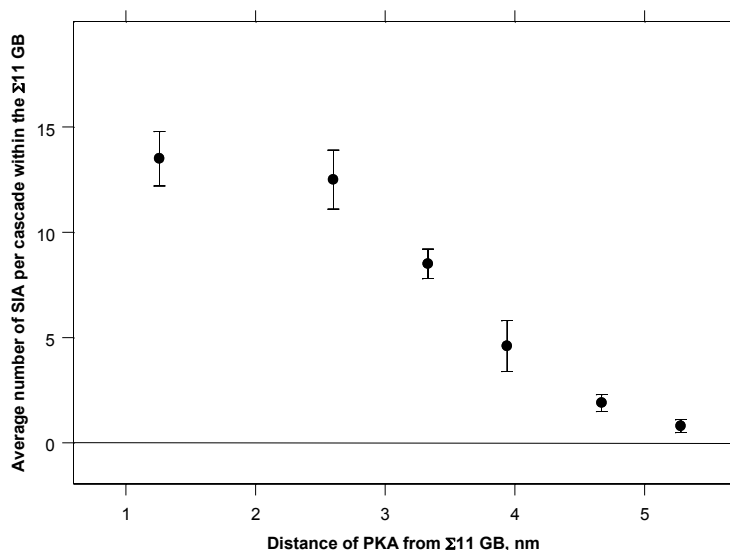
Figure 1.   Average number of SIA per cascade residing within the Σ11 GB as a function of distance from the GB.
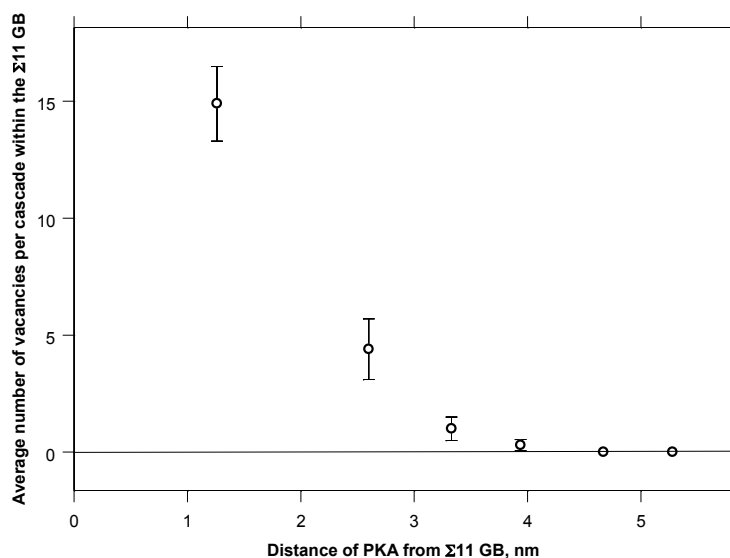
Figure 2. Average number of vacancies per cascade residing within the Σ11 GB as a function of distance from the GB.
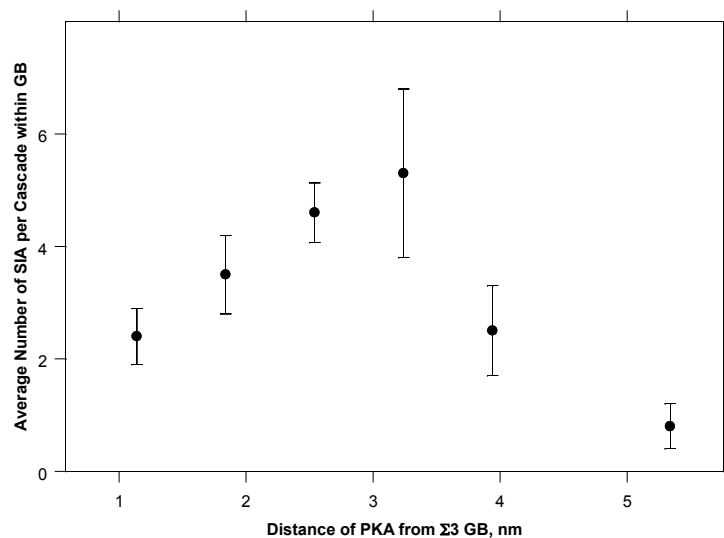
Figure 3. Average numbers of SIA produced within the Σ3 GB as a function of distance from the GB.
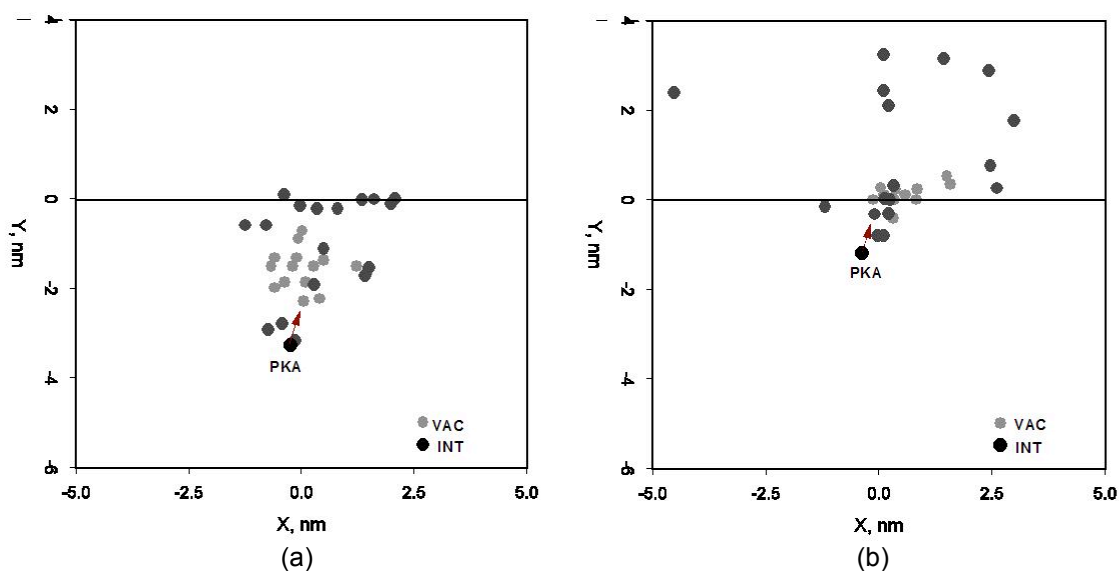
Figure 4. Distributions of vacancy (gray) and self-interstitial (black) cascade defects produced by 3 keV PKAs in the same direction at three distances from the Σ11 grain boundary. (a) Y=-3.27nm, (b) Y = -1.20 nm.
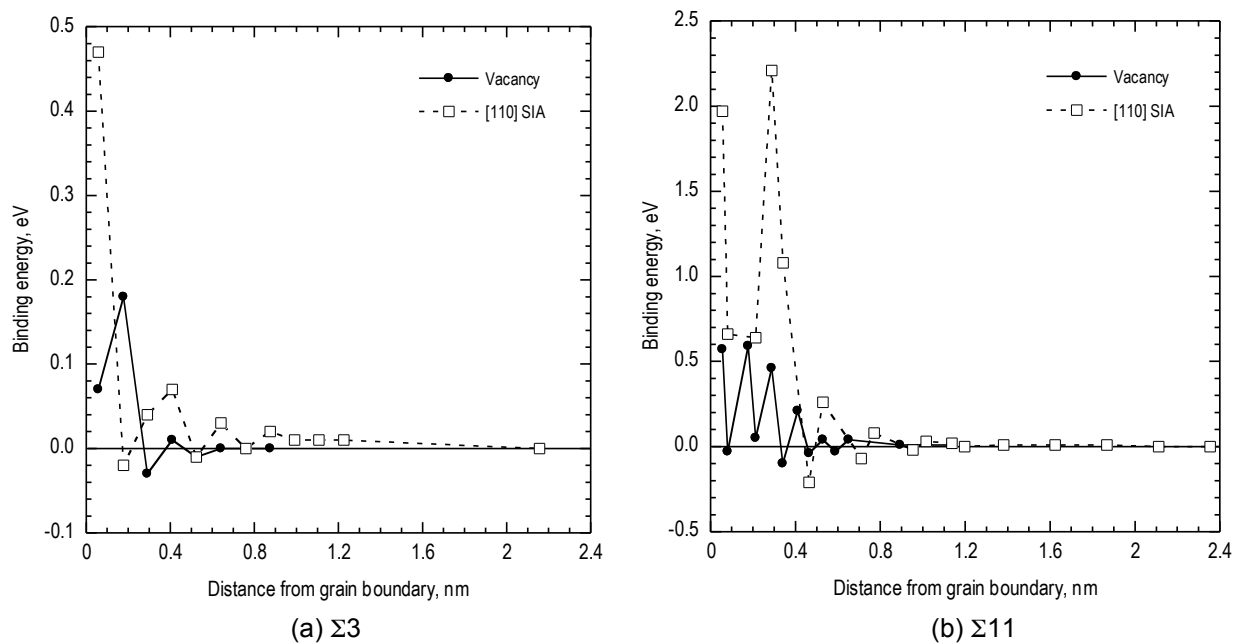
Figure 5. Binding energies (eV) of vacancies and self interstitial atoms to a) Σ3 grain boundary and b) Σ11 grain boundary.

8.6 Molecular Dynamics Modeling of Dislocation-Obstacle Interactions and Mechanisms of Hardening and Strengthening in Irradiated Metals — Y. N. Osetskiy and R. E. Stoller (Oak Ridge National Laboratory)

OBJECTIVE

The objective of this research is to investigate mechanisms of interaction between dislocations and obstacles (precipitates, voids, bubbles, etc.) induced at fusion irradiation conditions. These defects are usually very small, <10nm, and therefore atomic scale details are necessary to be understood.

SUMMARY

This extensive simulation program is design to investigate the basic mechanisms of strengthening and hardening during irradiation of fusion materials. Strength of spherical obstacles of different types and sizes is discussed for comparison. An interesting observation is that the relative strength of rigid particles (a model for oxide particles) depends on their size: small particles, 2 nm in diameter, are relatively weak compared to voids or equilibrium He-filled bubbles, while large particles are the strongest obstacle. The explanation is related to the atomic scale features of dislocation-obstacle interactions, particularly to cross-slip and climb mechanisms.

 PROGRESS AND STATUS

Introduction

Structural materials subjected to fusion conditions are changing their microstructure and hence mechanical properties. Understanding the details of this process is necessary for predicting changes, estimation of structural components lifetime and design of new materials tolerant to fusion conditions. Experimental studies have demonstrated that depending on the structural material composition and particular conditions (temperature, neutron flux, He accumulation due to irradiation and/or transmutation, etc.) different microstructural features can form and affect dislocation motion and therefore mechanical properties. These obstacles can be voids, secondary phase precipitates, gas filled bubbles and other microstructure features relevant to fusion structural materials e.g. oxide nanoclusters. In many cases, for example voids and He-bubbles, modern radiation damage theory models based on rate theory, may predict evolution of their population however to bridge this to mechanical properties changes is not a trivial task. In general, simple phenomenological models used to account hardening/strengthening effects due to microstructural features are focused mainly on statistics of defects distribution having particular obstacle strength as an input parameter. It is therefore practically important to obtain information on the interaction mechanisms and strength for particular obstacle types. The corresponding extensive simulation program was designed and some preliminary results are presented here focused mainly on comparison spherical localized obstacles of different types.

Formalism

We used Molecular Dynamics (MD) modeling technique to investigate dislocation motion in the present of obstacles. The scale of modern models i.e. ~10^7 atoms, allows to cover the most important obstacles appeared under irradiation such as voids, bubbles, precipitates, oxide

nanoclusters and dislocation loops. A computer code developed at ORNL was used for these modelings is based on the atomic-scale dislocation model described in [1].

Voids and coherent Cu-precipitates in bcc iron matrix where considered earlier [2-4] and are used here for comparison. The current simulation program is focused mainly on He-filled bubbles and rigid inclusions simulating oxide-particles by introducing infinitely high shear modulus inside an inclusion. We have simulated equilibrium bubbles taking into account the earlier results on the equilibrium He-to-vacancy ratio [5]. At the first stage we have considered ½<111>{110} edge dislocation in bcc iron matrix. This choice was governed by two reasons:

1. Edge component in the dislocation network is increasing under irradiation due to formation and growth of dislocation loops;
2. Because of its inability to cross-slip an edge dislocation can be pinned by the rigid inclusions much stronger than a screw dislocation which can overcome rigid obstacles by cross-slip.

In the report we present data on spherical obstacles of three sizes 1, 2 and 4 nm in diameter all simulated at 300K and the applied strain rate 10^6 s^{-1}. More details on temperature and strain rate effects for voids and precipitates can be found in [2-4] and those for bubbles and rigid obstacles are under current study.

RESULTS

The results on Critical Resolved Shear Stress (CRSS), which is the measure of the strength of the individual obstacle, obtained for coherent Cu-precipitates, voids, He-filled bubbles and rigid inclusions are presented in the Fig. 1 together with the data obtained in simulation of the Orowan mechanism for the corresponding obstacle size. One can see that in the size range studied, from 1 to 4 nm, coherent Cu-precipitates are the weakest obstacles. The interaction mechanism in this case is a simple shear without any additional changes in precipitate or dislocation structures. Voids are stronger obstacles and cause some climb due to absorption vacancies by an edge dislocation line. The comparative strength of He-bubbles depends on their size. Thus small bubbles (1nm) are stronger than voids however larger ones (4nm) are compatible. We expect that larger bubbles (>4nm) might be weaker obstacles than voids however more studies are necessary to reveal this. The mechanism of this size dependence is not understood yet but it might be related to the pressure of He inside bubbles which for equilibrium bubbles decreases when size increases. The size dependence of the rigid inclusion strength is even stronger as can be seen in
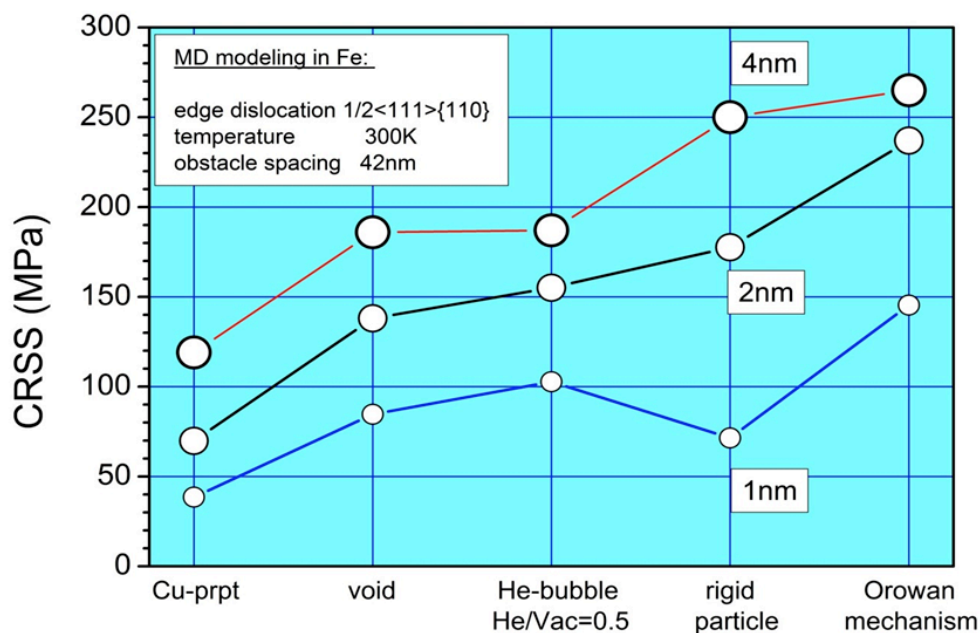
Figure 1. Critical resolved shear stress for different obstacles obtained in MD modeling.

Fig.1. Thus 1 nm inclusion is very weak, compatible with the corresponding Cu-precipitate. The 2nm inclusion is stronger than precipitate, void and bubble but still significantly weaker than the Orowan obstacle. And, finally, 4nm inclusion is compatible with the maximum possible strength given by the Orowan mechanism.   Atomic-scale modeling allows to rationalize mechanisms responsible for such behavior.   Thus, small 1nm inclusion is so weak because edge dislocation can easily emit few vacancies to climb around the rigid obstacle and to drag the corresponding interstitial atoms out as a superjog. At 2nm inclusion dislocation achieves shape of two parallel screw segments with spacing just below 2nm. Strong interaction between dipole leads to their cross-slip and unzipping from the obstacle when one of the screw dislocation segments reaches the edge of the obstacle. In this case a large superjog created on the dislocation line and the mechanism is similar to that discussed in [4] for voids. However, at large inclusion, 4nm, although the dislocation achieves the screw dipole configuration the driving force for cross slip is smaller because the separation is large. Moreover, the successful cross-slip that would release the dislocation from the inclusion must be more significant because of the large obstacle.   Therefore, in this case the dislocation dipole is elongating until attraction force exceeds the Peierls stress for these screw segments, dislocation segments annihilate and the Orowan loop is left around the inclusion. The maximum possible stress is realized for this mechanism.   We expect that larger obstacles will reproduce exactly the Orowan stress.

REFERENCES

1. Y. N. Osetsky and D. J. Bacon, "An atomic-level model for studying the dynamics of edge dislocations in metals," *Modelling Simul. Mat. Sci. Eng.* **11**, 427 (2003).
2. Y. N. Osetsky and D. J.Bacon, "Void and precipitate strengthening in alpha-iron: what can we learn from atomic level modelling?" Invited contribution for IEA Workshop (Les Diableretes, October 2002), *J. Nucl. Mater.* **323**, 268 (2003).
3. D. J. Bacon and Y. N. Osetsky, "Mechanisms of hardening due to cooper-precipitates in α-Iron, *Philos. Mag.* **89**, 34-36 (2009) 3333-3349.
4. Y. N. Osetsky and D. J. Bacon, "Atomic-scale mechanisms of void hardening in BCC and FCC metals," *Philos. Mag*. **90,** 945 (2010).
5. D. M. Stewart, Y. N. Osetsky, R. E. Stoller, S. I. Golubov, T. Seletskaia, and P. J. Kamenski, "Atomistic studies of Helium defects properties in BCC iron: comparison of He–Fe potentials," *Philos. Mag*. **90,** 923 (2010).
6. D. M. Stewart**,** Y. N. Osetskiy, and R. E. Stoller**, "**Atomistic studies of formation and diffusion of helium clusters and bubbles in BCC iron*," J. Nucl. Mater.* **147** (2011) 1110-1114.

8.7 Modeling of Deformation Processes and Irradiation Effects in Iron and Tungsten Alloys — *Jaime Marian and Wayne Meier (Lawrence Livermore National Laboratory)*

OBJECTIVES

The objectives of this work are the following:
- The application of micro and mesoscale modeling techniques to study dislocation properties in ferritic and W-based materials.
- The development of computational models and tools to study damage accumulation in >1 dpa (fusion-like) conditions, both for Fe and W-based alloys.

SUMMARY

The high-temperature strength of structural ferritic alloys (ferritic/martensitic steels, ODS steels, bcc refractory alloys) hinges on the thermal stability of second phase particles and their interactions with dislocations. Irradiation damage can modify the structure and stability of both the particles and dislocations, particularly by the introduction of gas atoms, point defects and point defect clusters. The three aspects of materials strength that we are studying are:

a) Computation of dislocation mobility functions (stress-velocity relations) as a function of temperature and dislocation character. This will be done via molecular dynamics (MD) simulations of single dislocation motion under applied shear stress. This is a fundamental input to dislocation dynamics (DD) simulations and also provides fundamental insights into the high-temperature plastic behavior of ferritic materials.

b) Simulations of dislocation-obstacle interactions using MD and DD. This subtask includes simulating the effect on dislocation glide of precipitates (e.g., α' Cr precipitates), ODS particles, and irradiation induced defect clusters (e.g. voids, dislocation loops, etc.).

c) Implementation of this information (dislocation mobilities and dislocation-defect interaction rules) into DD codes that will allow us to study plasticity of single crystals Fe alloys under relevant irradiation conditions.

BACKGROUND AND APPROACHES USED

Accelerated Stochastic Techniques for Radiation Damage Kinetics

The use of standard kinetic Monte Carlo (kMC) for radiation damage calculations suffers from a number of limitations that prevent it from accessing the fluences (doses) relevant for fast and fusion reactors. Among them, the stiffness of the rate spectrum, i.e. a large disparity in the rate constants of the evolving species, is one of the most noteworthy. Also, due to its intrinsic time discreticity, the 'next' time step is impossible to predict, which makes parallelization a difficult task. We have developed a method that circumvents this difficulty by using automatic time synchronization based on the use of 'null' events. The algorithm, termed spkMC (synchronous parallel kMC), has now been extended to discrete lattices with good success. At present, we have done only calculations in simple cubic Ising systems but the idea is to start binary alloys in the next fiscal year to study phenomena such as radiation-enhanced diffusion/segregation.

In addition, another line of work that being pursued within the base program is the development of stochastic cluster dynamics based on the Gillespie method. In contrast to providing existence probabilities for all possible species in an irradiated volume, as mean-field rate theory, this method samples from the cumulative probability distribution of the species existing at a given instant, adding new species as required by the kinetics of the system. In this fashion, the method introduces some natural stochastic variability to cluster dynamics calculations. Additionally, the method facilitates the treatment of multidimensional species such as vacancy-He complexes or mixed interstitial dumbbells. These two tasks build on well-known and thoroughly tested and applied computational techniques, but that had recently shown signs of saturation in terms of computational power. We have demonstrated the capabilities of the method by carrying out calculations of triple dpa/He/H irradiations in model FeCr alloys up to 50 dpa. Next, we will introduce chemical effects in the form of passivation of void surfaces by H atoms and H-He synergisms to study the effect of simultaneous vs. sequential implantation on swelling in these materials.

TECHNICAL PROGRESS

In the period covered by this report, we have calculated the mobilities of screw and edge dislocations in Fe, both of which have been published in Physical Review B. The stochastic cluster dynamics method was published in Journal of Nuclear Materials, as well as the calculation of the fraction of He that ends up in substitutional sites as part of its own collisional process. This is an important value in view of the extreme differences in mobility between substitutional and interstitial sites.

Also, we have tested five interatomic potentials for W and assessed their feasibility for screw dislocation simulations. We have identified two potentials that are superior to the rest for this kind of simulations. These two are advantageous because they predict the correct transition barriers for dislocation motion as given by electronic structure calculations. The findings of this work have been submitted to Physical Review B. A short but relevant study on the application of boundary conditions for MD simulations has also been performed and submitted for publication in Modelling and Simulation in Materials Science and Engineering.

CALCULATION OF EDGE DISLOCATION MOBILITIES IN BCC FE

In the traditional picture of plasticity in bcc metals, edge dislocations have been assumed to play a minor role due to their high mobility with respect to screw dislocations, which then control plastic flow. $\frac{1}{2}$<111>{110} edge dislocations indeed fit this description, as it has been shown by way of numerous atomistic simulations. However, $\frac{1}{2}$<111>{112}-edge dislocations have been comparatively much less studied. The recent discovery of a possible regime where they move slowly via thermally activated kink-pair nucleation may have implications in the plastic behavior of bcc materials. Because dislocation mobilities are very difficult to measure experimentally, we are calculating comprehensive mobility laws for both types of edge dislocations as a function of temperature and stress using molecular dynamics simulations. Our results confirm the existence of clearly delimited thermally activated and phonon drag dynamic regimes for $\frac{1}{2}$<111>{112} edge dislocations and of a single viscous drag regime for their $\frac{1}{2}$<111>{110} counterparts. We also provide an analysis to relate the difference in mobility to the dislocation core properties. Our fitted mobility laws may be used in dislocation dynamics simulations of plastic flow involving millions of segments.
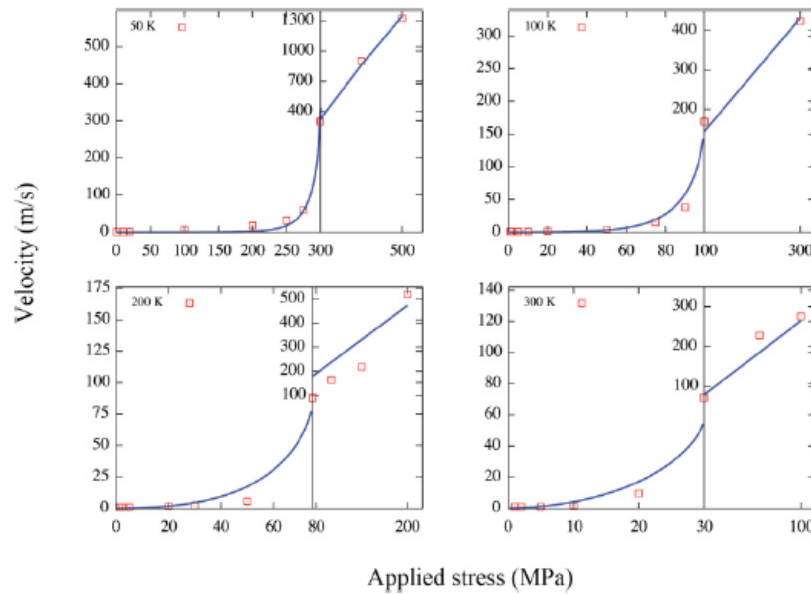
Fig. 1. ½<111>{112} edge dislocation velocities as a function of stress and temperature.

Dislocation velocities as a function of stress and temperature are known as mobility functions. The methodology to compute dislocation mobilities using MD simulations has been explained in detail elsewhere [8], but basically consists of generating a dislocation in a simulation box oriented along the line, glide, and plane normal directions (which, in turn, are dictated by the crystallography.   Figure 1 shows results of ½<111>{112} edge dislocation velocities as a function of temperature and stress. The mobility function that best fits these data is:

$$v_{(112)} = 1.68 \times 10^4 \frac{\tau_n(T)}{T} \exp\left\{ -0.15[1 - \tau_n(T)^{0.13}]^{0.68} \right\}$$

where T is the temperature and τ_n is a temperature normalized stress that marks the transition from thermally activated motion to phonon drag.

To obtain the above equation it was necessary to calculate the energy of a double kink on a ½<111>{112}-edge dislocation. The structure of the kinks can be seen in Figure 2. A value of 0.15 for the double kink was obtained. This parameter goes into the fitting of the mobility law.
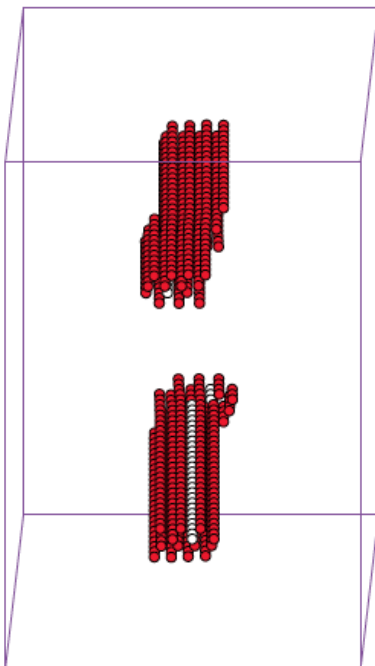
Fig. 2. Atomistic structure of two single kinks in a ½<111>{112} edge dislocation. The energy of one kink is 0.075 MeV.

DEVELOPMENT OF THE STOCHASTIC CLUSTER DYNAMICS METHODOLOGY

Mean field rate theory (MFRT) has been the workhorse method for simulations of radiation damage accumulation for over 40 years. As its name indicates, MFRT owes its high computational efficiency to the mean-field approximation, in which the details concerning the spatial distribution of defects are assumed unimportant.   MFRT models evolve in time by solving forward in time a set of ODEs for defects and defect cluster concentrations.

While efficient for simple material models, MFRT struggles to describe damage accumulation in realistically complex materials where it suffers from combinatorial explosion in the number of ODEs that must be solved. Simply put, rate theory calculations are prohibitively expensive for multidimensional cluster spaces. Our work here is to recast the MFRT method in the form of a stochastic cluster dynamics (SCD) algorithm following the approach proposed earlier by Gillespie in the context of bio-chemical reaction networks [6]. In SCD, rather than solving ODEs for defect cluster concentrations in an infinite material volume, integer-valued defect populations evolve stochastically in a finite material volume, one defect reaction (event) at a time. Thus, only those defects and defect clusters that are actually present in the simulation volume are considered. This circumvents combinatorial explosion allowing SCD simulations of complex defect populations defined in cluster spaces of arbitrary dimensionality. This newly gained ability of SCD to model complex defect populations is essential for our project. We intend to rely on the SCD method for simulations of irradiated materials involving multiple defect and chemical species.
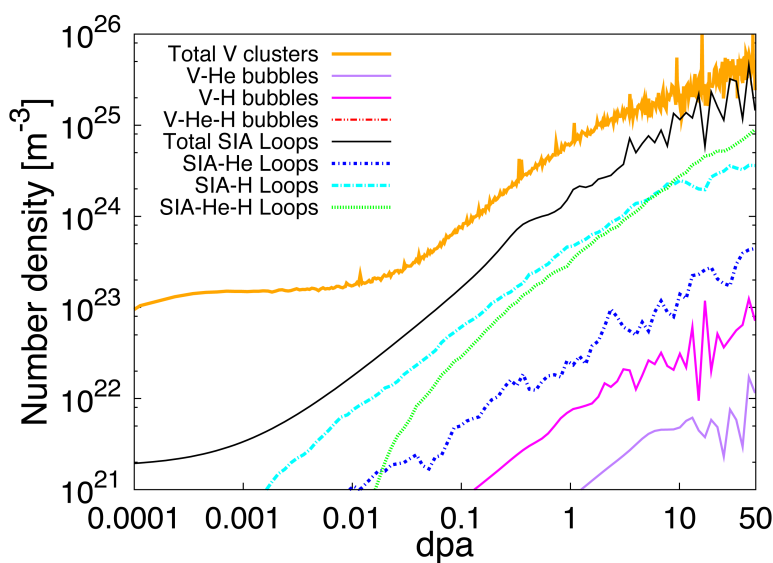
Figure 3. Accumulation of defect species with dose in triple-implanted (self ions, He, H) Fe alloys at 300K.

In conditions where spatial correlations and fluctuations in spatial distribution of defects are deemed important, (particle-based) object kinetic Monte Carlo (OKMC) is the method of choice. However, standard OKMC simulations can reach dose limit of the order of 0.01 dpa. By contrast, SCD enables simulations up to tens of dpa. As a demonstration of the method capabilities, Figure 3 shows a recent calculation of defect accumulation up to doses of 50 dpa in tri-implanted FeCr alloys.

STUDY OF THE EFFECT OF THE INTERATOMIC POTENTIAL ON DISLOCATION MOTION IN W

As mentioned in 16b, W is one of the main candidates for plasma-facing applications in magnetic fusion reactors. W, however, is very brittle and efforts are being conducted to find more ductile W alloys suitable for nuclear environments. In this sense, we are developing interatomic potentials for binary W systems aimed at obtaining ductile alloys from an atomistic perspective. Before these efforts are underway, we need to characterize pure W potentials properly. W has comparatively been less studied than other bcc metals at the atomistic level and thus much work is still required to come up with reliable atomistic models. In a certain sense, because the plastic behavior of bcc metals like W is governed by screw dislocations motion, ductility equals higher dislocation mobility. Here we compare five different interatomic potentials for W and calculate dislocation motion in a wide range of temperatures.
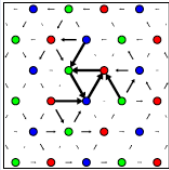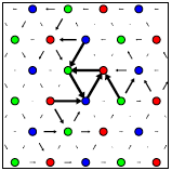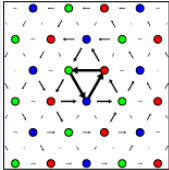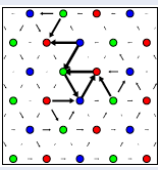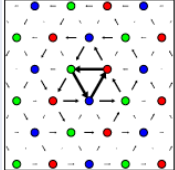
Potential	EAM1	EAM2	EAM3	BOP	MEAM
Source	Zhou *et al* (2001)	Ackland and Thetford (1987)	Marinica *et al* (2011)	Juslin *et al* (2005)	Lenosky *et al* (2010)
CPU cost	1.0	0.4	0.9	5.4	9.1
σ_P [GPa]	4.0	1.9	1.8	1.1	3.2
Core structure at 0K					

Table I: Comparison of static properties of semiempirical interatomic potentials for W.

The potentials tested include three EAM (embedded atom method), one BOP (bond order potential) and one modified EAM (MEAM). Table I describes the basic features predicted by each potential at 0K. On the basis of electronic structure calculations, which predict a compact core and a Peierls stress σ_P of 2.8 GPa, one can filter out potentials EAM1, EAM2 and BOP.

In addition we have calculated the Peierls barrier and the gamma surface for all potentials. The Peierls barrier is given in Fig. 4 along with some DFT data for reference. Clearly, the MEAM and EAM3 potentials come closest to the shape and value of the DFT results.
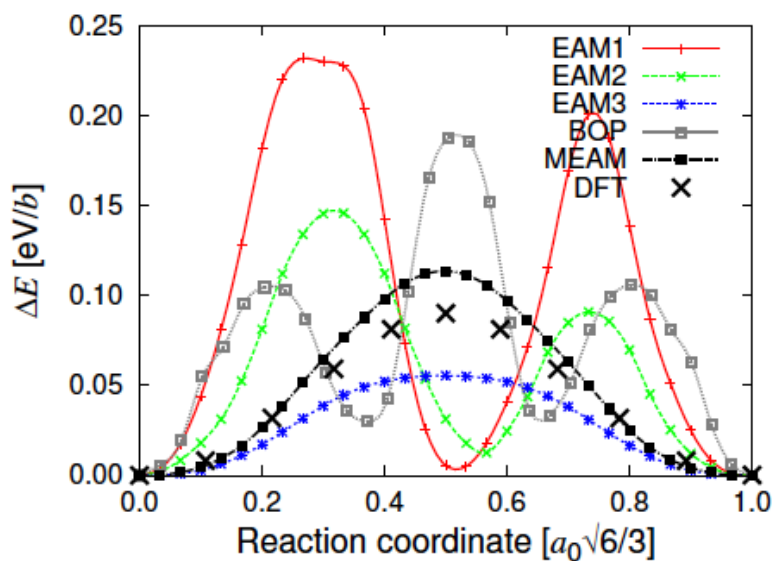
Fig. 4. Peierls trajectory for all five W potentials tested. DFT results are shown for comparison.

Fig. 5 shows the corresponding gamma surface. Again the EAM3 and MEAM do best in reproducing the DFT data.
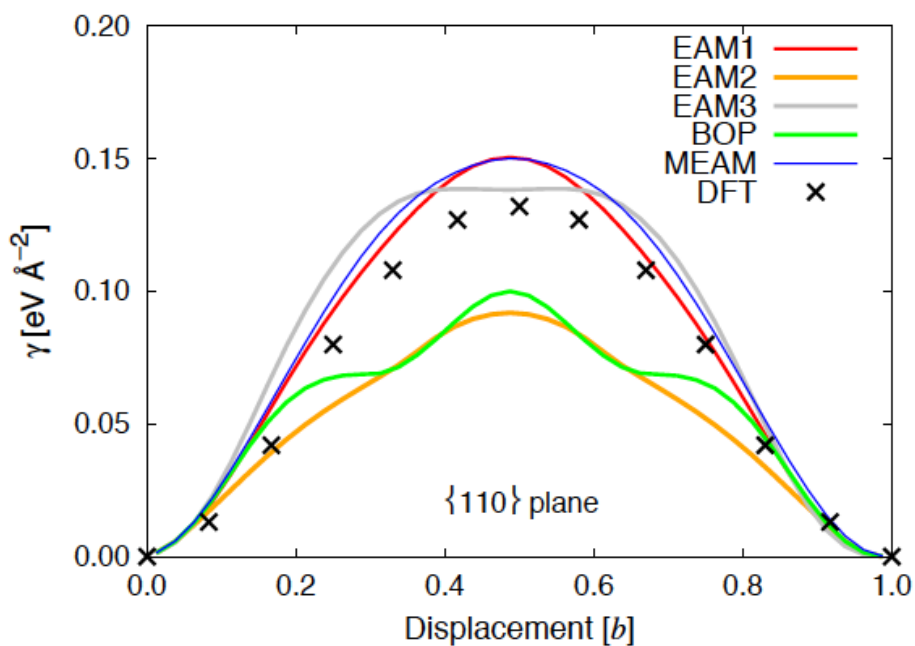
Fig. 5. Gamma surface for all five W potentials tested. DFT results are shown for comparison.

PUBLICATIONS

S. Queyreau, J. Marian, M. R. Gilbert, and B. D. Wirth, "Edge dislocation mobilities in bcc Fe obtained by molecular dynamics," *Phys. Rev.* B **84** (2011) 064106.

J. Marian and V. V. Bulatov, "Stochastic cluster dynamics method for simulations of multispecies irradiation damage accumulation," *J. Nucl. Mater.* **415** (2011) 84.

Paul Erhart and Jaime Marian, "Calculation of the substitutional fraction of ion-implanted He in an α-Fe target," *J. Nucl. Mater.* **414** (2011) 426.

D. Cereceda, J. M. Perlado and J. Marian, "The effect of boundary conditions on stress-controlled molecular dynamics simulations of dislocation motion in tungsten," submitted to *Modelling and Simulation in Materials Science and Engineering* (2012).

D. Cereceda, J. M. Perlado, S. Queyreau, A. Stukowski, M.-C. Marinica, L. Ventelon and J. Marian, "Temperature induced screw dislocation core transformation and its effect on mobility in pure W," submitted to *Physical Review* B (2012).

REFERENCES

[1]   C. J. Ortiz and M. J. Caturla, *J. Comp-Aided Mater Des* **14** (2007) 171.
[2]   M. J. Caturla, N. Soneda, E. Alonso, B. D. Wirth, T. Díaz de la Rubia, and J. M. Perlado, *J. Nucl. Mater*. **276** (2000) 13.
[3]   S. I. Golubov, R. E. Stoller, S. J. Zinkle, et al., *J. Nucl. Mater.* **361** (2007) 149.
[4]   R. E. Stoller, S. I. Golubov, C. Domain, et al., *J. Nucl. Mater.* **382** (2008) 77.
[5]   E. Martínez, J. Marian, M. H. Kalos, and J. M. Perlado, *J. Comput. Phy.* **227** (2008) 3804.
[6]   D. T. Gillespie, *J. Phys. Chem.* **81** (1977) 2340–2361.
[7]   V. V. Bulatov, et al., *Nature* **440** (2006) 1174-1178.
[8]   J. Marian and A. Caro, *Phys. Rev. B* **74** (2006) 024113.
[9]   E. Martinez, P. R. Monasterio, and J. Marian, *J. Comput. Phys.* **230** (2011) 1359.
[10] E. Martinez, J. Marian, M. H. Kalos, and J. M. Perlado, *J. Comput. Phys.* **227** (2008) 3804.
[11] L. Romaner, C. Ambroschl-Draxl, and R. Pippan, *PRL* **104** (2010) 195503.
[12] X. Tian and C. Woo, *Mater. Sci. Eng.* A **369** (2004) 210.
[13]   T. Ahlgren, K. Heinola, N. Juslin, and A. Kuronen, *J. Appl. Phys.* **107** (2010) 033516.
[14] X. W. Zhou, et al., *Acta Mater.* **49**, 4005 (2001).
[15] G. J. Ackland and R. Thetford, *Philos. Mag.* A **56**, 15 (1987).
[16] M.-C. Marinica, et al., (2012) to be submitted.
[17] N. Juslin, P. Erhart, P. Traskelin, J. Nord, K. O. E. Henriksson, K. Nordlund, E. Salonen, and K. Albe, *J. Appl. Phys*. **98**, 123520 (2005).
[18] T. J. Lenosky, B. Sadigh, E. Alonso, V. V. Bulatov, T. D. de la Rubia, J. Kim, A. F. Voter, and J. D. Kress, *Modeling Simul. Mater. Sci. Eng*. **8**, 825 (2000).

9.1 Assembly of the US-Japan JP-30 and JP-31 HFIR Target Irradiation Experiments —
T. Nozawa, T. Hirose, H. Tanigawa, M. Ando (Japan Atomic Energy Agency), J. L. McDuffee,
D. W. Heatherly, R. G. Sitterson, M. A. Sokolov, L. Tan, D. T. Hoelzer, R. E. Stoller, L. L. Snead
(Oak Ridge National Laboratory), and T. Yamamoto (University of California, Santa Barbara)

OBJECTIVE

This work is being carried out under the collaboration on fusion materials between the U.S. DOE
and the Japan Atomic Energy Agency (JAEA). The JP-30 and JP-31 target irradiation capsules
are parts of the Phase-VI experimental program with the goal to verify the irradiation response of
alloy F82H base metal, its joints and welds in the mid fluence region, i.e., the target dose of 20
dpa at the peak, including identification of the effects of post-weld heat treatments (PWHT).

SUMMARY

Assembly of the JP-30 and JP-31 capsules was completed in November, 2011 and installed in
HFIR.   Irradiation began with cycle 439, starting November 21, 2011.   A detailed specimen
loading list for the capsules is provided in this report.

PROGRESS AND STATUS

Introduction

Screening irradiation experiments of several types of joint and weld materials of the reduced-
activation ferritic/martensitic (RAFM) steels have been implemented by the past irradiation
campaigns such as HFIR MFE-RB-11J, -12J and -15J within the framework of the U.S. DOE-
JAEA collaboration on fusion materials. With verifying feasibility of these materials, the new
target irradiation experiments (JP-30 and JP-31) are being carried out.   The goals of the
experiment include investigation of the irradiation stability in the middle fluence region (~20 dpa),
evaluation of the impact of PWHT on mechanical properties, and development of engineering
data on the fusion candidate alloy F82H and its variants. It is planned to irradiate these capsules
for 11 cycles, assuming a dpa rate of 1.9 dpa/cycle, which was calculated with the recent data
from all the Greenwood reports for experiments in the target region.   This report provides a
description of the final design and a detailed list of specimens loaded into the JP-30 and JP-31
capsules.

Description of JP-30 and JP-31

The design of the JP-30 and JP-31 capsules is very similar to that of JP-28 and JP-29 [1]. The
main differences between these two sets are irradiation temperature and the type and number of
fracture toughness specimens.   The JP-30 and JP-31 capsules are designed for higher
temperature irradiation (~650 °C for JP-30 and JP-31 vs. ~500 °C for JP-28 and JP-29), as well as
irradiation at 300 and 400 °C (no change). All deformation fracture mini-beam (DFMB) specimens
and some of multi-3 pre-cracked Charpy V-notch (PCCVN) specimens are replaced by multi-2
PCCVN specimens and disk compact tension (DCT) specimens, respectively.   The detailed
capsule designs with thermal analysis were described elsewhere [2].

Specimen Loading

The materials used in this experiment are summarized in Table 1. The key materials tested are
variations of joints: a hot isostatic pressed (HIP) joint, TIG and electron beam (EB) weld joints, as
well as their base metals. Some variations of RAFM steels: heat treatment variations of the F82H
IEA heat and new ORNL 9Cr RAFM steels are also irradiated to accumulate the baseline data. In

addition, some variations of high-temperature tolerant oxide dispersion strengthening (ODS) ferritic/martensitic steels are tested by high-temperature irradiation (~650 °C).

The JP-30 and JP-31 capsules include 14 specimen holders for each designed to accommodate 6 types of specimens. The specimen types are (1) a sheet tensile specimen (SS-J3), (2) three types of PCCVN specimens (i.e., M2-, M3- and M5-PCCVN), (3) DCT specimens, (4) transmission electron microscopy (TEM) discs, (5) atom probe specimens (APFIM), and (6) miniature multi-purpose coupons (MMPC). Overall layouts of the JP-30 and JP-31 experiments are shown in Tables 2 and 3, respectively.

The location of each of the specimens in JP-30 and JP-31 is reported in Tables 4 and 5, respectively, which contain a box for each of the 14 specimen holder for each. Because coatings applied to some of the TEM discs required the discs to be loaded in a prescribed manner, the boxes for the TEM specimen holder (position 14) has a column labeled "Engr. Face" to indicate which way the engraved face of the specimen was loaded (if applicable). The multi-type PCCVN specimens (in positions 5, 10, 11, 12, and 13 for JP-30, and 4, 6, 8 and 9 for JP-31) were all loaded with the notches facing towards the center of the holders.

Table 1. Materials list for JP-30 and JP-31 experiments.

ID	Alloy Code	Description
F82H IEA	0	8Cr-2W RAF/Ms, F82H IEA heat (F82H-mod.)
F82H-IEA TIG WM	1	TIG weld metal of F82H joint
F82H-IEA TIG WJ	2	TIG weld joint of F82H joint
F82H-IEA TIG FG HAZ	21	Fine grained HAZ from TIG weld joint, heated above A_{C1} transformation temperature
F82H-IEA TIG OT HAZ	22	Over tempered HAZ from TIG weld joint, heated below A_{C1} transformation temperature
F82H-IEA EB WJ	25	Weld joint of F82H Electron Beam weld joint
F82H-IEA EB OT HAZ	26	Over tempered HAZ from EB weld joint, heated below A_{C1} transformation temperature
F82H-IEA EB WM	27 (or E)	Weld metal of F82H Electron Beam weld joint
F82H HIP	BA	HIP joint of F82H processed at 1100 °C followed by heat treatment at 960 °C and 750 °C
F82H-IEA EB BM (Std-PWHT)	XS	Base metal of F82H Electron Beam weld joint
F82H-IEA TIG BM (Std-PWHT)	XT	Base metal of F82H TIG weld joint
F82H-IEA EB BM PWHT1 (720C,1h/FCx3)	XW	Base metal of F82H Electron Beam weld joint with PWHT(720 °C,1h/FCx3)
F82H-IEA EB WM PWHT1 (720C,1h/FCx3)	XX	Weld metal of F82H Electron Beam weld joint with PWHT(720 °C,1h/FCx3)
F82H-IEA EB BM PWHT2 (680C,7h/FCx1)	XY	Base metal of F82H Electron Beam weld joint with PWHT(680 °C,7h/FCx1)
IEA CW20	C2	20% cold worked F82H IEA
IEA CW45	C5	45% cold worked F82H IEA
IEA CW80	C8	80% cold worked F82H IEA
F82H-mod3	H	F82H with 0.1% of Tantalum
US NFA1	YA	ORNL ODS steel (14YWT-SM12a-PR)
US NFA2	YB	ORNL ODS steel (14YWT-SM12c-PR)
US NFA3	YC	ORNL ODS steel (14YWT-SM12d-PR)
US NFA4	YD	ORNL ODS steel (14YWT-SM12d-CR)
U14YWT-HIP-D	HD	UCSB ODS steel
U14YWT-D1	Y	UCSB ODS steel
U14YWT-D2	G	UCSB ODS steel
NF616TMT	NF	Commercial ferritic boiler steel with TMT
US FM 1539T5	YJ	ORNL modified ferritic steel
US FM 1538T5	YK	ORNL modified ferritic steel
US FM 1537T5	YM	ORNL modified ferritic steel
US Modified NF616	YN	US Modified NF616
MA957Fr	ZQ	Commercial ODS steel (Inco MA957)
MA957US	ZS	Commercial ODS steel
MA956	MB	Commercial ODS steel
T91	TA	Commercial ferritic boiler steel
HP9Cr2WC	HPA	High-purity Fe-9Cr-2W-0.1C model alloy
KU15ODS	CB	ODS steel (Fe-15Cr-2W-0.2Ti-0.35Y_2O_3)
W/KU15ODS	(No ID)	KU15ODS alloy with a plasma splayed W layer

Table 2. Layout of the JP-30 experiment.

Position Number	Specimen Type	Design Temp. (°C)	Distance above HMP* (in)	
1	SS-J3, APFIM, MMPC	400	U	9.076
			D	8.440
2	DCT	650	1	7.815
			2	7.677
			3	7.539
			4	7.401
			5	7.263
			6	7.125
			7	6.987
			8	6.849
			9	6.711
3	SS-J3, APFIM, MMPC	300	U	6.085
			D	5.449
4	DCT	300	1	4.989
			2	4.851
			3	4.713
			4	4.575
			5	4.437
			6	4.299
			7	4.161
			8	4.023
			9	3.885
5	M3-PCCVN	300	U	3.387
			M	3.030
			D	2.673
6	DCT	400	1	2.051
			2	1.913
			3	1.775
			4	1.637
			5	1.499
			6	1.361
			7	1.223
			8	1.085
			9	0.947
7	SS-J3, APFIM, MMPC	400	U	0.487
			D	-0.149
8	DCT	400	1	-0.609
			2	-0.747
			3	-0.885
			4	-1.023
			5	-1.161
			6	-1.299
			7	-1.437
			8	-1.575
			9	-1.713
9	SS-J3, APFIM, MMPC	650	U	-2.296
			D	-2.932
10	M2-PCCVN	300	U	-3.602
			M	-3.956
			D	-4.310
11	M3-PCCVN	300	U	-4.872
			M	-5.229
			D	-5.585
12	M3-PCCVN	300	U	-6.322
			M	-6.679
			D	-7.035
13	M3-PCCVN	300	U	-7.772
			M	-8.129
			D	-8.485
14	TEM	300	-	-9.130

*HMP – Horizontal mid-plane of the HFIR

Table 3. Layout of the JP-31 experiment.

Position Number	Specimen Type	Design Temp. (°C)	Distance above HMP* (in)	
1	TEM	400	-	9.381
2	SS-J3, APFIM, MMPC	400	U	8.775
			D	8.139
3	SS-J3, APFIM, MMPC	650	U	7.357
			D	6.721
4	M2-PCCVN	300	U	6.063
			M	5.709
			D	5.355
5	DCT	300	1	5.019
			2	4.881
			3	4.743
			4	4.605
			5	4.467
			6	4.329
			7	4.191
			8	4.053
			9	3.915
6	M3-PCCVN	300	U	3.416
			M	3.060
			D	2.703
7	SS-J3, APFIM, MMPC	300	U	2.005
			D	1.369
8	M5-PCCVN	400	U	0.549
			UM	0.193
			M	-0.163
			MD	-0.519
			D	-0.875
9	M5-PCCVN	650	U	-1.733
			UM	-2.089
			M	-2.445
			MD	-2.801
			D	-3.157
10	SS-J3, APFIM, MMPC	300	U	-3.977
			D	-4.613
11	DCT	300	1	-5.116
			2	-5.254
			3	-5.392
			4	-5.530
			5	-5.668
			6	-5.806
			7	-5.944
			8	-6.082
			9	-6.220
12	SS-J3, APFIM, MMPC	300	U	-6.722
			D	-7.358
13	SS-J3, APFIM, MMPC	300	U	-8.017
			D	-8.653
14	TEM	650	-	-9.382

*HMP – Horizontal mid-plane of the HFIR

Table 4. JP-30 specimen and dosimetry loading list.

Pos. 1 JP-30	SS-J3 Tensile Specimen	APFIM/MMPC Specimen	Passive Thermometry
Top Half	1a. inner **XXG1**	1. **0G5**	1. **0001**
	1b. outer **2G1**		
	2a. inner **XXG2**	2. **2G5**	2. **0002**
	2b. outer **2G2**		
	3a. inner **XXG3**	3a. **XXG4**	3. **0003**
	3b. outer **2G3**	3b. **XXG5**	
	4a. inner **HDG1**	4a. **HDG1+HGAh**	4. **0004**
	4b. outer **2G4**	4b. **YEG1**	
Bottom Half	SS-J3 Tensile Specimen	APFIM/MMPC Specimen	Passive Thermometry
	5a. inner **XWG1**	5. **25G5**	5. **0005**
	5b. outer **25G1**		
	6a. inner **XWG2**	6. **HGJ**	6. **0006**
	6b. outer **25G2**		
	7a. inner **XWG3**	7a. **XWG4**	7. **0007**
	7b. outer **25G3**	7b. **XWG5**	
	8a. inner **HDG2**	8a. **YGG1**	8. **0008**
	8b. outer **25G4**	8b. **HGT**	

Pos. 2 JP-30	DCT Specimen
	1. **YCHG**
	2. **YCHH**
	3. **YCHJ**
	4. **YCHK**
	5. **YCHL**
	6. **YCHM**
	7. **YCHN**
	8. **YCHP**
	9. **YCHQ**

Pos. 3 JP-30	SS-J3 Tensile Specimen	APFIM/MMPC Specimen	Passive Thermometry
Top Half	1a. inner **2E1**	1. **0EAp**	1. **0009**
	1b. outer **2E3**		
	2a. inner **2E2**	2. **2E7**	2. **0010**
	2b. outer **2E4**		
	3a. inner **1E1**	3. **2E8**	3. **0011**
	3b. outer **25E3**		
	4a. inner **1E2**	4. **HEA**	4. **0012**
	4b. outer **25E4**		
Bottom Half	SS-J3 Tensile Specimen	APFIM/MMPC Specimen	Passive Thermometry
	5a. inner **27E1**	5. **0EAr**	5. **0013**
	5b. outer **0E1**		
	6a. inner **27E2**	6. **25E7**	6. **0014**
	6b. outer **0E2**		
	7a. inner **25E1**	7. **25E8**	7. **0015**
	7b. outer **0E3**		
	8a. inner **25E2**	8. **HEB**	8. **0016**
	8b. outer **0E4**		

Pos. 4 JP-30	DCT Specimen
	1. **0EQ**
	2. **0ER**
	3. **0ES**
	4. **0ET**
	5. **0EU**
	6. **0EZ**
	7. **0EAa**
	8. **YCEA**
	9. **YCEB**

Pos. 5 JP-30	M3-PCCVN Specimen	Passive Thermometry	
	1. outer **0E9**		
	2. inner **27E9**		
	3. inner **27E0**		
	4. outer **0E0**	1. **0111**	2. **0112**
	5. outer **0EA**		
	6. inner **27EA**		
	7. inner **27EB**		
	8. outer **0EB**		

Pos. 6 JP-30	DCT Specimen
	1. **1G5**
	2. **1G6**
	3. **1G9**
	4. **1G0**
	5. **1GA**
	6. **1GB**
	7. **HGV**
	8. **HGZ**
	9. **HGAb**

Pos. 7 JP-30	SS-J3 Tensile Specimen	APFIM/MMPC Specimen	Passive Thermometry
Top Half	1a. inner **1G1**	1. **0G6**	1. **0017**
	1b. outer **0G1**		
	2a. inner **1G2**	2. **2G6**	2. **0018**
	2b. outer **0G2**		
	3a. inner **1G3**	3. **25G6**	3. **0019**
	3b. outer **0G3**		
	4a. inner **1G4**	4. **HGK**	4. **0020**
	4b. outer **0G4**		
Bottom Half	SS-J3 Tensile Specimen	APFIM/MMPC Specimen	Passive Thermometry
	5a. inner **27G1**	5a. **HGG**	5. **0021**
	5b. outer **HGP**	5b. **HGH**	
	6a. inner **27G2**	6a. **YJG1**	6. **0084**
	6b. outer **HGQ**	6b. **YNG1**	
	7a. inner **27G3**	7a. **YAG0**	7. **0023**
	7b. outer **HGR**	7b. **YAG1**	
	8a. inner **27G4**	8a. **YCG0**	8. **0083**
	8b. outer **HGS**	8b. **YCG1**	

Pos. 8 JP-30	DCT Specimen
	1. **27G5**
	2. **27G6**
	3. **27G9**
	4. **27G0**
	5. **27GA**
	6. **27GB**
	7. **HGAc**
	8. **HGAe**
	9. **HGAf**

Pos. 9 JP-30	SS-J3 Tensile Specimen	APFIM/MMPC Specimen	Passive Thermometry
Top Half	1a. inner **HDH1**	1a. **YNH1**	1. **0025**
	1b. outer **YMH1**	1b. **YMH1**	
	2a. inner **HDH2**	2a. **HDH1**+**HDH2**	2. **0026**
	2b. outer **YMH2**	2b. **YEH2**	
	3a. inner **HDH3**	3a. **HDH3**+**HDH4**	3. **0027**
	3b. outer **YAHA**	3b. **YGH1**	
	4a. inner **HDH4**	4a. **YEH1**	4. **0028**
	4b. outer **YAHB**	4b. **YGH2**	
Bottom Half	SS-J3 Tensile Specimen	APFIM/MMPC Specimen	Passive Thermometry
	5a. inner **YBHA**	5a. **YKH1**	5. **0090**
	5b. outer **YJH1**	5b. **YJH1**	
	6a. inner **YBHB**	6. **YDH0**	6. **0030**
	6b. outer **YJH2**		
	7a. inner **YCHA**	7a. **YEH3**	7. **0031**
	7b. outer **YKH1**	7b. **YEH4**	
	8a. inner **YCHB**	8a. **YGH3**	8. **0032**
	8b. outer **YKH2**	8b. **YGH4**	

Pos. 10 JP-30	M2-PCCVN Specimen	Passive Thermometry	
	1. outer **23E2**		
	2. inner **24E1**		
	3. inner **24E2**		
	4. outer **23E3**	1. **0101**	2. **0102**
	5. outer **23E4**		
	6. inner **24E3**		
	7. inner **24E4**		
	8. outer **23E6**		

Pos. 11 JP-30	M3-PCCVN Specimen	Passive Thermometry	
	1. outer **HER**		
	2. inner **1E9**		
	3. inner **1EA**		
	4. outer **HES**	1. **0113**	2. **0121**
	5. outer **HET**		
	6. inner **1EB**		
	7. inner **YJE3**		
	8. outer **HEU**		

Pos. 12 JP-30	M3-PCCVN Specimen	Passive Thermometry	
	1. outer **YME1**		
	2. inner **YKE1**		
	3. inner **YKE2**		
	4. outer **YME2**	1. **0115**	2. **0122**
	5. outer **YME3**		
	6. inner **YKE3**		
	7. inner **YJE1**		
	8. outer **YJE2**		

Pos. 13 JP-30	M3-PCCVN Specimen	Passive Thermometry	
	1. outer **XWE4**		
	2. inner **XSE4**		
	3. inner **XSE5**		
	4. outer **XWE5**	1. **0117**	2. **0118**
	5. outer **XWE6**		
	6. inner **XSE6**		
	7. inner **XYE4**		
	8. outer **XYE6**		

Pos. 14 JP-30	TEM Specimen Numbers								Passive Thermometry in Center Hole
		Hole No. 1	Engr. Face	Hole No. 2	Engr. Face	Hole No. 3	Engr. Face	Hole No. 4	Engr. Face	
Bottom	1	**H 04**	Down	**HPA 07**	Either	**2 02**	Down	**YJE1**	Either	
	2	**O 03**	Up	**TA 09**	Down	**E 2**	Up	**YJE2**	Either	
	3	**H 05**	Down	**C8 02**	Up	**MB 04**	Down	**YJE3**	Either	
	4	**O 04**	Up	**HD 06**	Down	**C2 02**	Up	**YKE1**	Either	
	5	**2 04**	Down	**Y B**	Up	**MB 05**	Down	**YKE2**	Either	
	6	**E 3**	Up	**HD 09**	Down	**C2 01**	Up	**YKE3**	Either	
	7	**2 05**	Down	**Y 2**	Up	**NF 01**	Down	**YME1**	Either	
	8	**E 4**	Up	**HD 11**	Down	**C5 02**	Up	**YME2**	Either	
	9	**2 06**	Down	**G 2**	Up	**NF 03**	Down	**YME3**	Either	
	10	**HPA 03**	Up	**CB 01**	Down	**C5 01**	Up	**YNE1**	Either	
	11	**MB 01**	Down	**G E**	Up	**TA 07**	Down	**YNE2**	Either	
	12	**C2 03**	Up	**CB 03**	Down	**C8 01**	Up	**YNE3**	Either	
	13	**MB 02**	Down	**HPA 12**	Up	**TA 08**	Down	**YAE2**	Either	
	14	**C5 03**	Up	**NF 07**	Up	**C8 11**	Up	**YAE3**	Either	No ID
	15	**MB 03**	Down	**NF 06**	Up	**CB 05**	Down	**YAE4**	Either	
	16	**C8 04**	Up	**H 01**	Down	**HPA 14**	Up	**YAE5**	Either	
	17	**TA 01**	Down	**O 01**	Up	**CB 04**	Down	**YBE2**	Either	
	18	**C2 04**	Up	**H 02**	Down	**HPA 01**	Up	**YBE3**	Either	
	19	**TA 05**	Down	**O 07**	Up	**HD 01**	Up	**YBE4**	Either	
	20	**C5 04**	Up	**2 01**	Down	**HD 02**	Up	**YBE5**	Either	
	21	**NF 04**	Down	**E 1**	Up	**O 13**	Either	**YCE2**	Either	
	22	**(no ID)**	* 1	**CB 02**	Down	**C2 11**	Either	**YCE3**	Either	
	23			**(no ID)**	*1	**C5 11**	Either	**YCE4**	Either	
	24					**C8 08**	Either	**YCE5**	Either	
	25							**HD 28**	Either	
	26							**Y 9**	Either	
Top	27							**G 3**	Either	

*1 W/KU15ODS, shinier side to face down

Table 5. JP-31 specimen and dosimetry loading list.

Pos. 1 JP-31		TEM Specimen Numbers								Passive Thermometry in Center Hole
		Hole No. 1	Engr. Face	Hole No. 2	Engr. Face	Hole No. 3	Engr. Face	Hole No. 4	Engr. Face	
Bottom	1	H 07	Down	HPA 13	Either	2 08	Down	YJG1	Either	
	2	O 08	Up	TA 18	Down	E 6	Up	YJG2	Either	
	3	H 08	Down	C8 09	Up	MB 06	Down	YJG3	Either	
	4	O 05	Up	HD 12	Down	C2 05	Up	YKG1	Either	
	5	2 07	Down	Y 3	Up	MB 11	Down	YKG2	Either	
	6	E 7	Up	HD 13	Down	C5 05	Up	YKG3	Either	
	7	2 09	Down	Y 4	Up	NF 05	Down	YMG1	Either	
	8	E 8	Up	HD 18	Down	C2 09	Up	YMG2	Either	
	9	2 10	Down	G 3	Up	NF 10	Down	YMG3	Either	
	10	HPA 06	Up	CB 09	Down	C5 10	Up	YNG1	Either	
	11	MB 08	Down	G 4	Up	TA 13	Down	YNG2	Either	
	12	C2 07	Up	CB 11	Down	O 09	Up	YNG3	Either	
	13	MB 09	Down	HPA 08	Up	TA 17	Down	YAG2	Either	No ID
	14	C5 06	Up	NF 08	Up	C8 06	Up	YAG3	Either	
	15	MB 10	Down	NF 09	Up	CB 06	Down	YAG4	Either	
	16	C8 07	Up	H 03	Down	HPA 10	Up	YAG5	Either	
	17	TA 10	Down	O 06	Up	CB 14	Down	YBG2	Either	
	18	C2 08	Up	H 06	Down	HPA 15	Up	YBG3	Either	
	19	TA 15	Down	C8 05	Up	HD 15	Up	YBG4	Either	
	20	C5 09	Up	2 03	Down	HD 03	Up	YBG5	Either	
	21	CB 10	Down	E 5	Up	O 10	Either	YCG2	Either	
	22	(no ID)	*1	NF 12	Down	C2 10	Either	YCG3	Either	
	23			(no ID)	*1	C5 07	Either	YCG4	Either	
	24					C8 10	Either	YCG5	Either	
	25							HD 22	Either	
	26							Y 6	Either	
Top	27							G D	Either	

*1 W/KU15ODS, shinier side to face down

Pos. 2 JP-31	SS-J3 Tensile Specimen	APFIM/MMPC Specimen	Passive Thermometry
Top Half	1a. inner XYG1	1. 0G7	1. 0033
	1b. outer YJG3		
	2a. inner XYG2	2. 2G7	2. 0034
	2b. outer YKG1		
	3a. inner YJG1	3. 25G7	3. 0035
	3b. outer XTG1		
	4a. inner YJG2	4. HGM	4. 0036
	4b. outer XTG2		
Bottom Half	SS-J3 Tensile Specimen	APFIM/MMPC Specimen	Passive Thermometry
	5a. inner YKG2	5a. YMG1	5. 0037
	5b. outer XSG1	5b. YKG1	
	6a. inner YKG3	6a. XSG4	6. 0038
	6b. outer XSG2	6b. XSG5	
	7a. inner YMG1	7a. XYG4	7. 0039
	7b. outer XSG3	7b. XYG5	
	8a. inner YMG2	8. 0G8	8. 0040
	8b. outer XYG3		

Pos. 3 JP-31	SS-J3 Tensile Specimen	APFIM/MMPC Specimen	Passive Thermometry	
Top Half	1a. inner **YAHC**	1. **YDH1**	1. **0041**	
	1b. outer **YCHC**			
	2a. inner **YAHD**	2. **YDH2**	2. **0042**	
	2b. outer **YCHD**			
	3a. inner **YBHC**	3. **YDH3**	3. **0043**	
	3b. outer **YDHE**			
	4a. inner **YBHD**	4a. **YAH2**	4. **0044**	
	4b. outer **YDHF**	4b. **YCH2**		
Bottom Half	SS-J3 Tensile Specimen	APFIM/MMPC Specimen	Passive Thermometry	
	5a. inner **YAHE**	5a. **YAH0**	5. **0045**	
	5b. outer **YCHE**	5b. **YAH1**		
	6a. inner **YAHF**	6a. **YBH0**	6. **0046**	
	6b. outer **YCHF**	6b. **YBH1**		
	7a. inner **YBHE**	7a. **YCH0**	7. **0047**	
	7b. outer **YDHG**	7b. **YCH1**		
	8a. inner **YBHF**	8. **YDH4**	8. **0048**	
	8b. outer **YDHH**			

Pos. 4 JP-31	M2-PCCVN Specimen	Passive Thermometry	
	1. outer **23E7**		
	2. inner **24E5**		
	3. inner **24E6**		
	4. outer **23E8**	1. **0103**	2. **0104**
	5. outer **23E9**		
	6. inner **24E7**		
	7. inner **24E8**		
	8. outer **23E10**		

Pos. 5 JP-31	DCT Specimen
	1. **27E7**
	2. **27E8**
	3. **27EC**
	4. **27EE**
	5. **27EG**
	6. **27EH**
	7. **27EJ**
	8. **YCEC**
	9. **YCED**

Pos. 6 JP-31	M3-PCCVN Specimen	Passive Thermometry	
	1. outer **0EC**		
	2. inner **XXE6**		
	3. inner **XXE7**		
	4. outer **0EE**	1. **0119**	2. **0120**
	5. outer **0EH**		
	6. inner **XXE0**		
	7. inner **XYE5**		
	8. outer **0EJ**		

Pos. 7 JP-31	SS-J3 Tensile Specimen	APFIM/MMPC Specimen	Passive Thermometry
Top Half	1a. inner **1E3** 1b. outer **2E5**	1. **0EAe**	1. **0049**
	2a. inner **1E4** 2b. outer **2E6**	2. **2E9**	2. **0050**
	3a. inner **1E5** 3b. outer **25E5**	3. **2E0**	3. **0051**
	4a. inner **1E6** 4b. outer **25E6**	4a. **HE9** 4b. **HE0**	4. **0052**
Bottom Half	SS-J3 Tensile Specimen	APFIM/MMPC Specimen	Passive Thermometry
	5a. inner **27E3** 5b. outer **0E5**	5. **0EAf**	5. **0053**
	6a. inner **27E4** 6b. outer **0E6**	6. **25E9**	6. **0054**
	7a. inner **27E5** 7b. outer **0E7**	7. **25E0**	7. **0055**
	8a. inner **27E6** 8b. outer **0E8**	8a. **0EAb** 8b. **0EAc**	8. **0056**

Pos. 8 JP-31	M5-PCCVN Specimen	Passive Thermometry	
	1. outer **0G9**		
	2. inner **1G7**		
	3. inner **1G8**		
	4. outer **0G0**	1. **0135**	2. **0132**
	5. outer **YJG1**		
	6. inner **27G7**		
	7. inner **27G8**		
	8. outer **YJG2**		

Pos. 9 JP-31	M5-PCCVN Specimen	Passive Thermometry	
	1. outer **YJH3**		
	2. inner **YDHA**		
	3. inner **YDHB**		
	4. outer **YJH4**	1. **0136**	2. **0138**
	5. outer **YJH1**		
	6. inner **YDHC**		
	7. inner **YDHD**		
	8. outer **YJH2**		

Pos. 10 JP-31	SS-J3 Tensile Specimen	APFIM/MMPC Specimen	Passive Thermometry
Top Half	1a. inner **21E1**	1. **0EAg**	1. **0057**
	1b. outer **26E1**		
	2a. inner **21E2**	2. **2EA**	2. **0058**
	2b. outer **26E2**		
	3a. inner **22E1**	3. **25EA**	3. **0059**
	3b. outer **26E3**		
	4a. inner **22E2**	4. **HEC**	4. **0060**
	4b. outer **22E3**		
Bottom Half	SS-J3 Tensile Specimen	APFIM/MMPC Specimen	Passive Thermometry
	5a. inner **XXE1**	5. **0EAh**	5. **0061**
	5b. outer **HEK**		
	6a. inner **XXE2**	6. **HEE**	6. **0087**
	6b. outer **HEM**		
	7a. inner **XXE3**	7. **HEG**	7. **0088**
	7b. outer **HEP**		
	8a. inner **XXE4**	8a. **XXE8**	8. **0089**
	8b. outer **HEQ**	8b. **XXE9**	

Pos. 11 JP-31	DCT Specimen
	1. **1E7**
	2. **1E8**
	3. **1EC**
	4. **1EE**
	5. **1EG**
	6. **1EH**
	7. **1EJ**
	8. **YCEE**
	9. **YCEF**

Pos. 12 JP-31	SS-J3 Tensile Specimen	APFIM/MMPC Specimen	Passive Thermometry
Top Half	1a. inner **YCE6**	1. **0EAk**	1. **0065**
	1b. outer **YME1**		
	2a. inner **YCE7**	2a. **YNE1**	2. **0066**
	2b. outer **YME2**	2b. **YME1**	
	3a. inner **YCE8**	3a. **YAE0**	3. **0067**
	3b. outer **YME3**	3b. **YCE0**	
	4a. inner **YCE9**	4a. **YAE1**	4. **0068**
	4b. outer **YME4**	4b. **YCE1**	
Bottom Half	SS-J3 Tensile Specimen	APFIM/MMPC Specimen	Passive Thermometry
	5a. inner **YJE1**	5. **0EAm**	5. **0069**
	5b. outer **YKE1**		
	6a. inner **YJE2**	6a. **YJE1**	6. **0070**
	6b. outer **YKE2**	6b. **YKE1**	
	7a. inner **YJE3**	7a. **YBE0**	7. **0086**
	7b. outer **YKE3**	7b. **HDE1**+**HDE2**	
	8a. inner **HDE1**	8a. **YBE1**	8. **0072**
	8b. outer **HDE2**	8b. **HDE3**+**HDE4**	

143

Pos. 13 JP-31	SS-J3 Tensile Specimen	APFIM/MMPC Specimen	Passive Thermometry
Top Half	1a. inner **XTE1**	1. **0EAn**	1. **0073**
	1b. outer **XSE1**		
	2a. inner **XTE2**	2a. **XWE7**	2. **0074**
	2b. outer **XSE2**	2b. **XSE7**	
	3a. inner **XWE1**	3a. **XWE8**	3. **0075**
	3b. outer **XSE3**	3b. **XSE8**	
	4a. inner **XWE2**	4. **HEZ**	4. **0085**
	4b. outer **XTE3**		
Bottom Half	SS-J3 Tensile Specimen	APFIM/MMPC Specimen	Passive Thermometry
	5a. inner **XYE1**	5. **0EAo**	5. **0077**
	5b. outer **BAE1**		
	6a. inner **XYE2**	6a. **XYE7**	6. **0078**
	6b. outer **BAE2**	6b. **YEE2**	
	7a. inner **XYE3**	7a. **XYE8**	7. **0079**
	7b. outer **BAE3**	7b. **YGE1**	
	8a. inner **XWE3**	8a. **YEE1**	8. **0080**
	8b. outer **BAE4**	8b. **YGE2**	

Pos. 14 JP-31	TEM Specimen Numbers								Passive Thermometry in Center Hole
		Hole No. 1	Engr. Face	Hole No. 2	Engr. Face	Hole No. 3	Engr. Face	Hole No. 4	Engr. Face	
Bottom	1	**MB 15**	Down	**MB 18**	Down	**NF 11**	Down	**YJH1**	Either	No ID
	2	**ZS 03**	Up	**ZS 02**	Up	**ZQ 12**	Up	**YJH2**	Either	
	3	**MB 12**	Down	**MB 07**	Down	**NF 14**	Down	**YJH3**	Either	
	4	**ZQ 07**	Up	**ZQ 05**	Up	**ZQ 15**	Up	**YKH1**	Either	
	5	**MB 13**	Down	**MB 14**	Down	**HD 16**	Down	**YKH2**	Either	
	6	**ZQ 08**	Up	**ZQ 04**	Up	**Y 8**	Up	**YKH3**	Either	
	7	**MB 16**	Down	**MB 17**	Down	**HD 08**	Down	**YMH1**	Either	
	8	**ZQ 10**	Up	**ZS 11**	Up	**G D**	Up	**YMH2**	Either	
	9	**NF 15**	Down	**NF 02**	Down	**CB 19**	Up	**YMH3**	Either	
	10	**ZS 06**	Up	**ZS 12**	Up	**CB 21**	Either	**YNH1**	Either	
	11	**NF 17**	Down	**NF 13**	Down	**CB 23**	Either	**YNH2**	Either	
	12	**ZS 08**	Up	**Y 7**	Up	**ZQ 13**	Either	**YNH3**	Either	
	13	**NF 18**	Down	**NF 16**	Down	**ZQ 03**	Either	**YAH2**	Either	
	14	**ZS 10**	Up	**Y 5**	Up	**ZS 01**	Either	**YAH3**	Either	
	15	**HD 19**	Down	**HD 05**	Down	**ZS 05**	Either	**YAH4**	Either	
	16	**Y E**	Up	**Y C**	Up	**HD 23**	Either	**YAH5**	Either	
	17	**HD 20**	Down	**HD 14**	Down	**HD 24**	Either	**YBH2**	Either	
	18	**Y A**	Up	**G 5**	Up	**Y 1**	Either	**YBH3**	Either	
	19	**HD 21**	Down	**HD 17**	Down	**Y D**	Either	**YBH4**	Either	
	20	**G 9**	Up	**G 7**	Up	**G A**	Either	**YBH5**	Either	
	21	**CB 12**	Down	**CB 08**	Down	**G 8**	Either	**YCH2**	Either	
	22	**G 6**	Up	**G B**	Up	**CB 15**	Up	**YCH3**	Either	
	23	**CB 17**	Down	**CB 20**	Up	**CB 18**	Down	**YCH4**	Either	
Top	24	**(no ID)**	*1	**CB 16**	Up	**(no ID)**	*1	**YCH5**	Either	

*1 W/KU15ODS, shinier side to face down

REFERENCES

[1] D. K. Felde, D. W. Heatherly, S. H. Kim, R. G. Sitterson, R. E. Stoller, C. Wang, M. Ando and H. Tanigawa, Fusion Materials Semiannual Progress Report for Period Ending June 30, 2005, DOE/ER-0313/38, U. S. Department of Energy, 153.

[2] J. McDuffee, D. Heatherly, and N. Cetiner, Fusion Materials Semiannual Progress Report for Period Ending December 31, 2010, DOE/ER-0313/49, U. S. Department of Energy, 115.

9.2 HFIR IRRADIATION EXPERIMENTS – January 31, 2012 — Y. Katoh and J. McDuffee
(Oak Ridge National Laboratory)

Summary of Recent, Current and Planned Fusion Materials Program Experiments

Experiment Designation	Primary Materials	Specimen Types*	Irradiation Temperature (°C)	Max Exposure (dpa)	Number of Reactor Cycles	Irradiation Period (month/year)
Beryllium reflector (RB) irradiation positions						
RB-15J	F82H	T, F, FT	300, 400	6	10	6/08 – 12/09
Target zone full-length capsules						
JP-25	F82H	T, FT	300, 500	20	10	2/99 - 1/01
JP-26	F82H	T, FT	300,400,500	9	5	12/03-11/04
JP-27	F82H	T, FT	300, 400	21	13	12/03 - 1/08
JP-28	F82H	T, FT	300,400,500	80	~50	4/05 –
JP-29	F82H	T, FT	300,400,500	80	~50	1/05 -
12-DCT	F82H	DCT	50	1.6	1	7/11
JP-30	F82H	T, FT	300,400,650	20	~10	11/11 -
JP-31	F82H	T, FT	300,400,650	20	~10	11/11 -
Target zone rabbit capsules (DOE-JAEA)						
F8A1	F82H	T, FT	300	50	28	2/09 –
F8A2	"	"	"	"	"	"
F8B1	"	"	"	"	"	"
F8B2	"	"	"	"	"	"
JCR-1	SiC/SiC	Bend bars	800	30	15	10/04 – 1/09
JCR-2	"	"	"	"	"	"
JCR-3	"	"	"	"	"	"
JCR-4	"	"	"	"	"	"
JCR-5	"	"	"	>50	>25	10/04 -
JCR-6	"	"	"	"	"	"
JCR-7	"	"	"	"	"	"
JCR-8	"	"	"	"	"	"
JCR-9	"	"	500	30	15	10/04 – 1/09
JCR-10	"	"	"	"	"	"
JCR-11	"	"	"	"	"	"
JCR-12	"	"	"	"	"	"
F11A3	F82H	T, FT	300	20	12	5/11 –
F11A4	"	"	"	"	"	"
F11B3	"	"	"	"	"	"
M4-TEN	F82H	DCT	50	1.6	1	7/11

Experiment Designation	Primary Materials	Specimen Types*	Irradiation Temperature (°C)	Max Exposure (dpa)	Number of Reactor Cycles	Irradiation Period (month/year)
Target zone rabbit capsules (TITAN)						
T8A1	SiC	BSR	300	0.01	HT	10/09
T8A2	SiC	BSR	300	0.1	HT	10/09
T8B1	SiC	BSR	500	0.01	HT	10/09
T8B2	SiC	BSR	500	0.1	HT	10/09
T8C1	SiC	BSR	500	~1	1	5/09
T8D1	SiC	BSR	800	0.1	HT	3/11
T8E1	SiC	BSR	800	~1	1	8/09
T8F1	SiC	BSR	1200	~1	1	8/09
T9A1	W, Ni	Discs	90	0.1	HT	1/09
T9A2	W, Ni	Discs	90	1.2	1	1/09
T9C1	Steels	T, MC	500	5.5	3	11/09 – 2/10
T9C2	Steels	T, MC	500	9.6	5	11/09 – 6/10
T9G1	Steels	T, MC	300	1.2	1	6/09 – 8/09
T9G2	Steels	T, MC	300	9.6	8	6/09 – 8/11
MTTN01	Steels	T, MC	300	4.8	4	1/12 -
TTN09	SiC	Joint	500	3.4	2	8/11 - 11/11
TTN10	SiC	Joint	500	4.1	2	8/11 - 11/11
TTN11	SiC	Joint	800	4	2	3/12 - 5/12
TTN01	SiC	BSR	300	1	1	2/11 -
TTN02	SiC	BSR	300	10	6	2/11 -
TTN03	SiC	BSR	300	20	11	2/11 -
TTN04	SiC	BSR	500	10	6	5/11 -
TTN05	SiC	BSR	500	20	11	5/11 -
TTN06	SiC	BSR	800	10	6	5/11 -
TTN07	SiC	BSR	800	20	11	5/11 -
TTN08	SiC	BSR	1200	10	6	5/11 -
TTN16	SiC	Fiber BSR	500	1	1	
TTN17	SiC	Fiber BSR	500	10	6	8/11 -
TTN18	SiC	Fiber BSR	500	20	11	8/11 -
TTN19	SiC	Fiber BSR	1200	1	1	
TTN20	SiC	Fiber BSR	1200	10	6	

*T = Tensile, F = Fatigue, FT = Fracture Toughness, MC = Multipurpose Coupon, BSR = Bend Stress Relaxation Creep, DCT = Disc Compact Tension. Most experiments also contain TEM disks, other special purpose specimens, and monitors occupying small spaces.